

Université
de Toulouse

THÈSE

En vue de l'obtention du DOCTORAT DE L'UNIVERSITÉ DE TOULOUSE

Délivré par :
Institut National Polytechnique de Toulouse (INP Toulouse)

Discipline ou spécialité :
Dynamique des Fluides

Présentée et soutenue par :
Ali ÖZEL

le : Mardi 18 Octobre 2011

Titre :

Simulation aux grandes échelles des lits fluidisés U_d > U_{mf} fegaz-particule

Ecole doctorale :
Mécanique, Energétique, Génie civil et Procédés (MEGeP)

Unité de recherche :
Institut de Mécanique des Fluides de Toulouse (IMFT)

Directeur(s) de Thèse :

Olivier SIMONIN	Professeur à l'INP Toulouse	Directeur de Thèse
Pascal FEDE	Maître de Conférence à l'UPS	Co-directeur de Thèse

Rapporteurs :

Sankaran SUNDARESAN	Professeur à l'Université de Princeton
Berend van WACHEM	Professeur Associé à l'Imperial College London

Membre(s) du jury :

Olivier MASBERNAT	Directeur de Recherche au CNRS	Président
Berend van WACHEM	Professeur Associé à l'Imperial College London	Rapporteur
Amini SHAHRIAR	Chercheur Senior au SINTEF	Examineur
Régis ANDREUX	Yé [W]dà l'IFP7@	Examineur

Ali Özel

Anneme, babama,
guzel kız kardeşlerime,
dayıma, anneanneme, dedemin ve babaannemin hatırasına.

ACKNOWLEDGMENTS

Ce travail de thèse a été réalisé au sein de l'Institut de Mécanique des Fluides de Toulouse, dans le groupe Particule, Spray et Combustion et je veux remercier tous ceux qui en ont fait partie de manière directe ou indirecte.

Je tiens à remercier en tout premier lieu le Professeur Olivier Simonin, un mentor hors classe et à l'intuition géniale, qui m'a accueilli au sein son équipe de recherche au PSC. J'ai eu la chance de profiter de ses connaissances scientifiques et j'ai appris beaucoup à ses côtés. Merci pour la confiance que vous m'avez accordé. Enfin pour ses qualités humaines qui ont favorisé la relation qui nous lie au terme de ces quatre années.

J'adresse des remerciements particuliers à Pascal Fede de m'avoir son aide et ses précieux conseils. Ensuite, pour la qualité de son encadrement; la majorité de ce travail n'aurait pu être réalisé sans vous.

J'adresse toute ma reconnaissance aux membres de mon jury de thèse, notamment mes deux rapporteuses : le Professeur Sankaran Sundaresan, de l'Université de Princeton, le Professeur Associé Berend van Wachem, de l'Imperial College London. Mes sincères remerciements vont à Olivier Masbernat, le Directeur de Recherche au CNRS, pour sa gentillesse, ses conseils et ses encouragements. Ma reconnaissance s'adresse aussi à Amini Shahriar, Chercheur Senior au SINTEF et Régis Andreux, Habilitation à Diriger des Recherches à l'IFP, pour leur participation au jury de ma thèse.

Cette partie est dédiée à mes amis de Toulouse. Tugce ve Zafer'e, güzel geçirdiğimiz günleri, sıkıntılı anlarda bana olan desteğinizi ve sizde yediğim yemekleri unutamam, umarım bundan sonra herşey istediğiniz gibi olur, teşekkürler; Selime'ye, dengeyi yitirdiğimde dengeyi bulmama ve kut'um dağıldığında toplamama yardım ettiği için kucak dolusu sevgiler, Jean-Mathieu ile renkli güneşli günler dileğiyle; a Santiago y Rabia, para darme espero y el mejor amplificador de bajo, gracias; Mr. Benjamin François pour avoir organisé toutes ces fêtes, ton amitié et bonne continuation pour ta thèse; Fila for your shiny smiling face; Dr. Arthur Sarthou pour les discussions intéressantes sur le "black-magic", la vie végétarienne et les verres; Arthur N'dri Konan, pour ton accueil du début jusqu'à la fin de ma thèse; Guillaume Jacob et Guillaume Lecoq; pour vos amitiés, see you in Turkey guys this summer.

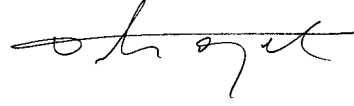
Je tiens à remercier l'ensemble des stagiaires, doctorants, post-doc et permanents qui contribuent à l'ambiance extrêmement conviviale qui règne dans le groupe PSC (anciennement EEC). Un merci aux collègues mignonnes, Marie-Charlotte et Marion P., à Enrica avec qui j'ai partagé clopes et cafés et à sa famille pour tous ces repas très délicieux, à Nicolas, Guillaume, Alice et Romain pour les souvenirs inoubliables aux bars Irlandaises, à Marco Martins Alfonso per la discussione di Genova, Galata ed il football, à Dirk et Jeanne pour les pinque-niques à Peche David, à Mehdi "Alzheimer" pour le mariage chinois-marocain, à Mehdi S. pour les mots Irlandais, clopes et cafés et bonne continuation pour la suite, à Anne pour les photos de ma sountance, à Renaud et Marion pour la photo de Guinness, à Amine, bonne continuation pour la future, à Florent et Florian, mes seigneurs et mes maiters, à Daniel, Aurélien, Adrien J. et Adrien B., Julien, Moïse, Olivier P. et Franck.

Türkiye'deki dostlarıma; hep orada olduğunu bildiğim için Hakan'a, İstanbul'da ve Türkiye'de geçirdiğimiz eğlenceli zamanlar için Busra ve balım Resul'e, beni dinç tuttuğu için Kesen'e, Toulouse'a beni ziyarete gelen Evren ile Mehlika'ya, bana gösterdikleri için Güneş'e, bana öğrettikleri için İlhan'a, harika sevimliliği için Güniz'e, tatlim Neco'ya, bombacı Veli'ye, Işıltan'a, Can'a, Kerem'e, Utku'ya, İlhan Yıldırım'a ve uzun konuşmalarımız için Emre'ye teşekkür ederim.

Mes derniers mots sont adressés à,

In pitch dark I go walking in your landscape
Broken branches trip me as I speak
Just 'cause you feel it doesn't mean it's there
There there, why so green and bright?

the boney king of nowhere



ABSTRACT

Eulerian two fluid approach is generally used to simulate gas-solid flows in industrial circulating fluidized beds. Because of limitation of computational resources, simulations of large vessels are usually performed by using too coarse grid. Coarse grid simulations can not resolve fine flow scales which can play an important role in the dynamic behaviour of the beds. In particular, cancelling out the particle segregation effect of small scales leads to an inadequate modelling of the mean interfacial momentum transfer between phases and particulate shear stresses by secondary effect. Then, an appropriate modelling accounting for influences of unresolved structures has to be proposed for coarse-grid simulations. For this purpose, computational grids are refined to get mesh-independent result where statistical quantities do not change with further mesh refinement for a 3-D periodic circulating fluidized bed. The 3-D periodic circulating fluidized is a simple academic configuration where gas-solid flow conducted with A-type particles is periodically driven along the opposite direction of the gravity. The particulate momentum and agitation equations are filtered by the volume averaging and the importance of additional terms due to the averaging procedure are investigated by budget analyses using the mesh independent result. Results show that the filtered momentum equation of phases can be computed on coarse grid simulations but sub-grid drift velocity due to the sub-grid correlation between the local fluid velocity and the local particle volume fraction and particulate sub-grid shear stresses must be taken into account. In this study, we propose functional and structural models for sub-grid drift velocity, written in terms of the difference between the gas velocity-solid volume fraction correlation and the multiplication of the filtered gas velocity with the filtered solid volume fraction. Particulate sub-grid shear stresses are closed by models proposed for single turbulent flows. Models' predictabilities are investigated by a priori tests and they are validated by coarse-grid simulations of 3-D periodic circulating, dense fluidized beds and experimental data of industrial scale circulating fluidized bed in manner of a posteriori tests.

RESUME

Les simulations numérique des équations d'Euler deux-fluides réalisé sur des maillages grossiers éliminent les structures fins d'écoulement gaz-solide dans les lits fluidisés. Pour précisément estimer la hydrodynamique globale de lit, il faut proposer une modélisation qui prend en compte les effets de structure non-résolue. Dans ce but, les maillages sont raffinées pour obtenir le résultat de simulation pleinement résolue ce que les grandeurs statistiques ne modifient plus avec un autre raffinement pour le lit fluidisé périodique dilué gaz-particules sur une géométrie 3D cartésienne et ce résultat est utilisé pour tests "a priori". Les résultats de tests "a priori" montrent que l'équation filtrée de la quantité de mouvement est effectuées mais il faut prendre en compte le flux de la fraction volumique de solide de sous-maille en raison de l'interaction locale de la vitesse du gaz et la fraction volumique de solide pour la force traniée. Nous proposons les modèles fonctionnels et structurels pour le flux de la fraction volumique de solide de sous-maille. En plus, Les modèles fermetures du tenseur de sous-maille de la phase dispersée sont similaires aux modèles classiquement utilisés en écoulement turbulent monophasique. Tout les modèles sont validés par test "a priori" et "a posteriori".

CONTENTS

1	INTRODUCTION	1
1.1	Fluidization of Particles	1
1.2	Circulating Fluidized Beds	1
1.3	State-of-the-art of CFB Simulations	2
1.4	Objective	5
1.5	Outlook of thesis	5
2	MATHEMATICAL MODELLING	7
2.1	Euler-Euler Formulation	7
2.2	Particulate Phase Model	7
2.2.1	Lagrangian Formulation	7
2.2.2	Kinetic Theory of Disperse Phase	8
2.2.3	Velocity Distribution Function	8
2.2.4	Transport Equations	10
2.2.5	Transport Equation of Particle Agitation, q_p^2	12
2.2.6	Collision Terms for Inelastic Rigid Particles	12
2.2.7	Radial Distribution Function	13
2.3	Gas Phase Model	13
2.4	Closure Models	16
2.4.1	Characteristic Time Scales	17
2.4.2	Modelling of Drift Velocity	17
2.4.3	Transport Equations of Gas Phase Turbulence	18
2.4.4	Modelling of Fluid-Particle Covariance, q_{fp}	19
2.4.5	Effective Kinetic Stress Tensor	20
2.4.6	Effective Diffusivity	21
2.5	Wall Boundary Conditions	22
2.6	Summary	23
3	PREDICTIONS USING BY URANS APPROACH	25
3.1	Introduction	25
3.1.1	Physical Models	25
3.1.2	Boundary Conditions	25
3.1.3	Convergence Criteria	26
3.1.4	Flow Characterisation	26
3.2	Simulations of Dilute Gas-particle Flow in a CFB riser	27
3.2.1	Description of Experimental Setup	27
3.2.2	Description of Numerical Simulation	29
3.2.3	Simulation Results	30
3.2.4	Parametric Studies	33
3.2.5	Summary	35
3.3	Simulations of dilute gas-particle flow in FCC riser-I	39
3.3.1	Description of Experimental Setup	39
3.3.2	Description of Numerical Simulation	39
3.3.3	Simulation Results	40

3.3.4	Parametric Studies	41
3.3.5	Summary	49
3.4	Simulations of Dilute Gas-Particle Flow in FCC riser-II	49
3.4.1	FCC System	49
3.4.2	Description of Numerical Simulations	49
3.4.3	Simulation Results	51
3.4.4	Parametric Studies	52
3.4.5	Summary	55
3.5	Conclusion	57
4	FILTERED TWO-FLUID MODEL APPROACH	59
4.1	Periodic Circulating Fluidized Bed Configuration	60
4.2	Mesh Independent Result	61
4.3	Derivation of Filtered Two-Fluid Model	65
4.4	Budget Analysis of Filtered Momentum Equation	71
4.5	Budget Analysis of The Random Kinetic Energy Equation of Particulate Phase	80
4.6	Summary	80
5	PARTICULATE SUB-GRID MODEL: DERIVATION AND A PRIORI STUDIES	83
5.1	Introduction	83
5.2	Functional Model for Effective Drag Force	84
5.3	Structural Models for Effective Drag Force	91
5.3.1	Germano's Decomposition	92
5.3.2	Gradient Model (Tensor Diffusivity Model)	93
5.3.3	Full Tensor Model	95
5.3.4	Mixed Model	96
5.3.5	Dynamic Structure Model	98
5.4	A Priori Analyses of Effective Drag Models' Predictability	99
5.5	Particle SGS Stress Tensor Models	100
6	PARTICULATE SUB-GRID MODEL: A POSTERIORI STUDIES	111
6.1	A Posteriori Studies of Periodic Circulating Fluidized Bed	111
6.1.1	Instantaneous Volume Fraction Field	112
6.1.2	Global Quantities	113
6.1.3	Radial Profiles of Time-averaged Variables by Smagorinsky-type Model (SGM)	115
6.1.4	Radial Profiles of Time-averaged Variables by Mixed Model (MM)	118
6.2	A Posteriori Studies of Dense Fluidized Bed	118
6.2.1	Flow Configuration	118
6.2.2	Simulation Results	121
6.3	Application to Dilute Gas-Particle Flow in FCC riser	121
7	CONCLUSION	125
A	APPENDIX	129
A.1	Appendix Section	129
	Bibliography	131

LIST OF FIGURES

Figure 1	The fluidization characteristics of solid particles by Geldart (1973).	2
Figure 2	Gas-solid classification according to Kunii and Levenspiel (1991) based on Geldart (1973)'s type of particles.	3
Figure 3	R2R resid FCC process (Andreux et al. 2008) (left) and the schematic view of CFBC (right).	3
Figure 4	The schematic view of the control volume containing both phases.	14
Figure 5	The experimental setup of Fabre (1995).	28
Figure 6	The computational domain of CERCHAR case.	29
Figure 7	Flow characteristics (CERCHAR).	31
Figure 8	Time characteristics (CERCHAR).	32
Figure 9	Instantaneous particle velocity vectors superimposed on the contour plot of instantaneous solid volume fraction at $z = 6.66$ m.	33
Figure 10	Predictions of reference case (mesh: $41 \times 31 \times 141, Fr_{\Delta, \min}^{-1} = 0.0093$) versus experimental data of Fabre (1995).	34
Figure 11	Predictions of reference case (mesh: $41 \times 31 \times 141, Fr_{\Delta, \min}^{-1} = 0.0093$) with and without turbulence model versus experimental data of Fabre (1995).	36
Figure 12	Predictions over fine mesh resolution (mesh: $81 \times 61 \times 161, Fr_{\Delta, \min}^{-1} = 0.0059$) with and without turbulence model versus experimental data of Fabre (1995).	37
Figure 13	Time-averaged gas and particle kinetic stresses.	38
Figure 14	The experimental setup of the pilot scale of FCC riser (Petit 2005).	39
Figure 15	The computational domain of FCC riser.	41
Figure 16	Flow characteristics (FCC).	42
Figure 17	Time characteristics (FCC).	43
Figure 18	Predictions of reference case (mesh: $11 \times 11 \times 900, Fr_{\Delta}^{-1} = 2.32$) versus experimental data of Petit (2005).	44
Figure 19	Instantaneous particle velocity vectors superimposed on the contour plot of instantaneous solid volume fraction at $z = 8.50$ m.	45
Figure 20	Predictions with different mesh resolutions (mesh: $11 \times 11 \times 900 - Fr_{\Delta}^{-1} = 2.32, 22 \times 22 \times 1800 - Fr_{\Delta}^{-1} = 1.16$) versus experimental data of Petit (2005).	46
Figure 21	Predictions of reference case (mesh: $11 \times 11 \times 900 - Fr_{\Delta}^{-1} = 2.32$) with different drag force models (Gobin et al. 2003, O'Brien and Syamlal 1993, Gibilaro et al. 1985) versus experimental data of Petit (2005).	48
Figure 22	Predictions of reference case (mesh: $22 \times 22 \times 1800, Fr_{\Delta}^{-1} = 1.16$) with different wall BCs for the particulate phase (free-slip and no-slip) versus experimental data of Petit (2005).	50
Figure 23	The experimental setup of Gauthier (2002) (FCC riser).	51

- Figure 24 The feeding of particle into riser. 51
- Figure 25 Predictions of reference case (mesh: $14 \times 14 \times 650$, $Fr_{\Delta}^{-1} = 18$) versus experimental data of Gauthier (2002). 53
- Figure 26 Predictions with different mesh resolutions (mesh: $14 \times 14 \times 650$ - $Fr_{\Delta}^{-1} = 18$, $28 \times 28 \times 1350$ - $Fr_{\Delta}^{-1} = 9$) versus experimental data of Gauthier (2002). 54
- Figure 27 Predictions of reference case (mesh: $14 \times 14 \times 650$, $Fr_{\Delta}^{-1} = 18$) with different drag forces (Gobin et al. 2003, O'Brien and Syamlal 1993, Gibilaro et al. 1985) versus experimental data of Gauthier (2002). 56
- Figure 28 Periodic circulating fluidized bed (PCFB). 60
- Figure 29 Instantaneous particle volume fraction field in the periodic circulating fluidized bed for different mesh resolutions (top: 3D view, bottom: $x - y$ plane). From right to left, the mesh resolution increases. White colour corresponds to $\alpha_p = 0$. Black colour corresponds to $\alpha_{p,max} = 0.64$. 62
- Figure 30 Influence of mesh size on the weighted gas-particle relative velocity $\langle \alpha_p (\overline{U_{p,z} - U_{g,z}})^t \rangle$ where o: corresponds to the homogeneous case and conv: corresponds to the converged case. 63
- Figure 31 Influence of mesh size on the non-dimensional total volumetric mass flux $\langle \overline{G_s} \rangle^t$ where o: corresponds to the homogeneous case and conv: corresponds to the converged case. 64
- Figure 32 Influence of mesh size on the random kinetic energy of particulate phase $\langle \overline{q_p^2} \rangle^t$ where conv: corresponds to the converged case. 64
- Figure 33 Time-averaged solid volume fraction along the radial direction for three mesh resolutions: moderate ($32 \times 32 \times 256$, $Fr_{\Delta}^{-1} = 0.128$), fine ($64 \times 64 \times 512$, $Fr_{\Delta}^{-1} = 0.064$) and finest ($128 \times 128 \times 1024$, $Fr_{\Delta}^{-1} = 0.032$) ($z = 0.11\text{m}$, $y = 0$). 65
- Figure 34 Time-averaged gas velocity along the radial direction for three mesh resolutions: moderate ($32 \times 32 \times 256$, $Fr_{\Delta}^{-1} = 0.128$), fine ($64 \times 64 \times 512$, $Fr_{\Delta}^{-1} = 0.064$) and finest ($128 \times 128 \times 1024$, $Fr_{\Delta}^{-1} = 0.032$) ($z = 0.11\text{m}$, $y = 0$). 66
- Figure 35 Time-averaged negative and positive solid mass flux along the radial direction for three mesh resolutions: moderate ($32 \times 32 \times 256$, $Fr_{\Delta}^{-1} = 0.128$), fine ($64 \times 64 \times 512$, $Fr_{\Delta}^{-1} = 0.064$) and finest ($128 \times 128 \times 1024$, $Fr_{\Delta}^{-1} = 0.032$) ($z = 0.11\text{m}$, $y = 0$). 66
- Figure 36 Time-averaged total solid mass flux along the radial direction for three mesh resolutions: moderate ($32 \times 32 \times 256$, $Fr_{\Delta}^{-1} = 0.128$), fine ($64 \times 64 \times 512$, $Fr_{\Delta}^{-1} = 0.064$) and finest ($128 \times 128 \times 1024$, $Fr_{\Delta}^{-1} = 0.032$) ($z = 0.11\text{m}$, $y = 0$). 67
- Figure 37 Time-averaged variance of solid volume fraction along the radial direction or three mesh resolutions: moderate ($32 \times 32 \times 256$, $Fr_{\Delta}^{-1} = 0.128$), fine ($64 \times 64 \times 512$, $Fr_{\Delta}^{-1} = 0.064$) and finest ($128 \times 128 \times 1024$, $Fr_{\Delta}^{-1} = 0.032$) ($z = 0.11\text{m}$, $y = 0$). 67

- Figure 38 CPU times required to simulate 1 s physical time using the kinetic theory based two-fluid model. 68
- Figure 39 Resolved and sub-grid contributions drag force and gas pressure gradient without hydrostatic part for different filter widths Δ_f (Normalised by gravity contribution). 73
- Figure 40 Resolved and sub-grid contributions of kinetic and sub-grid stresses for different filter widths Δ_f (Normalised by gravity contribution). 73
- Figure 41 Correlation coefficients between the filtered drag (l.h.s of Eq. (4.25)) and relative velocity weighted by solid volume fraction (r.h.s of Eq. (41)) for different filter widths Δ_f : \square, \circ : radial directions and \triangle : mean flow direction. 75
- Figure 42 Sub-grid drift velocity along the mean flow direction ($x = y = 0$) calculated directly from high resolution simulation, (4.24), and the difference between the weighted gas velocity by the particle volume fraction and the gas velocity, (4.28). for the filter width equal to $15\Delta_{DNS}$. 75
- Figure 43 Averaged sub-grid correlated energy $\sigma_{p,SGS}$ for different filter widths Δ_f . 77
- Figure 44 Sub-grid correlated energy $\bar{\alpha}_p \rho_p \sigma_{p,SGS}$ conditionally averaged by filtered volume fraction for filter widths, \blacksquare : $5\Delta_{DNS}$, \blacktriangle : $9\Delta_{DNS}$ and \blacklozenge : $13\Delta_{DNS}$. 77
- Figure 45 Resolved kinetic stress tensor trace $\bar{P}_p - \bar{\lambda}_p \frac{\partial \tilde{u}_{p,m}}{\partial x_m}$ conditionally averaged by filtered volume fraction for filter widths, \blacksquare : $5\Delta_{DNS}$, \blacktriangle : $9\Delta_{DNS}$ and \blacklozenge : $13\Delta_{DNS}$. 78
- Figure 46 Sub-grid dissipation $\bar{\alpha}_p \rho_p \sigma_{p,ij}^* \frac{\partial \tilde{u}_{p,i}}{\partial x_j}$ conditionally averaged by filtered volume fraction for filter widths, \blacksquare : $5\Delta_{DNS}$, \blacktriangle : $9\Delta_{DNS}$ and \blacklozenge : $13\Delta_{DNS}$. 78
- Figure 47 Resolved kinetic stress dissipation $\tilde{v}_p S_{p,ij}^* \frac{\partial u_{p,i}}{\partial x_j}$ conditionally averaged by filtered volume fraction for filter widths, \blacksquare : $5\Delta_{DNS}$, \blacktriangle : $9\Delta_{DNS}$ and \blacklozenge : $13\Delta_{DNS}$. 79
- Figure 48 Resolved and sub-grid contributions of production and destruction of the particle kinetic energy for different filter widths Δ_f . Production; \square : resolved and \blacksquare : sub-grid, Destruction; \triangle : resolved and \blacktriangle : sub-grid, Interaction with fluid; \circ : resolved and \bullet : sub-grid (Normalised by $\rho_p \tau_p^{St} (V_t^{St})^2$). 81
- Figure 49 Resolved and sub-grid contributions of kinetic and sub-grid diffusivity for different filter widths Δ_f . Kinetic diffusivity; \square : resolved and \blacksquare : sub-grid, \blacktriangle : Sub-grid diffusivity (Normalised by $\rho_p \tau_p^{St} (V_t^{St})^2$). 81
- Figure 50 Correlation coefficients between the sub-grid drift flux $\bar{\alpha}_p \tilde{V}_{d,z}$ and filtered variables with respect to different filter widths Δ_f :
 $+$: $\bar{\alpha}_p V_t$, \times : $\tau_p^{St} (V_t^{St})^2 \frac{\partial \bar{\alpha}_p}{\partial z}$, $*$: $(\tau_p^{St} V_t^{St})^2 \frac{\partial \bar{\alpha}_p}{\partial z} \frac{\partial \tilde{u}_{g,z}}{\partial z}$,
 \square : $(\tau_p^{St} V_t^{St})^2 \frac{\partial \bar{\alpha}_p}{\partial z} \frac{\partial \tilde{u}_{p,z}}{\partial z}$, \blacksquare : $\bar{\alpha}_p (\tilde{u}_{p,z} - \tilde{u}_{g,z})$. 85

Figure 51	Scattering plot of the sub-grid drift flux $\bar{\alpha}_p \tilde{V}_{d,z}$ versus $\bar{\alpha}_p (\tilde{U}_{g,z} - \tilde{U}_{p,z})$ for intermediate and large filter width ratios (Δ_f/Δ_{DNS}): * : 7, × : 9, + : 13 (top) and * : 17, × : 21, + : 25(bottom). 86
Figure 52	The function “g” for different filter size ratios: $9\Delta_f/\Delta_{DNS}$, $13\Delta_f/\Delta_{DNS}$ and $17\Delta_f/\Delta_{DNS}$. 87
Figure 53	The function “h” for different filter size ratios: $9\Delta_f/\Delta_{DNS}$, $13\Delta_f/\Delta_{DNS}$ and $17\Delta_f/\Delta_{DNS}$. 88
Figure 54	The proposed function “h” . 89
Figure 55	The function “f”. 90
Figure 56	Averaged Germano’s decomposition terms along the mean flow direction for different filter widths Δ_f . 93
Figure 57	Averaged Reynolds terms along mean flow, transverse and longitudinal directions for different filter widths Δ_f . 94
Figure 58	Gradient model coefficients $A_{\beta\beta}$ along mean, transverse and longitudinal directions for different filter widths Δ_f . 95
Figure 59	Full Tensor model coefficients B_{zz} and C_{zz} along the mean flow direction for different filter widths Δ_f . 96
Figure 60	Mixed model coefficients D_{zz} and E_{zz} along the mean flow for different filter widths Δ_f . 97
Figure 61	Dynamic Structure model coefficient C_{sgs} along the mean flow for different filter widths Δ_f . 99
Figure 62	Correlation coefficients r_x between the x-component of measured and modelled $\bar{\alpha}_p \tilde{V}_{d,\beta}$ for different filter widths Δ_f . The test filter width is $\hat{\Delta} = \sqrt{5}\Delta_f$. 100
Figure 63	Correlation coefficients r_y between the y-component of measured and modelled $\bar{\alpha}_p \tilde{V}_{d,\beta}$ for different filter widths Δ_f . The test filter width is $\hat{\Delta} = \sqrt{5}\Delta_f$. 101
Figure 64	Correlation coefficients r_z between the z-component of measured and modelled $\bar{\alpha}_p \tilde{V}_{d,\beta}$ for different filter widths Δ_f . The test filter width is $\hat{\Delta} = \sqrt{5}\Delta_f$. 102
Figure 65	Pdfs of relative error e_z of $\bar{\alpha}_p \tilde{V}_{d,\beta}$, computed as in Eq. (5.3), for $\Delta_f = 11\Delta_{DNS}$ along the mean flow direction. The test filter width is $\hat{\Delta} = \sqrt{5}\Delta_f$. 103
Figure 66	Pdfs of relative error e_z of the drag correction, computed as in Eq. (5.3), for $\Delta_f = 11\Delta_{DNS}$ along the mean flow direction. The test filter width is $\hat{\Delta} = \sqrt{5}\Delta_f$. 104
Figure 67	Mean squared error E_x , computed as in Eq. (5.4), for the x-component of measured and modelled $\bar{\alpha}_p \tilde{V}_{d,\beta}$ for different filter widths Δ_f . The test filter width is $\hat{\Delta} = \sqrt{5}\Delta_f$. 104
Figure 68	Mean squared error E_y , computed as in Eq. (5.4), for the y-component of measured and modelled $\bar{\alpha}_p \tilde{V}_{d,\beta}$ for different filter widths Δ_f . The test filter width is $\hat{\Delta} = \sqrt{5}\Delta_f$. 105
Figure 69	Mean squared error E_z , computed as in Eq. (5.4), for the z-component of measured and modelled $\bar{\alpha}_p \tilde{V}_{d,\beta}$ for different filter widths Δ_f . The test filter width is $\hat{\Delta} = \sqrt{5}\Delta_f$. 105

- Figure 70 Correlation coefficients r between the deviatoric part of the filtered particle sub-grid stress tensor $\sigma_{p,zj}^*$ and Smagorinsky model for different filter widths Δ_f at the tensor and scalar level. 106
- Figure 71 Correlation coefficients r between the filtered particle sub-grid energy $\sigma_{p,SGS}$ and Yoshizawa model for different filter widths Δ_f at the tensor and scalar level. 106
- Figure 72 Pdfs of particle sub-grid dissipation from DNS data and by the Smagorinsky model for filter width ratios: $\Delta_f/\Delta_{DNS} = 7(\text{top}), 15(\text{bottom})$. 107
- Figure 73 Pdfs of particle sub-grid energy $\sigma_{p,SGS}$ from DNS data and by the Yoshizawa model for filter width ratios: $\Delta_f/\Delta_{DNS} = 7(\text{top}), 15(\text{bottom})$. 108
- Figure 74 Yoshizawa and Smagorinsky model coefficients, C_Y and C_s , for different filter widths Δ_f . 109
- Figure 75 Instantaneous of solid volume fraction in the PCFB. White color corresponds to $\alpha_p = 0$. Black colour corresponds to $\alpha_{p,max} = 0.64$. a) Kinetic theory simulation with mesh resolution, $Fr_{\Delta}^{-1} = 0.032$ ($128 \times 128 \times 1024$), b) Kinetic theory simulation with mesh resolution, $Fr_{\Delta}^{-1} = 0.128$ ($32 \times 32 \times 256$), c) Simulation with SGM and SGS particle stress models with mesh resolution $Fr_{\Delta}^{-1} = 0.128$ ($32 \times 32 \times 256$), d) Simulation with MM and SGS particle stress models with mesh resolution $Fr_{\Delta}^{-1} = 0.128$ ($32 \times 32 \times 256$). 113
- Figure 76 The influence of mesh size on the weighted relative velocity $\overline{\langle \alpha_p(\mathbf{U}_{p,z} - \mathbf{U}_{g,z}) \rangle^t}$. Simulations with the effective drag and SGS particle stress models were performed for three mesh resolutions : coarse ($24 \times 24 \times 192$, $Fr_{\Delta}^{-1} = 0.175$), moderate ($32 \times 32 \times 256$, $Fr_{\Delta}^{-1} = 0.128$) and fine ($40 \times 40 \times 320$, $Fr_{\Delta}^{-1} = 0.104$). ●: SGM model for effective drag+SGS particle stress models, ▲: MM model for effective drag+ SGS particle stress models, ■: Kinetic theory based simulations without models. 114
- Figure 77 The influence of mesh size the non-dimensional total volumetric mass flux, $\overline{\langle G_s \rangle^t}$ where $G_{s,o}$ corresponds to the homogeneous case and $G_{s,conv}$ corresponds to the converged case. Simulations with the effective drag and SGS particle stress models were performed for three mesh resolutions : coarse ($24 \times 24 \times 192$, $Fr_{\Delta}^{-1} = 0.175$), moderate ($32 \times 32 \times 256$, $Fr_{\Delta}^{-1} = 0.128$) and fine ($40 \times 40 \times 320$, $Fr_{\Delta}^{-1} = 0.104$). ●: SGM model for effective drag+SGS particle stress models, ▲: MM model for effective drag+ SGS particle stress models, ■: Kinetic theory based simulations without models. 114
- Figure 78 The time-averaged solid volume fraction along the radial direction with SGM model for effective drag and SGS particle stress models for three mesh resolutions : coarse ($24 \times 24 \times 192$, $Fr_{\Delta}^{-1} = 0.175$), moderate ($32 \times 32 \times 256$, $Fr_{\Delta}^{-1} = 0.128$), fine ($40 \times 40 \times 320$, $Fr_{\Delta}^{-1} = 0.104$) and the mesh independent result obtained by kinetic theory based simulation ($128 \times 128 \times 1024$, $Fr_{\Delta}^{-1} = 0.032$) ($z = 0.11\text{m}$, $y = 0$). 115

- Figure 79 The time-averaged gas velocity along the radial direction with SGM model for effective drag and SGS particle stress models for three mesh resolutions: coarse ($24 \times 24 \times 192$, $Fr_{\Delta}^{-1} = 0.175$), moderate ($32 \times 32 \times 256$, $Fr_{\Delta}^{-1} = 0.128$), fine ($40 \times 40 \times 320$, $Fr_{\Delta}^{-1} = 0.104$) and the mesh independent result obtained by kinetic theory based simulation ($128 \times 128 \times 1024$, $Fr_{\Delta}^{-1} = 0.032$) ($z = 0.11\text{m}$, $y = 0$). 116
- Figure 80 The time-averaged negative and positive solid mass flux along the radial direction with SGM model for effective drag and SGS particle stress models for three mesh resolutions: coarse ($24 \times 24 \times 192$, $Fr_{\Delta}^{-1} = 0.175$), moderate ($32 \times 32 \times 256$, $Fr_{\Delta}^{-1} = 0.128$), fine ($40 \times 40 \times 320$, $Fr_{\Delta}^{-1} = 0.104$) and the mesh independent result obtained by kinetic theory based simulation ($128 \times 128 \times 1024$, $Fr_{\Delta}^{-1} = 0.032$) ($z = 0.11\text{m}$, $y = 0$). 116
- Figure 81 The time-averaged total solid mass flux along the radial direction with SGM model for effective drag and SGS particle stress models for three mesh resolutions: coarse ($24 \times 24 \times 192$, $Fr_{\Delta}^{-1} = 0.175$), moderate ($32 \times 32 \times 256$, $Fr_{\Delta}^{-1} = 0.128$), fine ($40 \times 40 \times 320$, $Fr_{\Delta}^{-1} = 0.104$) and the mesh independent result obtained by kinetic theory based simulation ($128 \times 128 \times 1024$, $Fr_{\Delta}^{-1} = 0.032$) ($z = 0.11\text{m}$, $y = 0$). 117
- Figure 82 The time-averaged solid volume fraction along the radial direction with MM model for effective drag and SGS particle stress models for three mesh resolutions: coarse ($24 \times 24 \times 192$, $Fr_{\Delta}^{-1} = 0.175$), moderate ($32 \times 32 \times 256$, $Fr_{\Delta}^{-1} = 0.128$), fine ($40 \times 40 \times 320$, $Fr_{\Delta}^{-1} = 0.104$) and the mesh independent result obtained by kinetic theory based simulation ($128 \times 128 \times 1024$, $Fr_{\Delta}^{-1} = 0.032$) ($z = 0.11\text{m}$, $y = 0$). 118
- Figure 83 The time-averaged gas velocity along the radial direction with MM model for effective drag and SGS particle stress models for three mesh resolutions: coarse ($24 \times 24 \times 192$, $Fr_{\Delta}^{-1} = 0.175$), moderate ($32 \times 32 \times 256$, $Fr_{\Delta}^{-1} = 0.128$), fine ($40 \times 40 \times 320$, $Fr_{\Delta}^{-1} = 0.104$) and the mesh independent result obtained by kinetic theory based simulation ($128 \times 128 \times 1024$, $Fr_{\Delta}^{-1} = 0.032$) ($z = 0.11\text{m}$, $y = 0$). 119
- Figure 84 The time-averaged negative and positive solid mass flux along the radial direction with MM model for effective drag and SGS particle stress models for three mesh resolutions: coarse ($24 \times 24 \times 192$, $Fr_{\Delta}^{-1} = 0.175$), moderate ($32 \times 32 \times 256$, $Fr_{\Delta}^{-1} = 0.128$), fine ($40 \times 40 \times 320$, $Fr_{\Delta}^{-1} = 0.104$) and the mesh independent result obtained by kinetic theory based simulation ($128 \times 128 \times 1024$, $Fr_{\Delta}^{-1} = 0.032$) ($z = 0.11\text{m}$, $y = 0$). 119

Figure 85	The time-averaged total solid mass flux along the radial direction with SGM model for effective drag and SGS particle stress models for three mesh resolutions: coarse ($24 \times 24 \times 192$, $Fr_{\Delta}^{-1} = 0.175$), moderate ($32 \times 32 \times 256$, $Fr_{\Delta}^{-1} = 0.128$), and fine ($40 \times 40 \times 320$, $Fr_{\Delta}^{-1} = 0.104$) and the mesh independent result obtained by kinetic theory based simulation ($128 \times 128 \times 1024$, $Fr_{\Delta}^{-1} = 0.032$) ($z = 0.11\text{m}$, $y = 0$). 120
Figure 86	The 2-D bubbling fluidized bed (see Parmentier 2010). 120
Figure 87	Vertical profiles of time-averaged solid volume fraction. Simulations results without and with the Smagorinsky-type model are the left and the right, respectively, for mesh resolution: $\Delta_{x,y} = 1\text{ mm}$ and $\Delta_{x,y} = 2\text{ mm}$. The reference case mesh size is equal to $\Delta_{x,y} = 100\text{ }\mu\text{m}$. 122
Figure 88	Vertical profiles of time-averaged solid volume fraction. Simulations results without and with the Mixed model are the left and the right, respectively, for mesh resolution: $\Delta_{x,y} = 1\text{ mm}$ and $\Delta_{x,y} = 2\text{ mm}$. The reference case mesh size is equal to $\Delta_{x,y} = 100\text{ }\mu\text{m}$. 122
Figure 89	Predictions with different mesh resolutions (mesh: $14 \times 14 \times 675$ - $Fr_{\Delta}^{-1} = 18$, $28 \times 28 \times 1350$ - $Fr_{\Delta}^{-1} = 9$) versus experimental data of Gauthier (2002). 124

LIST OF TABLES

Table 1	Empirical constants for modelling of gas phase turbulence.	19
Table 2	Flow properties of CERCHAR case (B-type particles).	28
Table 3	Flow properties of FCC case (A-type particles).	40
Table 4	Flow properties of FCC case (Gauthier 2002).	52

ACRONYMS

KTGF	Kinetic Theory of Granular Flow
PCFB	Periodic Circulating Fluidized Bed
FCC	Fluid Catalytic Cracking
CFBC	Circulating Fluidized Bed Combustion
URANS	Unsteady Reynolds-averaged Navier-Stokes Equations
DNS	Direct Numerical Simulation
SGS	Sub-grid Scale

- SGM Smagorinsky-type model
- MM Mixed model
- DYM Dynamic Yoshizawa model
- DSM Dynamic Smagorinsky model

NOMENCLATURE

Subscripts

k	Phase k (k = g for gas, k = p for particle)
o	Corresponds to homogeneous case
conv	Corresponds to converged case

Symbols

Δ	Characteristic length of cell volume
Δ_f	Characteristic length of filter width
Δ_{DNS}	Characteristic length of DNS cell volume
Δ_{sgs}	Characteristic length of sub-grid scale
$\overline{\langle Q \rangle^t}$	A time-averaged value $\overline{\langle Q \rangle^t}$ of the domain averaged quantity $\langle Q \rangle$
$\overline{\langle Q \rangle^{t,n}}$	A discrete ensemble average value of quantity Q
$\langle \cdot \rangle$	The averaging operator proposed by Simonin (1996)

Dimensionless numbers

Symbol	Signification
Re_p	Single particle Reynolds number
$\langle Re_p \rangle$	Mean particle Reynolds number
Fr_{Δ}^{-1}	Froude number based on cell volume, Stoke's relaxation time and gravity acceleration

Latin symbols		
Symbol	Signification	Dimension
$\tilde{u}_{g,i}$	Undisturbed gas velocity	m/s
$u_{g,i}$	Local instantaneous gas velocity	m/s
$u'_{g,i}$	Fluctuating local instantaneous gas velocity	m/s
\tilde{p}_g	Undisturbed gas pressure	Pa
p_g	Local instantaneous gas pressure	Pa
$n_{k,i}$	Normal unit vector	
g/g_i	Gravity acceleration	m/s ²
C_D	Drag coefficient of single particle	
$U_{k,i}$	Mean velocity of phase k	m/s
$\tilde{U}_{k,i}$	Filtered mean velocity of phase k	m/s
P_g	Mean pressure of gas phase	Pa
\tilde{P}_g	Filtered mean pressure of gas phase	Pa
P_p	Granular pressure of particulate phase	Pa
\tilde{P}_p	Filtered granular pressure of particulate phase	Pa
$S_{k,ij}$	Mean strain rate tensor of phase k	1/s
$S^*_{k,ij}$	Deviatoric part of mean strain rate tensor of phase k	1/s
$\tilde{S}_{k,ij}$	Filtered mean strain rate tensor of phase k	1/s
$\tilde{S}^*_{k,ij}$	Deviatoric part of filtered mean strain rate tensor of phase k	1/s
$\langle C_D \rangle$	Mean drag coefficient	
$\langle u'_{g,i} u'_{g,j} \rangle$	Reynolds stresses of gas phase	m ² /s ²
k	Turbulent kinetic energy of gas phase	m ² /s ²
\mathbf{v}_r	Local instantaneous relative velocity between particle and local undisturbed gas velocity	m/s
$V_{r,i}$	Mean relative velocity between particle and local undisturbed gas velocity	m/s
$V_{d,i}$	Drift velocity	m/s
$\tilde{V}_{d,i}$	Sub-grid drift velocity	m/s
V_t^{St}	Terminal settling velocity given by $\tau_p^{St} \mathbf{g} $	m/s
$G_{s,-,+}$	Downward and upward solid mass flux	kg/m ² s
G_s	Total solid mass flux	kg/m ² s
K_p^{Kin}	Kinematic diffusivity of particulate phase	m ² /s
\tilde{K}_p^{Kin}	Filtered kinematic diffusivity of particulate phase	m ² /s
K_p^{coll}	Collisional diffusivity of particulate phase	m ² /s
\tilde{K}_p^{coll}	Filtered collisional diffusivity of particulate phase	m ² /s
$K_{\beta\beta}$	Functional model's coefficient	
A_{jk}	Gradient model's coefficient	
B_{jk}, C_{jklm}	Full tensor model's coefficients	
$D_{\beta\beta}, E_{\beta\beta}$	Mixed model's coefficients	
C_{sgs}	Dynamic structure model's coefficient	
C_Y	Yoshizawa model's coefficient	
C_S	Smagorinsky model's coefficient	

Greek symbols

Symbol	Signification	Dimension
α_k	Volume fraction phase k	
$\bar{\alpha}_k$	Filtered volume fraction phase k	
ρ_k	Density of phase k	kg/m ³
ϵ_g	Microscopic scale of gas phase	
ϵ	Turbulent dissipation of gas turbulence	m ² /s ³
λ_k	Bulk viscosity of phase k	kg/m.s
$\tilde{\lambda}_k$	Filtered bulk viscosity of phase k	kg/m.s
μ_k	Dynamic viscosity of phase k	kg/m.s
ν_g	Kinematic viscosity of gas phase	m ² /s
ν_p^{kin}	Kinematic viscosity of particulate phase	m ² /s
$\tilde{\nu}_p^{kin}$	Filtered kinematic viscosity of particulate phase	m ² /s
ν_p^{coll}	Collisional viscosity of particulate phase	m ² /s
$\tilde{\nu}_p^{coll}$	Filtered collisional viscosity of particulate phase	m ² /s
χ_k	Phasic indicator function	
$\chi_{ij...}$	Source terms of the collisional rate	
$\Theta_{ij...}$	Flux terms of the collisional rate	
δ_k	Dirac delta function associated phase k	
τ_p^*	Relaxation time of a single particle	s
τ_p^{St}	Stoke's response time	s
τ_p	Mean relaxation time	s
$\tilde{\tau}_p$	Filtered mean relaxation time	s
τ_c	Particle-particle collision time	s
τ_t	Characteristic time scale of gas turbulence	s
τ_{fp}^t	Interaction between particle and gas phase fluctuations	s
η_r	Inverse Stoke's number	
Ω	Control volume containing phases	m ³
Ω_p	Single particle volume	m ³
$\Sigma_{p,ij}$	Effective stress tensor of particulate phase	Pa
$\tilde{\Sigma}_{p,ij}$	Filtered effective stress tensor of particulate phase	Pa
$\sigma_{p,ij}$	Particle sub-grid stresses	m ² /s ²
$\sigma_{p,SGS}$	Particle sub-grid stress trace	m ² /s ²

INTRODUCTION

1.1 FLUIDIZATION OF PARTICLES

Fluidization is a process where large ensemble of solid particles is converted from static solid-state to quasi dynamic liquid-state through in liquid or gas suspension. Fluid or gas is introduced upward through a bed of particles and passes by spaces between particles. As flow rate increases, fluid velocity reaches a critical value called fluidization velocity which causes particles to become suspended within the fluid. At this critical flow rate, particles exhibit fluidic behaviour. By further increasing flow rate, fluidization becomes more violent, until the particles no longer form a bed and are transported upwards by the flow.

According to fluidization characteristics, Geldart (1973) classified particles into four groups. Group A consists of aeratable particles with a small diameter and low density that can be fluidized very easily. Group B is a group of sand-like particles. Formations of bubbles can be seen in the fluidization of B-type particles. Group C consists of cohesive particles that are very difficult to fluidize and the fluidization of group D particles forms spouting beds. The classification of fluidization characteristics of solid particles by Geldart (1973) due to the difference of particle and gas densities, $\rho_p - \rho_g$, and particle diameter, d_p , is shown in Figure 1. Another classification done by Kunii and Levenspiel (1991) based on fluidization velocity and particle properties is shown in Figure 2. The particles studied in this thesis belong to Group A and Group B.

1.2 CIRCULATING FLUIDIZED BEDS

When particles are transported by the flow in the bed, they are returned into bed by a looping process. Hence, it is called circulating fluidized bed (CFB). Circulating fluidized beds are used in many industrial applications such as fluid catalytic cracking (FCC) in petroleum refineries, and circulating fluidized bed combustion (CFBC) of fossil or biomass in power plants. FCC is the chemical process which converts the petroleum crude oils to more valuable gasoline, olefin gases and other products. FCC process is more preferable than the conventional process because it produces more gasoline with a higher octane rating and as of 2006, FCC units were in operation at 400 petroleum refineries worldwide and about one-third of the crude oil refined in those refineries is processed in an FCC (Sadeghbeigi 2000, Jones and Pujadó 2006). In CFBCs, solid fuels are blown by gas during the combustion process and unburnt solid particles are separated from gas by use of a cyclone and returned into the bed that provides more effective chemical reactions and heat transfer. CFBC supplies a flexibility of choice of fuel, which are difficult to burn using other technologies, a low emission of nitric oxides and the possibility of removing sulphur (Yang 2003). The schematic views of FCC process and CFBC are shown in Figure 3. The performances of CFBC and FCC processes have to be improved because of energy demand and global warming which are the main issues in front of mankind. Most cur-

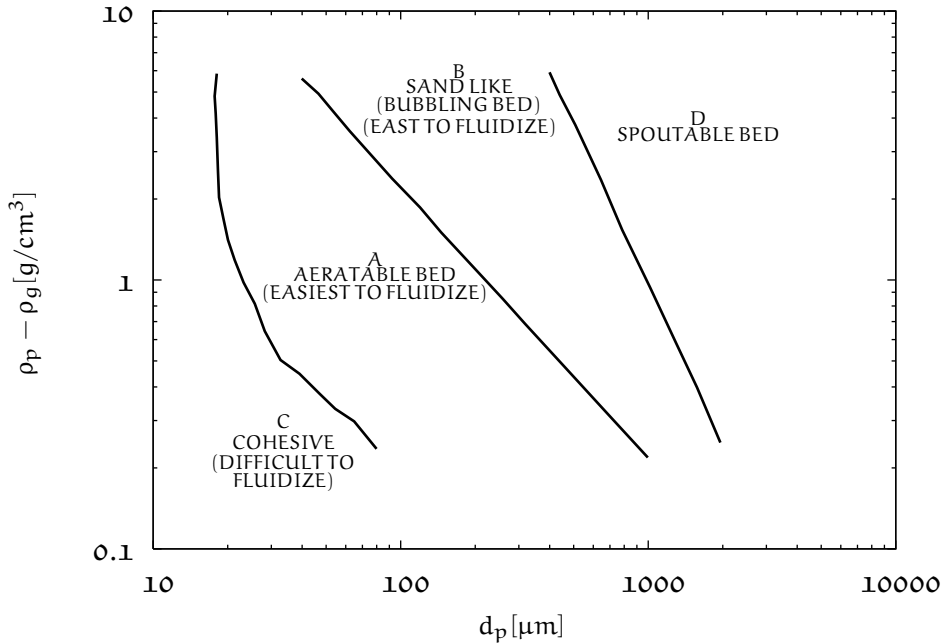


Figure 1: The fluidization characteristics of solid particles by Geldart (1973).

rent research aims to quantify and explain the physical phenomena of gas-particle flows in the bed to design better, more efficient reactors that may effectively deal with the current disadvantages of the technology and expand the range of usages. To achieve this goal, several experimental researches were performed and more of them will be done to measure flow parameters. With improvements in the computer technology, the numerical simulation of gas-particle flows in fluidized beds has been started about twenty years ago. Numerical studies are useful especially in complex geometries and under conditions in which experimental studies can not be carried out. However, numerical approaches have to be improved for precise reproductions of phenomena in beds. This study is concerned to deal with accurate prediction of the gas-particle flows in the circulating fluidized beds by numerical approach.

1.3 STATE-OF-THE-ART OF CFB SIMULATIONS

Two approaches are generally applied in the mathematical modelling of gas-solid flows in CFBs: Discrete element modelling (DEM), or Discrete particle simulation (DPS), and continuum or Euler-Euler modelling. The DEM involves Eulerian modelling of fluid or gas phase and Lagrangian tracking of discrete particles. The Lagrangian formulation gives an accurate description of the motion of a single particle such as dragging by fluid, rotation and collision with another particle. However, numerical simulations by DEM have to resolve millions of particles that is not feasible with available computational sources for industrial type CFBs.

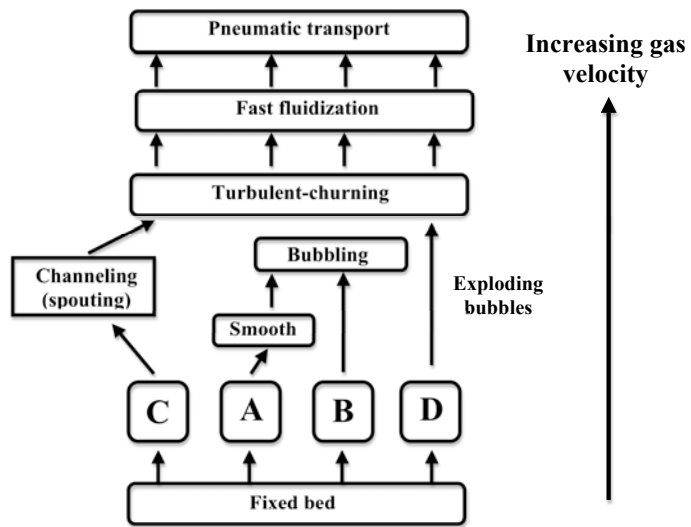


Figure 2: Gas-solid classification according to Kunii and Levenspiel (1991) based on Geldart (1973)'s type of particles.

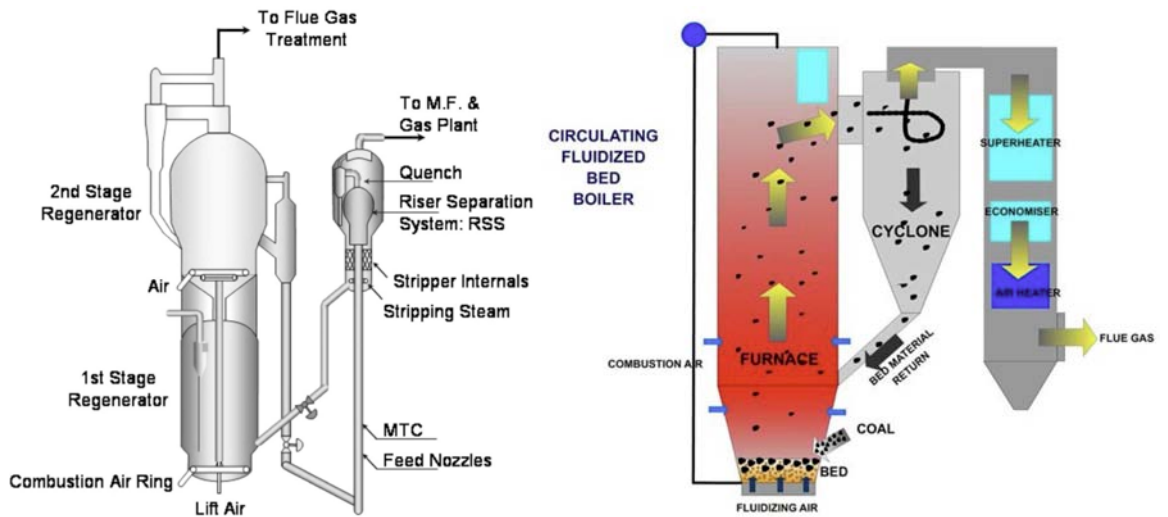


Figure 3: R2R resid FCC process (Andreux et al. 2008) (left) and the schematic view of CFBC (right).

At that point, Euler-Euler approach takes the role in which all phases are modelled as interpenetrating continuum media. In Euler-Euler approach, a statistical procedure is followed to derive basic continuum balance equations from the local instantaneous equations for each phase in a suitable way, in space, on time or ensemble. The averaging procedure introduces unknowns and thus, closure relations are necessary. These relations describe interactions between phases and physical properties of phases. The relations related to physical properties of gas phase are defined as a single phase flow. Empirical models and the Kinetic Theory of Granular Flow (KTGF) are used for the physical properties of particulate phases such as; granular pressure, dynamic and bulk viscosity. Because of the lack of universality of empirical models, the majority of Euler-Euler studies are performed by KTGF. In this study, we follow the averaging procedure and basic equations of He and Simonin (1993) and use closure relations of Balzer et al. (1995).

Lun et al. (1984), Jenkins and Richman (1985) and Ding and Gidaspow (1990) derived disperse phase closures in frame of KTGF with introducing an additional transport equation called the pseudo-thermal energy balance for the random kinetic energy motion of particulate phase. These approaches neglect influences of gas phase turbulence and are valid for dense regime such as bubbling fluidized beds. Reeks (1991) and Simonin (1991b) used a similar approach based on the particle probability density function to take into account the fluid turbulence. Balzer et al. (1995) and Cao and Ahmadi (1995) accounted for the effect of gas turbulence on particle viscosity and diffusivity. Following these studies, Agrawal et al. (2001) used modified the expression of the solid phase granular viscosity and conductivity. Several studies have been carried out to verify Eulerian models by comparisons with experimental data. Samuelsberg and Hjertager (1996), Nieuwland et al. (1996), Neri and Gidaspow (2000) and Benyahia et al. (2000) simulated the riser of CFB and compared with experimental measurements of particle velocities and volume fractions. By improvement of computational resources, 3-D simulations of CFBs are available in recent years. Kuipers et al. (1998), Agrawal et al. (2001), Zhang and VanderHeyden (2002), Andrews et al. (2005) and Andreux et al. (2008) have performed 3-D simulations in a square section riser. Recent developments of Euler-Euler modelling with KTGF have been reviewed by Arastoopour (2001), Gidaspow et al. (2004) and van der Hoef et al. (2008).

Although tremendous progress has been made over the past two decades, Eulerian approach fails to predict the hydrodynamic characteristics of industrial applications in particular cases (Sundaresan 2000, Wang 2009). Several authors have investigated failures of Euler-Euler approach (O'Brien and Syamlal 1993, Agrawal et al. 2001, Yang et al. 2003, Heynderickx et al. 2004, Andrews et al. 2005, Igci et al. 2008, Wang 2009, Parmentier 2010). It was revealed that the existence of meso-scale structures, such as streamers and clusters, have dramatic effects on the overall dynamic behaviours and they are cancelled out by coarse grid simulations. Although formations and breakage of meso-scale structures can be captured by Euler-Euler formalism and transport equations developed in the frame of the KTGF on a small domain, large ranges of spatial and temporal variations of these structures restrict the resolution of calculations for large industrial units due to computational cost. Agrawal et al. (2001) addresses that the effect of meso-scale structures on the macroscopic behaviour in coarse grid simulations can be taken into account by sub-grid scales through additional closure relations.

Several attempts to extend the Eulerian models by accounting for these unresolved structures have been made for coarse grid simulations through different ways. O'Brien

and Syamlal (1993), Heynderickx et al. (2004) proposed a correlation for the effective drag force to take into account meso-scale effects for dilute limit. McKeen and Pugsley (2003), Hosseini et al. (2009) used the size of clusters to define effective drag as flow dependent tuning parameter. Andrews et al. (2005) proposed ad hoc sub-grid models for effective drag force and particle stresses which accounts for the effects of unresolved structures on the resolved flow. Igci et al. (2008) presented a filtering approach methodology to construct closures for the effective drag force and the effective particle stresses for different filter sizes. Parmentier (2010) proposed an effective drag model dependent on the filter size and the solid volume fraction for 2-D bubbling fluidized bed. Different from the studies paying their attention to the effective drag force model, Dasgupta et al. (1994) and Hrenya and Sinclair (1997) investigated the effects of meso-scales on the particle phase stresses by the fluctuations of clusters and streamers in risers. An alternative approach based on Energy Minimization Multi-Scale (EMMS) was originally proposed by Li and Kwauk (1994). The EMMS method was integrated into the Eulerian formalism in the form of a sub-grid drag correction by Wang and Li (2007) to take into account effects of clustering. The EMMS method predicts steady flows inside circulating fluidized beds, assumes that particles move in the form of clusters through a dilute phase composed by the surrounding gas and a few randomly distributed particles. The last revised EMMS model can be found in Wang et al. (2008).

1.4 OBJECTIVE

The objective of this thesis is to propose an appropriate modelling approach which takes into account the influences of unresolved structures for coarse grid simulations by Euler-Euler approach of CFBs. By constructing an analogy with direct numerical simulation of single phase turbulent flow, the first aim of this study is to obtain mesh-independent result where statistical quantities do not change with further mesh refinement on a simplified CFB configuration. The next step comprises of derivation of filtered equations from balances equations of phases by volume averaging. Then, a priori methodology is followed to investigate the additional terms due to volume filtering in order to identify sub-grid contributions from database of mesh independent result. By following a priori methodology, the construction of systematic procedure is the core part of the study to provide constitutive closures for the additional terms. The final goal is to validate these closures by a posteriori tests with comparing simulations of simple configuration of CFB and available experimental data of pilot and industrial applications of CFBs.

1.5 OUTLOOK OF THESIS

This thesis is organised as follows. In §2, we present the mathematical modelling of gas-solid flow in the framework of Eulerian approach. In this study, we deal with gas-solid flows including gas and a single solid particle phase. This modelling consists of a set of conservation and closure equations for the gas and particulate phase. In the framework of Unsteady Reynolds Averaged Numerical Simulation (URANS), the modified two-equation turbulence model (turbulent kinetic and dissipation energy) that takes into account effects of dispersed phase is used to solve gas-phase turbulence. Two transport equations, developed in the frame of kinetic theory of granular media supplemented by

the interstitial fluid effect and the interaction with the turbulence (Balzer et al. 1995, Gobin et al. 2003), are resolved to model the effect of velocity fluctuations and inter-particle collisions on the dispersed phase hydrodynamics.

In §3, we concern simulations of dilute gas-particle flow in cold CFB and FCC risers by RANS approach. The results are validated with experimental data in terms of solid mass flux and pressure drop. Parametric studies have been carried out to determine influences of physical parameters, turbulence model and wall boundary conditions for the dispersed phase. The influence of mesh resolution on results is also investigated and main drawbacks of the model are discussed.

In §4, we introduce the flow configuration, a 3-D periodic circulating fluidized bed (PCFB), where the mean gas-solid flow is periodically driven along the opposite direction of gravity. We demonstrate the mesh dependency of the time and domain averaged quantities such as: the relative velocity weighted by solid volume fraction, volumetric solid mass flux, random kinetic energy of particles and we discuss the mesh independent result where averaged quantities are converged constant values.

We present the filtering approach in §5. By following, the filtered particle momentum and agitation equations are derived. Mesh independent result obtained in §4 is used to calculate budget analyses of filtered particle momentum and agitation equation. The importance of additional terms due to the filtering procedure, which stands for sub-grid contributions, is investigated. Thereafter, we carry out a priori tests on the sub-grid contribution of drag force and sub-grid scale stress tensor of particulate phase.

In §6, models for additional terms appearing in the filtered particulate phase momentum equation are proposed and their predictabilities are investigated by making comparisons with evaluations of sub-grid contributions from the mesh independent result.

In §7, proposed models are validated by a posteriori tests in a simplified 3-D CFB, 2-D dense fluidized bed and available experimental data. Last part of this thesis consists of discussions and perspectives of study.

MATHEMATICAL MODELLING

2.1 EULER-EULER FORMULATION

Euler-Euler simulations are computationally more efficient in pilot and large CFBs with available computational resources even though the complexity of Euler-Euler model is considerable. In this study, Euler-Euler approach is preferred, but an understanding of Lagrangian approach is necessary. It is to be noted that this study deals with gas phase and a single particulate phase.

The Euler-Euler approach is based on the fundamental definition of interpenetrating continua for multiphase flows. According to this approach, different phases can be present at the same time in the same computational volume. Such an idea is made by the introduction of a new dependent variable, the volume fraction α_k of each phase k . The equations of mass, momentum, and energy conservation are then solved for each considered phase coupled through interphase transfer terms. Appropriate constitutive equations have to be specified in order to describe the physical and rheological properties of each phase and to close the conservation equations. Balance equations of gas and particulate phases, interfacial momentum transfer and closures for isothermal flow condition without mass transfer between phases are given in the following sections.

2.2 PARTICULATE PHASE MODEL

2.2.1 Lagrangian Formulation

The Lagrangian approach provides a direct description of discrete phases by tracking particles of the system. The motion of single particle is predicted by solving ordinary differential equation on the Lagrangian coordinates. By following Gatignol (1983) and Maxey (1983), the equation of particle motion taking into account the interaction with fluid and the external flow fields can be written in general form:

$$m_p \frac{du_{p,i}}{dt} = F_{r,i}^{unp} + F_{r,i}^p. \quad (2.1)$$

The first term is the force that would act on the fluid at the particle centre where the flow would be observed if the particle were not present. This force term is transmitted as a force on the particle because of the pressure and the viscous stresses transferred from the neighbouring gas. It also accounts for buoyancy effects. It can be written as practical form:

$$\frac{F_{r,i}^{unp}}{m_p} = -\frac{1}{\rho_p} \frac{\partial \tilde{p}_g}{\partial x_i} + g_i. \quad (2.2)$$

where the first term is the instantaneous undisturbed pressure gradient at the particle centre (Archimede's force) and g_i is the acceleration due to gravity.

The second term represents the perturbation of the fluid velocity field due to the presence of the solid particle. This term represents the aerodynamic forces and reduces to the drag force for large density of particle to that of gas as

$$\frac{F_{r,i}^p}{m_p} = -\frac{3}{4} \frac{\rho_g}{\rho_p} \frac{C_D |\mathbf{u}_p - \tilde{\mathbf{u}}_g|}{d_p} (\mathbf{u}_{p,i} - \tilde{\mathbf{u}}_{g,i}) \quad (2.3)$$

where $m = \rho_p \pi d_p^3 / 6$ is the mass of a particle, ρ_p is the particle density, d_p is the particle diameter, ρ_g is the fluid density, $\tilde{\mathbf{u}}_{g,i}$ is the gas velocity of the undisturbed flow and $\mathbf{u}_{p,i}$ is the particle velocity. C_D is the drag coefficient and given by Schiller and Naumann (1935) as

$$C_D = \frac{24}{Re_p} (1 + 0.15 Re_p^{0.687}) \quad Re_p = \frac{|\mathbf{u}_p - \tilde{\mathbf{u}}_g| d_p}{\nu_g} \quad (2.4)$$

with the kinematic viscosity of the gas, ν_g . The relaxation time of a single particle τ_p^* is given by

$$\frac{1}{\tau_p^*} = \frac{3}{4} \frac{\rho_g}{\rho_p} \frac{C_D}{d_p} |\mathbf{u}_p - \tilde{\mathbf{u}}_g|. \quad (2.5)$$

2.2.2 Kinetic Theory of Disperse Phase

Separate balance equations derived in the framework of the classical Euler-Euler approach using suitable averaging with empirical constitutive laws for disperse phase do not account for collisions between particles and restricted to particular cases. However, collisions between particles have significant effect on hydrodynamics of particulate phase, especially, the case in which solid volume fraction is greater than 0.1. The kinetic theory of particulate phase based on the similarities between the flow of a granular material, a population of particles with or without an interstitial gas, allows to take into account inter-particle collisions and particle-wall interactions. Inter-particle and particle-wall collisions can be modelled by the kinetic theory of granular flow with the methodology of Grad (1949) and Jenkins and Richman (1985). Particles are assumed to be identical, spherical and only binary collisions occur at one time instant. Briefly, the particle velocity distribution function is expanded in series using Hermite polynomials expressed in terms of the Maxwellian distribution function and analytical solutions supplemented with collision terms of Jenkins and Richman (1985) are made to propose closure relations for particulate phase properties. Detailed description can be found in the work of He and Simonin (1993).

2.2.3 Velocity Distribution Function

The statistical dynamical state of particles can be determined by a velocity distribution function $f(\mathbf{c}, \mathbf{x}, t)$. This function is used to derive moment equations of particulate phase

for Euler-Euler model. The mean number of identical, spherical particles with the centre at a position $\mathbf{x}_p(t)$ with velocity $\mathbf{u}_p(t)$ in the volume element $[\mathbf{x}; \mathbf{x} + d\mathbf{x}]$ and in the velocity space $[\mathbf{c}; \mathbf{c} + d\mathbf{c}]$ is given by $f(\mathbf{c}, \mathbf{x}, t) d\mathbf{x} d\mathbf{c}$. The mean number of particles per unit volume at t is defined by

$$n_p(\mathbf{x}, t) = \langle n \rangle_p(\mathbf{x}, t) = \int f(\mathbf{c}, \mathbf{x}, t) d\mathbf{c} \quad (2.6)$$

and with an assumption of $\alpha_p \approx n_p(\mathbf{x}, t) \pi d_p^3/6$. The mean particle velocity at a position \mathbf{x} and at t is

$$U_{p,i}(\mathbf{x}, t) = \frac{1}{n_p} \int c_i f(\mathbf{c}, \mathbf{x}, t) d\mathbf{c}. \quad (2.7)$$

The fluctuating velocity of particle is defined by

$$C_i(\mathbf{c}, \mathbf{x}, t) = c_i - U_{p,i}(\mathbf{x}, t) \quad \text{or} \quad u_{p,i}'' = u_{p,i} - U_{p,i}. \quad (2.8)$$

Second and third order moments of velocity fluctuations can be obtained by

$$\langle u_{p,i}'' u_{p,j}'' \rangle_p = \frac{1}{n_p} \int C_i C_j f(\mathbf{c}, \mathbf{x}, t) d\mathbf{c} \quad (2.9)$$

$$\langle u_{p,i}'' u_{p,j}'' u_{p,m}'' \rangle_p = \frac{1}{n_p} \int C_i C_j C_m f(\mathbf{c}, \mathbf{x}, t) d\mathbf{c}. \quad (2.10)$$

In general form, if ψ is the property, which is the function of particle velocity \mathbf{c} we can define the mean of variable as

$$\langle \psi \rangle_p(\mathbf{x}, t) = \frac{1}{n_p} \int \psi(\mathbf{x}, t; \mathbf{c}) f(\mathbf{c}, \mathbf{x}, t) d\mathbf{c}. \quad (2.11)$$

The transport equation of the velocity distribution function in a volume element $d\mathbf{x} d\mathbf{c}$, with a increment at time $t + dt$ can be written by

$$\frac{\partial f}{\partial t} + \frac{\partial}{\partial x_j} (c_j f) + \frac{\partial}{\partial c_i} \left(\frac{F_i}{m_p} f \right) = \left(\frac{\partial f}{\partial t} \right)_{coll} \quad (2.12)$$

where F_i is the instantaneous external force acting on a particle at the position \mathbf{x} and the velocity \mathbf{c} . The external force per unit mass for a given flow realisation $\tilde{u}_{g,i}$ is defined as follows:

$$\frac{F_i}{m_p} = -\frac{1}{\rho_p} \frac{\partial \tilde{p}_g}{\partial x_i} - \frac{1}{\tau_p^*} (u_{p,i} - \tilde{u}_{g,i}) + g_i. \quad (2.13)$$

With the assumption of molecular chaos, the collision term is

$$\left(\frac{\partial f}{\partial t}\right)_{\text{coll}} = \iiint_{\boldsymbol{\omega} \cdot \mathbf{k} > 0} [f' f^{+'} - f f^+] |\boldsymbol{\omega} \cdot \mathbf{k}| d\mathbf{k} d\boldsymbol{\omega} d\mathbf{c}^+ \quad (2.14)$$

where f and f^+ are the values of velocity distribution function due to velocities \mathbf{c} and \mathbf{c}^+ before collision, f' and $f^{+'}$ are the values of same velocity distribution function with velocities after collision. $|\boldsymbol{\omega} \cdot \mathbf{k}|$ is the magnitude of relative velocity between particles before collision.

By multiplication of Eq. (2.12) by $\psi(\mathbf{c})$ and integration over velocity space, we can obtain the transport equation of mean quantity $\langle \psi \rangle_p$

$$\frac{\partial}{\partial t} (n_p \langle \psi \rangle_p) + \frac{\partial}{\partial x_i} (n_p \langle c_i \psi \rangle_p) - n_p \left[\left\langle \frac{\partial \psi}{\partial t} \right\rangle + \langle c_i \frac{\partial \psi}{\partial x_i} \rangle + \left\langle \frac{F_i}{m_p} \frac{\partial \psi}{\partial c_i} \right\rangle_p \right] = C(\psi) \quad (2.15)$$

where $C(\psi)$ is called collisional rate of change and represents the integral over all possible collisions of the change ψ :

$$C(\psi) = \int \psi \left(\frac{\partial f}{\partial t}\right)_{\text{coll}} d\mathbf{c}. \quad (2.16)$$

The collision rate of change is defined by Jenkins and Richman (1985):

$$C(\psi) = \chi(\psi) - \frac{\partial}{\partial x_i} \Theta_i(\psi) \quad \text{with} \quad (2.17)$$

1st term : Source term (represents the redistribution of ψ caused by collisions) and

2nd term : Flux term (represents the transfer of ψ during collisions). These terms can be analytically calculated.

2.2.4 Transport Equations

Eq. (2.15) can be written up to 2rd order moments by substitution of $n_p m_p$ by $\alpha_p \rho_p$ and definitions of $\psi = m_p, m_p C_i, m_p C_i C_j$. For the sake of simplicity, we define the following variables as moments

$$R_{p,ij} = \langle u_{p,i}'' u_{p,j}'' \rangle_p \quad (2.18)$$

$$S_{p,ijm} = \langle u_{p,i}'' u_{p,j}'' u_{p,m}'' \rangle_p. \quad (2.19)$$

Continuity Equation

The continuity equation is obtained from Eq. (2.15) with $\psi = m_p$

$$\frac{\partial}{\partial t} \alpha_p \rho_p + \frac{\partial}{\partial x_i} \alpha_p \rho_p U_{p,i} = 0. \quad (2.20)$$

The collisions without breakage or agglomeration do not change the number of particles, thus $\chi(m_p) = \Theta(m_p) = 0$ where $\chi_{ij\dots n} = \chi(m_p C_i C_j \dots C_n)$ and $\Theta_{ij\dots n} = \Theta(m_p C_i C_j \dots C_n)$.

Momentum Equation :

The momentum equation is obtained from the general transport equation with $\psi = m_p C_i$

$$\begin{aligned} \frac{\partial}{\partial t} \alpha_p \rho_p U_{p,i} + \frac{\partial}{\partial x_j} \alpha_p \rho_p U_{p,i} U_{p,j} &= -\alpha_p \frac{\partial P_g}{\partial x_i} - \frac{\partial}{\partial x_j} [\alpha_p \rho_p R_{p,ij} + \Theta_{ij}] \\ &+ I_{g \rightarrow p,i} + \alpha_p \rho_p g_i \\ &+ \chi_i \end{aligned} \quad (2.21)$$

with the mean drag term $I_{g \rightarrow p,i}$ given by

$$I_{g \rightarrow p,i} = \alpha_p \rho_p \left\langle \frac{1}{\tau_p^*} (\tilde{u}_{g,i} - u_{p,i}) \right\rangle. \quad (2.22)$$

Transport equation of 2nd-order Moment :

The transport equation of 2nd order moment is obtained by similar way with $\psi = m_p C_i C_i$

$$\begin{aligned} \frac{\partial}{\partial t} \alpha_p \rho_p R_{p,ij} + \frac{\partial}{\partial x_k} \alpha_p \rho_p U_{p,k} R_{p,ij} &= -\frac{\partial}{\partial x_k} [\alpha_p \rho_p S_{p,ijk} + \Theta_{ijk}] \\ &- [\alpha_p \rho_p R_{p,ik} + \Theta_{ik}] \frac{\partial U_{p,j}}{\partial x_k} \\ &- [\alpha_p \rho_p R_{p,jk} + \Theta_{jk}] \frac{\partial U_{p,i}}{\partial x_k} \\ &+ \alpha_p \rho_p \left\langle \frac{F_i}{m} u_{p,j} \right\rangle \\ &+ \chi_{ij}. \end{aligned} \quad (2.23)$$

The first term on the right-hand side can be interpreted as a diffusion term and represents the transport of kinetic stresses by fluctuating motion. The second and third terms are the production of kinetic stresses by the mean particle velocity gradients. The fourth term represents the interaction of kinetic stresses with the fluid. The last term represents the redistribution of kinetic stresses by collisions.

2.2.5 Transport Equation of Particle Agitation, q_p^2

The transport equation of particle agitation can be obtained from the transport equation of 2^{nd} order moment equation of particulate phase, Eq. (2.23), by summation of i and j indices as

$$\begin{aligned} \frac{\partial}{\partial t} \alpha_p \rho_p q_p^2 + \frac{\partial}{\partial x_k} \alpha_p \rho_p U_{p,k} q_p^2 &= -\frac{1}{2} \frac{\partial}{\partial x_j} [\alpha_p \rho_p S_{p,ijj} + \Theta_{ijj}] \\ &\quad - (\alpha_p \rho_p R_{p,ij} + \Theta_{ij}) \frac{\partial U_{p,i}}{\partial x_j} \\ &\quad + 2 \frac{\alpha_p \rho_p}{\tau_p} q_p^2 + \frac{1}{2} \chi_{jj}. \end{aligned} \quad (2.24)$$

2.2.6 Collision Terms for Inelastic Rigid Particles

To close the system, source terms; χ_i , χ_{ij} and flux terms; Θ_{ij} , Θ_{ijm} of the collisional rate of change in the momentum, Eq. (2.21), and 2^{nd} order moment, Eq. (2.23), equations of the particulate phase can be analytically given by using Jenkins and Richman (1985)'s approach. Source term; χ_{jj} and flux terms; Θ_{jk} , Θ_{jjk} appear in the particle agitation equation, Eq. (2.24).

Source terms in the particle momentum, Eq. (2.21), and 2^{nd} order moment, Eq. (2.23), equations are

$$\begin{aligned} \chi_i &= 0 \\ \chi_{ij} &= -8\alpha_p^2 \rho_p \frac{g_0}{d_p} (1 - e_c^2) \sqrt{\frac{2}{3} \frac{q_p^2}{\pi} \frac{2}{3} q_p^2} \delta_{ij} \\ &\quad + \frac{2}{5} \alpha_p^2 \rho_p g_0 (1 + e_c) (3e_c - 1) \frac{2}{3} q_p^2 D_{kk} \delta_{ij} \\ &\quad - \frac{12}{5} \alpha_p^2 \rho_p g_0 (1 + e_c) (e_c - 2) \frac{2}{3} q_p^2 D_{ij} \\ &\quad - \frac{24}{5} \alpha_p^2 \rho_p \frac{g_0}{d_p} (1 + e_c) (3 - e_c) \sqrt{\frac{2}{3} \frac{q_p^2}{\pi}} (R_{p,ij} - \frac{2}{3} q_p^2 \delta_{ij}). \end{aligned} \quad (2.26)$$

Source term in the particle agitation equation, Eq. (2.24), is

$$\begin{aligned} \chi_{jj} &= -12\alpha_p^2 \rho_p \frac{g_0}{d_p} (1 - e_c^2) \sqrt{\frac{2}{3} \frac{q_p^2}{\pi} \frac{2}{3} q_p^2} \\ &\quad + 3\alpha_p^2 \rho_p g_0 (1 - e_c^2) D_{kk} \frac{2}{3} q_p^2 \end{aligned} \quad (2.27)$$

where $D_{ij} = \frac{1}{2} \left[\frac{\partial U_{p,i}}{\partial x_j} + \frac{\partial U_{p,j}}{\partial x_i} \right]$.

Flux term in the particle momentum equation, Eq. (2.21), is

$$\begin{aligned}
\Theta_{ij} = & \left[2\alpha_p^2 \rho_p g_0 (1 + e_c) \frac{2}{3} q_p^2 - \frac{4}{5} \alpha_p^2 \rho_p g_0 (1 + e_c) \sqrt{\frac{2}{3} \frac{q_p^2}{\pi}} D_{kk} \right] \delta_{ij} \\
& - \frac{8}{5} \alpha_p^2 \rho_p d_p g_0 (1 + e_c) \sqrt{\frac{2}{3} \frac{q_p^2}{\pi}} D_{ij} \\
& + \frac{4}{5} \alpha_p^2 \rho_p g_0 (1 + e_c) (R_{p,ij} - \frac{2}{3} q_p^2 \delta_{ij}).
\end{aligned} \tag{2.28}$$

Source term in the particle agitation equation, Eq. (2.24), is

$$\begin{aligned}
\Theta_{ijj} = & \frac{6}{5} \alpha_p^2 \rho_p g_0 (1 + e_c) S_{imm} \\
& - 2\alpha_p^2 \rho_p g_0 (1 + e_c) \sqrt{\frac{2}{3} \frac{q_p^2}{\pi}} \frac{\partial}{\partial x_i} \left(\frac{2}{3} q_p^2 \right).
\end{aligned} \tag{2.29}$$

2.2.7 Radial Distribution Function

To extend the kinetic theory of dilute gases, the radial distribution function g_0 takes into account the increase of the probability of collision as the gas becomes denser. In dilute gases, g_0 is equal to unity, whereas g_0 diverges to infinity when molecules reach maximum packing. Several researches proposed different radial distributions for the granular media (Chapman and Cowling 1991, Ma and Ahmadi 1986, Ogawa et al. 1980, Ding and Gidaspow 1990). Here, we use the function proposed by Lun and Savage (1986) as

$$g_0 = \left(1 - \frac{\alpha_p}{\alpha_{p,max}} \right)^{-2.5\alpha_{p,max}} \tag{2.30}$$

with $\alpha_{p,max} = 0.64$ corresponding to spherical solid objects in random close packing.

2.3 GAS PHASE MODEL

In this section, derivations of macroscopic mass and momentum equations of gas phase in given control volume containing both phases are presented. The local instantaneous mass and momentum equations of the gas phase are

$$\frac{\partial}{\partial t} \rho_g + \frac{\partial}{\partial x_i} \rho_g u_{g,i} = 0 \tag{2.31}$$

$$\frac{\partial}{\partial t} \rho_g u_{g,i} + \frac{\partial}{\partial x_j} \rho_g u_{g,i} u_{g,j} = \frac{\partial}{\partial x_j} \sigma_{g,ij} + \rho_g g_i. \tag{2.32}$$

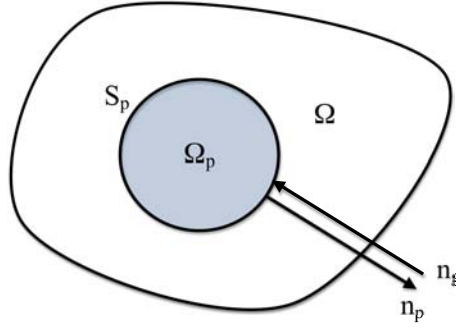


Figure 4: The schematic view of the control volume containing both phases.

The distribution characteristics of the phase k is defined by the phasic indicator function χ_k which is 1 if the phase k is present and 0 otherwise. The phasic indicator function follows the topological equation;

$$\frac{\partial \chi_k}{\partial t} + w_j \frac{\partial \chi_k}{\partial x_j} = 0 \quad \text{and} \quad \frac{\partial \chi_k}{\partial x_j} = -n_{k,j} \delta_k \quad (2.33)$$

where w_j is the propagation of the interface. The schematic view of the control volume Ω containing a single spherical particle in the gas is shown in Figure 4. The outwardly directed normal unit vector to the interface S_p of the volume occupied by the phases is $n_{k,j}$ and δ_k is the Dirac delta function associated with phase k .

Multiplying the local instantaneous mass and momentum equations by the phasic indicator function $\chi_g(\mathbf{x}, t)$ associated to gas phase ($k = g$) one can write

$$\frac{\partial}{\partial t} \rho_g \chi_g + \frac{\partial}{\partial x_i} \rho_g \chi_g u_{g,i} = 0 \quad (2.34)$$

$$\frac{\partial}{\partial t} (\chi_g \rho_g u_{g,i}) + \frac{\partial}{\partial x_j} (\chi_g \rho_g u_{g,i} u_{g,j}) = \frac{\partial}{\partial x_j} (\chi_g \sigma_{g,ij}) + \chi_g \rho_g g_i + \sigma_{g,ij} n_{g,j} \delta_g \quad (2.35)$$

If particles are much smaller than the characteristic length of flow, Eqs. (2.34) and (2.35) can be averaged by a spatial $\{.\}$ over a control volume Ω which is much larger than the particle scale but much smaller than the smallest length scale of the undisturbed flow (He and Simonin 1993, Druzhinin and Elghobashi 1998).

This allows us to define filtered undisturbed flow with following equations:

$$\epsilon_g \tilde{u}_{g,i} = \{u_{g,i} \chi_g\} = \frac{1}{\Omega} \int_{\Omega} u_{g,i} \chi_g d\omega \quad (2.36)$$

where

$$\epsilon_g = \{\chi_g\} = \frac{1}{\Omega} \int_{\Omega} \chi_g d\omega. \quad (2.37)$$

ϵ_g is the "microscopic" scale of the gas phase. With the spatial average over volume Ω , Eqs. (2.34) and (2.35) give,

$$\frac{\partial}{\partial t} \epsilon_g \rho_g + \frac{\partial}{\partial x_i} \epsilon_g \rho_g \tilde{u}_{g,i} = 0 \quad (2.38)$$

$$\frac{\partial}{\partial t} \epsilon_g \rho_g \tilde{u}_{g,i} + \frac{\partial}{\partial x_j} \epsilon_g \rho_g \tilde{u}_{g,i} \tilde{u}_{g,j} = \frac{\partial}{\partial x_j} \epsilon_g \tilde{\tau}_{g,ij} + \epsilon_g \rho_g g_i + \sigma_{g,ij} n_{g,j} \delta_g \quad (2.39)$$

where $\epsilon_g \tilde{\tau}_{g,ij}$ is the shear stress tensor defined by:

$$\epsilon_g \tilde{\tau}_{g,ij} = \{\tau_{g,ij} \chi_g\} - [\{\chi_g \rho_g \mathbf{u}_{g,i} \mathbf{u}_{g,j}\} - \epsilon_g \rho_g \tilde{u}_{g,i} \tilde{u}_{g,j}]. \quad (2.40)$$

The last term on the right-hand side in Eq. (2.39) is equal to the integration of stress on the total volume of particles by the flow. Assuming that the viscous terms in the undisturbed flow can be neglected and that the gradient of undisturbed pressure is uniform in Ω , $\{\tilde{\sigma}_{g,ij} n_{g,j} \delta_g\}$ is equal to $-\epsilon_g \partial \tilde{p}_g / \partial x_i$. The second term represents the force applied by the flow on the particle due to the perturbations in the flow created by the particle. This term can be replaced by the integration of force which is exerted due to total volume of particles as

$$\{\delta \sigma_{g,ij} n_{g,j} \delta_g\} \approx \frac{1}{\Omega} \int_{\Omega} \rho_p \frac{1}{\tau_p^*} (\mathbf{u}_p - \tilde{\mathbf{u}}_g) \chi_p d\omega. \quad (2.41)$$

In order to derive macroscopic equations of phases, the second statistical treatment is necessary. The Favre averaging operator $\langle \cdot \rangle$, proposed by Simonin (1996) is applied on Eq. (2.39). The macroscopic variables are decomposed into averaged and fluctuating part with following relations:

$$\alpha_g = \langle \epsilon_g \rangle \quad (2.42)$$

$$\alpha_g \mathbf{U}_{g,i} = \langle \epsilon_g \tilde{u}_{g,i} \rangle \quad (2.43)$$

$$\alpha_g P_g = \langle \epsilon_g \tilde{p}_g \rangle. \quad (2.44)$$

This leads us to the macroscopic mass and momentum equation of gas phase:

$$\frac{\partial}{\partial t} \alpha_g \rho_g + \frac{\partial}{\partial x_i} \alpha_g \rho_g \mathbf{U}_{g,i} = 0 \quad (2.45)$$

$$\begin{aligned} \frac{\partial}{\partial t} \alpha_g \rho_g \mathbf{U}_{g,i} + \frac{\partial}{\partial x_j} \alpha_g \rho_g \mathbf{U}_{g,i} \mathbf{U}_{g,j} &= -\alpha_g \frac{\partial P_g}{\partial x_i} + \alpha_g \rho_g g_i + I_{p \rightarrow g,i} \\ &\quad - \frac{\partial}{\partial x_j} [\Theta_{g,ij} + \alpha_g \rho_g \langle \mathbf{u}'_{g,i} \mathbf{u}'_{g,j} \rangle_g] \end{aligned} \quad (2.46)$$

where P_g is the mean pressure of the gas phase, $\langle \mathbf{u}'_{g,i} \mathbf{u}'_{g,j} \rangle_g$ is the Reynolds stress tensor, $\Theta_{g,ij}$ is the viscous part of the stress tensor and $I_{p \rightarrow g,i}$ is the mean drag force provided by

$$I_{p \rightarrow g, i} = -I_{g \rightarrow p, i} = \alpha_p \rho_p \left\langle \frac{1}{\tau_p^*} (\mathbf{u}_{p, i} - \tilde{\mathbf{u}}_{g, i}) \right\rangle \quad (2.47)$$

where the correlation between the gas pressure fluctuations and particulate phase is neglected (Fedhila and Simonin 1992). The mean relaxation time τ_p can be written as follows:

$$\tau_p = \langle \tau_p^* \rangle = \frac{4}{3} \frac{\rho_p}{\rho_g} \frac{d_p}{\langle C_D \rangle \langle |\mathbf{u}_p - \tilde{\mathbf{u}}_g| \rangle_p} \quad (2.48)$$

where

$$\langle C_D \rangle = \frac{24}{\langle Re_p \rangle} [1 + 0.15 \langle Re_p \rangle^{0.687}] \quad (2.49)$$

and

$$\langle Re_p \rangle = \frac{d_p \langle |\mathbf{u}_p - \tilde{\mathbf{u}}_g| \rangle_p}{\nu_g} \quad \langle |\mathbf{u}_p - \tilde{\mathbf{u}}_g| \rangle_p \approx \sqrt{V_{r, i} V_{r, i} + \langle v_{r, i}'' v_{r, i}'' \rangle_p}. \quad (2.50)$$

$V_{r, i}$ is the mean relative velocity between particle and local undisturbed gas velocity and defined by $V_{r, i} = \langle \mathbf{u}_{p, i} - \tilde{\mathbf{u}}_{g, i} \rangle_p = (\mathbf{U}_{p, i} - \mathbf{U}_{g, i}) - \mathbf{V}_{d, i}$ with the drift velocity $\mathbf{V}_{d, i}$. The drift velocity $\mathbf{V}_{d, i}$ is given by $\langle \tilde{\mathbf{u}}_{g, i} - \mathbf{U}_{g, i} \rangle_p = \langle \tilde{\mathbf{u}}'_{g, i} \rangle_p$ (Simonin 1990, Simonin et al. 1993). This velocity represents the dispersion of the particles transported by the large scale of the fluctuating motion in the gas phase. The closure model for drift velocity will be presented in §2.4.

The viscous part of the stress tensor $\Theta_{g, ij}$ can be written by using the classical expression for Newtonian fluids,

$$\Theta_{g, ij} = -\alpha_g \lambda_g S_{g, mm} \delta_{ij} + \mu_g S_{g, ij}^* \quad (2.51)$$

where λ_g is the bulk viscosity and μ_g is the dynamic viscosity. The strain rate tensor is given by $S_{g, ij} = \frac{1}{2} \left(\frac{\partial u_{g, i}}{\partial x_j} + \frac{\partial u_{g, j}}{\partial x_i} \right)$ and the deviatoric part by $S_{g, ij}^* = S_{g, ij} - S_{g, mm} \delta_{ij} / 3$.

2.4 CLOSURE MODELS

The mass and momentum equations are derived for gas and particulate phases, but closure relations are needed. The drift velocity $\mathbf{V}_{d, i}$ needs a closure in the drag force term, Eq. (2.50). Reynolds stresses arise in gas momentum equation, Eq. (2.46), and can be modelled by Reynolds Averaged Navier-Stokes (RANS) approach introducing two additional transport equations; turbulent kinetic energy k and turbulent energy dissipation ϵ by accounting for existence of particles. The transport equations for the second order moments of particulate, Eq. (2.23), phase contains third order moments. Third order moments have to be modelled or transport equation have to be derived. Herein, we use Boussinesq hypothesis for third order moments. Collisional terms in second order moment equations will have to be defined. We will perform analytical solution for collision terms. For fluidity of the writing and better understanding of physical mechanisms beyond equations, several time scales used in closure equations will be firstly mentioned.

2.4.1 Characteristic Time Scales

The characteristic time scale of large eddies of gas turbulence can be calculated by the ratio of the turbulent kinetic energy k , and the turbulent dissipation energy ϵ as classical RANS approach for single phase flows:

$$\tau_t = C_\mu \frac{3}{2} \frac{k}{\epsilon} \quad k = \langle u'_{g,i} u'_{g,i} \rangle_g / 2 \quad (2.52)$$

where C_μ is equal to 0.09.

Relaxation time or characteristic time of particle entrapped by the fluid is defined by

$$\tau_p = \frac{4}{3} \frac{\rho_p}{\rho_g} \frac{d_p}{\langle C_D \rangle \langle |\mathbf{v}_r| \rangle_p} \quad (2.53)$$

The time of interaction between particle motion and gas phase fluctuations or the eddy-particle interaction time is defined by

$$\tau_{fp}^t = \frac{\tau_t}{\sigma_{g,Pr}} \left[1 + C_\beta \xi_r^2 \right]^{-1/2} \quad \xi_r = |\mathbf{V}_r| / \sqrt{\frac{2}{3} k} \quad (2.54)$$

where $\sigma_{g,Pr}$ is the Schmidt or Prandtl number of gas phase and C_β is a constant equal to 1.8. Theoretically, it corresponds to the Lagrangian integral scale of turbulence seen by particles. We make another definition that will give information about competition between particle dragging and entrainment by gas turbulence;

$$\eta_r = \frac{\tau_{fp}^t}{\tau_p} \quad (2.55)$$

The particle-particle collision time in the frame of the KTGF (uncorrelated collision model) is given by

$$\tau_c = \left(24 \alpha_p \frac{g_0}{d_p} \sqrt{\frac{2}{3} \frac{q_p^2}{\pi}} \right)^{-1} \quad (2.56)$$

2.4.2 Modelling of Drift Velocity

The drift velocity $V_{d,i}$ represents the dispersion of particles by large eddies of fluid turbulence (Simonin 1990). Simonin and Viollet (1990) proposed the following model for the drift velocity:

$$V_{d,i} = -D_{fp,ij}^t \left[\frac{1}{\alpha_p} \frac{\partial \alpha_p}{\partial x_j} - \frac{1}{\alpha_g} \frac{\partial \alpha_g}{\partial x_j} \right] \quad (2.57)$$

where $D_{fp,ij}^t$ is the dispersion coefficient which is function of characteristic time of gas turbulence seen by particle and correlations between phase velocities;

$$D_{fp,ij}^t = \tau_{fp}^t \langle \tilde{u}'_{g,i} u''_{p,j} \rangle_p \quad (2.58)$$

$\langle \tilde{u}'_{g,i} u''_{p,j} \rangle_p$ is the tensor of covariance between phase velocity fluctuations.

2.4.3 Transport Equations of Gas Phase Turbulence

In Eq. (2.46), Reynolds stresses raise due to fluctuations of gas velocity. The transport equation for Reynolds stresses can be obtained by the multiplication of the undisturbed momentum equation of gas phase, Eq. (2.39), by velocity $\tilde{u}_{g,i}$ or $\tilde{u}_{g,j}$ with respect to Einstein summation indices (Vermorel et al. 2003). Then the general averaging operator $\langle \cdot \rangle$ is applied and following relation can be obtained

$$\frac{\partial}{\partial t} \alpha_g \rho_g \langle u'_{g,i} u'_{g,j} \rangle_g + \frac{\partial}{\partial x_k} U_{g,k} \langle u'_{g,i} u'_{g,j} \rangle_g = \frac{\partial}{\partial x_k} S_{g,ijk} + P_{g,ij} + \Phi_{g,ij} - \varepsilon_{g,ij} + \Pi_{g,ij} \quad (2.59)$$

It should be noted that $\langle \tilde{u}'_{g,i} \tilde{u}'_{g,i} \rangle_g$ is assumed to be equal to $\langle u'_{g,i} u'_{g,i} \rangle_g$. The first term on the right hand side is the dispersion of fluctuations which is transported by the fluctuations of velocity and pressure and can be written by

$$S_{g,ijk} = -\alpha_g \rho_g \langle u'_{g,i} u'_{g,j} u'_{g,k} \rangle_g - \alpha_g \langle u'_{g,i} \tilde{p}'_g \sigma_{g,jk} \rangle_g - \alpha_g \langle u'_{g,j} \tilde{p}'_g \sigma_{g,ik} \rangle_g. \quad (2.60)$$

The second term is the production due to the mean velocity gradient of gas phase

$$P_{g,ij} = -\alpha_g \rho_g \left[\langle u'_{g,i} u'_{g,k} \rangle_g \frac{\partial U_{g,j}}{\partial x_k} + \langle u'_{g,j} u'_{g,k} \rangle_g \frac{\partial U_{g,i}}{\partial x_k} \right]. \quad (2.61)$$

The third term is the correlation of pressure fluctuations with particulate phase

$$\Phi_{g,ij} = \langle \tilde{p}'_g \frac{\partial}{\partial x_j} [\varepsilon_g u'_{g,i}] \rangle + \langle \tilde{p}'_g \frac{\partial}{\partial x_i} [\varepsilon_g u'_{g,j}] \rangle. \quad (2.62)$$

The fourth term corresponds to the dissipation term of single-phase turbulent flows. In multi-phase flows, $\varepsilon_{g,ij}$ represents the viscous dissipation of small scale of local undisturbed flow and written as

$$\varepsilon_{g,ij} = \langle \varepsilon_g \tilde{\tau}_{g,ik} \frac{\partial u'_{g,j}}{\partial x_k} \rangle + \langle \varepsilon_g \tilde{\tau}_{g,jk} \frac{\partial u'_{g,i}}{\partial x_k} \rangle. \quad (2.63)$$

The last term in Eq. (2.59) is raised by the existence of particles in the flow. This term represents the effects of forces which exerted by particles on the turbulence of gas phase. Enhancing or suppression of the turbulence of gas phase is modelled by this term. It is written as

$$\Pi_{g,ij} = \frac{\alpha_g \rho_g}{\tau_p} [-2 \langle u''_{g,i} u''_{g,j} \rangle_p + \langle u''_{g,i} u''_{p,j} \rangle_p + \langle u''_{p,j} u''_{g,i} \rangle_p + V_{d,i} V_{r,j} + V_{r,i} V_{d,j}]. \quad (2.64)$$

C_μ	$C_{\epsilon,1}$	$C_{\epsilon,2}$	$C_{\epsilon,3}$	σ_k	σ_ϵ
0.09	1.44	1.92	1.2	1.0	1.3

Table 1: Empirical constants for modelling of gas phase turbulence.

The transport equation of the turbulent kinetic energy k can be obtained by summation of indices ($i = j$) of Reynolds stress tensor:

$$\begin{aligned} \frac{\partial}{\partial t} \alpha_g \rho_g k + \frac{\partial}{\partial x_m} \alpha_g \rho_g U_{g,m} k &= -\frac{\partial}{\partial x_j} \left[\alpha_g \rho_g \frac{\nu_g^t}{\sigma_k} \frac{\partial k}{\partial x_j} \right] \\ &\quad - \alpha_g \rho_g \langle u'_{g,i} u'_{g,j} \rangle_g \frac{\partial U_{g,i}}{\partial x_j} \\ &\quad - \alpha_g \rho_g \epsilon + \Pi_k \end{aligned} \quad (2.65)$$

where ν_g^t is the turbulent viscosity and is defined as in classical single phase flow, $\nu_g^t = C_\mu \frac{k^2}{\epsilon}$ (Viollet and Simonin 1994, Elghobashi et al. 1984).

The transport equation of the turbulent dissipation ϵ , is given by

$$\begin{aligned} \frac{\partial}{\partial t} \alpha_g \rho_g \epsilon + \frac{\partial}{\partial x_m} \alpha_g \rho_g U_{g,m} \epsilon &= -\frac{\partial}{\partial x_j} \left[\alpha_g \rho_g \frac{\nu_g^t}{\sigma_\epsilon} \frac{\partial \epsilon}{\partial x_j} \right] \\ &\quad - \alpha_g \rho_g \frac{\epsilon}{k} C_{\epsilon,1} \langle u'_{g,i} u'_{g,j} \rangle_g \frac{\partial U_{g,i}}{\partial x_j} \\ &\quad - \alpha_g \rho_g \frac{\epsilon}{k} C_{\epsilon,2} \epsilon + \Pi_\epsilon. \end{aligned} \quad (2.66)$$

Terms accounting for particles effects on gas phase turbulence can be modelled by

$$\Pi_k = \frac{\alpha_p \rho_p}{\tau_p} [-2 \langle k \rangle_p + q_{fp} + V_{d,i} V_{\tau,i}] \quad (2.67)$$

$$\Pi_\epsilon = C_{\epsilon,3} \frac{\epsilon}{k} \Pi_k \quad (2.68)$$

where q_{fp} is the fluid-particle covariance and $\langle k \rangle_p$ is the turbulence kinetic energy seen by particles and approximately calculated by (He and Simonin 1993) as

$$\langle k \rangle_p \approx \frac{1}{2} \langle u'_{g,i} u'_{g,i} \rangle_g. \quad (2.69)$$

Empirical constants for Eqs. (2.65) and (2.66) are given in Table 1.

2.4.4 Modelling of Fluid-Particle Covariance, q_{fp}

The tensor of fluid-particle fluctuations correlation can be modelled by constructing an analogy by single phase flow with eddy viscosity concept (Simonin et al. 1993):

$$\langle \tilde{u}'_{g,i} u''_{p,j} \rangle_p = -\nu_{fp}^t \left[\frac{\partial U_{g,i}}{\partial x_j} + \frac{\partial U_{p,j}}{\partial x_i} \right] + \frac{1}{3} \delta_{ij} \left[q_{fp} + \nu_{fp}^t \left(\frac{\partial U_{g,k}}{\partial x_k} + \frac{\partial U_{p,k}}{\partial x_k} \right) \right] \quad (2.70)$$

where fluid-particle turbulent viscosity can be written by multiplication of fluid-particle covariance and characteristic time of particle and fluid turbulence interaction:

$$\nu_{fp}^t = \frac{1}{3} q_{fp} \tau_{fp}^t \quad q_{fp} = \langle \tilde{u}'_{g,i} u''_{p,i} \rangle_p. \quad (2.71)$$

Simonin et al. (1993) proposed the following transport equation for the fluid-particle covariance:

$$\begin{aligned} \frac{\partial}{\partial t} \alpha_p \rho_p q_{fp} + \frac{\partial}{\partial x_k} \alpha_p \rho_p U_{p,k} q_{fp} &= -\frac{\partial}{\partial x_j} \left[\alpha_p \rho_p \frac{\nu_{fp}^t}{\sigma_q} \frac{\partial q_{fp}}{\partial x_j} \right] \\ &\quad -\alpha_p \rho_p \epsilon_{fp} + \Pi_{fp} \\ &\quad -\alpha_p \rho_p \langle \tilde{u}'_{g,i} u''_{p,j} \rangle_p \frac{\partial U_{p,i}}{\partial x_j} \\ &\quad -\alpha_p \rho_p \langle \tilde{u}'_{g,j} u''_{p,i} \rangle_p \frac{\partial U_{g,i}}{\partial x_j}. \end{aligned} \quad (2.72)$$

The first term on the right-hand side of the equation represents the turbulent transport of velocity correlations. The second term represents the destruction of correlations by fluid viscosity and de-correlation of fluctuations due to the relative velocity. It can be modelled by the ratio between fluid-particle correlation and characteristic time of particle and fluid turbulence interaction:

$$\epsilon_{fp} = \frac{q_{fp}}{\tau_{fp}^t}. \quad (2.73)$$

The third term characterises the interaction between phase fluctuations and is given by:

$$\Pi_{fp} = -\alpha_p \rho_p \frac{1}{\tau_p} \left[\left(1 + \frac{\alpha_p \rho_p}{\alpha_g \rho_g} \right) q_{fp} - 2k - 2 \frac{\alpha_p \rho_p}{\alpha_g \rho_g} q_p^2 \right]. \quad (2.74)$$

The fourth and fifth terms represent productions by gradients of the mean phase velocity gradients.

2.4.5 Effective Kinetic Stress Tensor

The term $\alpha_p \rho_p R_{p,ij} + \Theta_{ij}$ in the particle momentum equation, Eq. (2.21), and the agitation equation, Eq. (2.24), is called as the effective stress tensor $\Sigma_{p,ij}$ by Balzer et al. (1995). With an assumption of local equilibrium of production and dissipation terms in

the particle kinetic stress equation, Balzer et al. (1995) proposed a practical form of the effective stress including collisional effects:

$$\Sigma_{p,ij} = \left[P_p - \lambda_p \frac{\partial U_{p,m}}{\partial x_m} \right] \delta_{ij} - \mu_p \left[\frac{\partial U_{p,i}}{\partial x_j} + \frac{\partial U_{p,j}}{\partial x_i} - \frac{2}{3} \frac{\partial U_{p,m}}{\partial x_m} \delta_{ij} \right] \quad (2.75)$$

where the granular pressure is given as

$$P_p = \alpha_p \rho_p \frac{2}{3} q_p^2 [1 + 2\alpha_p g_0 (1 + e_c)], \quad (2.76)$$

the solid bulk viscosity is defined by

$$\lambda_p = \frac{4}{3} \alpha_p^2 \rho_p d_p g_0 (1 + e_c) \sqrt{\frac{2}{3} \frac{q_p^2}{\pi}} \quad (2.77)$$

and the solid shear viscosity is written by

$$\mu_p = \alpha_p \rho_p (\nu_p^{\text{kin}} + \nu_p^{\text{coll}}) \quad (2.78)$$

with the kinematic viscosity

$$\nu_p^{\text{kin}} = \left[\frac{1}{3} \tau_{fp}^t q_{fp} + \frac{1}{2} \tau_p \frac{2}{3} q_p^2 (1 + \alpha_p g_0 \phi_c) \right] / \left[1 + \frac{\sigma_c \tau_p}{2 \tau_c} \right] \quad (2.79)$$

and the collisional viscosity

$$\nu_p^{\text{coll}} = \frac{4}{5} \alpha_p g_0 (1 + e_c) \left(\nu_p^{\text{kin}} + d_p \sqrt{\frac{2}{3} \frac{q_p^2}{\pi}} \right). \quad (2.80)$$

The constants are $\sigma_c = \frac{1}{5}(1 + e_c)(3 - e_c)$ and $\phi_c = \frac{2}{5}(1 + e_c)(3e_c - 1)$. The expressions for the kinematic and collisional viscosity are obtained from the diagonal transport equations for a homogeneous shear flow (Balzer et al. 1995). This viscosity expression comprises of a competition between different mechanisms according to the characteristic time scales given in 2.4.1. For very dilute regime, the viscosity is controlled by the fluid turbulence and in the dense regime, the viscosity is controlled by inter-particle collisions. In intermediate regime, there is a competition between mechanisms.

2.4.6 Effective Diffusivity

In similar manner, the term $\alpha_p \rho_p S_{p,ijj} + \Theta_{ijj}$, in the agitation equation, Eq. (2.24), is called as the effective diffusivity by Balzer et al. (1995). They decomposed this diffusivity into the kinematic and collisional part. The kinematic diffusivity is given by

$$K_p^{\text{kin}} = \left[\frac{1}{3} \tau_{fp}^t q_{fp} + \frac{5}{9} \tau_p \frac{2}{3} q_p^2 (1 + \alpha_p g_0 \varphi_c) \right] / \left[1 + \frac{5}{9} \xi_c \frac{\tau_p}{\tau_c} \right] \quad (2.81)$$

and the collisional diffusivity:

$$K_p^{\text{coll}} = \alpha_p g_0 (1 + e_c) \left(\frac{6}{5} K_p^{\text{kin}} + \frac{4}{3} d_p \sqrt{\frac{2}{3} \frac{q_p^2}{\pi}} \right) \quad (2.82)$$

with $\xi_c = \frac{1}{100} (1 + e_c) (49 - 33e_c)$ and $\varphi_c = \frac{3}{5} (1 + e_c)^2$.

2.5 WALL BOUNDARY CONDITIONS

Interactions of particles and gas with wall have an important effect on the flow dynamics. It is necessary to derive boundary conditions representing physical mechanisms accurately. For gas phase, no-slip boundary conditions on solid surface introduced with wall functions. The friction velocity is defined by

$$u_{g,\tau} = C_\mu^{0.25} k^{0.5} \quad (2.83)$$

Then, wall functions can be written as

$$\frac{\partial U_g}{\partial n} = \frac{u_*}{\kappa y}, \quad (\nu_g + \nu_g^t) \frac{\partial U_g}{\partial n} = u_* u_\tau, \quad \epsilon = \frac{u_{g,\tau}^3}{\kappa y}, \quad \frac{\partial k}{\partial n} = 0 \quad (2.84)$$

with the logarithmic law $u_* = \frac{1}{\kappa} \log\left(\frac{U_g \pi y}{\nu_g}\right) + C$ where U_g is the mean gas velocity, κ is the von Karman constant, y is the distance to the wall and n is the wall normal direction.

For particulate phase, the wall is modelled as a smooth and an undeformable surface interacting with particles by inelastic collisions. Boundary conditions are given by He and Simonin (1993) as functions of wall restitution coefficient e_w and friction coefficient, μ_w . Flux along the wall can be implemented by

$$\alpha_p U_{p,n} = 0. \quad (2.85)$$

Boundary condition for the mean particle velocity along the streamwise direction is

$$\nu_p^{\text{kin}} \frac{\partial U_{p,s}}{\partial n} = \mu_w \frac{2}{3} q_p^2. \quad (2.86)$$

Turbulent flux condition for particle agitation is defined by

$$K_p^{\text{kin}} \frac{\partial q_p^2}{\partial n} = \frac{(1 - e_w)}{\sqrt{e_w}} \sqrt{\frac{2}{\pi}} \left[\frac{2}{3} q_p^2 \right]^{3/2}. \quad (2.87)$$

No-slip wall boundary conditions for the particulate phase are defined as follows (Fede et al. 2009):

$$U_s = 0 \quad \text{and} \quad \frac{\partial q_p^2}{\partial n} = 0. \quad (2.88)$$

2.6 SUMMARY

In this section, we discuss some final remarks on the kinetic theory of granular flow and on closure models. Euler-Euler model presented in this study consists of a single particle phase and a gas phase. This model accounts for the influence of the interstitial gas on the granular flow. This approach improves accuracy for dilute regimes, $\tau_c \gg \tau_{fp}^t$. Concerning the turbulent motion, equations for particle kinetic stresses based on the particle velocity distribution function supplemented by Grad's moments for collisions terms are derived. The correlation between phase fluctuations is realised by the fluid-particle correlation tensor. As this term, it is crucial for accurate prediction of turbulence enhancement and destruction. Drift velocity which represents particle movements due to large eddies of gas turbulence is closed with dispersion coefficient based on the fluid correlation tensor. It is pointed out that models are free from empirical constants except the restitution coefficient e_c and the radial distribution function g_0 .

For applications of fluidized beds, it is practical to use the transport equation for particle agitation equation q_p^2 and fluid-particle covariance q_{fp} . With assumption of the local equilibrium hypothesis, Balzer et al. (1995) proposed the effective stresses and diffusivity with collisional effects for transport properties of particulate phase. For gas velocity fluctuations, the two equation model $k - \epsilon$, are proposed with accounting for the existence of particles in frame of RANS approach. In the next chapter, models are used to perform numerical simulations of different configuration of CFBs and results will be compared with available experimental data.

PREDICTIONS USING BY URANS APPROACH

3.1 INTRODUCTION

Three flow configurations were used to perform simulations of gas-solid flows in CFB risers by URANS approach. The first configuration is a pilot scale of CFB which is a typical replica of fluidized bed used for industrial applications such as; coal or biomass combustion. B-type particles were conducted in this configuration. The second case is a typical pilot-scale FCC application in which A-type particles are driven by relatively high fluidization velocity as compared with the first case. For the last configuration, particle type is the same as the second case with a different particle diameter and particles are supplied into the riser by same sense due to the fluidization velocity direction. These simulations allow us to determine drawbacks of available model and make comparisons between available experimental data in terms of predictability of flow characteristics for different types of particles.

3.1.1 Physical Models

The fluidization gas is the incompressible and isothermal ambient air for all cases. The modified two-equation turbulence model $k - \epsilon$ that takes into account the effects of particulate phase is used to solve gas-phase turbulence. Particle velocity fluctuations are resolved by the two transport equations $q_p^2 - q_{fp}$. The effects of collisions between particles are taken into account by granular pressure, kinematical and collisional viscosity. The destruction of particle agitation by inelastic collisions between particles is realised by the restitution coefficient e_c set to 0.9 for all cases. The influence of particles on the gas phase dynamics is taken into account. The interfacial transfer between gas and particles is accounted by the mean gas pressure gradient (Archimede force) and drag force defined by Wen and Yu (1966)'s equation limited by Ergun (1952)'s relation. The combination of two correlations was given by Gobin et al. (2003):

$$\langle C_D \rangle = \begin{cases} \min[\langle C_D^{\text{Ergun}} \rangle, \langle C_D^{\text{Wen\&Yu}} \rangle] & \text{if } \alpha_p > 0.3 \\ \langle C_D^{\text{Wen\&Yu}} \rangle & \text{if not} \end{cases} \quad (3.1)$$

where $\langle C_D^{\text{Wen\&Yu}} \rangle = \frac{24}{\langle Re_p \rangle} [1 + 0.15 \langle Re_p \rangle^{0.687}] \alpha_g^{-1.7}$ and $\langle C_D^{\text{Ergun}} \rangle = 1.75 + \frac{150}{\langle Re_p \rangle}$.

3.1.2 Boundary Conditions

For each case, gas and particle velocities are specified at gas and particle inlets. The turbulent kinetic energy k and dissipation ϵ of gas phase are calculated by the following equations:

$$k_{\text{inlet}} = \frac{2}{3} \frac{u_*^2}{\sqrt{C_\mu}} \quad (3.2)$$

$$\varepsilon_{\text{inlet}} = \frac{C_\mu}{\kappa u_*} \frac{k_{\text{inlet}}^2}{D_{\text{inlet}}/10} \quad (3.3)$$

where u_* is the friction velocity given by $U_g \sqrt{\lambda/8}$ with $\lambda = 0.3164\text{Re}^{-0.25}$ if $\text{Re} < 3000$ and $\lambda = 0.184\text{Re}^{-0.22}$ if $\text{Re} > 3000$. The Reynolds number is defined by : $\text{Re} = \frac{D_{\text{inlet}} U_{g,\text{inlet}}}{\nu_g}$. C_m and κ are constants, equal to 0.09 and 0.41, respectively. Bouncing of particles from walls are elastic and frictionless (the coefficient of wall normal restitution $e_w = 1.0$ and the friction coefficient $\mu_w = 0$). For the gas phase, the friction wall is defined. The outlet of riser is free-outlet and a Neumann condition $\frac{\partial}{\partial n} \left(\frac{\partial P_g}{\partial \tau} \right) = 0$ determines the gas pressure at the outlet where τ is the tangential direction and n is the normal direction.

3.1.3 Convergence Criteria

We assume that simulations are reached “steady-state” condition as the total mass of particles in the riser oscillated around a constant value. After the flow regime reaches “stabilised-state” and time averaged values of pressure, mass fluxes and velocity fluctuations of phases are calculated. A time averaged value \bar{Q}^t of the quantity Q can be defined by

$$\bar{Q}^t(x, t) = \frac{1}{\Delta t} \int_t Q(x, t) dt. \quad (3.4)$$

3.1.4 Flow Characterisation

The time averaged value of macroscopic variables are compared with available experimental data. The time-averaged mean gas pressure allows us to know that total mass in the riser is well-predicted or not. Additionally, we can classify the flow structure into two parts: mixing and developed by the gradient of gas pressure. The mean pressures are obtained on wall parallel to inlet location and the pressure gradient is calculated by the central difference scheme as follows:

$$\nabla \bar{P}^t(x_j) = \frac{\bar{P}^t(x_{j+1}) - \bar{P}^t(x_{j-1}))}{x_{j+1} - x_{j-1}} \quad (3.5)$$

with $\bar{P}^t(x_j)$ mean pressure and x_j node coordinate indices by j in the computational domain. To investigate segregation of particles close to the wall, we split axial mass fluxes into negative (downward) and positive (upward) parts. The axial negative and positive mass fluxes are calculated by following equations:

$$\overline{G_{s,+}}^t = \overline{\alpha_p(x_j)\rho_p(x_j)U_{p,z}(x_j)}^t \quad \text{if } U_{p,z}(x_j) > 0 \quad (3.6)$$

$$\overline{G_{s,-}}^t = \overline{\alpha_p(x_j)\rho_p(x_j)U_{p,z}(x_j)}^t \quad \text{if } U_{p,z}(x_j) < 0. \quad (3.7)$$

We use the following definitions to determine the mechanism through the flow:

$\frac{\tau_{fp}^t}{\tau_p}$: the competition between the drag force and particle entrapment by the gas turbulence,

$\frac{\tau_p}{\tau_c}$: the competition between entrainment by particle dragging and collisions between particles. Remind that τ_{fp}^t is the turbulence time scale of flow seen by particles and takes into account the crossing trajectory effect, τ_p is the mean relaxation time and τ_c is the characteristic time of collisions between a pair of particles.

The non-dimensional mesh size Fr_{Δ}^{-1} is

$$Fr_{\Delta}^{-1} = \frac{(\Delta x \Delta y \Delta z)^{1/3}}{(\tau_p^{St})^2 |g|}. \quad (3.8)$$

with the Stoke's relaxation time τ_p^{St} given by $\frac{\rho_p}{\rho_g} \frac{d_p^2}{18\nu_g}$.

Investigations of velocity fluctuations of phases in risers are presented and anisotropic behaviour of fluctuations will be discussed. In addition to that, we perform parametric studies to improve the quality of results and to verify accuracy of parameters.

3.2 SIMULATIONS OF DILUTE GAS-PARTICLE FLOW IN A CFB RISER

This case concerns the numerical simulation of hydrodynamics of a cold CFB for transported B-type particles. The experimental setup is a representative cold model of CERCHAR and measurements of pressure and mass flux were done by Fabre (1995).

3.2.1 Description of Experimental Setup

The experimental data for this case was realised by Fabre (1995) on the industrial pilot of CERCHAR. Figure 5 shows the experimental setup and the physical properties of gas and solid are in given in Table 2 . The riser cross-section is rectangular area with 0.8m in depth and 1.2m in length. The height of riser is equal to 9.4m and the cross-section of riser at 10.0m is re-sized with homethety equal to 0.5. During the experiment, Fabre (1995) filled up 1000 kg of sand into the setup and make circulation with air of which the fluidization velocity is equal to 4.01 m/s (with 1% error). Solids are injected with $5.65 \text{ kg}\cdot\text{m}^{-2}\text{s}^{-1}$ mass flux (with 7% error) and it is stated that the gas temperature never exceeded 50°C.

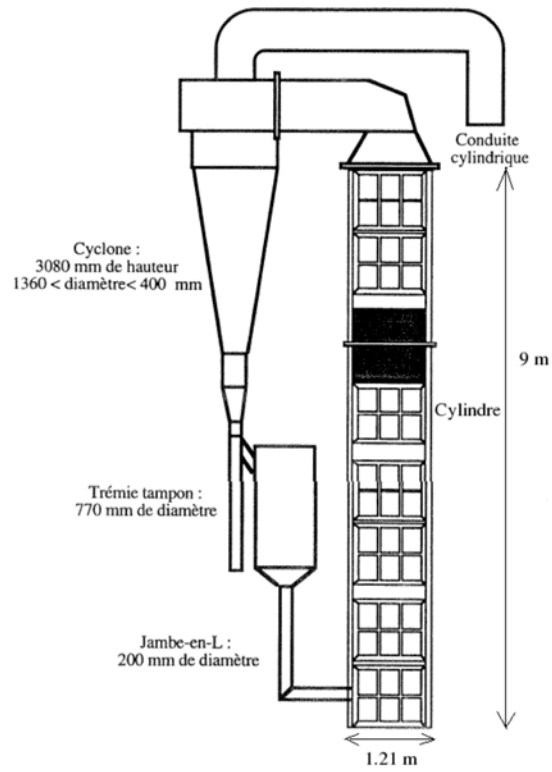


Figure 5: The experimental setup of Fabre (1995).

Gas Phase	
ρ_g	1.123 kg/m ³
μ_g	1.9×10^{-5} Pa.s
$U_{p,inlet}$	4 m/s
Particle Phase	
$d_{p,50}$	260 μ m
ρ_p	2650 kg/m ³
$U_{p,Linlet}$	0.64 m/s
$\alpha_{p,Linlet}$	0.1
Mass flux	5.65 kg/m ² s

Table 2: Flow properties of CERCHAR case (B-type particles).

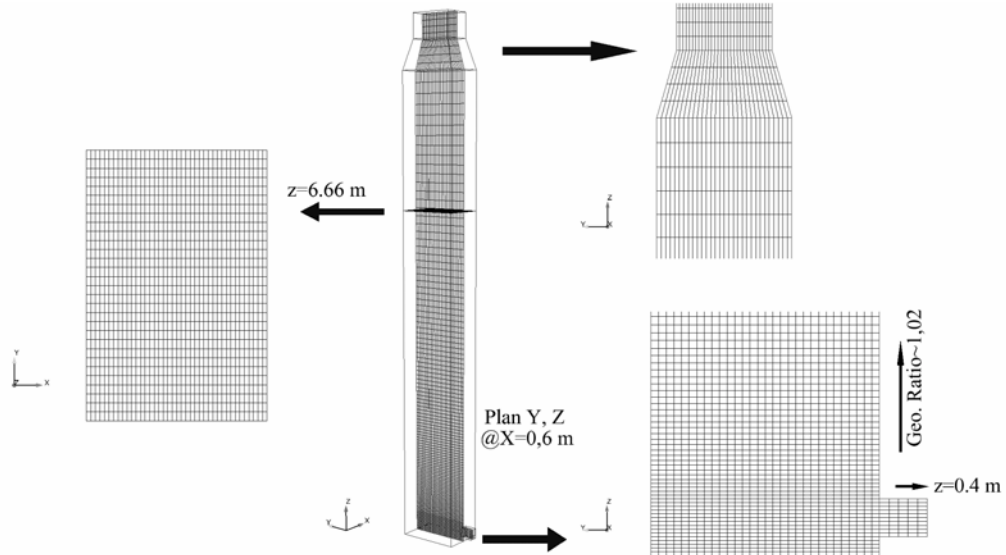


Figure 6: The computational domain of CERCHAR case.

3.2.2 Description of Numerical Simulation

Computational Grid

For three-dimensional simulations, the experimental setup of Fabre (1995) was simplified by removing cyclone, tampon and return pipe. The injector area is 0.032 m^2 and located at $z = 0.1 \text{ m}$ and the length of the particle inlet is equal to 0.25 m . The grid is defined in Cartesian coordinate and has approximately 150 000 cells. The number of nodes is 41 in direction x , 31 in the direction y and 131 in the direction z . The grid is uniform along directions x, y ($\Delta x = 0.02 \text{ m}$, $\Delta y = 0.04 \text{ m}$). In the direction z , it is uniform up to $z = 0.4 \text{ m}$ with $\Delta z = 0.02 \text{ m}$, and then it is extended with successive ratio equal to 1.02 (see Figure 6). The minimum non-dimensional mesh size $Fr_{\Delta, \min}^{-1}$ is equal to 0.0093.

Fluidization Grid

At the inlet of experimental setup of CERCHAR, there is a grid which supplies homogeneous distribution of the fluidization air and this grid is not modelled for the simulations. Indeed, the homogeneity of fluidization air is taken into account by the implementation of uniform distribution of air and frictionless wall for particles. The velocity is set to 4.0 m/s and the mass flux of air at the inlet is equal to 4.31 kg/s .

Particle Injection

The solid volume fraction at the feeding pipe was set to 0.1 for the simulation with mass flux of air equal to 0.0267 kg/s by following Batrak (2005). The velocity of particle $u_{L,inlet}$ was 0.64 m/s and the gas velocity at the feeding pipe was identical of the particles. The values of turbulent kinetic energy and dissipation were calculated by Eqs. (3.2) and (3.3). For velocity fluctuations of particles, values imposed by Batrak (2005) were implemented. (i.e $q_p^2 = 0.01 \text{ m}^2/\text{s}^2$, $q_{fp} = 0.02 \text{ m}^2/\text{s}^2$).

Initialisation of the Computational Domain

To shorten the transition period, we decided to initialise the bed with 120 kg solid in which the volume fraction is homogeneous and equal to 0.005. Velocities of phases were set to zero.

3.2.3 Simulation Results

Flow structures in dense and dilute zones are shown in Figure 7a. The formation of dense zone can be seen close to particle inlet and clusters are formed. In the upper dilute part of CFB riser, clusters disappear in the gas suspension. Figure 7b shows the instantaneous axial velocity of particle normalised by the terminal settling velocity of a single particle V_t^{St} given by $V_t^{St} = \tau_p^{St} |g|$. Particles fall down with a higher velocity than terminal settling velocity close to the acceleration zone. In the dilute part, particles are transported by the gas in the centre of the riser and falling particles significantly exceed the terminal settling velocity at the vicinity the wall.

Ratios of the instantaneous characteristic time-scales, τ_{fp}^t/τ_p and τ_p/τ_c , are shown in Figure 8a and 8b. It can be seen that gas turbulence is suppressed by particles close to the gas inlet. In this region, particles are sensible to gas turbulence ($\tau_{fp}^t/\tau_p < 0.25$). Except this region, particle entrapped by fluid is the main mechanism as compared with turbulence dispersion. Close to the particles injection, collision frequency is important due to lateral accumulation of particles ($\tau_c \ll \tau_p$). A competition between particle dragging by fluid and collisions occurs in some local regions. Particle-particle collisions are significant where clustering are formed. In the dilute part, collisions are rare, as expected ($\tau_c \gg \tau_p$).

Particles behaviours at the dilute zone ($z = 6.66 \text{ m}$) are shown in Figure 9. The clusters are formed wall to wall, in particular cases at the centre of the riser in the dilute region. Particles tend to accumulate at the corners and along walls between corners. This phenomena is reported by the experimental study of van der Meer et al. (2000) for risers with a square section. Particle velocity vectors show that highest velocity occur in the centre of the riser and negative values at the wall.

The evolution of solid mass in the riser is shown in Figure 10a. Simulation has an oscillating behaviour throughout time and it can be seen that particles initially presented in the riser are blown out. After 50 seconds, the flow reaches steady state condition. Then, we calculated time averaged variables for 100 seconds.

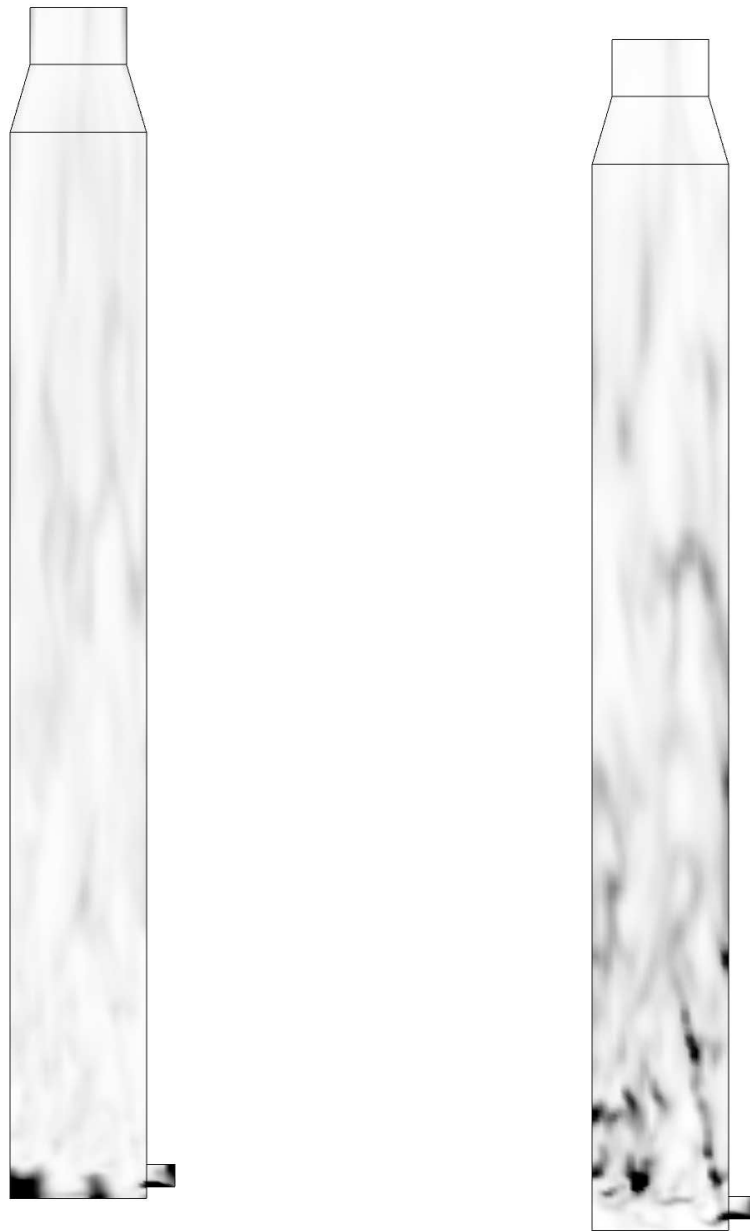
The air hydrostatic pressure was subtracted from numerical results $\overline{P_g^*}^t(z) = \overline{P_g}^t - \rho_g g(z_{ref} - z)$. z_{ref} is at 9m from the gas inlet. Time averaged pressure profile shows a good agreement with experimental results in the dilute region and the close to the gas



(a) The instantaneous solid volume fraction field
 (White: $\alpha_p = 0$, Black: $\alpha_p = 0.05$, $x - y @ 0.0$ m).

(b) The ratio between the axial particle velocity and the single particle terminal velocity, $U_{p,z}/V_t^{St}$ (White: $U_{p,z}/V_t^{St} = 0$, Black: $U_{p,z}/V_t^{St} = -1$, $x - y @ 0.0$ m).

Figure 7: Flow characteristics (CERCHAR).



(a) The ratio between the gas turbulence seen by particle and the particle relaxation time, τ_{fp}^t/τ_p (White: $\tau_{fp}^t/\tau_p = 0$, Black: $\tau_{fp}^t/\tau_p = 0.1$, $x - y@0.0$ m).

(b) The ratio between the particle relaxation and the collision time, τ_p/τ_c (White: $\tau_p/\tau_c = 0$, Black: $\tau_p/\tau_c = 100$, $x - y@0.0$ m).

Figure 8: Time characteristics (CERCHAR).

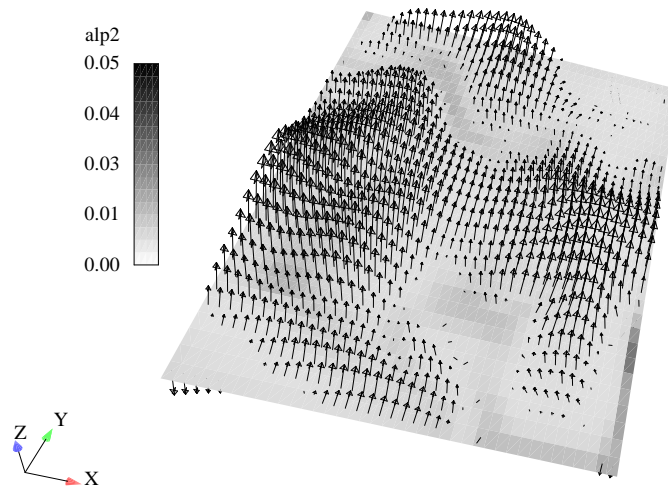


Figure 9: Instantaneous particle velocity vectors superimposed on the contour plot of instantaneous solid volume fraction at $z = 6.66$ m.

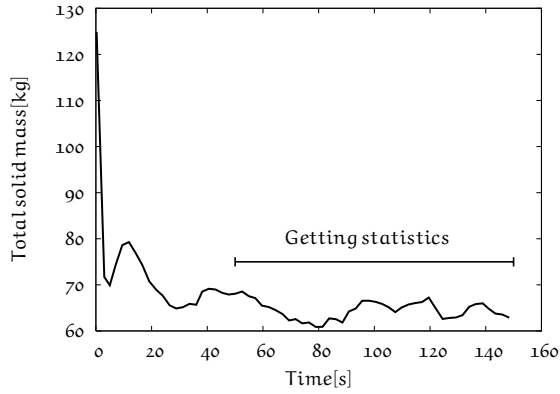
inlet (see Figure 10b). Positive, negative and net solid mass fluxes are shown along radial directions in Figures 10c-10f. The time-averaged solid mass flux profiles show the core-annulus flow and capture the general trend in flux profile of experimental data. Particle clusters move downwards along the riser and create a negative flux close to the wall. However, net mass flux is underestimated in the centre of riser and overestimated close to the wall.

3.2.4 Parametric Studies

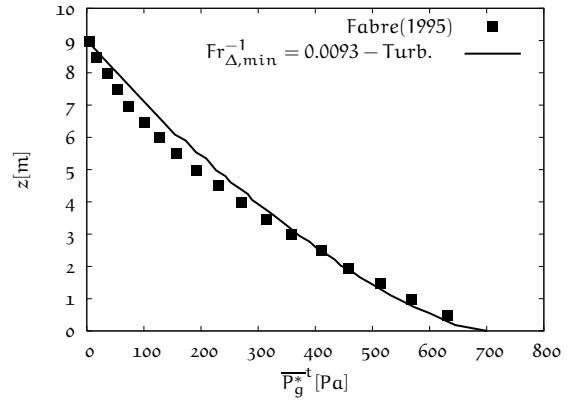
Influence of Turbulence Modelling and Mesh Resolution

URANS is a questionable approach for these kinds of fluidized bed applications and in this part, the sensitivity analysis of the turbulence modelling is discussed. Turbulent kinetic energy is damped by the source term due to the existence of particles. To investigate the influence of the turbulence modelling, the case with laminar flow has been done. Another remarkable point is that the same turbulent scale may be predicted by the laminar case because of too coarse mesh. To investigate this effect, the turbulent case has been redone by finer mesh configuration. In order to reduce the computational cost, the mesh was refined two times in x,y and only close to mixing area for z direction. After mesh refinement, number of cell is approximately 720 000 and the minimum non-dimensional mesh size $Fr_{\Delta, \min}^{-1}$ is equal to 0.0059. This case is then namely called $81 \times 61 \times 161$ in discussions.

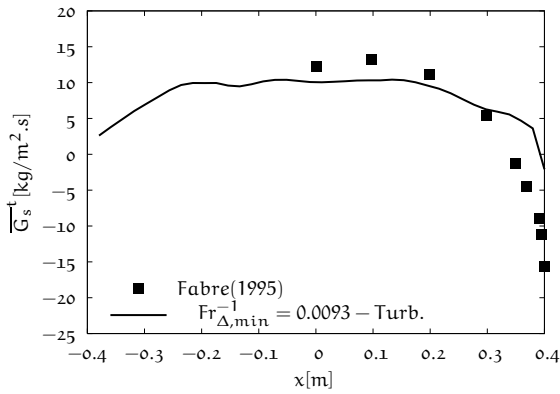
Time evolution of total solid in the riser with and without turbulence model are shown in Figure 11a for coarse mesh configuration ($41 \times 31 \times 141$). Predictions of total solid mass with and without turbulence model do not show significant difference. Figure 11b shows the profiles of the time-averaged axial gas pressure and profiles are the same except slight difference occurred at the developed zone. Mass flux profiles show similar behaviour,



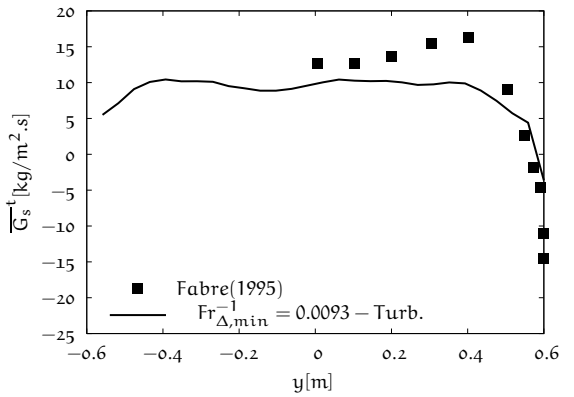
(a) The evolution of total solid mass in the riser.



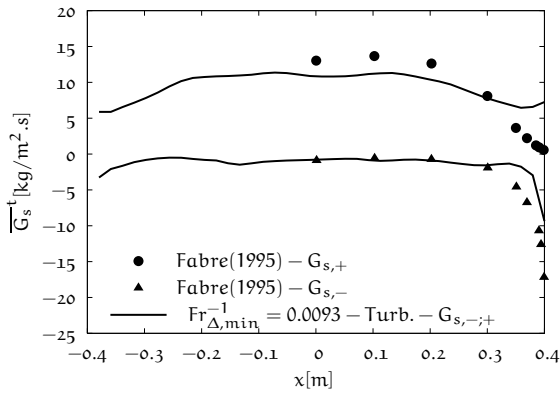
(b) Time-averaged gas pressure along the vertical direction.



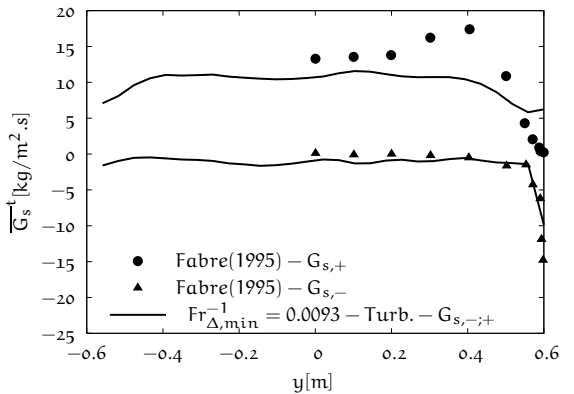
(c) Profiles of time-averaged vertical mass flow rate at $z = 6.66$ m along the radial direction, $x = [-0.4; 0.4]$ m ($y = 0.0$ m).



(d) Profiles of time-averaged vertical mass flow rate at $z = 6.66$ m along the radial direction, $y = [-0.6; 0.6]$ m ($x = 0.0$ m).



(e) Profiles of time-averaged vertical negative and positive mass flow rate at $z = 6.66$ m along the radial direction, $x = [-0.4; 0.4]$ m ($y = 0.0$ m).



(f) Profiles of time-averaged vertical negative and positive mass flow rate at $z = 6.66$ m along the radial direction, $y = [-0.6; 0.6]$ m ($x = 0.0$ m).

Figure 10: Predictions of reference case (mesh: $41 \times 31 \times 141, Fr_{\Delta, min}^{-1} = 0.0093$) versus experimental data of Fabre (1995).

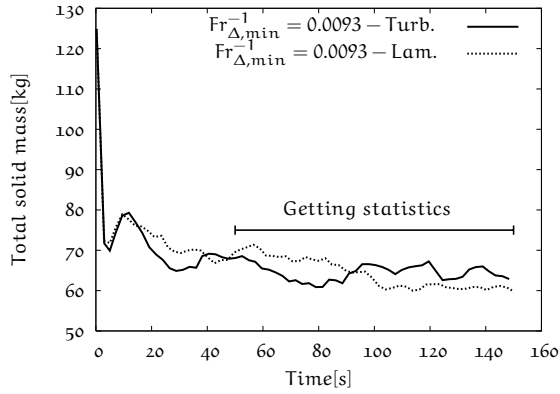
both cases underestimate total fluxes at the centre of the riser and capture negative flux close to the wall (see Figures 11c-11f).

For fine mesh configuration ($81 \times 61 \times 161$), total solid mass evolution in the riser with and without turbulence model are shown by Figure 12a. Mass inventory predicted with turbulence model is less than of the case with laminar gas flow. Total mass with laminar flow is equal to 62 ± 2 kg and total mass with turbulent model is 60 ± 2 kg. Figure 12b shows profiles of the time-averaged axial gas pressure. Pressure drops predicted by both cases at the developed zone are same and are in good agreement with experimental data. There is difference at the mixing zone. Mass flux profiles are shown in Figures 12c-11f. Total mass flux close to wall is over-predicted by both cases. Although total solid mass in the bed is accurately predicted by the case with turbulence model over fine mesh resolution, overestimation of mass fluxes close to the wall causes to underestimation of mass fluxes at the centre of the riser.

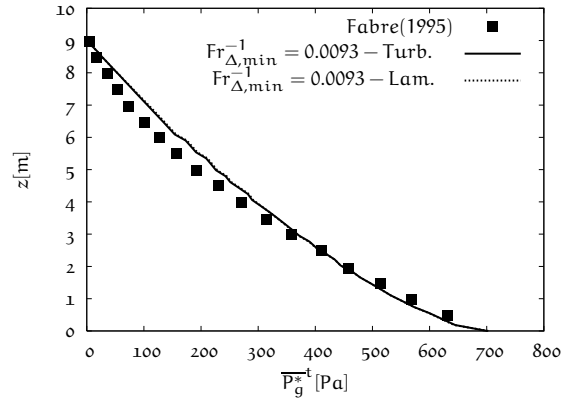
Mesh refinement study gives accurate prediction of overall hydrodynamics of beds. For further investigation, the validation of the model $q_p^2 - q_{fp}$ can be concerned. This model is very effective for CFB application, but it is also questionable. Particle velocity fluctuations are considered as isotropic according to all direction by the model. However, there are significant differences between scales for directions, the assumption of isotropy is not valid anymore. The random kinetic energy of particulate phase q_p^2 and variance of particle and gas velocity fluctuations along the vertical direction are shown in Figures 13a-13d. Along radial directions, values of variance of particle and gas velocity fluctuations are one order greater than of the random kinetic energy of particulate phase. This underestimation can be caused of isotropy assumption.

3.2.5 Summary

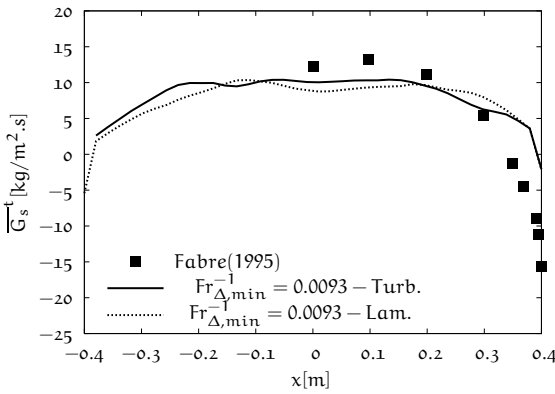
This test case concerns the numerical simulation of hydrodynamics of the laboratory pilot scale of cold fluidized bed in which B-type particles are conducted. The results were compared with pressure and mass flux data realised by Fabre (1995). The influence of gas turbulence model have been tested over two different mesh resolutions. With coarse mesh configuration, there is no significant difference between results obtained with and without turbulence model. Pressure drop at the dense regime is very well predicted, but at the dilute zone, pressure drop is overestimated. Pressure profile shows us that mass inventory is in good agreement with the experiment. We refined mesh along radial directions two times and close to mixing area and performed simulations over the refined mesh configuration with and without turbulence model. With laminar and turbulent cases, pressure drop is well predicted at dilute part and slightly underestimated at the mixing zone. Although total mass in the riser is correctly predicted, there is overestimation of mass fluxes close to the wall and underestimation of total mass flux at the centre of riser.



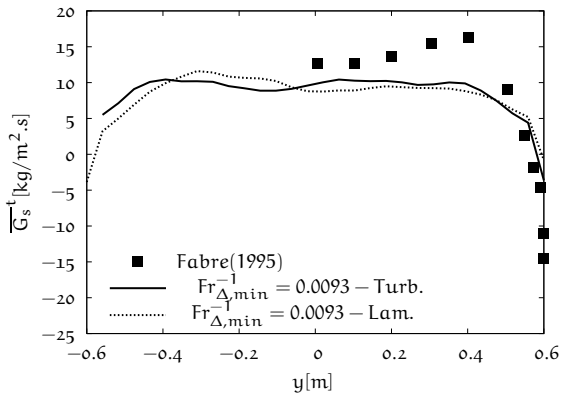
(a) The evolution of total solid mass in the riser.



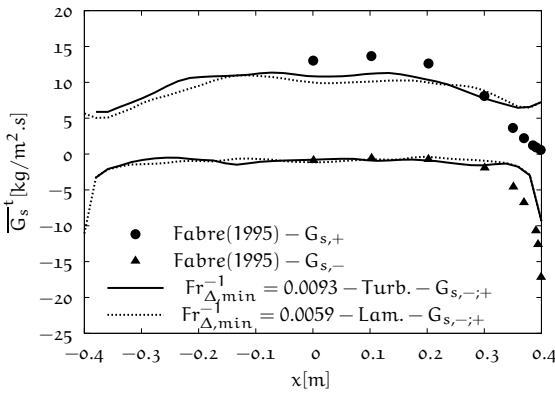
(b) Time-averaged gas pressure along the vertical direction.



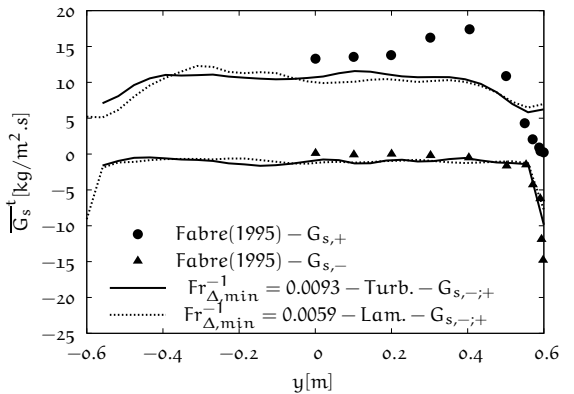
(c) Profiles of time-averaged vertical mass flow rate at $z = 6.66$ m along the radial direction, $x = [-0.4; 0.4]$ m ($y = 0.0$ m).



(d) Profiles of time-averaged vertical mass flow rate at $z = 6.66$ m along the radial direction, $y = [-0.6; 0.6]$ m ($x = 0.0$ m).

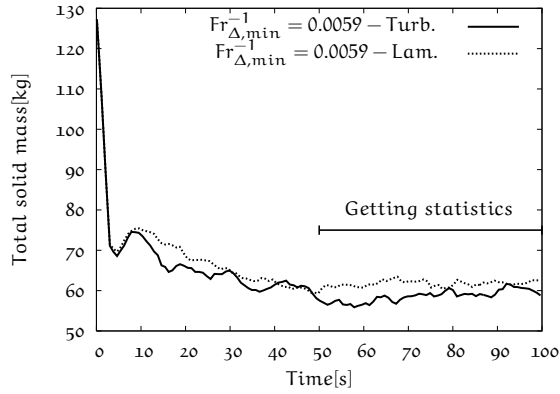


(e) Profiles of time-averaged vertical negative and positive mass flow rate at $z = 6.66$ m along the radial direction, $x = [-0.4; 0.4]$ m ($y = 0.0$ m).

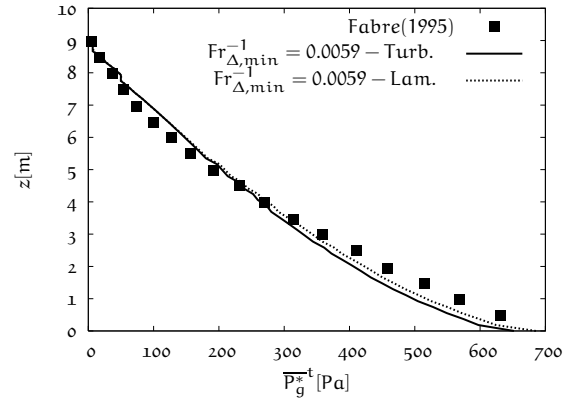


(f) Profiles of time-averaged vertical negative and positive mass flow rate at $z = 6.66$ m along the radial direction, $y = [-0.6; 0.6]$ m ($x = 0.0$ m).

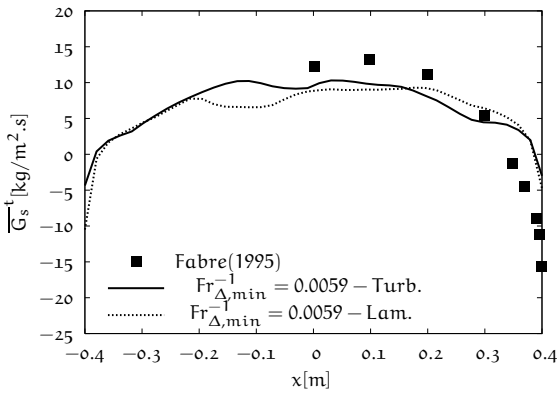
Figure 11: Predictions of reference case (mesh: $41 \times 31 \times 141, Fr_{\Delta, min}^{-1} = 0.0093$) with and without turbulence model versus experimental data of Fabre (1995).



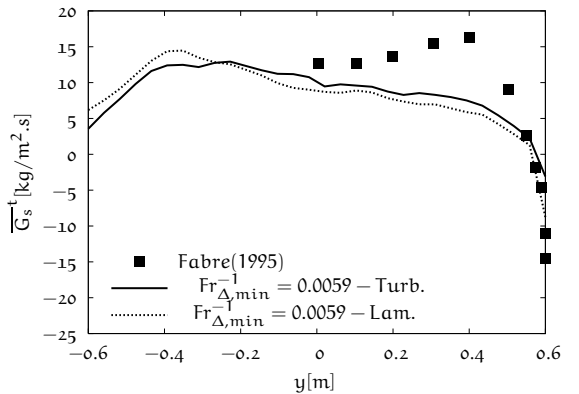
(a) The evolution of total solid mass in the riser.



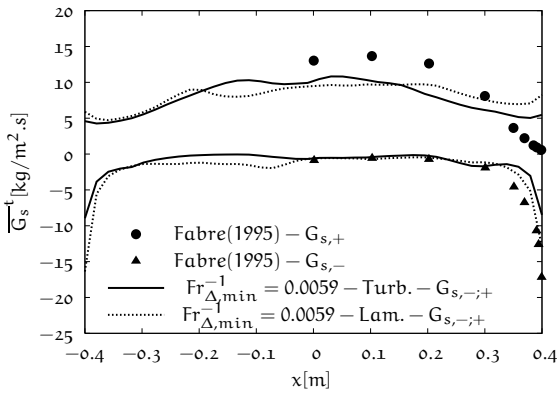
(b) Time-averaged gas pressure along the vertical direction.



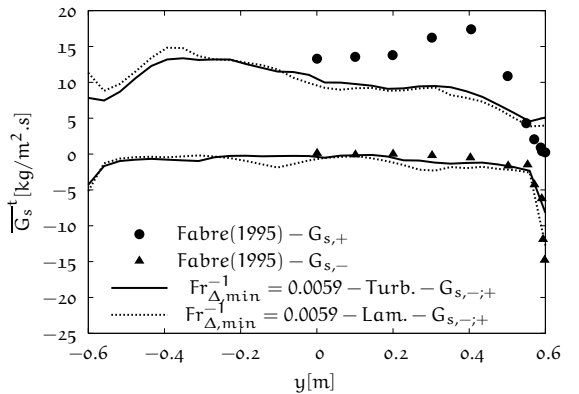
(c) Profiles of time-averaged vertical mass flow rate at $z = 6.66$ m along the radial direction, $x = [-0.4; 0.4]$ m ($y = 0.0$ m).



(d) Profiles of time-averaged vertical mass flow rate at $z = 6.66$ m along the radial direction, $y = [-0.6; 0.6]$ m ($x = 0.0$ m).

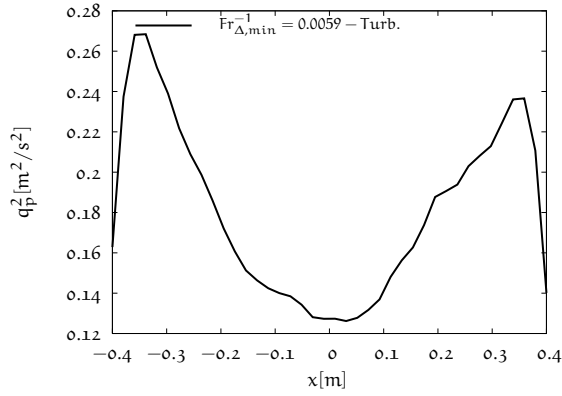


(e) Profiles of time-averaged vertical negative and positive mass flow rate at $z = 6.66$ m along the radial direction, $x = [-0.4; 0.4]$ m ($y = 0.0$ m).

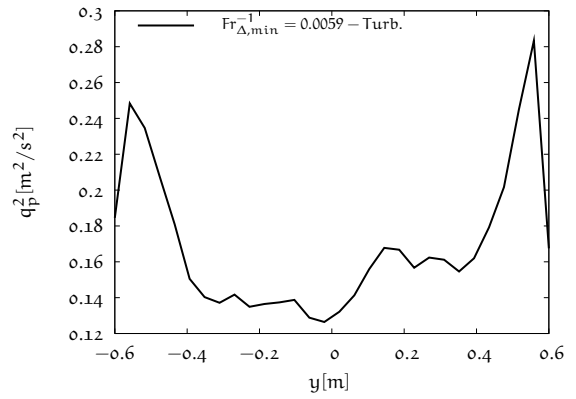


(f) Profiles of time-averaged vertical negative and positive mass flow rate at $z = 6.66$ m along the radial direction, $y = [-0.6; 0.6]$ m ($x = 0.0$ m).

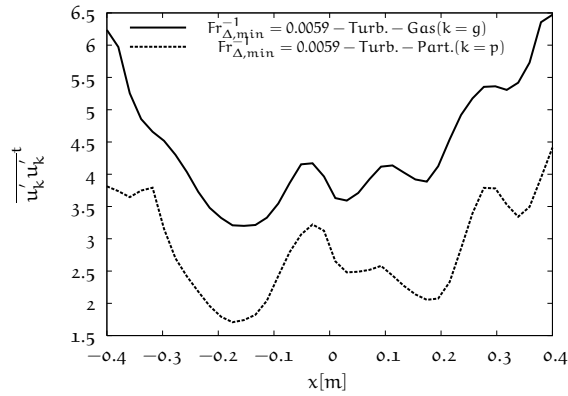
Figure 12: Predictions over fine mesh resolution (mesh: $81 \times 61 \times 161, Fr_{\Delta, min}^{-1} = 0.0059$) with and without turbulence model versus experimental data of Fabre (1995).



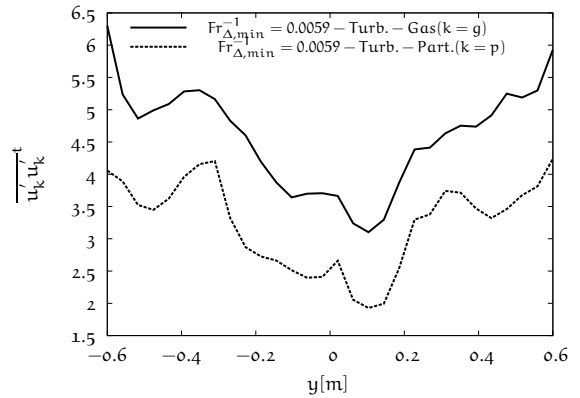
(a) Profile of time-averaged particle agitation, q_p^2 , at $z = 6.66$ m along the radial direction, $x = [-0.4; 0.4]$ m ($y = 0.0$ m).



(b) Profile of time-averaged particle agitation, q_p^2 , at $z = 6.66$ m along the radial direction, $y = [-0.6; 0.6]$ m ($x = 0.0$ m).



(c) Profiles of particle and gas velocity fluctuations variance at $z = 6.66$ m along the radial direction, $x = [-0.4; 0.4]$ m ($y = 0.0$ m).



(d) Profiles of particle and gas velocity fluctuations variance at $z = 6.66$ m along the radial direction, $y = [-0.6; 0.6]$ m ($x = 0.0$ m).

Figure 13: Time-averaged gas and particle kinetic stresses.

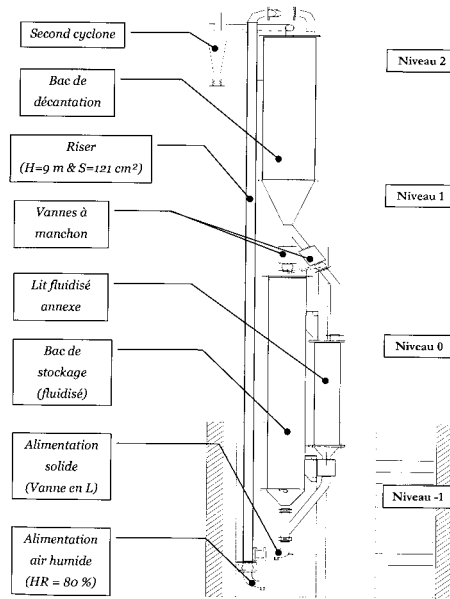


Figure 14: The experimental setup of the pilot scale of FCC riser (Petit 2005).

3.3 SIMULATIONS OF DILUTE GAS-PARTICLE FLOW IN FCC RISER-I

In this section, we deal with the prediction of hydrodynamics of gas-solid in the riser of a small scale cold CFB. In this configuration, typical FCC particles are conducted. The experimental study was done by Petit (2005) and the axial profiles of gas pressure, horizontal profiles of vertical solid mass flux are assessed.

3.3.1 Description of Experimental Setup

The experimental setup representing a FCC system was studied by Petit (2005) (see Figure 14). The riser cross-section is square with 0.11m edge. The height of riser is equal to 9 m and the cross-section of riser at 9.25 m is re-sized with homethety equal to 0.5. The injector area is $3 \times 10^{-3} \text{ m}^2$ and is located at $z = 0.01 \text{ m}$. Experiment study was carried out at a superficial velocity of 7 m/s and solid mass flux from 46 to 133 kg/m²s, equivalent to solid/gas mass loading ratios of 5.5 – 15.8. The flow properties are given in Table 3.

3.3.2 Description of Numerical Simulation

Computational Grid

For 3D simulations, the computational domain geometry is identical to the experimental setup except the geometry of the particle inlet. The circular cross section of particle inlet was transformed to rectangular section with the same hydraulic diameter in order to avoid non-conformal mesh configuration. The computational domain was constructed by

Gas Phase	
ρ_g	1.2 kg/m ³
μ_g	1.8×10^{-5} Pa.s
$U_{p,inlet}$	7 m/s
Particle Phase	
$d_{p,50}$	70 μ m
ρ_p	1400 kg/m ³
$U_{p,Linlet}$	2.5 m/s
$\alpha_{p,Linlet}$	0.044
Mass flux	46 kg/m ² s

Table 3: Flow properties of FCC case (A-type particles).

approximately 110 000 cells and the grid is uniform through all directions ($\Delta x = \Delta y = \Delta z = 0.01$ m, $Fr_{\Delta}^{-1} = 2.32$ see Figure 15).

Fluidization Grid & Particle Injection

To account for the homogeneity of fluidization air, we defined uniform velocity and volume fraction of gas at the gas inlet as done for CERCHAR case. The velocity was set to 7.0 m/s due to the mass flux of fluidization air equal to 0.106 kg/s. The mass flux of air at the particle injection was set to 1.7×10^{-3} kg/s. Particle velocity at the particle inlet was 2.5 m/s. The gas velocity at the particle inlet was equal to the particle velocity which was defined by Andreux (2001) for the circulation of gas in the bed without solid. The solid volume fraction at the feeding pipe was set to 0.044 for the simulation with mass flux of solid equal to 46 kg/s. The values of turbulent kinetic energy and dissipation were calculated by Eqs. (3.2) and (3.3). The particle agitation q_p^2 was 0.015 m²/s², and the fluid-particle covariance q_{fp} was 0.03 m²/s². Initially, the computational domain was filled up by the solid with the volume fraction equal to 0.01.

3.3.3 Simulation Results

In Figure 16a, the instantaneous solid volume fraction in the riser is shown and note that the particles are immediately transported by gas. Particles accumulate along the axial direction at the centre of the riser. Dense zone does not form and the mixing of gas/solid is not well-predicted. The formation of clusters is not observed, but unphysical accumulation of particles in the quarter part of riser deviates gas and increases gas velocity close to wall. Segregation of particles disappears at the dilute zone of the riser. Figure 16b shows the instantaneous axial velocity of particle normalised by the single particle terminal settling velocity V_t^{St} . Particles never fall down and they are rapidly transported by gas.

Figure 17a and 17b present the time characteristics of flow. At the mixing zone, the gas turbulence seen by particle is disappeared by introducing particles ($\tau_{fp}^t \gg \tau_p$). The gas

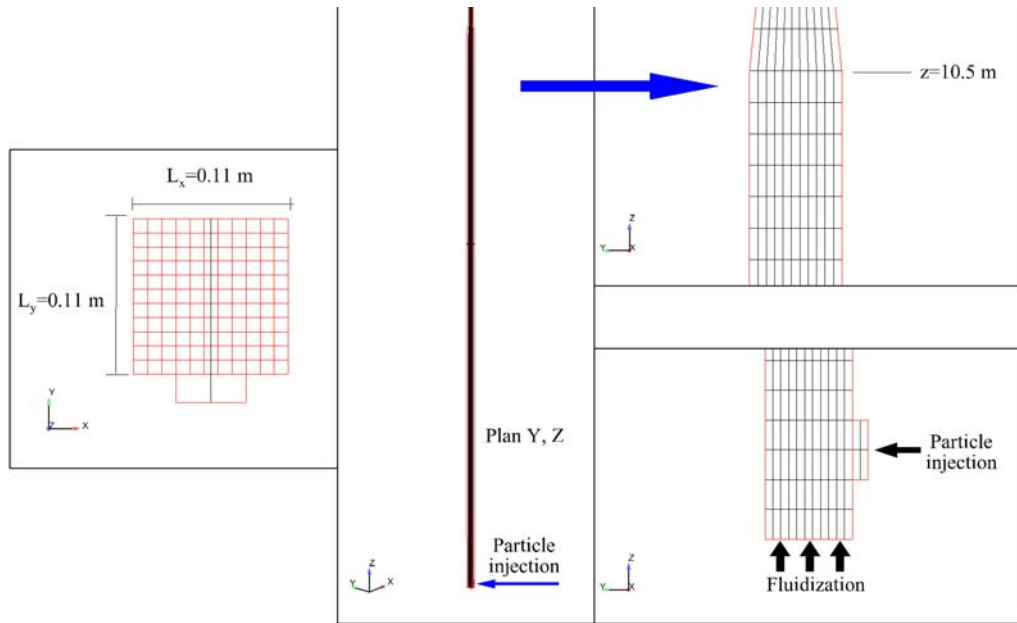


Figure 15: The computational domain of FCC riser.

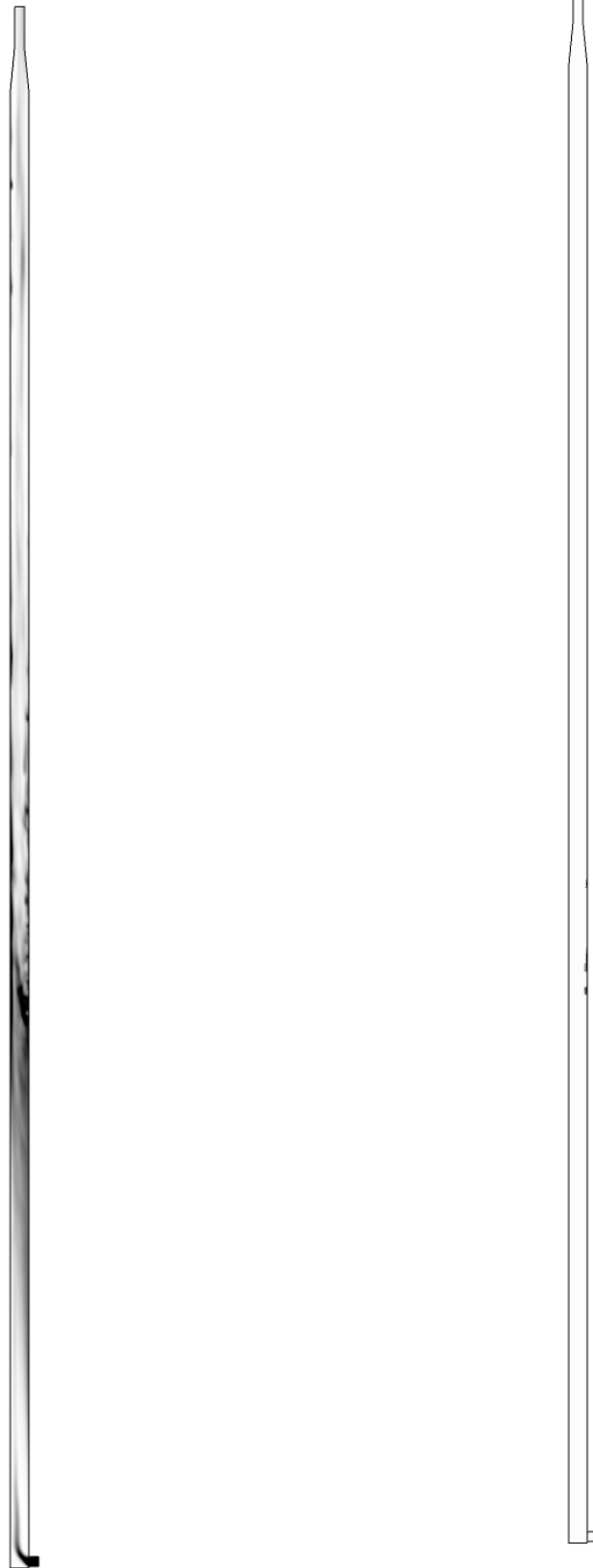
turbulence seen by particle is effective at some local points through the riser ($\tau_{fp}^t/\tau_p \approx 0.5$). Collisions are especially important in the quarter part of the riser where the accumulation of particles occurs and close the lateral feeding ($\tau_c \ll \tau_p$). It can be concluded that the main mechanism through the flow is the entrainment of particles by gas.

Time evolution of total solid in the riser is shown in Figure 18a. The predicted total mass is 1.22 ± 0.25 kg. The time-averaged axial pressure gradient, solid mass fluxes are compared with experimental data of Petit (2005). We present the time-averaged of pressure gradient and positive and negative solid mass fluxes in Figure 18b-18f. The accumulation of particles in the quarter part of the riser can be seen easily in Figure 18b. The axial profile of time-averaged pressure gradient is not accurately predicted. The time-averaged pressure underestimated at the acceleration zone. However, the fully developed part is in fairly agreement with the experimental data. Figures 18c-18f show positive, negative and net mass fluxes along radial directions, x, y at $z = 8.50$ m. Negative flux is never predicted. Particle behaviour at dilute zone is also shown in Figure 19. The instantaneous particle velocity vectors are superimposed on the instantaneous solid volume fraction field. The vectors show that particles never descend and the core-annulus flow does not occur in an instantaneous manner.

3.3.4 Parametric Studies

Influence of Mesh Resolution

Different mesh configurations have been tested in order to determine the mesh dependency of results. We refined mesh along all directions two times. These cases are called as $22 \times 22 \times 1800$ ($Fr_{\Delta}^{-1} = 1.16$). Time evolution of total solid in the riser is shown in Figure

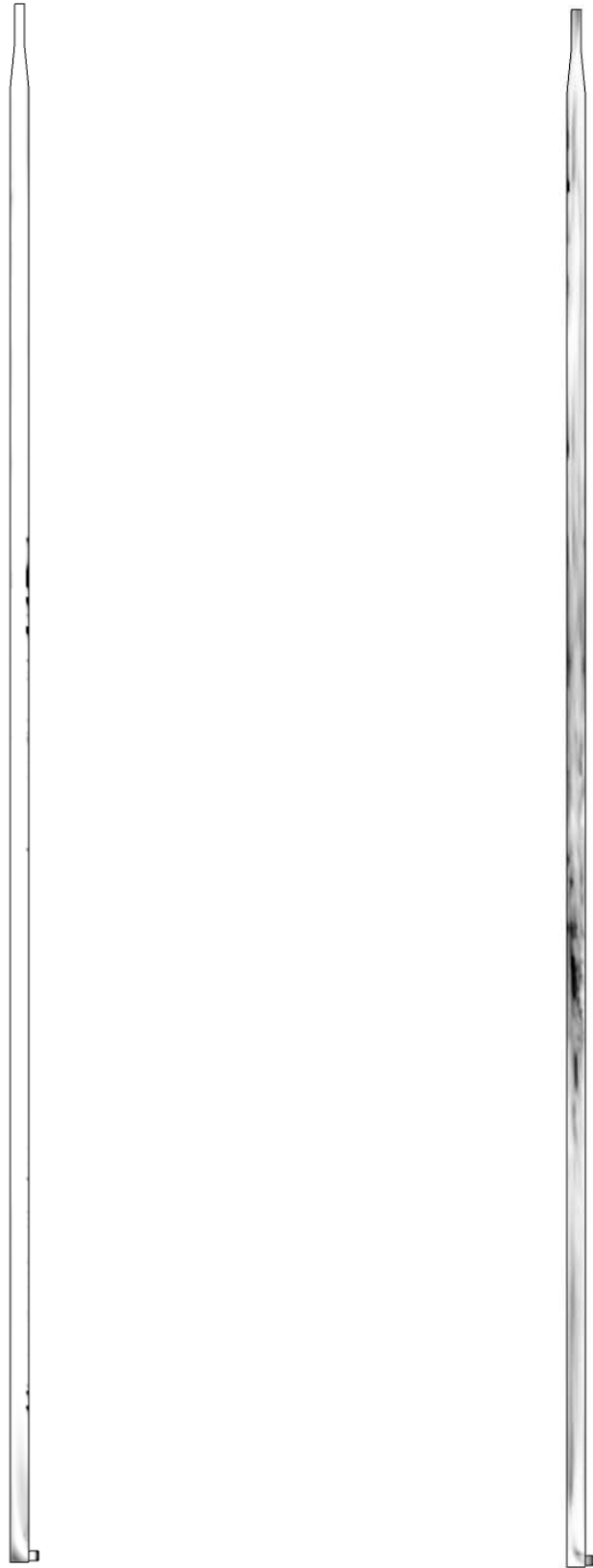


42

(a) The instantaneous solid volume fraction field
 (White: $\alpha_p = 0$, Black: $\alpha_p = 0.05$, $x - y @ 0.0 \text{ m}$).

(b) The ratio between the axial particle velocity and the single particle terminal velocity,
 $U_{p,z}/V_t^{St}$ (White: $U_{p,z}/V_t^{St} = 0$, Black: $U_{p,z}/V_t^{St} = -1$, $x - y @ 0.0 \text{ m}$).

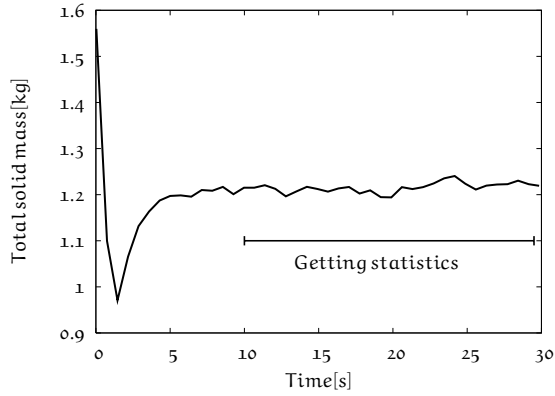
Figure 16: Flow characteristics (FCC).



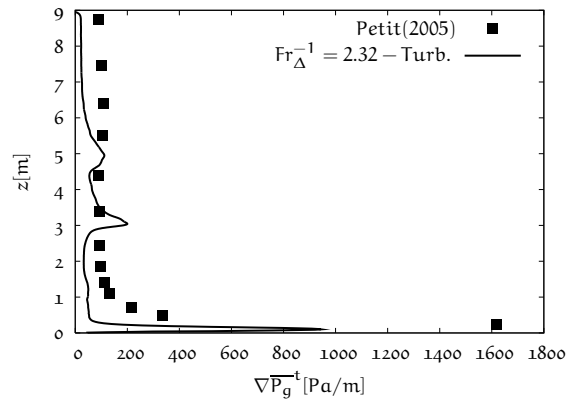
(a) The ratio between the gas turbulence seen by particle and the particle relaxation time, τ_{fp}^t/τ_p (White: $\tau_{fp}^t/\tau_p = 0$, Black: $\tau_{fp}^t/\tau_p = 0.1$, $x - y@0.0$ m).

(b) The ratio between the particle relaxation time and the collision time, τ_p/τ_c (White: $\tau_p/\tau_c = 0$, Black: $\tau_c/\tau_p = 100$, $x - y@0.0$ m)..

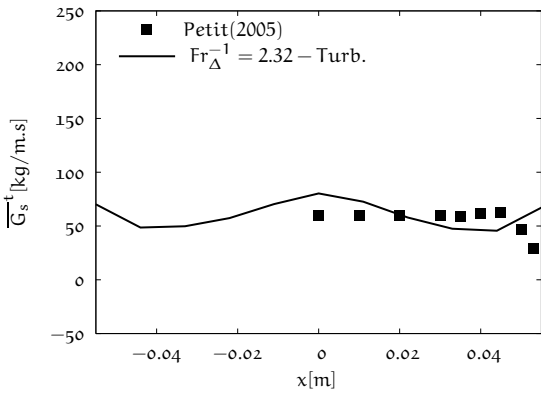
Figure 17: Time characteristics (FCC).



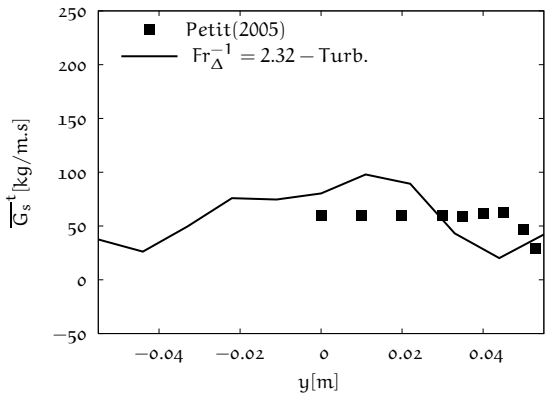
(a) The evolution of total solid mass in the riser.



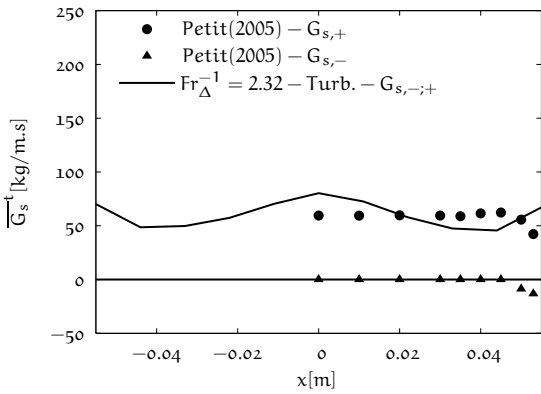
(b) Time-averaged gas pressure along the vertical direction.



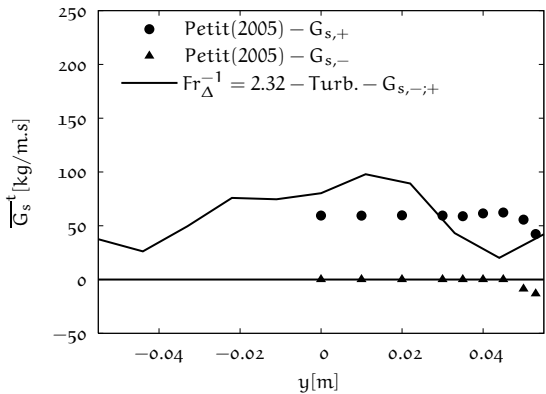
(c) Profiles of time-averaged vertical mass flow rate at $z = 8.5$ m along the radial direction, $x = [-0.055; 0.055]$ m ($y = 0.0$ m).



(d) Profiles of time-averaged vertical mass flow rate at $z = 8.5$ m along the radial direction, $y = [-0.055; 0.055]$ m ($x = 0.0$ m).



(e) Profiles of time-averaged vertical negative and positive mass flow rate at $z = 8.5$ m along the radial direction, $x = [-0.055; 0.055]$ m ($y = 0.0$ m).



(f) Profiles of time-averaged vertical negative and positive mass flow rate at $z = 8.5$ m along the radial direction, $y = [-0.055; 0.055]$ m ($x = 0.0$ m).

Figure 18: Predictions of reference case (mesh: $11 \times 11 \times 900$, $Fr_{\Delta}^{-1} = 2.32$) versus experimental data of Petit (2005).

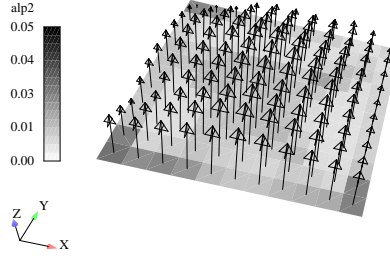


Figure 19: Instantaneous particle velocity vectors superimposed on the contour plot of instantaneous solid volume fraction at $z = 8.50$ m.

20a for different mesh resolutions. The fine mesh resolution ($Fr_{\Delta}^{-1} = 1.16$) simulations predict roughly 1.1 kg solid in the riser which is less than of predicted with coarse mesh simulation ($Fr_{\Delta}^{-1} = 2.32$).

We present the time-averaged statistics of the pressure gradient with different mesh resolutions in Figure 20b. The axial profile of time-averaged pressure gradient is not accurately predicted and the results obtained with intermediate and fine mesh have the same behaviour. Figures 20c-20f show positive, negative and net mass fluxes along radial directions, x, y at $z = 8.50$ m. Negative total flux is never predicted with intermediate and fine mesh resolution. Results are slightly improved by mesh refinement but it is not satisfactory. It is obvious that computational grid has to be too fine to resolve flow characteristics accurately. Due to the computational cost, it is not feasible.

Influence of Drag Force Model

In Euler-Euler approach, the drag force model has a significant effect on the predictability of simulations. Herein, we compare the model of Wen and Yu (1966) limited by Ergun (1952)'s relation with the model of O'Brien and Syamlal (1993) and Gibilaro et al. (1985). O'Brien and Syamlal (1993) proposed an empirical correlation to consider the effect of clustering structure on the drag coefficient. This correlation is obtained from A-type particles conducted by air system with specific solid circulation fluxes. It was revealed that this clustering effect gives reasonable results in terms of the axial pressure gradient of a CFB riser. The drag force by O'Brien and Syamlal (1993) is defined as:

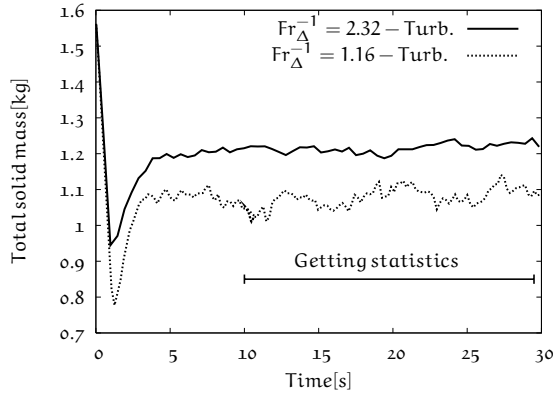
$$I_{g \rightarrow p} = \beta_e (U_{p,i} - U_{g,i}) \quad (3.9)$$

where

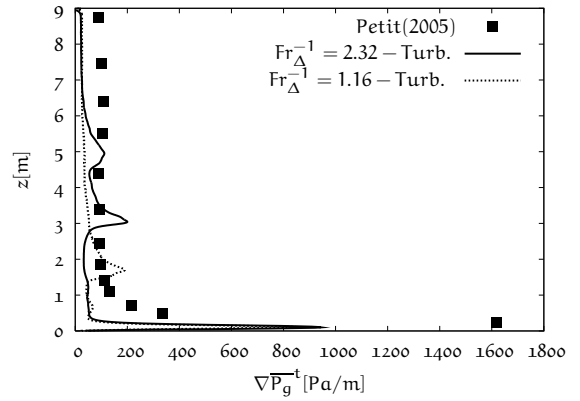
$$\beta_e = \frac{3}{4} C_D \rho_g \frac{1}{R_t^2} \alpha_p \alpha_g |\mathbf{v}_r| \quad (3.10)$$

with

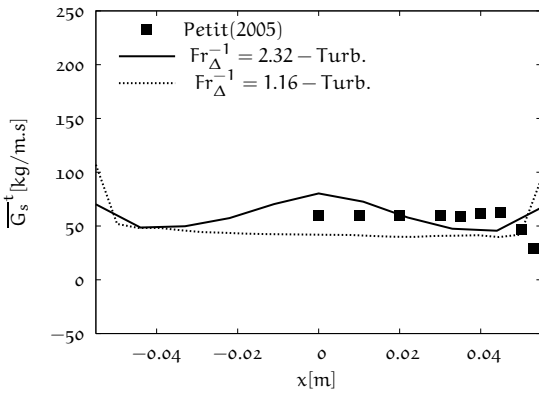
$$R_t = \frac{1}{2} A - 0.03 Re_p + \sqrt{0.0036 Re_p + 0.12 Re_p (2B - A) + A^2} \quad (3.11)$$



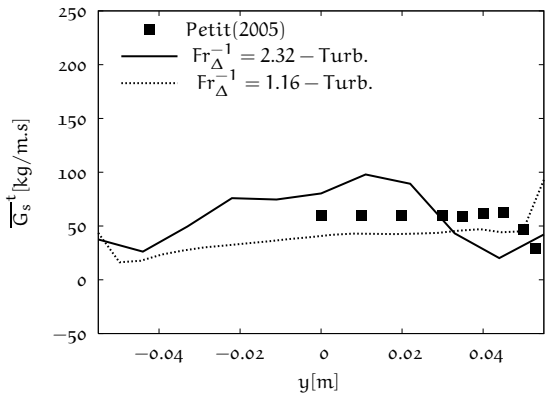
(a) The evolution of total solid mass in the riser.



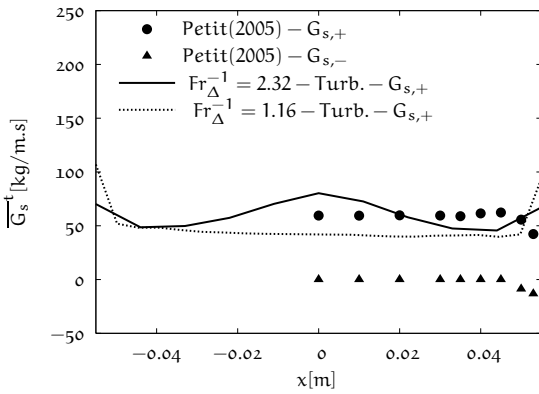
(b) Time-averaged gas pressure along the vertical direction.



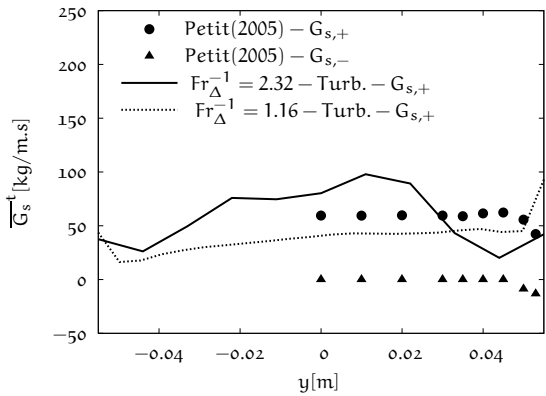
(c) Profiles of time-averaged vertical mass flow rate at $z = 8.5$ m along the radial direction, $x = [-0.055; 0.055]$ m ($y = 0.0$ m).



(d) Profiles of time-averaged vertical mass flow rate at $z = 8.5$ m along the radial direction, $y = [-0.055; 0.055]$ m ($x = 0.0$ m).



(e) Profiles of time-averaged vertical negative and positive mass flow rate at $z = 8.5$ m along the radial direction, $x = [-0.055; 0.055]$ m ($y = 0.0$ m). (Negative mass fluxes are not shown for cases. For all cases, $G_{s,-} = 0$.)



(f) Profiles of time-averaged vertical negative and positive mass flow rate at $z = 8.5$ m along the radial direction, $y = [-0.055; 0.055]$ m ($x = 0.0$ m). (Negative mass fluxes are not shown for cases. For all cases, $G_{s,-} = 0$.)

Figure 20: Predictions with different mesh resolutions (mesh: $11 \times 11 \times 900$ - $Fr_{\Delta}^{-1} = 2.32$, $22 \times 22 \times 1800$ - $Fr_{\Delta}^{-1} = 1.16$) versus experimental data of Petit (2005).

$$A = \alpha_g^{4.14} \quad (3.12)$$

and

$$B = \begin{cases} 0.8\alpha_g^{-1.28} & \text{for } \alpha_g \leq 0.85 \\ \alpha_g^{2.65} & \text{for } \alpha_g > 0.85. \end{cases} \quad (3.13)$$

The drag coefficient and Reynolds number without the gas phase volume fraction are formulated by following relations

$$C_D = \left(0.63 + 4.8 \sqrt{\frac{R_t}{Re_p}} \right) \quad (3.14)$$

$$Re_p = \frac{d_p \rho_g |\mathbf{v}_T|}{\mu_g}. \quad (3.15)$$

The model of Gibilaro et al. (1985) is given by

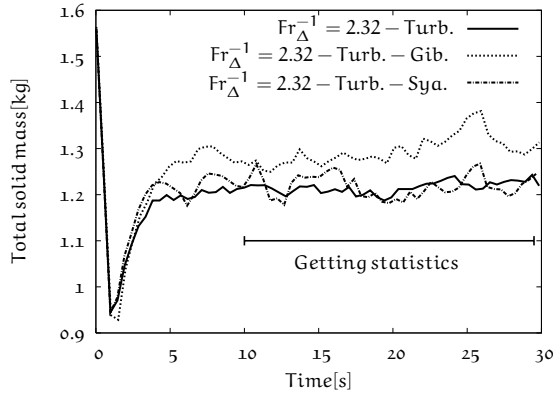
$$\beta_e = \left(\frac{17.3}{Re_p} + 0.336 \right) \frac{\rho_g}{d_p} \alpha_p \alpha_g^{-1.8} |\mathbf{v}_T|. \quad (3.16)$$

Time evolutions of total solid in the riser are shown in Figure 21a for different drag force models. There is no significant difference between results with different drag force models. Figure 21b shows the axial profile of time-averaged pressure gradient and the results obtained with different drag force models have the same behaviour. Figures 20c-20f show positive, negative and net mass fluxes along radial directions, x, y at $z = 8.50$ m. Negative total flux is never predicted and it is concluded that models of Gibilaro et al. (1985) and O'Brien and Syamlal (1993) do not give any improvements of results.

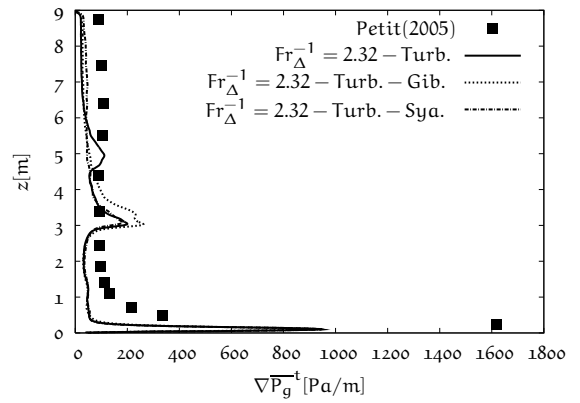
Influence of Wall Boundary Condition

Solid mixing process within a riser is affected by bounding walls. It is known that in high velocity flows of gas-particle mixtures through large risers, the pressure gradient is largely due to solid hold-up and the wall shear is only weak effect. However, if the riser width is small, the wall effect is expected to become more important and free slip BC, which is used for all references cases, is not a suitable choice for solid boundaries for particulate phase. Herein, we investigate the no-slip boundary condition for the particulate phase. It is noted that gas flow is assumed to be laminar.

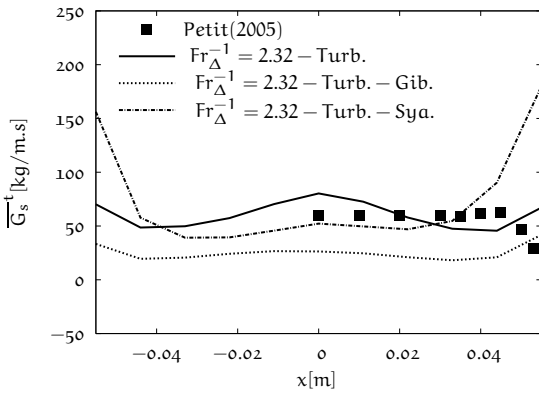
Time evolutions of total solid in the riser are shown in Figure 22a for free- and no-slip boundary conditions for mesh resolution, $Fr_{\Delta}^{-1} = 1.16$. Mass inventory predicted by the simulation with no-slip condition is than of the case with free-slip condition. Figure 22b shows the axial profile of time-averaged pressure gradient and the results obtained



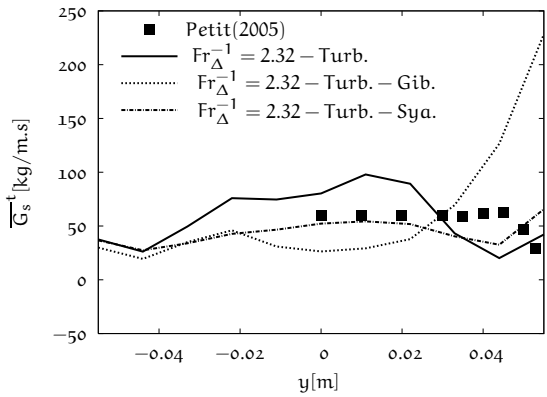
(a) The evolution of total solid mass in the riser.



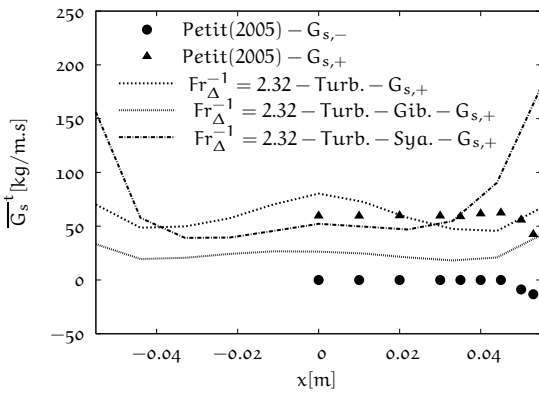
(b) Time-averaged gas pressure along the vertical direction.



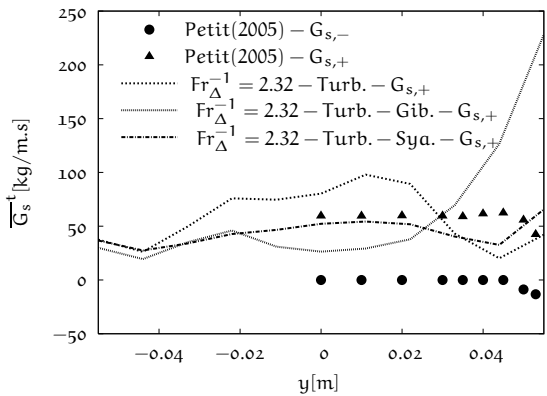
(c) Profiles of time-averaged vertical mass flow rate at $z = 8.5$ m along the radial direction, $x = [-0.055; 0.055]$ m.



(d) Profiles of time-averaged vertical mass flow rate at $z = 8.5$ m along the radial direction, $y = [-0.055; 0.055]$ m.



(e) Profiles of time-averaged vertical negative and positive mass flow rate at $z = 8.5$ m along the radial direction, $x = [-0.055; 0.055]$ m. (Negative mass fluxes are not shown for cases. For all cases, $G_{s,-} = 0$.)



(f) Profiles of time-averaged vertical negative and positive mass flow rate at $z = 8.5$ m along the radial direction, $y = [-0.055; 0.055]$ m. (Negative mass fluxes are not shown for cases. For all cases, $G_{s,-} = 0$.)

Figure 21: Predictions of reference case (mesh: $11 \times 11 \times 900$ - $Fr_{\Delta}^{-1} = 2.32$) with different drag force models (Gobin et al. 2003, O'Brien and Syamlal 1993, Gibilaro et al. 1985) versus experimental data of Petit (2005).

with no-slip boundary condition improves the results, especially in the transient region (@ $z = 1.4$ m). Figures 21c-21f show positive, negative and net mass fluxes along radial directions, x, y at $z = 8.50$ m. Total flux prediction is in good agreement with experimental data and general trend is very well captured. However, negative flux is never predicted. Flux profiles show antisymmetric behaviour along the y -direction due to the effect of feeding pipe.

3.3.5 Summary

This test case deals with hydrodynamic prediction of a pilot scale FCC system. The experimental data was assessed by Petit (2005) in terms of the vertical gas pressure gradient and solid mass fluxes. Reference case ($11 \times 11 \times 900$) gives unphysical accumulation of particles in the riser due to poor prediction of mixing of particles. To avoid these kind unphysical results, the computational grid was refined two times in all directions. However, the results obtained with finer mesh have the same behaviour. Results were slightly improved but due to computational cost, further mesh refinement is not practicable. Different drag models are also tested and we can not see any improvements of results. It is pointed out that gas-particle flow patterns in the riser strongly dependent on the particulate phase BCs. No-slip BCs for particulate phase improves results and total flux is fairly good predicted.

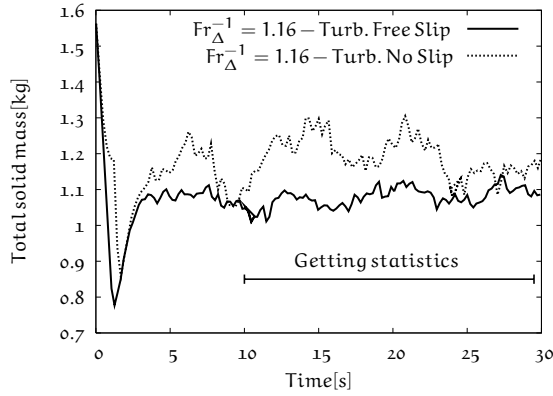
3.4 SIMULATIONS OF DILUTE GAS-PARTICLE FLOW IN FCC RISER-II

3.4.1 FCC System

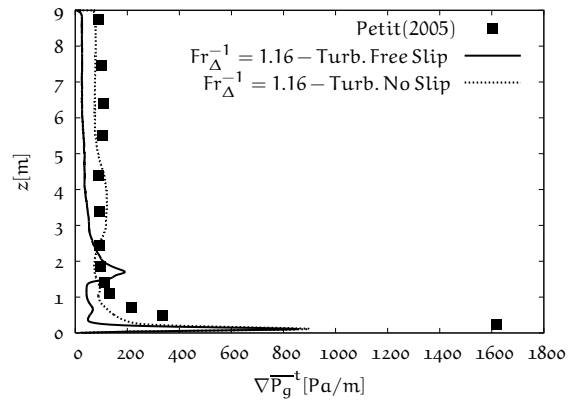
In this case, typical FCC particles are used with small diameter and heavier than of particles conducted in the previous case. The case consists of FCC system consists with a 15m steel riser with diameter of 311mm. The FCC particles is laterally introduced at the bottom of the riser and fluidized by secondary air of which mass flux is equal to 0.00162kg/s. Primary air is vertically delivered by a center pipe with diameter of 103mm. The mass flux air flow through central pipe is 0.6247kg/s. The computational domain is shown in Figure 23. A full description of the FCC system and the measurements may be found in Gauthier (2002).

3.4.2 Description of Numerical Simulations

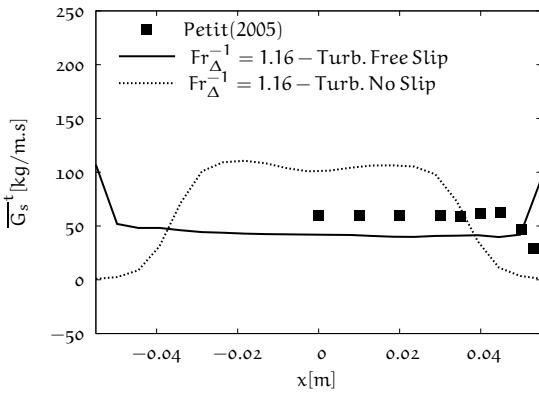
Hansen (2005) performed three dimensional simulations by the Cartesian Eulerian-Eulerian CFD code FLOTACS-MP-3D. By following Hansen (2005), the circular FCC riser was modelled by square section. Four inlets corresponding to circular feeding of catalyst were constructed. The fluidization velocity is supplied through the central of square section. Solids are introduced to riser by volume fraction equal to 0.5. Solid inlet velocity are then adjusted to match the experimental conditions. The secondary air is fed as the same velocity of particles. At the main inlet, the gas velocity was equal to 10m/s and particle velocity was set to 0.5m/s. Gas and particle velocities have uniform distribution. The reference simulation consist of 50 000 cells ($14 \times 14 \times 650$, $Fr_{\Delta}^{-1} = 18$). The main inlet



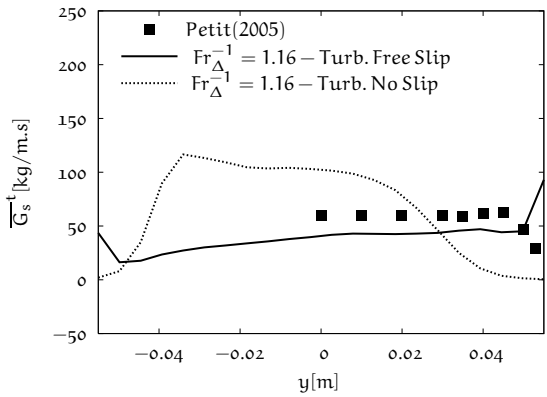
(a) The evolution of total solid mass in the riser.



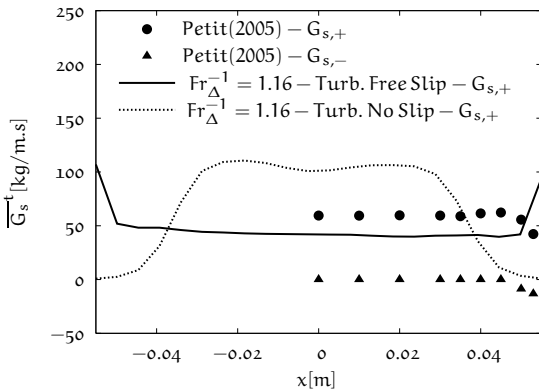
(b) Time-averaged gas pressure along the vertical direction.



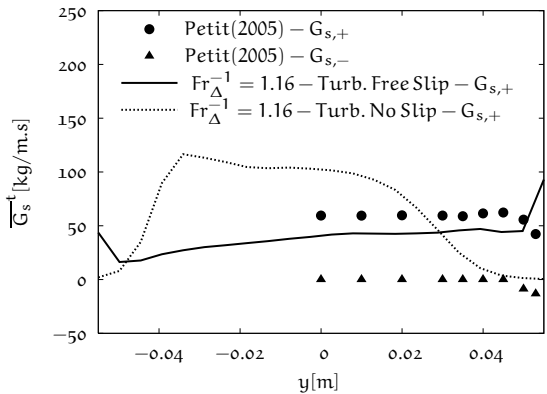
(c) Profiles of time-averaged vertical mass flow rate at $z = 8.5$ m along the radial direction, $x = [-0.055; 0.055]$ m ($y = 0.0$ m).



(d) Profiles of time-averaged vertical mass flow rate at $z = 8.5$ m along the radial direction, $y = [-0.055; 0.055]$ m ($x = 0.0$ m).



(e) Profiles of time-averaged vertical negative and positive mass flow rate at $z = 8.5$ m along the radial direction, $x = [-0.055; 0.055]$ m ($y = 0.0$ m). (Negative mass fluxes are not shown for cases. For all cases, $G_{s,-} = 0$.)



(f) Profiles of time-averaged vertical negative and positive mass flow rate at $z = 8.5$ m along the radial direction, $y = [-0.055; 0.055]$ m ($x = 0.0$ m). (Negative mass fluxes are not shown for cases. For all cases, $G_{s,-} = 0$.)

Figure 22: Predictions of reference case (mesh: $22 \times 22 \times 1800$, $Fr_{\Delta}^{-1} = 1.16$) with different wall BCs for the particulate phase (free-slip and no-slip) versus experimental data of Petit (2005).

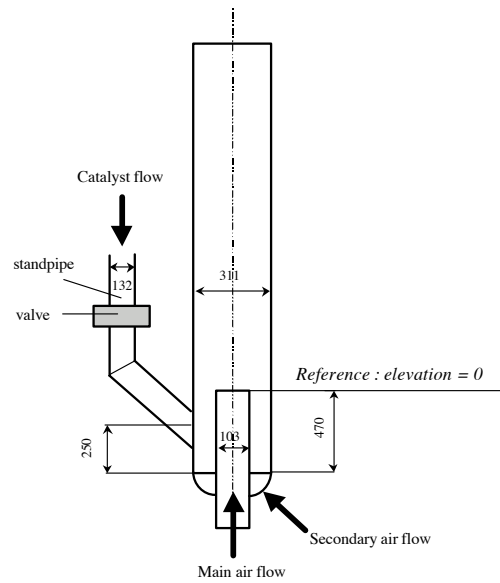


Figure 23: The experimental setup of Gauthier (2002) (FCC riser).

for gas phase and particle feeding is shown in Figure 24. The shaded areas indicate where solids are introduced into the riser. The flow parameters are given in Table 4.

3.4.3 Simulation Results

The simulation run for 25 s of physical time, then time-averaged quantities are calculated during 50 physical time. Time evolution of mass in the riser are shown in Figure 25a. Total mass in the riser shows oscillating behaviour and the mean value is 88 ± 4 kg. Predicted and calculated pressure drop are shown in Figure 25b. In the upper part of the riser, or namely developed part, pressure gradient is constant. Close to the mixing zone, cruel pressure drop can be seen. The trend is well captured by simulation, but total

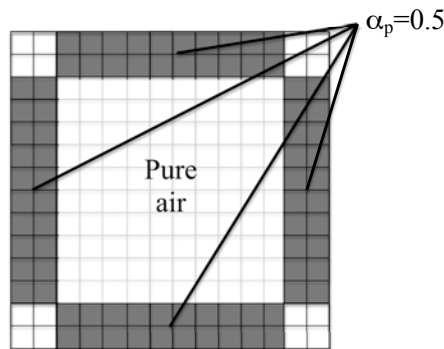


Figure 24: The feeding of particle into riser.

Gas Phase	
ρ_g	1.26 kg/m ³
μ_g	1.8×10^{-5} Pa.s
$U_{p,inlet}$	10m/s
Particle Phase	
$d_{p,50}$	53.1 μ m
ρ_p	1600 kg/m ³
$U_{p,Linlet}$	0.5 m/s
$\alpha_{p,Linlet}$	0.5
Mass flux	146 kg/m ² s

Table 4: Flow properties of FCC case (Gauthier 2002).

pressure drop which relates to the total mass is underestimated. It means that total mass inventory around 90 kg is low.

Negative, positive and total mass fluxes by simulations and measured total mass flux are shown at two different elevations, $z = 1.325$ m and $z = 7$ m (see Figures 25c-25f). At 1.325 m, the simulation captures the trend and negative fluxes can be predicted close to the wall. Due to lack of downward solid flux, the flux in the centre is underestimated. Highest flux is found between the centre line and the wall with consistent manner of experiments. At 7 m, the flux shape is parabolic and smoother and it is away from effects of feeding of particles. Negative flux is also seen at this level, but simulation were not able to reproduce this behaviour.

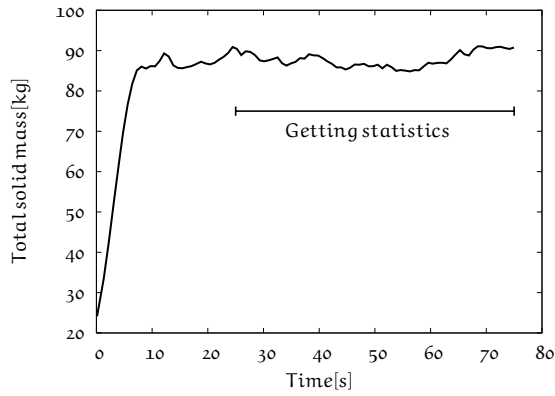
3.4.4 Parametric Studies

Influence of Turbulence Modelling and Mesh Dependency

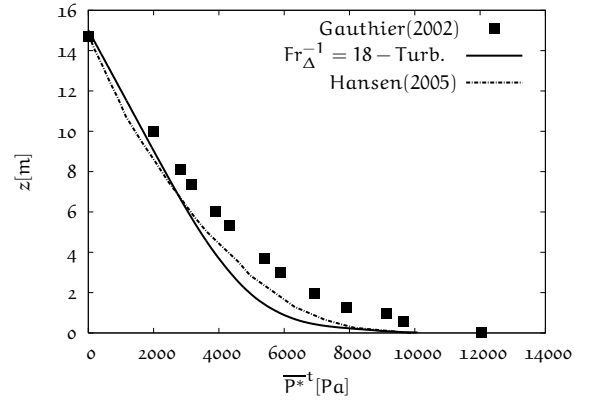
To investigate mesh dependency of results, we refined mesh two times along all directions ($28 \times 28 \times 1350$, $Fr_{\Delta}^{-1} = 9$). Mesh refinement has no significant effect on pressure drop (see Figure 26b). Profiles of mass fluxes are smoother and small negative fluxes is obtained at 1.325 m (see Figures 26c-26f).

Influence of Drag Force

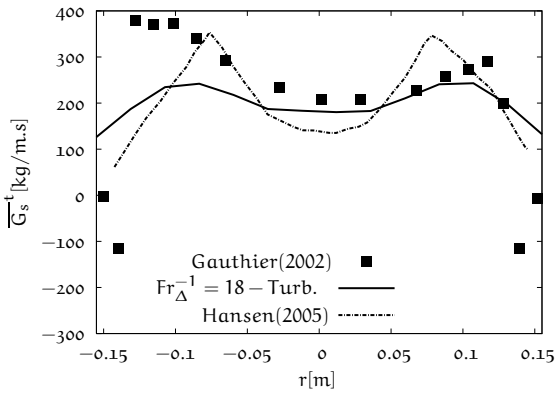
The drag formulation previously described by O'Brien and Syamlal (1993) and the model of Gibilaro et al. (1985) are compared with reference drag model. As done for reference case, simulations run for 25 s of physical time, then time-averaged quantities are calculated during 50 physical time. Total mass in the riser are shown by Figure 27a with different drag force models. Gibilaro et al. (1985)'s model predict slightly more mass inventory in the riser. As a consequence, the drag model of Gibilaro et al. (1985) leads to have better agreement with measured pressure profile. The fluxes at 1.325 m and 7 m in better agreement with experimental data. At 7 m, the model Gibilaro et al. (1985) predict negative fluxes close to wall, but results are not satisfactorily improved. The reference



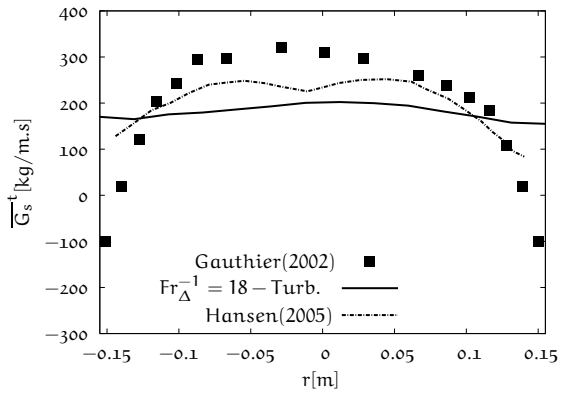
(a) The evolution of total solid mass in the riser.



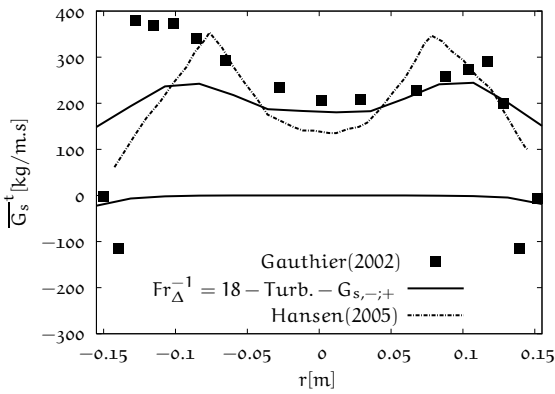
(b) Time-averaged gas pressure along the vertical direction.



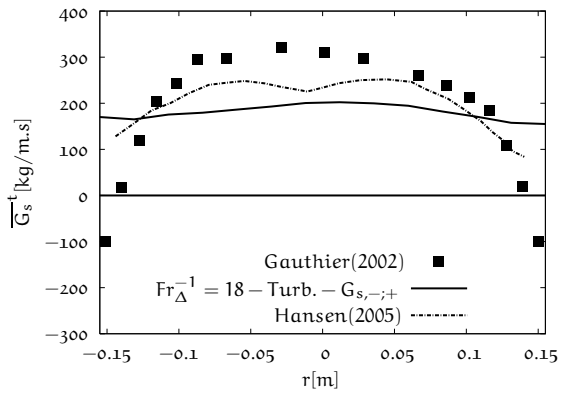
(c) Profiles of time-averaged vertical mass flow rate at $z = 1.325$ m along the radial direction.



(d) Profiles of time-averaged vertical mass flow rate at $z = 7$ m along the radial direction.

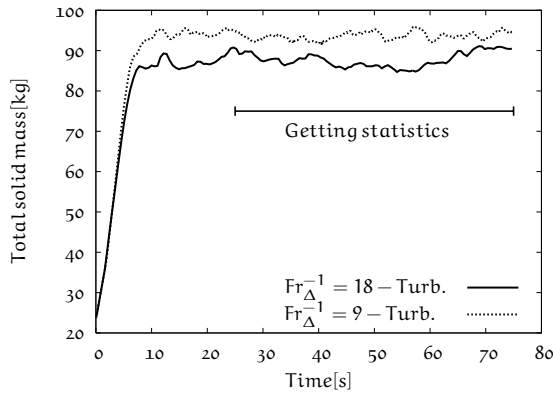


(e) Profiles of time-averaged vertical negative and positive mass flow rate at $z = 1.325$ m along the radial direction.

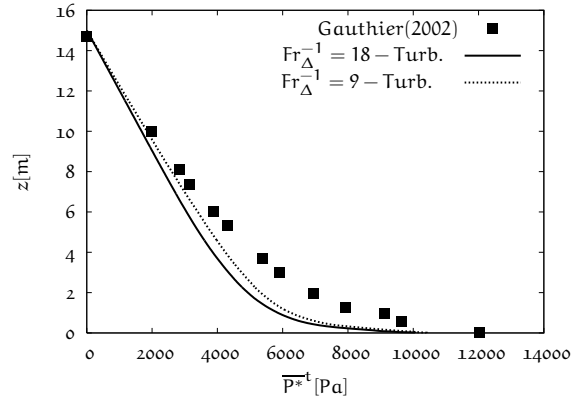


(f) Profiles of time-averaged vertical negative and positive mass flow rate at $z = 7$ m along the radial direction.

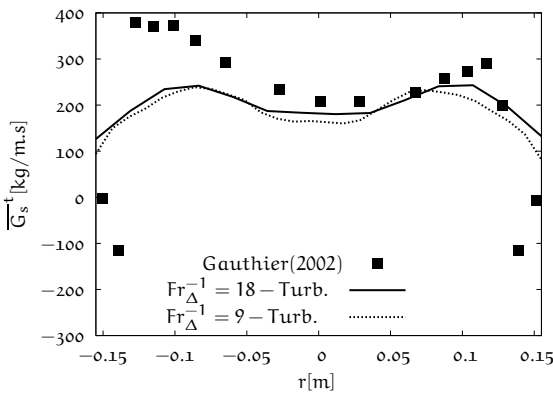
Figure 25: Predictions of reference case (mesh: $14 \times 14 \times 650$, $Fr_{\Delta}^{-1} = 18$) versus experimental data of Gauthier (2002).



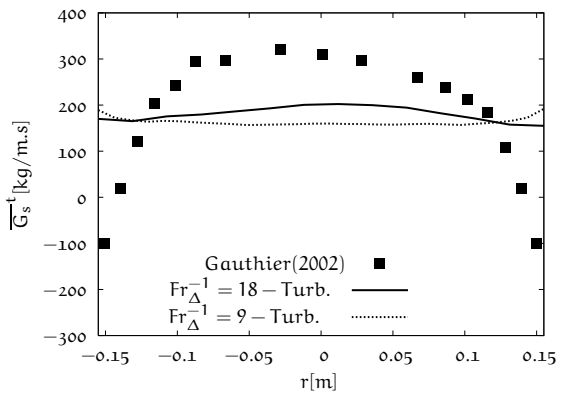
(a) The evolution of total solid mass in the riser.



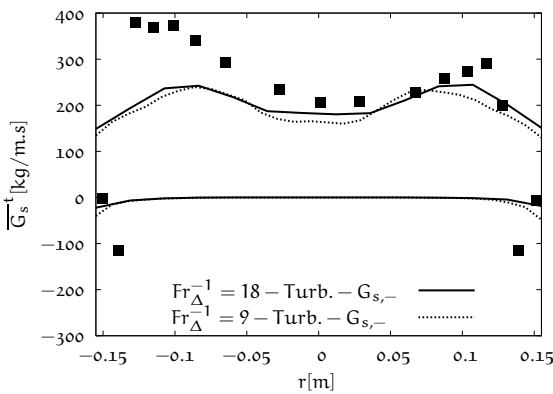
(b) Time-averaged gas pressure along the vertical direction.



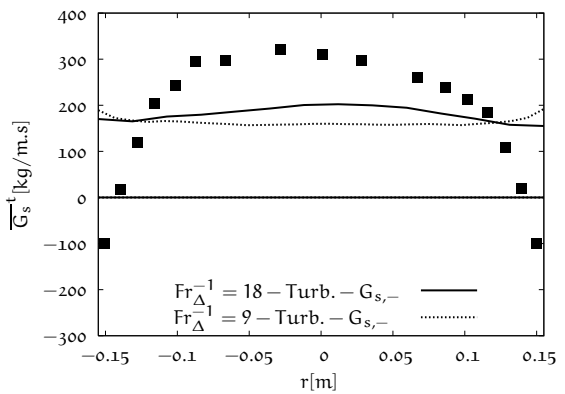
(c) Profiles of time-averaged vertical mass flow rate at $z = 1.325$ m along the radial direction.



(d) Profiles of time-averaged vertical mass flow rate at $z = 7$ m along the radial direction.



(e) Profiles of time-averaged vertical negative and positive mass flow rate at $z = 1.325$ m along the radial direction.



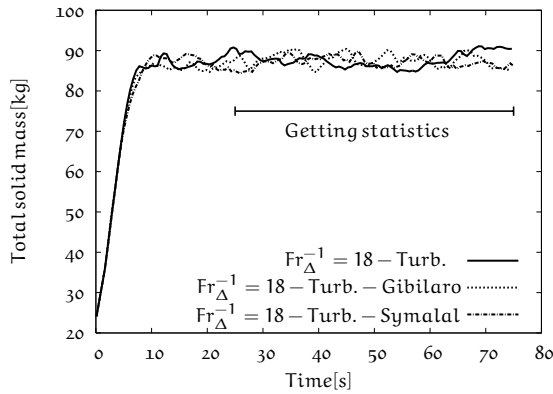
(f) Profiles of time-averaged vertical negative and positive mass flow rate at $z = 7$ m along the radial direction.

Figure 26: Predictions with different mesh resolutions (mesh: $14 \times 14 \times 650$ - $Fr_{\Delta}^{-1} = 18$, $28 \times 28 \times 1350$ - $Fr_{\Delta}^{-1} = 9$) versus experimental data of Gauthier (2002).

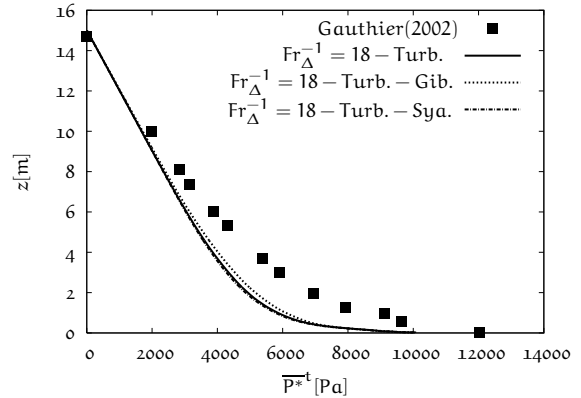
drag model and O'Brien and Syamlal (1993)'s correlation almost coincide for profiles of pressure drop and mass fluxes at two elevation (see Figures 27c-27f).

3.4.5 *Summary*

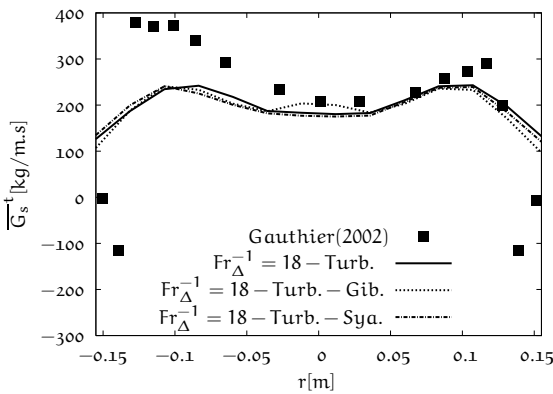
Numerical predictions of a cold FCC riser have been performed and compared with experimental data in terms of solid mass flux and pressure drop provided in the 10th International Workshop on Two-Phase Flow Prediction held in Merseburg, Germany, 2002 (Gauthier 2002). The shape of pressure drop is well produced and but total pressure drop is underestimated. Thereby, total mass in the riser is less than of which conducted in experiment. Mass flux profiles at two different elevations shows reasonable agreement with the experimental findings. Parametric studies have been by mesh refinement and choice of drag force modelling. Gibilaro et al. (1985)'s drag model slightly improve results. Further mesh refinement is needed, but CPU time will increase dramatically.



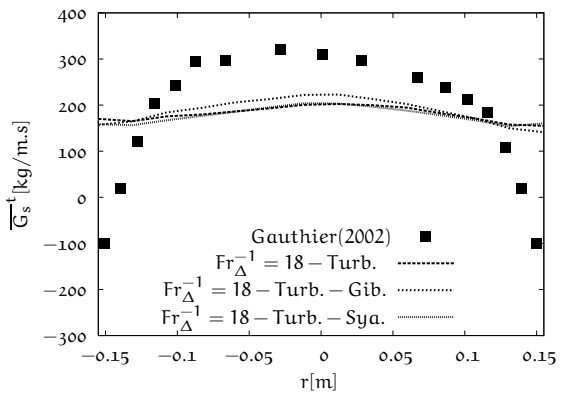
(a) The evolution of total solid mass in the riser.



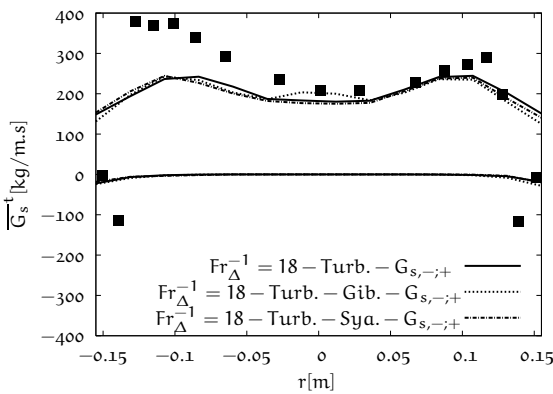
(b) Time-averaged gas pressure along the axial direction



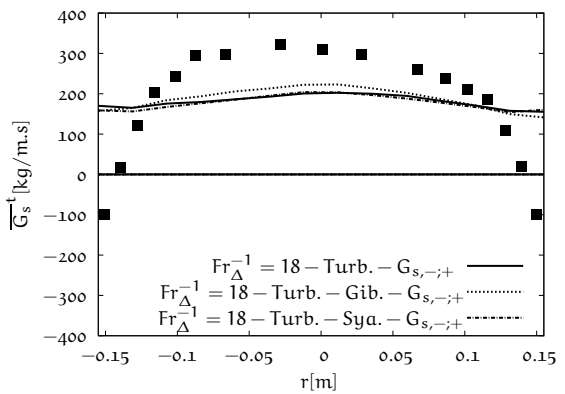
(c) Profiles of time-averaged vertical mass flow rate at $z = 1.325$ m along the radial direction.



(d) Profiles of time-averaged vertical mass flow rate at $z = 7$ m along the radial direction.



(e) Profiles of time-averaged vertical negative and positive mass flow rate at $z = 1.325$ m along the radial direction



(f) Profiles of time-averaged vertical negative and positive mass flow rate at $z = 7$ m along the radial direction.

Figure 27: Predictions of reference case (mesh: $14 \times 14 \times 650$, $Fr_{\Delta}^{-1} = 18$) with different drag forces (Gobin et al. 2003, O'Brien and Syamlal 1993, Gibilaro et al. 1985) versus experimental data of Gauthier (2002).

3.5 CONCLUSION

In this section, mono-disperse flows in squared risers conducted with A and B-type particles were simulated. Two different flow configurations are used for simulations conducted with A-type particles; fluidization velocity and feeding of particles on the same sense and cross-flow condition and two different particle diameters. The studied flow geometries are three-dimensional vertical cold channels excluding cyclone, tampon and returning pipe of a typical circulating fluidized bed. Two transport equations $q_p^2 - q_{fp}$ developed in the frame of kinetic theory of granular media supplemented by the interstitial fluid effect and the interaction with the turbulence are resolved to model the effect of velocity fluctuations and inter-particle collisions on the dispersed phase hydrodynamic. For both types of particles, parametric studies were carried out to determine influences of turbulence modelling and boundary conditions for the particulate phase. The grid dependency was analysed with mesh refinement in horizontal, axial directions. For B-type particles, the results are in good qualitative agreement with the experiments and numerical predictions are improved by the mesh refinement. On the contrary, the simulations with A-type particles show a less satisfactory agreement with available measurements and are sensitive to mesh refinement. Different drag force models are tested for simulations of A-type particles. As we presented, the model of Gibilaro et al. (1985) improves results for one case. It is well known that this kind of empirical formulations are case-sensitive. It can be concluded that Euler-Euler approach has been successfully applied to the hydrodynamics of CFBs, especially for B-type particles. However, realistic prediction of A-type particles remains a challenge (Wang 2009 and Sundaresan 2000) and a consistent manner with this study, many studies have shown that Euler-Euler approach fails to reproduce the hydrodynamics of fluidized beds using A-type particles (O'Brien and Syamlal 1993, Agrawal et al. 2001, Yang et al. 2003, Heynderickx et al. 2004, Andrews et al. 2005, Igci et al. 2008, Wang 2009). It was revealed that the existence of meso-scale structures, such as streamers and clusters, have dramatic effects on the overall dynamic behaviours and they are cancelled out by coarse grid simulations. Agrawal et al. (2001) addresses that the effect of meso-scale on the macroscopic behaviour in coarse grid simulations, can be taken into account by sub-grid scales through additional closure relations. For this purpose, we will look for an alternative way to account for these unresolved structures. By constructing analogy with single phase flow, large eddy simulation or herein, filtered approach for Euler-Euler modelling can be used to get over this problem. This approach will be discussed in the next chapter.

Eulerian model discretized with spatially coarse mesh are performed for large units because of limited computational resources (Wang 2009, Sundaresan 2000, Andrews et al. 2005, Igci et al. 2008). Now, it is well established that meso-scale structures cancelled out by coarse mesh simulations have dramatic effect on overall behaviour of flows (O'Brien and Syamlal 1993, Agrawal et al. 2001, Yang et al. 2003, Heynderickx et al. 2004, Andrews et al. 2005, Igci et al. 2008, Wang 2009). The meso-scale structures are also well established by some experimental studies. Weinstein et al. (1984)'s study on high-velocity gas-solid flow in a vertical pipe pointed out that there are segregations of the particles over cross section. These meso-scale structure sizes are typically on the order of 10 – 100 particle diameters and they are found to segregate near riser walls and in some cases, large region of high concentration exists in the centre of riser (Weinstein et al. 1984, Gidaspow 1994). Reasons of existence of these structures were studied by Agrawal et al. (2001) and it was stated that clusters and streamers continuously occur in risers by a reason of local instabilities, such as damping of fluctuating motion of particles by the interstitial fluid, inelastic collisions, the non-linear drag between phases. High resolution simulation of two-fluid is capable of resolving these structures in correct manner, but it is not suitable for practical applications. Agrawal et al. (2001) proposed a methodology by constructing an analogy with large eddy simulation of a single phase turbulence where the effect of meso-scale structures on the macroscopic behaviour in coarse grid simulations, can be taken into account by sub-grid scales through additional closure relations. For this purpose, we perform the direct numerical integration of local instantaneous phase equations by Eulerian approach in a 3-D periodic circulating fluidized bed to study the influences of meso-scale structures on drag force and particulate phase stresses.

This section is organised as follows. In the first part, we introduce flow configuration, a 3-D periodic circulating fluidized bed (PCFB), where the mean gas-solid flow is periodically driven along the opposite direction of gravity. Then, we demonstrate the mesh dependency of domain statistical quantities such as: the relative velocity weighted by solid volume fraction, volumetric solid mass flux, random kinetic energy of particles and we discuss the mesh independent result where time and domain averaged quantities are converged to constant values. This mesh independent result make us be sure that we can resolve all time and spatial scales of the flow. By following, we present the filtering approach, filtered particle momentum and random kinetic energy equations. Mesh independent result obtained are used to calculate budget analyses of filtered particle momentum and random kinetic energy equations and the importance of additional terms due to filtering procedure, which stands for sub-grid contributions, are investigated. Thereafter, we carry out a priori tests on the sub-grid contribution of drag force and sub-grid scale (SGS) stress tensor of particulate phase. This part of study aims to identify sub-grid contributions due to filtering approach. The following part of this study will be addressed to propose models for sub-grid contributions and then validate the modelling of these terms by means of a priori tests.

4.1 PERIODIC CIRCULATING FLUIDIZED BED CONFIGURATION

Gas-particle flows were simulated in a 3-D PCFB. Typical FCC particles, $d_p = 75 \mu\text{m}$, $\rho_p = 1500 \text{ kg/m}^3$, were interacting with the ambient gas ($\rho_g = 1.186 \text{ kg/m}^3$, $\mu_g = 1.8 \times 10^{-5} \text{ Pa.s}$). Concerning the transfers between the phases with non-reactive isothermal flow, the drag and buoyancy (Archimedes) forces were accounted for the momentum transfer. The restitution coefficient e_c was set to 0.9. The computational domain is shown in Figure 28. The PCFB was initialised by the homogeneous distribution of the particle volume fraction $\alpha_{p,ini}$ equal to 0.05. The flow was driven through the opposite direction to the gravity by the source term due to the total mass in the bed added into momentum equations. No-slip condition for the gas phase was imposed at the walls. Momentum loss due to no-slip boundary condition was compensated by adding source term into the momentum equation for every timestep. Agrawal et al. (2001) tested three different choices of boundary condition for particulate phase: no-slip, free-slip and partial slip (defined by the particle-wall coefficient of restitution and the specular coefficient) and it was shown that the meso-scale structures were formed with all boundary conditions. Under these observations, we chose to impose free-slip condition for particulate phase at the walls.

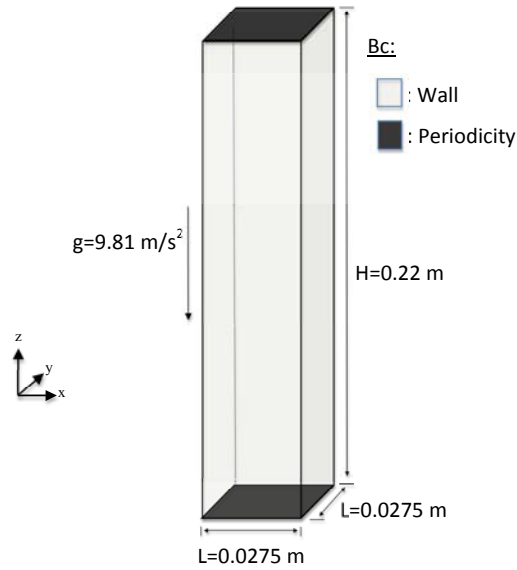


Figure 28: Periodic circulating fluidized bed (PCFB).

4.2 MESH INDEPENDENT RESULT

Agrawal et al. (2001) stated that statistical quantities over the whole domain were strongly dependent on the mesh size and they became mesh-independent when mesh sizes were the order of few particle diameters. In this study, the mesh refinement studies were carried out to insure that the mesh resolution was sufficient and all spatial and temporal scales of solid and gas phases were captured. Figure 29 shows instantaneous particle volume fraction fields in the PCFB obtained by different mesh resolutions. As the mesh resolution increases, inhomogeneous structures are better resolved. The coarsest mesh resolution was constructed by 110 000 cells ($24 \times 24 \times 192$, $\Delta x = \Delta y = \Delta z = 1.145 \times 10^{-3}$ m with inverse Froude number, $Fr_{\Delta}^{-1} = 0.175$). The highest mesh resolution case consists of approximately 17 million cells ($128 \times 128 \times 1024$, $\Delta x = \Delta y = \Delta z = 0.215 \times 10^{-3}$ m with inverse Froude number, $Fr_{\Delta}^{-1} = 0.032$).

To investigate the dynamic behaviour of particles in the PCFB, we define the following statistic quantities averaged over domain and in time. A time-averaged value $\overline{\langle Q \rangle}^t$ of the domain averaged quantity $\langle Q \rangle$ is defined as

$$\overline{\langle Q \rangle}^t = \frac{1}{T} \frac{1}{V} \int_T \int_V Q(\mathbf{x}, t) d\mathbf{x} dt. \quad (4.1)$$

A discrete ensemble averaged value $\overline{\langle Q \rangle}^{t,n}$ over n time instants of the domain averaged quantity $\langle Q \rangle$ is given by

$$\overline{\langle Q \rangle}^{t,n} = \sum_{k=1}^{k=n} \langle Q \rangle / n. \quad (4.2)$$

The time-domain averaged relative velocity weighted by solid volume fraction along the mean flow direction can be described by $\overline{\langle \alpha_p (U_{p,z} - U_{g,z}) \rangle}^t$.

The time-domain averaged volumetric solid flux along mean flow direction is calculated by dividing into two parts: downward and upward (see Eqs. (3.6) and (3.7)). For the sake of simplicity, we refer to time-averaged of any domain-averaged quantity as the average value of the quantity for the following sections. Each simulation has been run for a long duration to ensure that a statistically stationary state has been reached (225 non-dimensional physical time, the reference time scale is set to τ_p^{St}). To obtain domain statistics for all mesh resolutions, equivalent number of realisations can be assured by sample number which is set to number of cells multiplied by non-physical time. For highest mesh resolution, we obtained statistics during another 225 non-dimensional physical time. The total realisations for coarsest mesh was yielded by carrying out simulation for sufficient duration which was more than 50 times of the highest mesh resolution.

After the flow reached steady-state condition, the time-averaged statistics were gathered. The mesh dependencies of $\overline{\langle \alpha_p (U_{p,z} - U_{g,z}) \rangle}^t$ and non-dimensional total volumetric mass fluxes with definitions of o: homogeneous case and conv: converged case are shown in Figures 30 and 31. In the homogenous case, particles with homogenous distribution $\alpha = 0.05$ are falling down with the terminal settling velocity V_t^{St} . As mesh resolution or Fr_{Δ} number increases, inhomogeneous structures are better predicted and it can be seen from Figure 31 that influences of these structures on domain statistics are crucial for

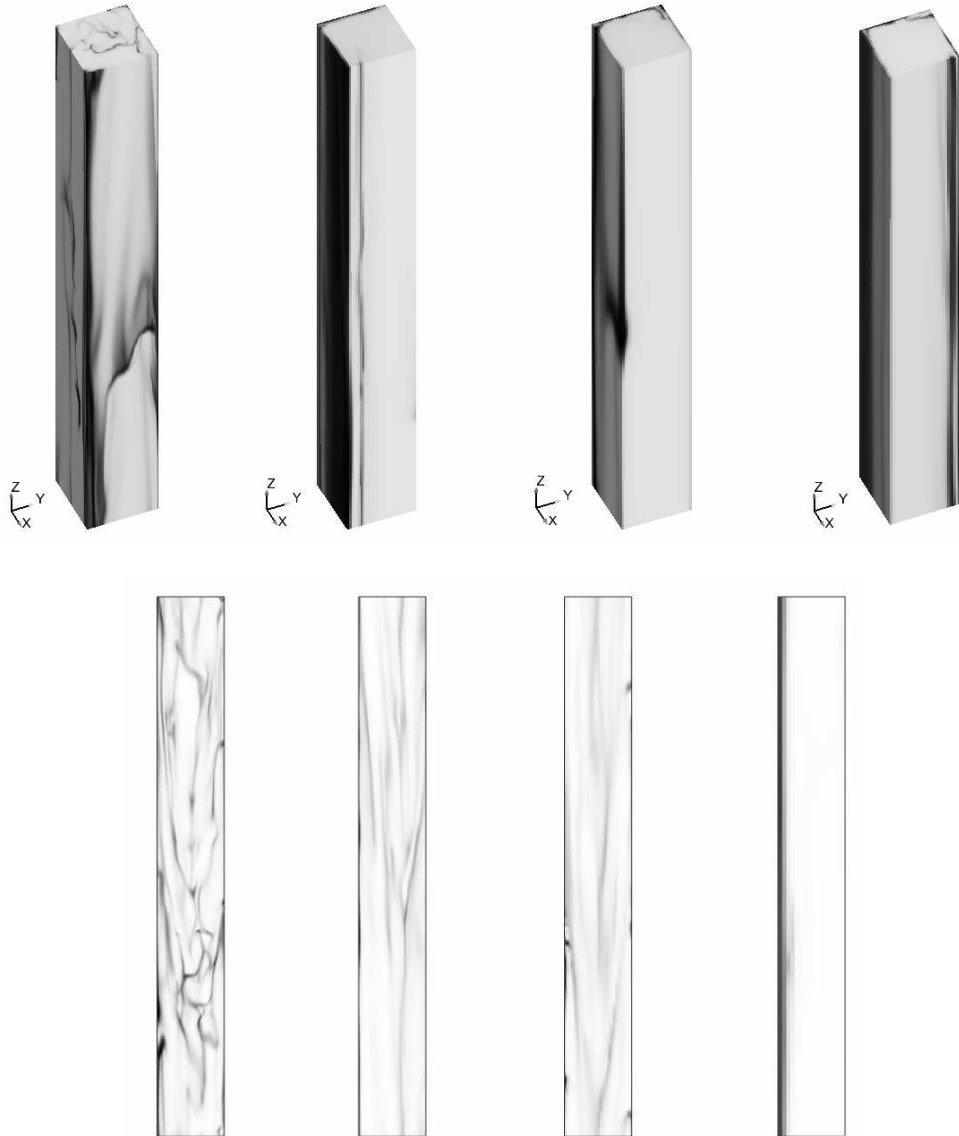


Figure 29: Instantaneous particle volume fraction field in the periodic circulating fluidized bed for different mesh resolutions (top: 3D view, bottom: $x - y$ plane). From right to left, the mesh resolution increases. White colour corresponds to $\alpha_p = 0$. Black colour corresponds to $\alpha_{p,max} = 0.64$.

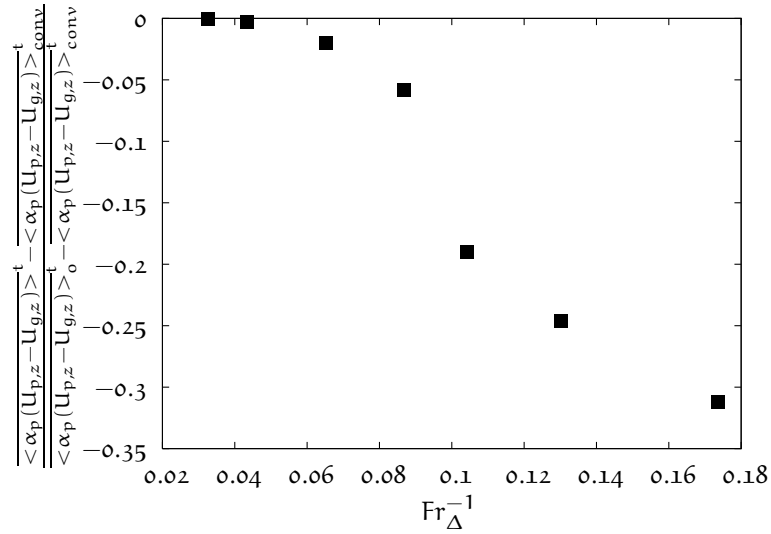


Figure 30: Influence of mesh size on the weighted gas-particle relative velocity $\frac{\langle \alpha_p (\mathbf{U}_{p,z} - \mathbf{U}_{g,z}) \rangle^t}{\langle \alpha_p (\mathbf{U}_{p,z} - \mathbf{U}_{g,z}) \rangle_0^t}$ where o: corresponds to the homogeneous case and conv: corresponds to the converged case.

solid hold-up in the bed. For the cases which Fr_{Δ} number's order is 10^1 , the weighted relative velocity and volumetric solid mass flux slightly change and converge constant values. It can be seen from Figure 32, the average granular temperature becomes roughly independent of mesh resolution as well.

The radial distribution of time-averaged variables are shown in Figures 33-37 for three mesh resolutions: moderate ($32 \times 32 \times 256$, $\Delta_x = \Delta_y = \Delta_z = 8.5 \times 10^{-4}$ m, $Fr_{\Delta}^{-1} = 0.128$), fine ($64 \times 64 \times 512$, $\Delta_x = \Delta_y = \Delta_z = 4.25 \times 10^{-4}$ m, $Fr_{\Delta}^{-1} = 0.064$) and finest ($128 \times 128 \times 1024$, $\Delta_x = \Delta_y = \Delta_z = 2.125 \times 10^{-4}$ m, $Fr_{\Delta}^{-1} = 0.032$). In Figure 33, the time-averaged of solid volume fraction is shown for different resolutions. The case with moderate resolution shows a symmetric distribution of solid fraction. Particles tend to accumulate the close the wall for moderate mesh resolution. By increasing mesh resolution, more particles are transported at the centre of the riser than of the moderate case. The time-averaged gas velocities normalised by the terminal settling velocity V_t^{St} are shown in Figure 34. For moderate mesh resolution, the gas velocity has positive values even close to the wall. With mesh refinement, we obtained the negative gas velocity close to the wall and reduction of the magnitude of mean flow. We present negative, positive and total mass flux normalised by uniform distribution of solid falling down with V_t^{St} in Figures 35 and 36. The core-annulus flow are obtained for moderate, fine and finest mesh resolutions. Solids are transported at the centreline and close to wall, but they descend only at the vicinity to wall. The negative solid flux decreases close to the wall with the increasing mesh resolution due to the better prediction of flow mixing. In Figure 37, the variance of the solid volume fraction normalised by the initial solid volume fraction is shown. The variance of solid volume flux, which represents the clustering effect, reaches the maximum value close to the wall.

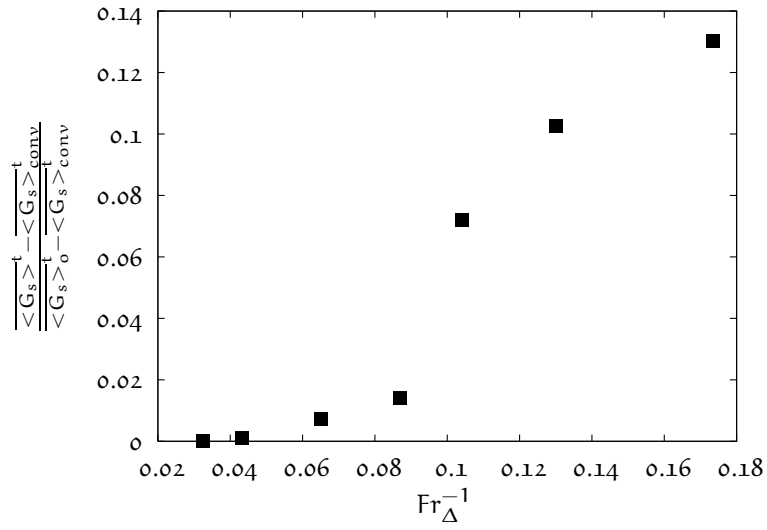


Figure 31: Influence of mesh size on the non-dimensional total volumetric mass flux $\overline{\langle G_s \rangle^t}$ where o: corresponds to the homogeneous case and conv: corresponds to the converged case.

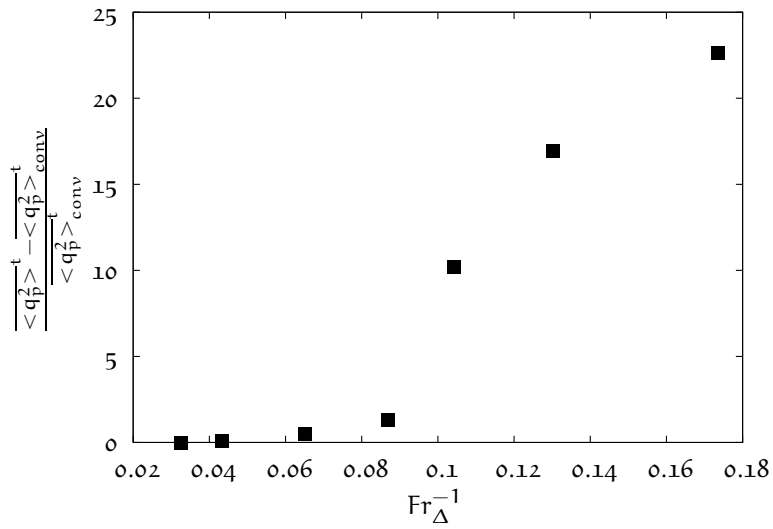


Figure 32: Influence of mesh size on the random kinetic energy of particulate phase $\overline{\langle q_p^2 \rangle^t}$ where conv: corresponds to the converged case.

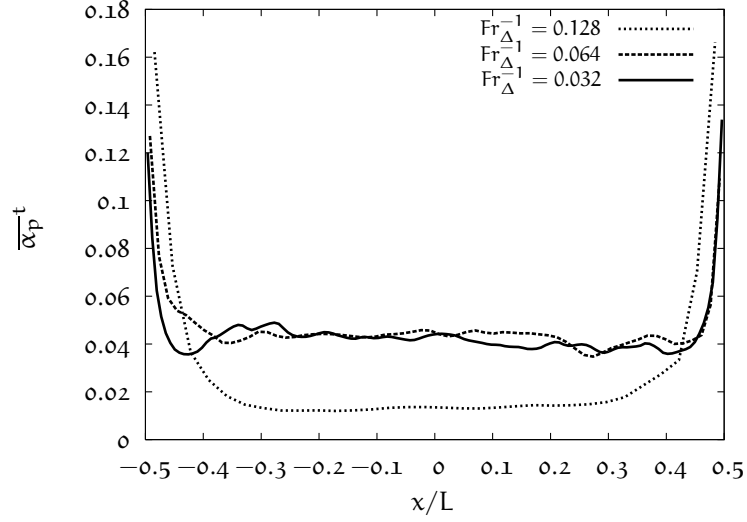


Figure 33: Time-averaged solid volume fraction along the radial direction for three mesh resolutions: moderate ($32 \times 32 \times 256$, $Fr_{\Delta}^{-1} = 0.128$), fine ($64 \times 64 \times 512$, $Fr_{\Delta}^{-1} = 0.064$) and finest ($128 \times 128 \times 1024$, $Fr_{\Delta}^{-1} = 0.032$) ($z = 0.11\text{m}$, $y = 0$).

The finest mesh resolution ($128 \times 128 \times 1024$, $Fr_{\Delta}^{-1} = 0.032$) results were then used to construct a database comprised of solid volume fraction, gas and particle velocities obtained on 10 time instants. This database is called as DNS database and consists of 180 million of realisations of desired macro variables. This database was used to filter variables by volume averaging. For further investigations, the filtered variables corresponded same value at a different region of the domain at a given instant were picked up by various markers such as; filtered volume fraction or phase velocities.

CPU time

Figure 38 shows the CPU times required to compute 1 physical time of flow for different mesh resolutions. The CPU times linearly increases as mesh resolution increases. Due to computational limits (see the CPU time required for the mesh resolution, $Fr_{\Delta}^{-1} = 0.032$), fully resolved simulations using the two-fluid model for industrial applications are unaffordable. The simulations were performed on Bi-Xeon E5472 processors running at 3 Ghz.

4.3 DERIVATION OF FILTERED TWO-FLUID MODEL

Let $\alpha_p(\mathbf{x}, t)$ denote the particle volume fraction at location \mathbf{x} and time t obtained by solving the two-fluid equations. We can define the filtered phase volume fraction $\overline{\alpha}_k(\mathbf{x}, t)$ as

$$\overline{\alpha}_p(\mathbf{x}, t) = \iiint \alpha_p(\mathbf{r}, t) G(\mathbf{x} - \mathbf{r}) d\mathbf{r} \quad (4.3)$$

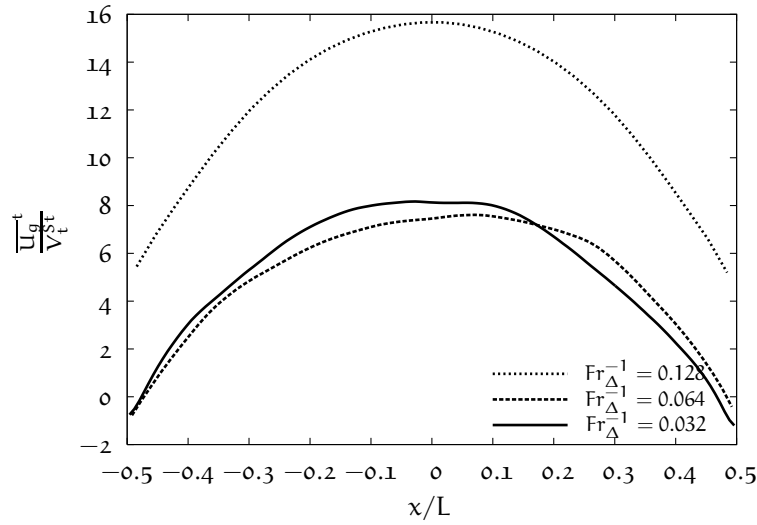


Figure 34: Time-averaged gas velocity along the radial direction for three mesh resolutions: moderate ($32 \times 32 \times 256$, $Fr_{\Delta}^{-1} = 0.128$), fine ($64 \times 64 \times 512$, $Fr_{\Delta}^{-1} = 0.064$) and finest ($128 \times 128 \times 1024$, $Fr_{\Delta}^{-1} = 0.032$) ($z = 0.11\text{m}$, $y = 0$).

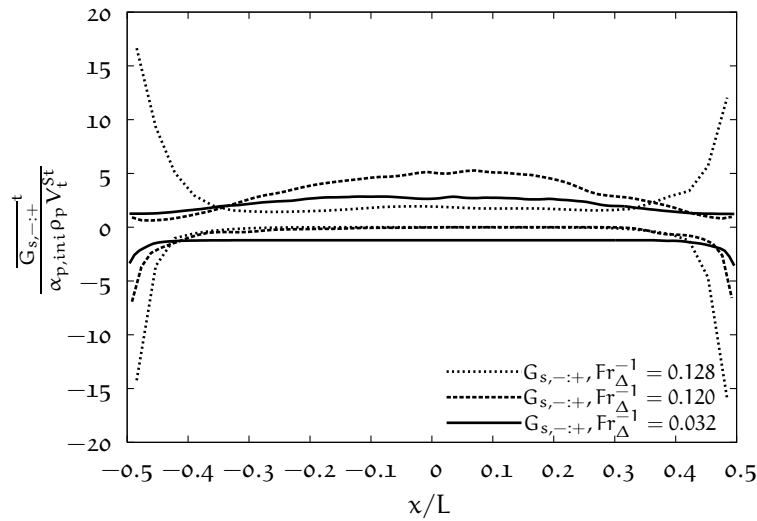


Figure 35: Time-averaged negative and positive solid mass flux along the radial direction for three mesh resolutions: moderate ($32 \times 32 \times 256$, $Fr_{\Delta}^{-1} = 0.128$), fine ($64 \times 64 \times 512$, $Fr_{\Delta}^{-1} = 0.064$) and finest ($128 \times 128 \times 1024$, $Fr_{\Delta}^{-1} = 0.032$) ($z = 0.11\text{m}$, $y = 0$).

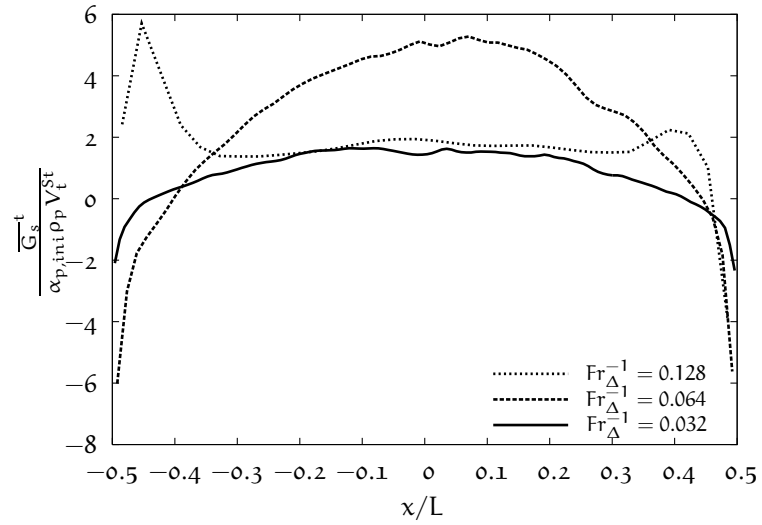


Figure 36: Time-averaged total solid mass flux along the radial direction for three mesh resolutions: moderate ($32 \times 32 \times 256$, $Fr_{\Delta}^{-1} = 0.128$), fine ($64 \times 64 \times 512$, $Fr_{\Delta}^{-1} = 0.064$) and finest ($128 \times 128 \times 1024$, $Fr_{\Delta}^{-1} = 0.032$) ($z = 0.11\text{m}$, $y = 0$).

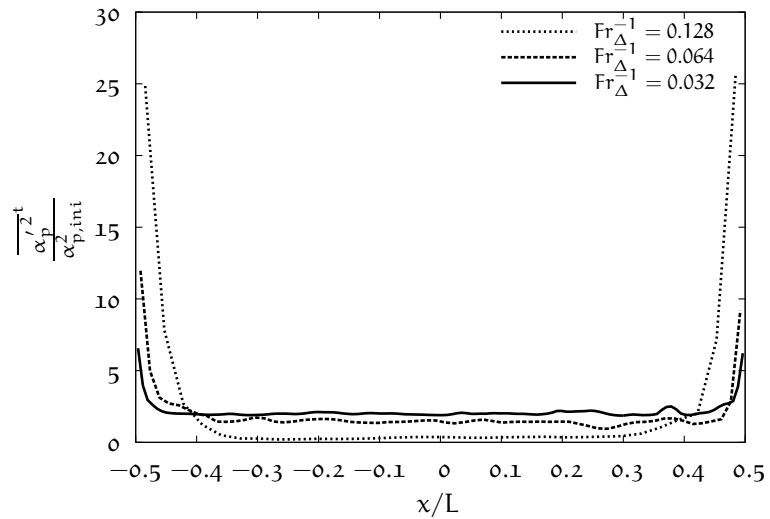


Figure 37: Time-averaged variance of solid volume fraction along the radial direction for three mesh resolutions: moderate ($32 \times 32 \times 256$, $Fr_{\Delta}^{-1} = 0.128$), fine ($64 \times 64 \times 512$, $Fr_{\Delta}^{-1} = 0.064$) and finest ($128 \times 128 \times 1024$, $Fr_{\Delta}^{-1} = 0.032$) ($z = 0.11\text{m}$, $y = 0$).

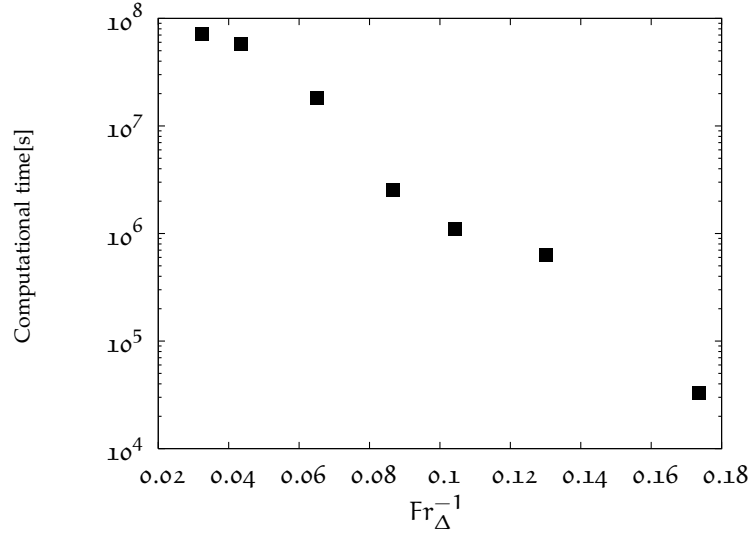


Figure 38: CPU times required to simulate 1 s physical time using the kinetic theory based two-fluid model.

where G is a weight function which satisfies $\int \int \int G(\mathbf{r}) d\mathbf{r} = 1$. Filtered phase velocities are defined according to

$$\tilde{U}_p(\mathbf{x}, t) = \frac{1}{\bar{\alpha}_p} \int \int \int G(\mathbf{x} - \mathbf{r}) \alpha_p(\mathbf{r}, t) \mathbf{U}_p(\mathbf{r}, t) d\mathbf{r} \quad (4.4)$$

and

$$\tilde{U}_g(\mathbf{x}, t) = \frac{1}{\bar{\alpha}_g} \int \int \int G(\mathbf{x} - \mathbf{r}) \alpha_g(\mathbf{r}, t) \mathbf{U}_g(\mathbf{r}, t) d\mathbf{r}. \quad (4.5)$$

Applying such a filter to the continuity equations of phases, one can obtain

$$\frac{\partial}{\partial t} \bar{\alpha}_k \rho_k + \frac{\partial}{\partial x_j} \rho_k \bar{\alpha}_k \tilde{U}_{k,j} = 0. \quad (4.6)$$

Repeating this filtering procedure to momentum balances, the filtered momentum balance for particle and continuous phase are

$$\begin{aligned}
\frac{\partial}{\partial t} \rho_k \bar{\alpha}_k \tilde{u}_{k,i} + \frac{\partial}{\partial x_j} \rho_k \bar{\alpha}_k \tilde{u}_{k,i} \tilde{u}_{k,j} &= -\bar{\alpha}_k \frac{\partial \bar{P}_g}{\partial x_i} - \varphi_{k,i}^{sgs} \\
&+ \tilde{I}_{k,i} + I_{k,i}^{sgs} \\
&- \frac{\partial}{\partial x_j} \tilde{\Sigma}_{k,ij} - \frac{\partial}{\partial x_j} \Sigma_{k,ij}^{sgs} \\
&- \frac{\partial}{\partial x_j} \rho_k \bar{\alpha}_k \sigma_{k,ij}^{sgs} + \bar{\alpha}_k \rho_k g_i. \tag{4.7}
\end{aligned}$$

Additional terms arise in Eq. (4.7) due to the filtering process and they represent the interaction between resolved and sub-grid contributions. The term $\varphi_{k,i}^{sgs}$ represents the correlation between the volume fractions of phases and gas pressure and defined as:

$$\varphi_{k,i}^{sgs} = \overline{\alpha_k \frac{\partial P_g}{\partial x_i}} - \bar{\alpha}_k \frac{\partial \bar{P}_g}{\partial x_i}. \tag{4.8}$$

A Reynolds stress-like contribution coming from the gas or particle phase velocity fluctuations $\sigma_{k,ij}^{sgs}$ is defined by the following equation:

$$\bar{\alpha}_k \sigma_{k,ij}^{sgs} = \bar{\alpha}_k (\widetilde{u_{k,i} u_{k,j}} - \tilde{u}_{k,i} \tilde{u}_{k,j}). \tag{4.9}$$

The terms $\tilde{I}_{k,i}$ and $I_{k,i}^{sgs}$ are the resolved and sub-grid contribution of the drag term and defined as:

$$\tilde{I}_{g \rightarrow p,i} = -\tilde{I}_{p \rightarrow g,i} = \frac{\bar{\alpha}_p \rho_p}{\tilde{\tau}_p} (\tilde{u}_{p,i} - \tilde{u}_{g,i}) \tag{4.10}$$

$$I_{g \rightarrow p,i}^{sgs} = -I_{p \rightarrow g,i}^{sgs} = \frac{\overline{\alpha_p \rho_p}}{\tau_p} v_{r,i} - \frac{\bar{\alpha}_p \rho_p}{\tilde{\tau}_p} (\tilde{u}_{p,i} - \tilde{u}_{g,i}). \tag{4.11}$$

The terms $\tilde{\Sigma}_{p,ij}$ and $\Sigma_{p,ij}^{sgs}$ are the resolved and sub-grid contribution of the particle kinetic stress tensor and given by

$$\tilde{\Sigma}_{p,ij} = (\bar{P}_p - \tilde{\lambda}_p \frac{\partial \tilde{u}_{p,m}}{\partial x_m}) \delta_{ij} - \tilde{\mu}_p (\frac{\partial \tilde{u}_{p,i}}{\partial x_j} + \frac{\partial \tilde{u}_{p,j}}{\partial x_i} - \frac{2}{3} \frac{\partial \tilde{u}_{p,m}}{\partial x_m} \delta_{ij}) \tag{4.12}$$

$$\begin{aligned}
\Sigma_{p,ij}^{sgs} &= (\overline{P_p^r} - \lambda_p \frac{\partial \overline{u_{p,m}}}{\partial x_m}) \delta_{ij} - \mu_p (\frac{\partial \overline{u_{p,i}}}{\partial x_j} + \frac{\partial \overline{u_{p,j}}}{\partial x_i} - \frac{2}{3} \frac{\partial \overline{u_{p,m}}}{\partial x_m} \delta_{ij}) \\
&- \left[(\bar{P}_p - \tilde{\lambda}_p \frac{\partial \tilde{u}_{p,m}}{\partial x_m}) \delta_{ij} - \tilde{\mu}_p (\frac{\partial \tilde{u}_{p,i}}{\partial x_j} + \frac{\partial \tilde{u}_{p,j}}{\partial x_i} - \frac{2}{3} \frac{\partial \tilde{u}_{p,m}}{\partial x_m} \delta_{ij}) \right] \tag{4.13}
\end{aligned}$$

with the following equations for filtered particle pressure P_p^r , resolved particle pressure \bar{P}_p , bulk $\tilde{\lambda}_p$, and shear viscosity $\tilde{\mu}_p = \bar{\alpha}_p \rho_p (\tilde{\nu}_p^{\text{kin}} + \tilde{\nu}_p^{\text{coll}})$:

$$\begin{aligned} P_p^r &= \frac{2}{3} \rho_p (\overline{\alpha_p q_p^2} + (1 + e_c) \overline{\alpha_p^2 g_0 q_p^2}) \\ \bar{P}_p &= \frac{2}{3} \rho_p (\bar{\alpha}_p \bar{q}_p^2 + (1 + e_c) \bar{\alpha}_p^2 \bar{g}_0 \bar{q}_p^2) \\ \tilde{\lambda}_p &= \frac{4}{3} \rho_p d_p (1 + e_c) \bar{\alpha}_p^2 \bar{g}_0 \sqrt{\frac{2}{3} \frac{\bar{q}_p^2}{\pi}} \\ \tilde{\nu}_p^{\text{kin}} &= \frac{1}{2} \tilde{\tau}_p \frac{2}{3} \bar{q}_p^2 (1 + \bar{\alpha}_p \bar{g}_0 \phi_c) \left[1 + \frac{\sigma_c}{2} \frac{\tilde{\tau}_p}{\tilde{\tau}_c} \right]^{-1} \\ \tilde{\nu}_p^{\text{coll}} &= \frac{4}{5} \bar{\alpha}_p \bar{g}_0 (1 + e_c) (\tilde{\nu}_p^{\text{kin}} + d_p \sqrt{\frac{2}{3} \frac{\bar{q}_p^2}{\pi}}). \end{aligned}$$

One can perform the filtering procedure on the random kinetic energy of particulate phase. The filtered particle kinetic energy equation is given by

$$\begin{aligned} \frac{\partial}{\partial t} \bar{\alpha}_p \rho_p \bar{q}_p^2 + \frac{\partial}{\partial x_j} \bar{\alpha}_p \rho_p \tilde{U}_{p,j} \bar{q}_p^2 &= \frac{\partial}{\partial x_j} (\bar{\alpha}_p \rho_p (\tilde{K}_p^{\text{kin}} + \tilde{K}_p^{\text{coll}}) \frac{\partial \bar{q}_p^2}{\partial x_j}) + \frac{\partial}{\partial x_j} (\rho_p \mathcal{K}_j) \\ &\quad - \tilde{\Sigma}_{p,ij} \frac{\partial \tilde{U}_{p,i}}{\partial x_j} - \mathcal{S} \\ &\quad + \frac{1}{3} [1 - e_c^2] \frac{\bar{\alpha}_p \rho_p}{\tilde{\tau}_c} \frac{2}{3} \bar{q}_p^2 + \mathcal{E} \\ &\quad - 3 \frac{\bar{\alpha}_p \rho_p}{\tilde{\tau}_p} \frac{2}{3} \bar{q}_p^2 - \mathcal{F} \\ &\quad + \mathcal{Q} \end{aligned} \tag{4.14}$$

with \tilde{K}_p^{kin} and $\tilde{K}_p^{\text{coll}}$ the resolved kinematic and collisional diffusivity respectively, given by

$$\tilde{K}_p^{\text{kin}} = \frac{2}{3} \bar{q}_p^2 \tilde{\tau}_c (1 + \bar{\alpha}_p g_0 \phi_c) \left(\xi_c + \frac{9}{5} \frac{\tilde{\tau}_c}{\tilde{\tau}_p} \right)^{-1} \tag{4.15}$$

$$\tilde{K}_p^{\text{coll}} = \frac{6}{5} \bar{\alpha}_p g_0 (1 + e_c) (\tilde{K}_p^{\text{kin}} + \frac{10}{9} d_p \sqrt{\frac{2}{3} \frac{\bar{q}_p^2}{\pi}}). \tag{4.16}$$

$\tilde{\Sigma}_{p,ij} \frac{\partial \tilde{U}_{p,i}}{\partial x_j}$ is the production of resolved particle kinetic energy by resolved particle velocity gradient. The terms, \mathcal{K}_j , \mathcal{S} , \mathcal{E} , \mathcal{F} and \mathcal{Q} are sub-grid contributions and defined by following relations:

$$\mathcal{K}_j = \overline{\alpha_p (K_p^{\text{kin}} + K_p^{\text{coll}}) \frac{\partial q_p^2}{\partial x_j}} - \bar{\alpha}_p (\tilde{K}_p^{\text{kin}} + \tilde{K}_p^{\text{coll}}) \frac{\partial \tilde{q}_p^2}{\partial x_j} \quad (4.17)$$

$$\mathcal{S} = \overline{\Sigma_{p,ij} \frac{\partial U_{p,j}}{\partial x_i}} - \tilde{\Sigma}_{p,ij} \frac{\partial \tilde{U}_{p,j}}{\partial x_i} \quad (4.18)$$

$$\mathcal{E} = \frac{1}{3} [1 - e_c^2] \rho_p \left[\overline{\frac{\alpha_p}{\tau_c} \frac{2}{3} q_p^2} - \bar{\alpha}_p \frac{2}{\tilde{\tau}_c} \frac{2}{3} \tilde{q}_p^2 \right] \quad (4.19)$$

$$\mathcal{F} = 3\rho_p \left[\overline{\frac{\alpha_p}{\tau_p} \frac{2}{3} q_p^2} - \bar{\alpha}_p \frac{2}{\tilde{\tau}_p} \frac{2}{3} \tilde{q}_p^2 \right] \quad (4.20)$$

$$\mathcal{Q} = -\frac{\partial}{\partial x_j} \bar{\alpha}_p \rho_p (\overline{q_p^2 \tilde{U}_{p,j}} - \tilde{q}_p^2 \tilde{U}_{p,j}) \quad (4.21)$$

Additional terms arising due to volume filtering require closure models. The contribution of additional terms can be examined by performing budget analyses of the filtered particle momentum and random kinetic energy equations. These budget analyses allow us to neglect some additional terms depending on their magnitude.

4.4 BUDGET ANALYSIS OF FILTERED MOMENTUM EQUATION

To obtain better insight into the influences of additional terms in the filtered momentum equation of particulate phase, resolved and sub-grid contribution terms are calculated for different filter widths. The average of the momentum balance along the mean flow for particulate phase is defined as follows:

$$\begin{aligned} 0 = & \overline{-\langle \bar{\alpha}_p \frac{\partial \bar{P}_g}{\partial z} \rangle}^{t,n} & \overline{-\langle \varphi_{p,z}^{sgs} \rangle}^{t,n} \\ & + \overline{\langle \frac{\bar{\alpha}_p \rho_p}{\tilde{\tau}_p} (\tilde{U}_{g,z} - \tilde{U}_{p,z}) \rangle}^{t,n} & + \overline{\langle I_{p,z}^{sgs} \rangle}^{t,n} \\ & \overline{-\langle \frac{\partial}{\partial x_j} \tilde{\Sigma}_{p,zj} \rangle}^{t,n} & \overline{-\langle \frac{\partial}{\partial x_j} \Sigma_{p,zj}^{sgs} \rangle}^{t,n} \\ & \overline{-\langle \frac{\partial}{\partial x_j} \rho_p \bar{\alpha}_p \sigma_{p,zj}^{sgs} \rangle}^{t,n} & + \overline{\langle \bar{\alpha}_p \rho_p g_z \rangle}^{t,n} \end{aligned} \quad (4.22)$$

Eq. (4.22) states the global equilibrium of fluidized particles between buoyancy (gas pressure gradient), drag force, particle stresses and gravity contribution. First and second terms represent the resolved and sub-grid buoyancy. Terms in the second line are the resolved and the sub-grid drag force. The third term shows the resolved and sub-grid particle kinetic stress tensor. The seventh term is the sub-grid contribution of particle phase velocity fluctuations. The last term is the gravity contribution.

The resolved and sub-grid contributions of each terms normalised by the gravity contribution for different filter widths are shown in Figure 39 and 40. It can be seen that drag and gravity forces are the main contributions of the momentum equation and con-

sistent with findings of Zimmermann and Taghipour (2005). The sub-grid contribution of drag force dramatically increases as filter width increases. The resolved drag force increases with the similar behaviour and the sum of resolved and sub-grid contribution of drag force remains constant (see Figure 39). For simulation over coarse meshes, the sub-grid contribution is not taken into account and eventually, the drag term is overestimated. This outcome is in agreement with the evaluation of Agrawal et al. (2001) and Parmentier et al. (2012). The order of the sub-grid contribution of buoyancy force without hydrostatic part is the same as of the resolved buoyancy for intermediate and large filter widths ($10 < \Delta_f / \Delta_{DNS}$). The resolved particle kinetic stress is independent of filter width and the sub-grid contribution can be negligible (see Figure 40). The sub-grid stress tensor increases asymptotically as filter width increases and it is expected that it reaches the value of the resolved particle kinetic stress for large filter widths. Zhang and VanderHeyden (2002) and De Wilde (2005) stated that buoyancy term has to be accounted for simulations over coarse meshes. However, we demonstrated that the sub-grid contribution of drag force are greater than of buoyancy term. Several researches have been devoted to the influence of meso-scale structures on the sub-grid stress tensor. Dasgupta et al. (1994) solved unsteady fully developed flow in a vertical riser with Reynolds averaging equation model based on the mixing velocity in the framework of turbulence modelling. For the closure equations for mixture fluctuations, the additional transport equations of the turbulent kinetic energy k and the turbulent rate of dissipation ϵ are coupled with mixture mass and momentum balances. They revealed that particles are driven to regions having a low intensity of particle-phase velocity fluctuations from regions of high intensity at rates proportional to the gradients in the intensity of fluctuations. Hrenya and Sinclair (1997) applied Reynolds decomposition on the gas and particulate equations separately and described the Reynolds stresses for particulate phase with an eddy assumption. It was found that turbulence viscosity of particulate phase significantly flattened mean variable profiles. Under consequences of previous studies with our analyses, herein, we pay attention to drag term and particle sub-grid stress tensor to investigate influences of clustering.

A Priori Analysis on Drag Term

We stated that the sub-grid contribution of drag force was cancelled out by coarse mesh resolutions and as a consequence, resolved drag force is over-predicted and thereby, poor prediction of overall bed dynamic is obtained. In order to investigate variables participating the drag force sub-grid contribution, we perform a priori analyses on the filtered drag term. We carried out correlation analyses between the filtered drag term and the filtered variables such as filtered particle volume fraction, gas and particle velocities. Following Özel et al. (2010), Parmentier (2010) and Parmentier et al. (2012) we propose to decompose the filtered drag force in two contributions: the difference between filtered gas and particle velocities, $\tilde{U}_{g,i} - \tilde{U}_{p,i}$, and a sub-grid drift velocity $\tilde{V}_{d,i}$. Then, the filtered drag force is defined by

$$\frac{\overline{\alpha_p \rho_p}}{\tau_p} V_{r,i} = \frac{\overline{\alpha_p \rho_p}}{\tilde{\tau}_p} \left(\tilde{U}_{g,i} - \tilde{U}_{p,i} + \tilde{V}_{d,i} \right). \quad (4.23)$$

The sub-grid contribution of drag force can be written from Eq. (4.11) as follows:

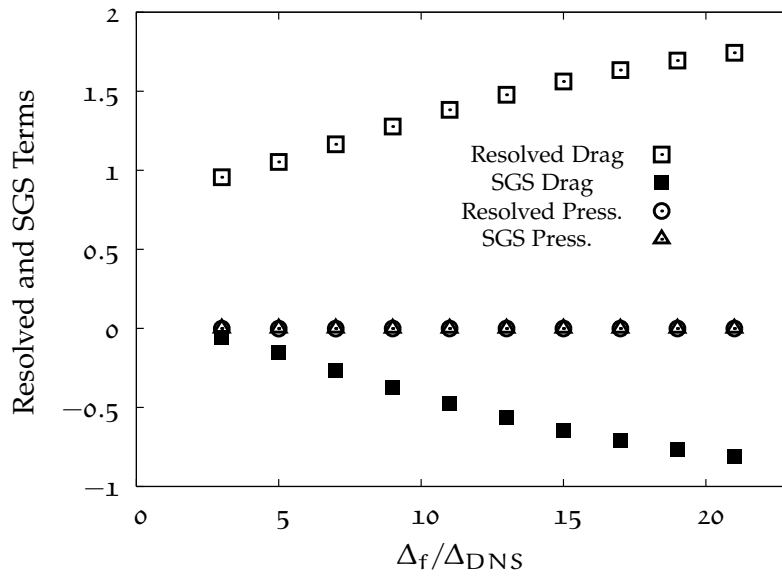


Figure 39: Resolved and sub-grid contributions drag force and gas pressure gradient without hydrostatic part for different filter widths Δ_f (Normalised by gravity contribution).

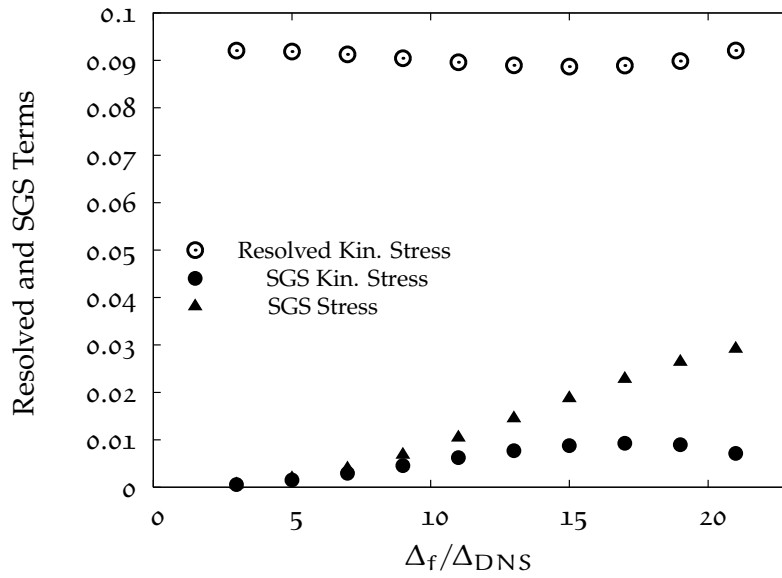


Figure 40: Resolved and sub-grid contributions of kinetic and sub-grid stresses for different filter widths Δ_f (Normalised by gravity contribution).

$$I_{p,i}^{sgs} = \frac{\rho_p}{\tilde{\tau}_p} \bar{\alpha}_p \tilde{V}_{d,i} \quad (4.24)$$

This decomposition allows us to identify physically the meaning of sub-grid drift velocity and to understand the origin of the difference between the filtered and resolved drag force. The correlation analysis is performed to indicate the predictive relations between the sub-grid drift velocity and other filtered variables. Correlative analyses show that the filtered drag force can be approximated by the following expression:

$$\frac{\bar{\alpha}_p \rho_p}{\tau_p} V_{r,i} \simeq \frac{\rho_p}{\tilde{\tau}_p} \bar{\alpha}_p V_{r,i}. \quad (4.25)$$

Figure 41 shows that correlation coefficients¹ between left and right-hand-side of are around 99% for each directions, even for large filter widths. It shows that the sub-grid drag term occurs by the filtered relative velocity averaged by particle volume fraction, $\bar{\alpha}_p V_{r,i}$.

Using Eqs. (4.23), (4.25) and (4.4), the SGS solid volume fraction flux or simply drift flux is approximated by:

$$\bar{\alpha}_p \tilde{V}_{d,i} = \overline{\alpha_p U_{g,i}} - \bar{\alpha}_p \tilde{U}_{g,i} \quad (4.27)$$

and the sub-grid drift velocity is

$$\tilde{V}_{d,i} \simeq \tilde{U}_{g@p,i} - \tilde{U}_{g,i} \quad (4.28)$$

where $\tilde{U}_{g@p,i} = \overline{\alpha_p U_{g,i}} / \bar{\alpha}_p$ is the filtered gas velocity seen by the particle phase. Figure 42 shows the profile of sub-grid velocity along the mean direction calculated from DNS database (exact) and the difference between the weighted gas velocity by particle volume fraction and gas velocity (approx.). This graph corporates that sub-grid contribution of drag force described by sub-grid drift velocity can be attributed to the difference between the weighted gas velocity by particle volume fraction and gas velocity. This allows us to prescribe the physical interpretation which is the inhomogeneities of solid volume fraction and gas velocity inside the volume filtering. The sub-grid drift velocity $\tilde{V}_{d,i}$ cannot obtain from kinetic theory based simulation and needs a closure relation.

1. Pearson correlation coefficients between fields A and B are given by:

$$r(A; B) = \frac{\langle AB \rangle - \langle A \rangle \langle B \rangle}{\sqrt{(\langle A^2 \rangle - \langle A \rangle^2)(\langle B^2 \rangle - \langle B \rangle^2)}} \quad (4.26)$$

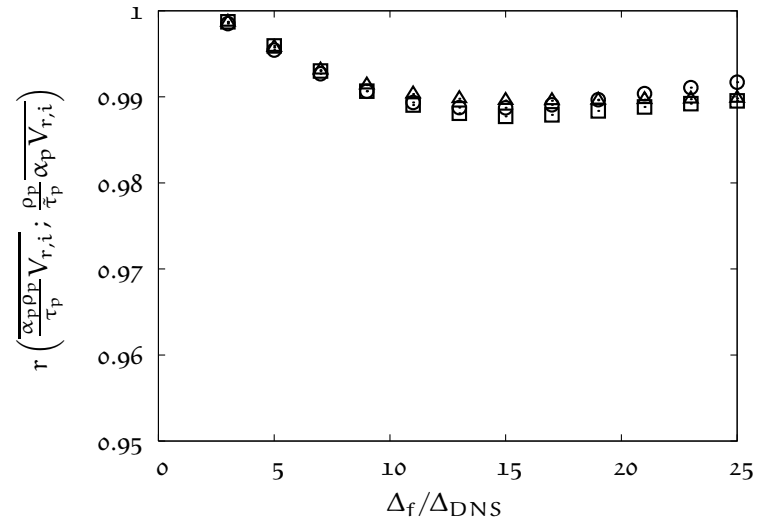


Figure 41: Correlation coefficients between the filtered drag (l.h.s of Eq. (4.25)) and relative velocity weighted by solid volume fraction (r.h.s of Eq. (41)) for different filter widths Δ_f : □, ○: radial directions and △ : mean flow direction.

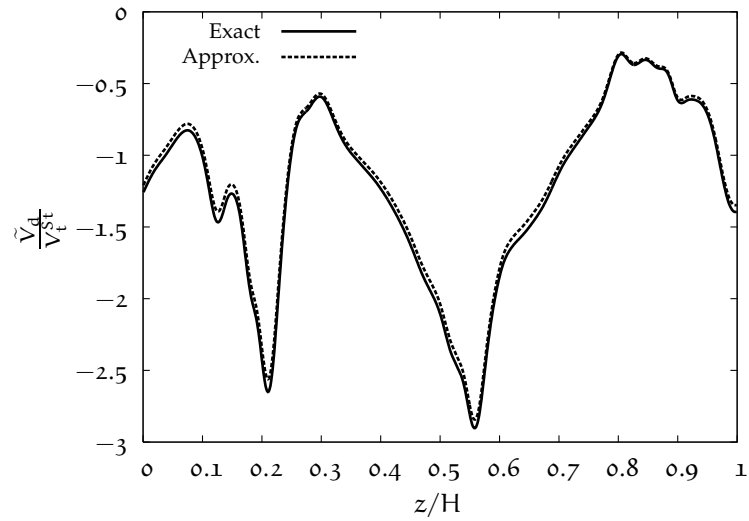


Figure 42: Sub-grid drift velocity along the mean flow direction ($x = y = 0$) calculated directly from high resolution simulation, (4.24), and the difference between the weighted gas velocity by the particle volume fraction and the gas velocity, (4.28). for the filter width equal to $15\Delta_{DNS}$.

A Priori Test on Particle SGS Stress Tensor

The particle SGS stress tensor is defined in Eq. (4.7) as:

$$-\frac{\partial}{\partial x_j} \rho_p \bar{\alpha}_p \sigma_{p,ij}^{sgs} = -\frac{\partial}{\partial x_j} \rho_p \bar{\alpha}_p (\widetilde{U_{p,i} U_{p,j}} - \tilde{U}_{p,i} \tilde{U}_{p,j}) \quad (4.29)$$

In incompressible single phase flow, the trace of the sub-grid stress tensor is not modelled but it is incorporated into the filtered pressure. In the context of dispersed phase, the trace of $\bar{\alpha}_p \sigma_{p,ij}^{sgs}$ will have the dispersive characteristic and it is crucial to have better prediction of particle segregation (Moreau et al., 2009). Then, the particle sub-grid stress tensor $\sigma_{p,ij}^{sgs}$ can be divided into deviatoric and spherical parts:

$$\bar{\alpha}_p \sigma_{p,ij}^{sgs} = \bar{\alpha}_p \sigma_{p,ij}^* + \bar{\alpha}_p \frac{1}{3} \sigma_{p,kk} \delta_{ij} \quad (4.30)$$

The sub-grid correlated energy is given by $\sigma_{p,SGS} = 1/2 \sigma_{p,kk}$. The sub-grid correlated energy $\sigma_{p,SGS}$ are compared for different filter widths (Figure 43). As expected, the sub-grid correlated energy increases almost linearly with the filter width (as in single phase turbulent flows). The latter includes comparisons of sub-grid correlated energy and the resolved kinetic stress tensor trace: $(\bar{P}_p - \bar{\lambda}_p \frac{\partial \tilde{U}_{p,m}}{\partial x_m})$. Both terms are conditionally averaged by filtered solid volume fraction. It is pointed out that sub-grid correlated energy is larger than the resolved kinetic stress tensor trace (see Figure 44), especially for larger filter widths.

The deviatoric part of particle sub-grid stress tensor can be studied on the scalar level (dissipation) by multiplying tensor with particle velocity gradients. The sub-grid dissipation by correlated and resolved kinetic stress tensor are respectively given by $\sigma_{p,ij}^* \frac{\partial \tilde{U}_{p,i}}{\partial x_j}$ and $\tilde{\nu}_p S_{p,ij}^* \frac{\partial \tilde{U}_{p,i}}{\partial x_j}$ where $S_{p,ij}^*$ is the trace-free strain-rate tensor expressed by $(\frac{\partial \tilde{U}_{p,i}}{\partial x_j} + \frac{\partial \tilde{U}_{p,j}}{\partial x_i} - \frac{2}{3} \frac{\partial \tilde{U}_{p,m}}{\partial x_m} \delta_{ij})$. The conditional averaged of these terms by filtered volume fraction are shown in Figure 46. It is clear that sub-grid dissipation is higher than the resolved kinetic stress dissipation. It can be concluded that the sub-grid correlated energy $\sigma_{p,SGS}$ and dissipation due to sub-grid stress $\sigma_{p,ij}^* \frac{\partial \tilde{U}_{p,i}}{\partial x_j}$ has to be accounted for in coarse grid simulations and sub-grid contributions of kinetic theory based stresses can be ignored.

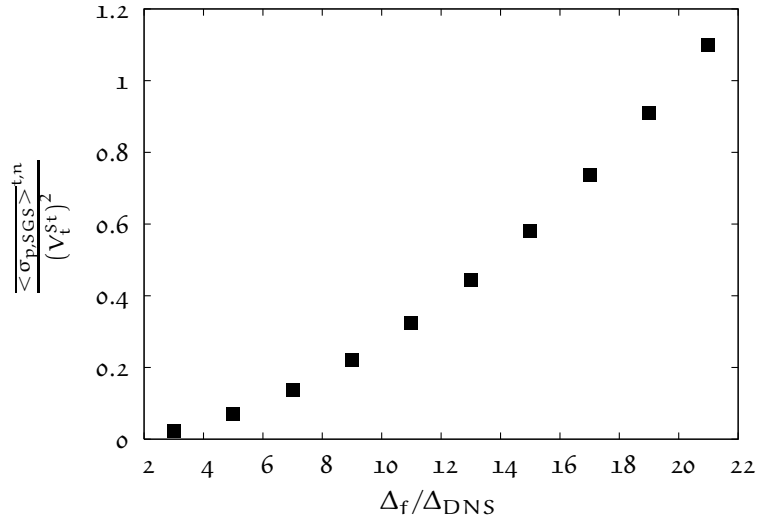


Figure 43: Averaged sub-grid correlated energy $\sigma_{p,SGS}$ for different filter widths Δ_f .

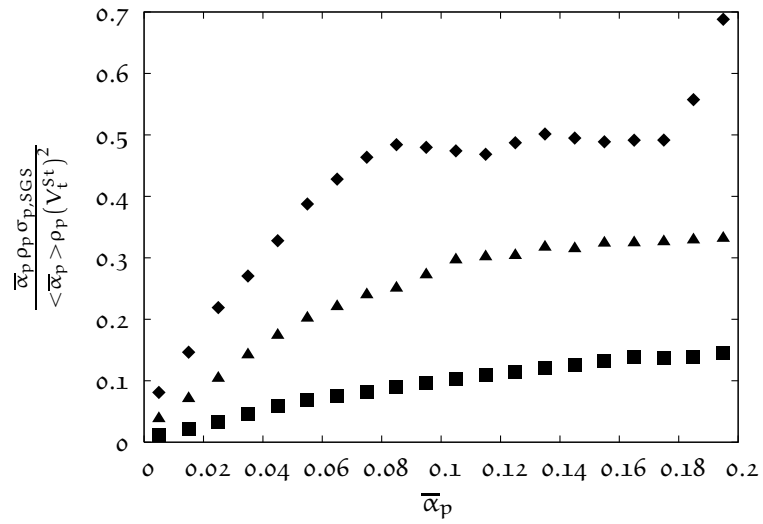


Figure 44: Sub-grid correlated energy $\overline{\alpha_p} \rho_p \sigma_{p,SGS}$ conditionally averaged by filtered volume fraction for filter widths, ■ : $5\Delta_{DNS}$, ▲ : $9\Delta_{DNS}$ and ◆ : $13\Delta_{DNS}$.

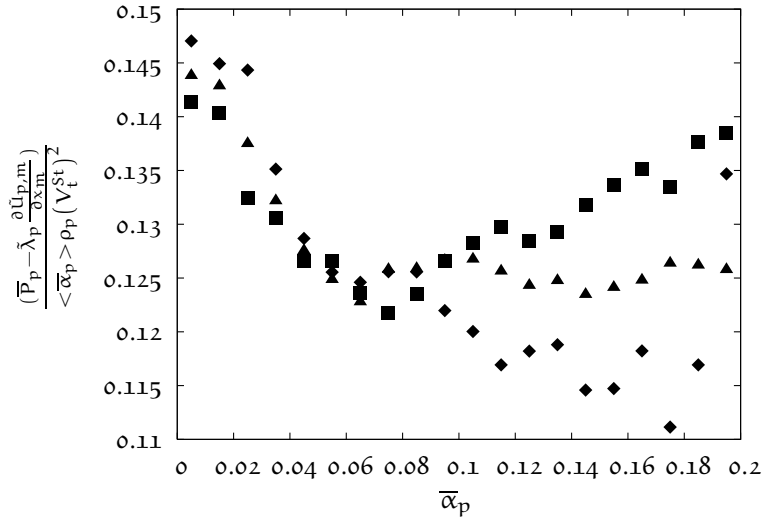


Figure 45: Resolved kinetic stress tensor trace $\bar{P}_p - \bar{\lambda}_p \frac{\partial \bar{U}_{p,m}}{\partial x_m}$ conditionally averaged by filtered volume fraction for filter widths, \blacksquare : $5\Delta_{DNS}$, \blacktriangle : $9\Delta_{DNS}$ and \blacklozenge : $13\Delta_{DNS}$.

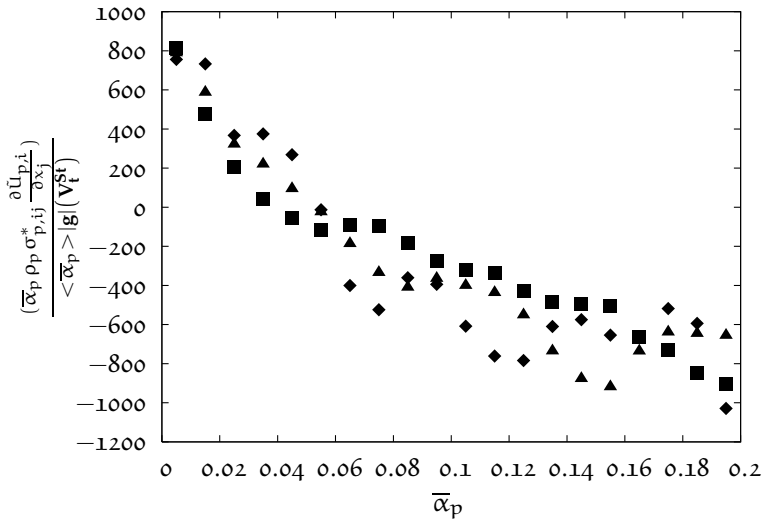


Figure 46: Sub-grid dissipation $\bar{\alpha}_p \rho_p \sigma_{p,ij}^* \frac{\partial \bar{U}_{p,i}}{\partial x_j}$ conditionally averaged by filtered volume fraction for filter widths, \blacksquare : $5\Delta_{DNS}$, \blacktriangle : $9\Delta_{DNS}$ and \blacklozenge : $13\Delta_{DNS}$.

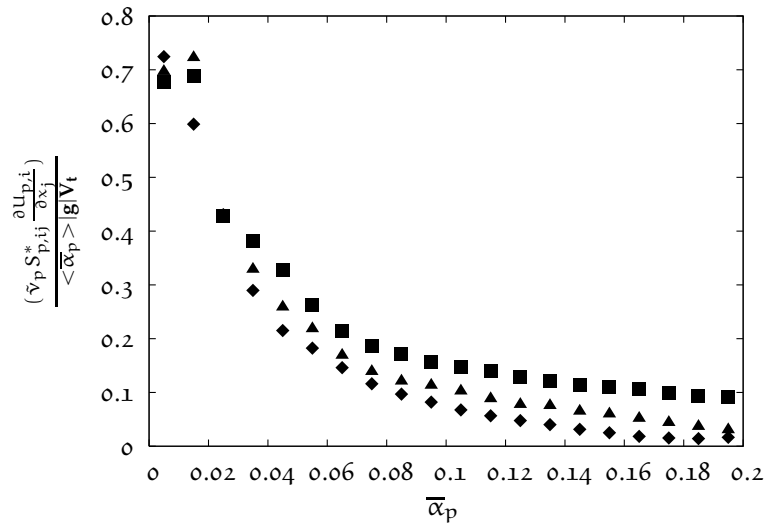


Figure 47: Resolved kinetic stress dissipation $\tilde{v}_p S_{p,ij}^* \frac{\partial u_{p,i}}{\partial x_j}$ conditionally averaged by filtered volume fraction for filter widths, ■ : $5\Delta_{DNS}$, ▲ : $9\Delta_{DNS}$ and ◆ : $13\Delta_{DNS}$.

4.5 BUDGET ANALYSIS OF THE RANDOM KINETIC ENERGY EQUATION OF PARTICULATE PHASE

By following the filtering process applied on the particle momentum equation, contributions of additional terms in the particle random kinetic energy equation are calculated for different filter widths. The average of the energy balance for particulate phase is defined as follows:

$$\begin{aligned}
0 = & \overline{\left\langle \frac{\partial}{\partial x_j} (\bar{\alpha}_p \rho_p (\tilde{K}_p^{\text{kin}} + \tilde{K}_p^{\text{coll}}) \frac{\partial \tilde{q}_p^2}{\partial x_j}) \right\rangle}^{t,n} + \overline{\left\langle \frac{\partial}{\partial x_j} (\rho_p \mathcal{K}_j) \right\rangle}^{t,n} \\
& - \overline{\left\langle \tilde{\Sigma}_{p,ij} \frac{\partial \tilde{u}_{p,j}}{\partial x_i} \right\rangle}^{t,n} - \overline{\left\langle \mathcal{V} \right\rangle}^{t,n} \\
& + \overline{\left\langle \frac{\bar{\alpha}_p \rho_p}{\tau_c} \frac{2}{3} \tilde{q}_p^2 \right\rangle}^{t,n} + \overline{\left\langle \mathcal{E} \right\rangle}^{t,n} \\
& - \overline{\left\langle 3 \frac{\bar{\alpha}_p \rho_p}{\tau_p} \frac{2}{3} \tilde{q}_p^2 \right\rangle}^{t,n} - \overline{\left\langle \mathcal{S} \right\rangle}^{t,n} \\
& - \overline{\left\langle \mathcal{Q} \right\rangle}^{t,n}
\end{aligned} \tag{4.31}$$

Eq. (4.31) states the global equilibrium of fluidized particles between the transport energy by velocity fluctuations, production and destruction of energy, interaction with the gas phase, sub-grid random kinetic energy flux. First and second terms represent the resolved and the sub-grid kinetic diffusivity. Terms in the second line are the resolved and the sub-grid contribution of the energy production by resolved particle velocity gradient. The loss of energy due to collisions on the resolved and unresolved scales are accounted by the fifth and the sixth terms. The terms in the fourth line show the resolved and sub-grid interaction of energy with gas phase. The last term is the sub-grid particle kinetic energy flux.

Figure 48 shows that the sub-grid contributions of destruction of kinetic energy by interaction with fluid and the sub-grid contribution of dissipation can be negligible. The sub-grid contribution of production is significant. For coarse grid simulation, these terms are not taken into account and this causes underestimation of production of particle kinetic energy. The rates of production is smaller for coarse grid simulations due to diminishing of non-uniformity of clustering and smaller magnitudes of velocity gradients. Agrawal et al. (2001) determined domain-averaged values of the production term and the same consequences was obtained. The sub-grid contribution of diffusivity of particle kinetic energy and the SGS kinetic energy flux can be neglected (see Fig. 49).

4.6 SUMMARY

In this part, we have obtained mesh independent Euler-Euler simulation of gas-solid flow in the periodic circulating fluidized bed. This simulation is then used to perform the budget analysis of the filtered momentum and random kinetic energy equation of

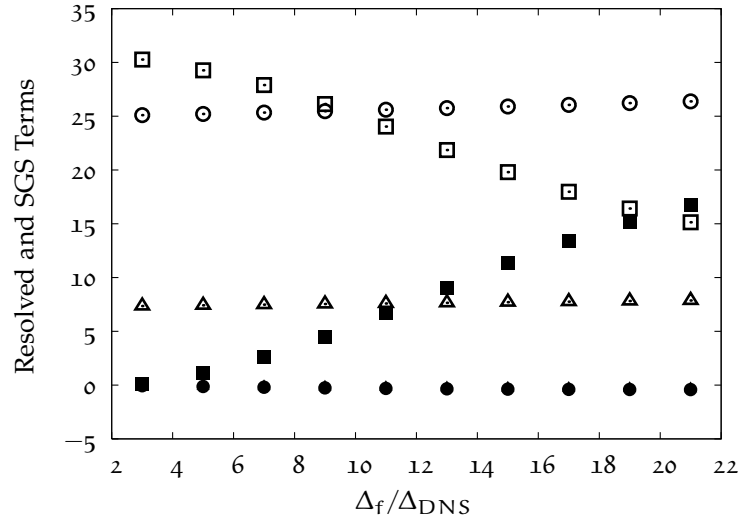


Figure 48: Resolved and sub-grid contributions of production and destruction of the particle kinetic energy for different filter widths Δ_f . Production; \square : resolved and \blacksquare : sub-grid, Destruction; \triangle : resolved and \blacktriangle : sub-grid, Interaction with fluid; \circ : resolved and \bullet : sub-grid (Normalised by $\rho_p \tau_p^{St} (V_t^{St})^2$).

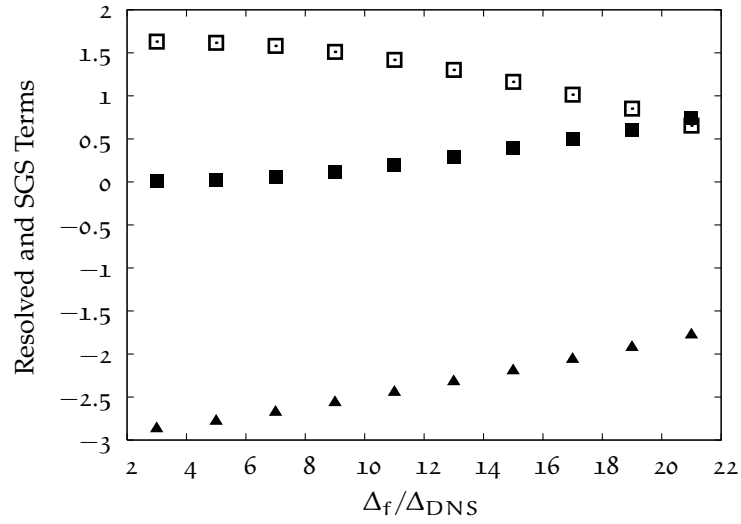


Figure 49: Resolved and sub-grid contributions of kinetic and sub-grid diffusivity for different filter widths Δ_f . Kinetic diffusivity; \square : resolved and \blacksquare : sub-grid, \blacktriangle : Sub-grid diffusivity (Normalised by $\rho_p \tau_p^{St} (V_t^{St})^2$).

particulate phase. Budget analyses show us that meso-scale structures affect the flow characteristics profoundly in particular, cancellation of these structures by coarse-grid simulations overestimate the drag force. By performing a priori tests on the mesh independent simulation results, it is pointed out that the sub-grid drift velocity has to be accounted to obtain the correct drag force. This velocity is defined as the difference between the filtered gas velocity seen by the particle phase and the resolved filtered gas velocity and has to be modelled. By the secondary effect, meso-scale structures increase the effective viscosity and normal stresses of the particulate phase. The budget analysis of the filtered random kinetic energy equation of particulate phase points out that coarse-grid simulations underestimate the production of random kinetic energy. We have briefly presented the computational time to obtain the mesh independent Euler-Euler simulation and it is unrealistic to perform this kind of fully resolved 3-D simulation of industrial applications.

PARTICULATE SUB-GRID MODEL: DERIVATION AND A PRIORI STUDIES

5.1 INTRODUCTION

The analogy can be constructed between SGS scalar flux in single phase turbulent flows and the sub-grid drift flux defined by Eq. (4.27). The modelling of the SGS scalar flux in the single phase turbulent flows is briefly presented and capability of these models are investigated to model the sub-grid contribution of the drag force. The SGS scalar flux can be possibly modelled by the Smagorinsky-type model as also referred the functional model and structural models such as; the Gradient and the Scale Similarity (Sagaut, 2004). The Smagorinsky model is based on the eddy viscosity concept and accounts for the sub-grid scale scalar flux in terms of the resolved strain-rate tensor and the scalar gradients. The Gradient model assumes that the SGS scalar flux can be modelled as a function of a tensor which is the product of the filtered scalar gradient with the filtered velocity gradient (Clark et al., 1979), as follows

$$\theta_i = C_{gr} \bar{\Delta}^2 \frac{\partial \bar{\xi}}{\partial x_j} \frac{\partial \tilde{U}_i}{\partial x_j} \quad (5.1)$$

where $\bar{\Delta}$ is the implicit filter width, C_{gr} is the proportionality constant to be determined from comparison with the DNS database, θ_i is the SGS scalar flux, \tilde{U}_j is the j component of the Favre averaged flow velocity and $\bar{\xi}$ is the averaged scalar.

The Scale Similarity model assumes that the full structure of the velocity field below $\bar{\Delta}$ is postulated to be similar to that at scales above $\bar{\Delta}$ (Bardina et al., 1983). This model introduces a second filter with a given scale $\gamma \bar{\Delta}$ with $\gamma \geq 1$. The SGS scalar flux is modelled as being proportional to the difference between the re-filtered of product of resolved velocity and scalar, and the product of the re-filtered of resolved velocity and scalar:

$$\theta_i = C_{ss} (\widehat{\xi \tilde{U}_i} - \widehat{\xi} \widehat{\tilde{U}_i}) \quad (5.2)$$

with “ $\widehat{\quad}$ ” is the second filter and C_{ss} is a given constant. The original model was proposed by Bardina et al. (1983) and γ was set to 1. Various versions of this model are proposed such as Liu et al. (1994) in which γ was set to 2. The Gradient and the Scale Similarity model can be directly applied to model the sub-grid drift flux with introducing the solid volume fraction as a scalar. However, the interactions between resolved and unresolved time-spatial scales has not been well-established in contrary to the Smagorinsky model for single phase turbulent flows, intensive correlation analyses between the sub-grid drift flux ($\bar{\alpha}_p \bar{V}_{d,i}$) and filtered variables have to be performed to prescribe unresolved drag term in terms of resolved quantities for the Smagorinsky-type sub-grid model. Evaluation

of the sub-grid drift flux models will be proceed here with a priori analyses. The mesh independent result, which has sufficient spatial resolution to allow the determination of sub-grid quantities, are filtered; the models are applied to the filtered data and then the model estimates are compared with actual values determined directly from the filtered mesh independent result. For filtering process, the volume averaging process, as given in §4.3, is applied.

The primary interest is the accuracy of the sub-grid drift flux models, which can be assessed by computing a correlation coefficient between model terms and exact calculated from mesh independent results or namely to be called DNS. The correlation coefficient r , computed as in Eq. (4.26), shows a priori predictability of basic model assumptions by quantifying the degree which the structure of $\bar{\alpha}_p \tilde{V}_{d,i}$ captured by models. Meanwhile, to quantify the statistical accuracy of the models, we define the relative error as

$$e \equiv \frac{\text{model} - \text{measured}}{\langle (\text{measured})^2 \rangle^{1/2}} \quad (5.3)$$

and the mean squared error as

$$E \equiv \frac{\langle (\text{model} - \text{measured})^2 \rangle^{1/2}}{\langle (\text{measured})^2 \rangle^{1/2}}. \quad (5.4)$$

5.2 FUNCTIONAL MODEL FOR EFFECTIVE DRAG FORCE

Correlation coefficients were calculated between $\bar{\alpha}_p \tilde{V}_{d,i}$ and filtered variables for different filter widths along mean flow direction and shown in Figure 50. It is shown that $\bar{\alpha}_p \tilde{V}_{d,z}$ is strongly related to $\bar{\alpha}_p (\tilde{U}_{g,z} - \tilde{U}_{p,z})$ for larger filter widths. For larger filter widths, we have more uniform flow structure and the gas velocity and particle volume fraction is not strongly correlated. The dependency of $\bar{\alpha}_p \tilde{V}_{d,z}$ on the variable $\bar{\alpha}_p (\tilde{U}_{g,z} - \tilde{U}_{p,z})$ with different filter widths can be seen on the scatter plots (see Figure 51). Because of visualisation difficulty of plotting all data, $\bar{\alpha}_p \tilde{V}_{d,z}$ and $\bar{\alpha}_p (\tilde{U}_{g,z} - \tilde{U}_{p,z})$ were randomly sampled.

Based on the correlation analysis on the sub-grid drag term, we propose to write the filtered drag force by modelling $\bar{\alpha}_p \tilde{V}_{d,i}$ (see also Özel et al. 2010, Parmentier 2010 and Parmentier et al. 2012) as:

$$\bar{\alpha}_p \tilde{V}_{d,i} = g_{ij}(\Delta_{sgs}, \bar{\alpha}_p) \bar{\alpha}_p (\tilde{U}_{g,j} - \tilde{U}_{p,j}) \quad (5.5)$$

where g_{ij} , the drag correction tensor, is a function of the dimensionless sub-grid length scale Δ_{sgs} and the filtered particle volume fraction. We assume that g_{ij} is diagonal ($g_{ij} = 0$ if $i \neq j$) and $g_{xx} = g_{yy} = \lambda g_{zz}$ in the specific frame where the mean flow direction (z -) is aligned with the direction of gravity. The function “ g ” can be calculated from the mesh independent result for a given flow configuration by the following relation:

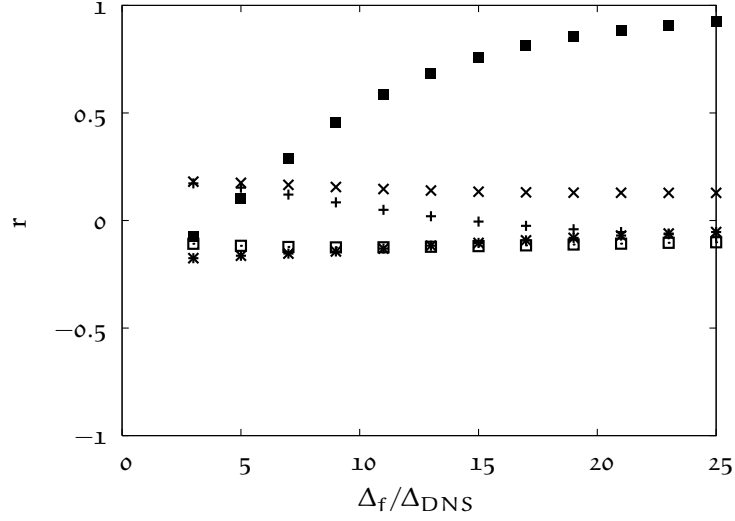


Figure 50: Correlation coefficients between the sub-grid drift flux $\bar{\alpha}_p \tilde{V}_{d,z}$ and filtered variables with respect to different filter widths Δ_f :

$$\begin{aligned}
 + : & \bar{\alpha}_p V_t, \quad \times : \tau_p^{St} (V_t^{St})^2 \frac{\partial \bar{\alpha}_p}{\partial z}, \quad * : (\tau_p^{St} V_t^{St})^2 \frac{\partial \bar{\alpha}_p}{\partial z} \frac{\partial \tilde{u}_{g,z}}{\partial z}, \\
 \square : & (\tau_p^{St} V_t^{St})^2 \frac{\partial \bar{\alpha}_p}{\partial z} \frac{\partial \tilde{u}_{p,z}}{\partial z}, \quad \blacksquare : \bar{\alpha}_p (\tilde{u}_{p,z} - \tilde{u}_{g,z}).
 \end{aligned}$$

$$g(\Delta_f/\Delta_{DNS}, \bar{\alpha}_p) = \frac{\overline{\langle \bar{\alpha}_p \tilde{V}_{d,z} | \bar{\alpha}_p \rangle}^{t,n}}{\overline{\langle [\bar{\alpha}_p (\tilde{u}_{g,z} - \tilde{u}_{p,z})] | \bar{\alpha}_p \rangle}^{t,n}}. \quad (5.6)$$

$\bar{\alpha}_p \tilde{V}_{d,z}$ and $\bar{\alpha}_p (\tilde{u}_{g,z} - \tilde{u}_{p,z})$ are conditionally averaged by the filtered solid volume fraction. We propose the model in general form as:

$$\bar{\alpha}_p \tilde{V}_{d,\beta} = K_{\beta\beta} g (\tilde{u}_{g,\beta} - \tilde{u}_{p,\beta}) \quad (5.7)$$

where $\beta = x, y, z$ and β is used to indicate that there is no implicit summation. The model constant $K_{\beta\beta}$ is case-dependent and dynamically adjusted by following the methodology of Germano et al. (1991) and Lilly (1992). Then, the effective drag term can be written as follows:

$$\frac{\bar{\alpha}_p \rho_p}{\tau_p} V_{r,\beta} = \frac{\rho_p}{\tau_p} [1 + K_{\beta\beta} g(\Delta_{sgs}, \bar{\alpha}_p)] \bar{\alpha}_p (\tilde{u}_{g,\beta} - \tilde{u}_{p,\beta}) \quad (5.8)$$

This definition is coherent with the studies of Heynderickx et al. (2004), Andrews et al. (2005), Igci et al. (2008). They introduced an effective drag coefficient β_e to express the filtered drag force term as

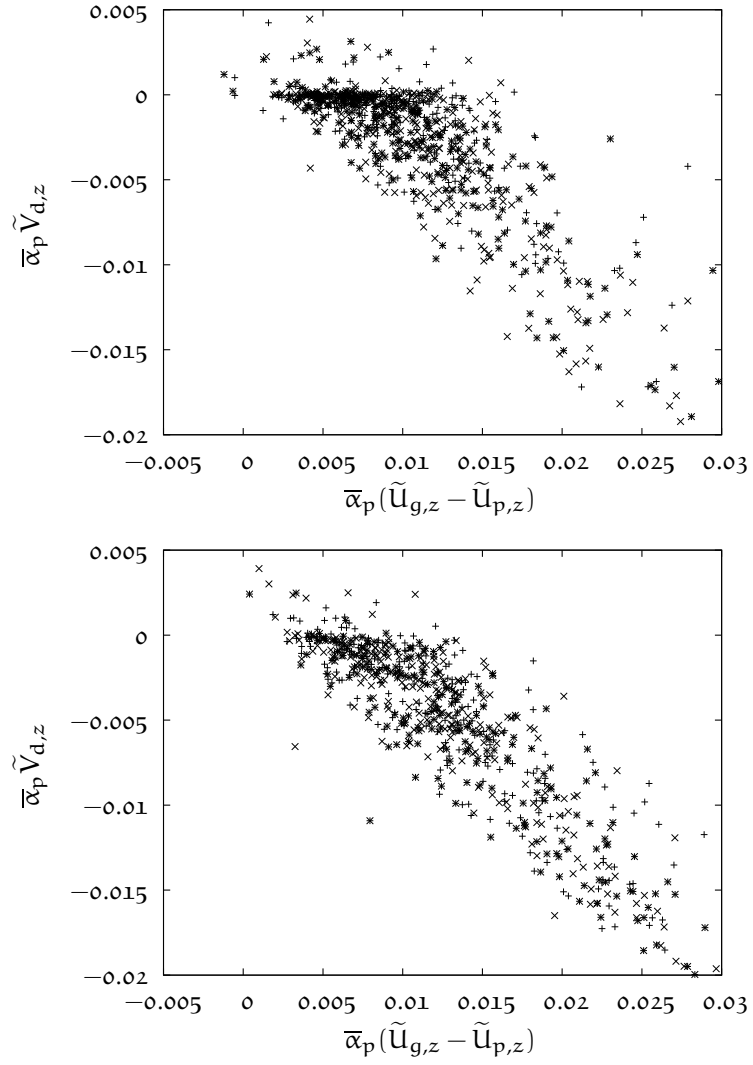


Figure 51: Scattering plot of the sub-grid drift flux $\bar{\alpha}_p \tilde{V}_{d,z}$ versus $\bar{\alpha}_p(\tilde{u}_{g,z} - \tilde{u}_{p,z})$ for intermediate and large filter width ratios (Δ_f/Δ_{DNS}): *: 7, x : 9, + : 13 (top) and *: 17, x : 21, + : 25(bottom).

$$\frac{\overline{\alpha_p \rho_p}}{\tau_p} V_{r,i} = \beta_e \left(\tilde{U}_{g,i} - \tilde{U}_{p,i} \right). \quad (5.9)$$

Heynderickx et al. (2004) and Andrews et al. (2005) write the effective drag coefficient as a function of the filtered particle volume fraction while Igci et al. (2008) suggests that this coefficient is a function of the filter width. Igci and Sundaresan (10.1021/ie200190q) proposed an extended model with a function of both the filtered volume fraction and the filter width. McKeen and Pugsley (2003), Hosseini et al. (2009) and Gao et al. (2008) suggested to use a constant scale factor for the effective drag coefficient. However, the predictability of this model based on a constant scale factor is case limited.

The calculated function “g” for different filter widths along mean flow direction are shown in Figure 52. The shape of function “g” is nearly independent of Δ_f/Δ_{DNS} , then we can decompose the function “g” as:

$$g(\Delta_f/\Delta_{DNS}, \bar{\alpha}_p) \approx f(\Delta_f/\Delta_{DNS})h(\bar{\alpha}_p) \quad (5.10)$$

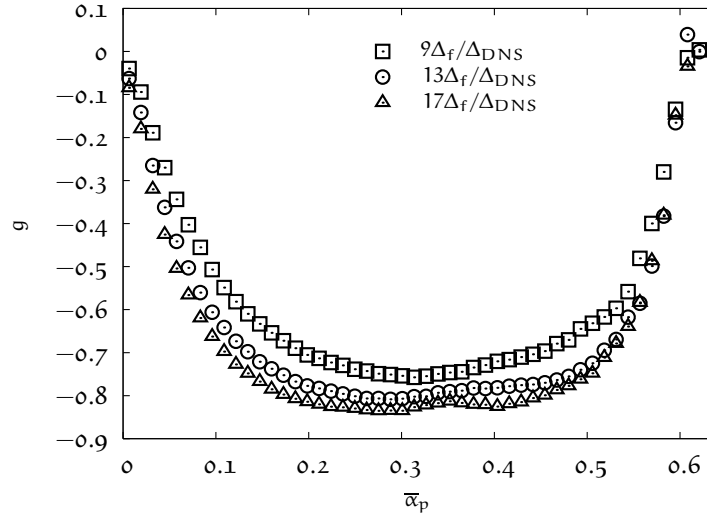


Figure 52: The function “g” for different filter size ratios: $9\Delta_f/\Delta_{DNS}$, $13\Delta_f/\Delta_{DNS}$ and $17\Delta_f/\Delta_{DNS}$.

The function “f” will be later constructed in detail. We normalised the function “g” by the area under curve for each filter width and then we propose the form for the function “h” from DNS database. The function “h” is nearly equal to zero for the values of $\bar{\alpha}_p$ greater than 0.62 and it means that the correction for drag force is not needed. For the intermediate values of $\bar{\alpha}_p$ ($0.2 < \bar{\alpha}_p < 0.4$), the function “h” reaches maximum value. Hereby, the maximum value of drag correction coefficient occurs in this interval (see Figure 53). The form suggested by (Parmentier et al., 2012) is also shown in Figure 53. It is reminded that Parmentier et al. (2012) performed the fully resolved simulation of gas-solid flow in 2-D dense fluidized bed. For the intermediate values of $\bar{\alpha}_p$ ($0.2 < \bar{\alpha}_p < 0.35$),

both functions have same values. For values $\bar{\alpha}_p$ smaller than 0.2, fully developed 3D PCFB simulation shows less drag correction. It is reasonable due to gas passing through 3D meso-scale structures which is easier than through 2-D meso-scale structures. The same manner is also discussed by Igci and Sundaresan (10.1021/ie200190q) for 2D and 3D flows in periodic domains. However, for values $\bar{\alpha}_p$ bigger than 0.4, PCFB simulation shows higher drag correction and this is unphysical. This probably occurs because of lack of enough realisations in this interval. Therefore, we propose the following modification of Parmentier et al. (2012) function "h" for $\bar{\alpha}_p$ smaller than 0.2 as

$$h(\bar{\alpha}_p) = -\tanh\left(2\frac{\bar{\alpha}_p}{0.2}\right) \sqrt{\frac{\bar{\alpha}_p}{\alpha_{p,\max}} \left(1 - \frac{\bar{\alpha}_p}{\alpha_{p,\max}}\right)^2} \left(1 - C_{h,1} \frac{\bar{\alpha}_p}{\alpha_{p,\max}} + C_{h,2} \left(\frac{\bar{\alpha}_p}{\alpha_{p,\max}}\right)^2\right) \quad (5.11)$$

with $C_{h,1}$ equal to 1.88 and $C_{h,2}$ equal to 5.16. The maximum volume fraction of solid phase $\alpha_{p,\max}$ is set to 0.64. It is shown in Figure 54.

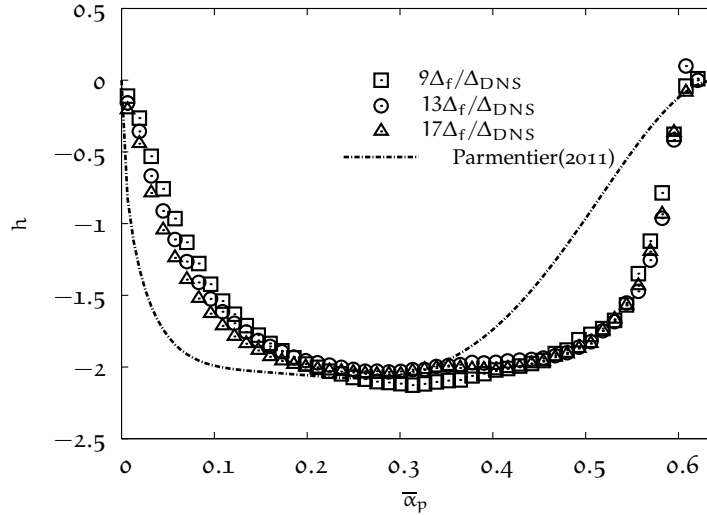


Figure 53: The function "h" for different filter size ratios: $9\Delta_f/\Delta_{DNS}$, $13\Delta_f/\Delta_{DNS}$ and $17\Delta_f/\Delta_{DNS}$.

After determination of the function "h", we calculated the function "f" which accounts for the mesh dependency. The function "f" can be evaluated by :

$$f(\Delta_{sgs}) = \frac{\overline{\langle \bar{\alpha}_p \tilde{V}_{d,z} \rangle}^{t,n}}{\overline{\langle h(\bar{\alpha}_p) \bar{\alpha}_p (\tilde{U}_{g,z} - \tilde{U}_{p,z}) \rangle}^{t,n}}. \quad (5.12)$$

By following Igci et al. (2008), it is a function of Fr_{Δ}^{-1} . The following form is proposed:

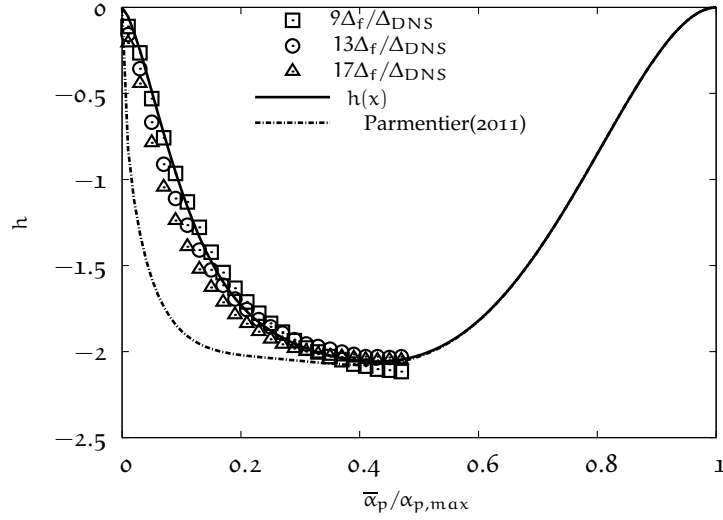


Figure 54: The proposed function “h” .

$$f(\Delta_{sgs}) = \frac{Fr_{\Delta}^{-1.6}}{a + Fr_{\Delta}^{-1.6}} \quad (5.13)$$

with $a = 0.3$. This relation is equivalent to the function proposed by Igci and Sundaresan (10.1021/ie200190q) except the constant a set to 0.4. The exact and proposed “ f ” functions are shown in Figure 55. One can expect that the clusters will not grow beyond some critical sizes and the effective drag coefficient will be independent of filter width at sufficiently large filter widths. For larger filter widths, the function “ f ” reaches a constant value which is equal to 1. Additionally, we can notice that the shape of the function “ f ” could be sensitive to the filtering method.

Dynamic Adjustment of The Model Constant, $K_{\beta\beta}$

Parmentier (2010) proposed to adjust the model constants $K_{\beta\beta}$ dynamically by using a method adapted from Germano et al. (1991) and Lilly (1992). They are dependent on both the simulated case and the direction. The idea is to estimate values of $K_{\beta\beta}$ for each cell during the simulation on a coarse grid, by performing a filtering operation of variables over neighbourhood cells. Test-level filtered function \hat{f} can be averaged over the base level function \bar{f} for three dimensional cases as:

$$\begin{aligned} \hat{f}(\mathbf{x}, t) = \frac{1}{7} & \left(\bar{f}(\mathbf{x}, t) \right. \\ & + \bar{f}(\mathbf{x} + \hat{\Delta}\mathbf{e}_x, t) + \bar{f}(\mathbf{x} - \hat{\Delta}\mathbf{e}_x, t) \\ & + \bar{f}(\mathbf{x} + \hat{\Delta}\mathbf{e}_y, t) + \bar{f}(\mathbf{x} - \hat{\Delta}\mathbf{e}_y, t) \\ & \left. + \bar{f}(\mathbf{x} + \hat{\Delta}\mathbf{e}_z, t) + \bar{f}(\mathbf{x} - \hat{\Delta}\mathbf{e}_z, t) \right) \end{aligned} \quad (5.14)$$

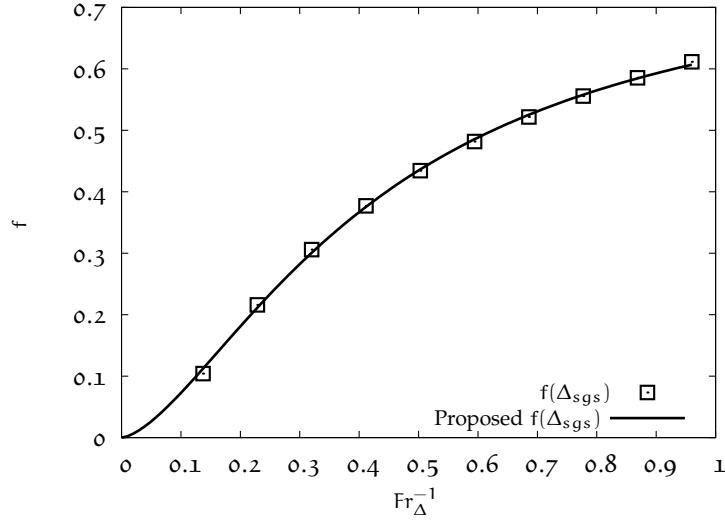


Figure 55: The function “f”.

where $\hat{\Delta}$ is the test-level filter width. Parmentier (2010) tested functions “f” and “g” at the test and the base filter level, it was stated that both function is nearly independent of the choice of the filter width. The model at the base level is given by:

$$\begin{aligned}\bar{\alpha}_p \tilde{V}_{d,\beta} &= \overline{\alpha_p (\mathbf{U}_{g,\beta} - \mathbf{U}_{p,\beta})} - \bar{\alpha}_p (\tilde{\mathbf{U}}_{g,\beta} - \tilde{\mathbf{U}}_{p,\beta}) \\ &= K_{\beta\beta} f(\Delta_{sgs}) h(\bar{\alpha}_p) \bar{\alpha}_p (\tilde{\mathbf{U}}_{g,\beta} - \tilde{\mathbf{U}}_{p,\beta})\end{aligned}\quad (5.15)$$

Consequently, one can define the sub-grid drift flux \mathcal{T}_β at test scale as:

$$\mathcal{T}_\beta = \overline{\alpha_p (\mathbf{U}_{g,\beta} - \mathbf{U}_{p,\beta})} - \hat{\alpha}_p (\hat{\mathbf{U}}_{g,\beta} - \hat{\mathbf{U}}_{p,\beta}).\quad (5.16)$$

The difference between the sub-grid drift at the test scale and the filtered sub-grid drift flux $\overline{\alpha_p \tilde{V}_{d,\beta}} = \overline{\alpha_p (\mathbf{U}_{g,\beta} - \mathbf{U}_{p,\beta})} - \bar{\alpha}_p (\tilde{\mathbf{U}}_{g,\beta} - \tilde{\mathbf{U}}_{p,\beta})$ is

$$\mathcal{L}_\beta = \mathcal{T}_\beta - \overline{\alpha_p \tilde{V}_{d,\beta}} = \overline{\alpha_p (\mathbf{U}_{g,\beta} - \mathbf{U}_{p,\beta})} - \hat{\alpha}_p (\hat{\mathbf{U}}_{g,\beta} - \hat{\mathbf{U}}_{p,\beta}).\quad (5.17)$$

\mathcal{T}_β at scale $\hat{\Delta}$ is given by

$$\mathcal{T}_\beta = K_{\beta\beta} f(\hat{\Delta}_{sgs}) h(\hat{\alpha}_p) \hat{\alpha}_p (\hat{\mathbf{U}}_{g,\beta} - \hat{\mathbf{U}}_{p,\beta}).\quad (5.18)$$

$\overline{\alpha_p \tilde{V}_{d,\beta}}$ is calculated by

$$\overline{\alpha_p \tilde{V}_{d,\beta}} = K_{\beta\beta} f(\Delta_{sgs}) h(\bar{\alpha}_p) \bar{\alpha}_p (\tilde{\mathbf{U}}_{g,\beta} - \tilde{\mathbf{U}}_{p,\beta})\quad (5.19)$$

Substitution of these expressions into Eq. (5.17) leads us the following relations:

$$\mathcal{L}_\beta \approx K_{\beta\beta} \mathcal{M}_\beta \quad (5.20)$$

where $\mathcal{M}_\beta = f(\hat{\Delta}_{sgs})h(\hat{\alpha}_p)\hat{\alpha}_p(\hat{\mathbf{U}}_{g,\beta} - \hat{\mathbf{U}}_{p,\beta}) - f(\Delta_{sgs})h(\bar{\alpha}_p)\bar{\alpha}_p(\widehat{\mathbf{U}}_{g,\beta} - \tilde{\mathbf{U}}_{p,\beta})$. We assume that the scale variance of $K_{\beta\beta}$ is negligible at two different scale levels. Then, we can have a model coefficient as

$$K_{\beta\beta} \approx \frac{\mathcal{L}_\beta}{\mathcal{M}_\beta}. \quad (5.21)$$

To avoid numerically unstable values of $K_{\beta\beta}$, we calculate **the domain averaged model coefficient** along the mean flow as follows:

$$K_{\beta\beta} \approx \frac{\langle \mathcal{L}_\beta \mathcal{M}_\beta \rangle}{\langle \mathcal{M}_\beta \mathcal{M}_\beta \rangle}. \quad (5.22)$$

In three-dimensional simulations, the model coefficients along longitudinal and transverse directions are assumed to be the same and given by following relation:

$$K_{ll} = K_{tt} = \frac{\langle \mathcal{L}_l \mathcal{M}_l + \mathcal{L}_t \mathcal{M}_t \rangle}{\langle \mathcal{M}_l^2 + \mathcal{M}_t^2 \rangle}. \quad (5.23)$$

The proposed model is constructed on the separation of the correlation of the gas velocity and the solid volume fraction by a correction which is the function of solid volume fraction, filter width and the velocity differences between phase velocities. Most of industrial applications are conducted in the channel flow and it is well known that gas-solid flow is highly anisotropic. To take into account the effect of anisotropy on the effective drag force, the dynamical adjustment proposed by Parmentier et al. (2012) are applied to calculate the model constant $K_{\beta\beta}$ depending on direction and flow. In addition, the sub-grid length scale of the model remains as an open question. Parmentier et al. (2012) proposed the mesh dependency as a function of the bed length. Herein, we proposed the model as the function of **the particle Stoke's relaxation time** and **the filter width**. Mesh independent results for different PCFB lengths are further have to be performed and proposed methodology can be applied to validate studies of the mesh dependency. It is worth noting that this model might be incapable of prediction of transient regime in the circulating fluidized beds and transient regime can not be investigated by fully developed PFBC simulations.

5.3 STRUCTURAL MODELS FOR EFFECTIVE DRAG FORCE

The proposed functional model has several parameters such as; particle properties, the solid volume fraction and the mesh size dependencies. These parameters were gathered by using a particular fluidized bed and the predictability of the proposed model may

be restricted for some applications. Because of this reason, we look for an alternative method which leads to some structural models. As has already been said, the interactions between resolved and unresolved time-spatial scales has not been well-established and for structural models, it is not needed to have prior knowledge of the nature of the interactions between the sub-grid scales (Sagaut, 2004).

5.3.1 Germano's Decomposition

The sub-grid drift flux $\bar{\alpha}_p \tilde{V}_{d,i}$ can be decomposed by Germano's decomposition (Germano, 1986):

$$\bar{\alpha}_p \tilde{V}_{d,i} = \mathcal{L}_i + \mathcal{C}_i + \mathcal{R}_i \quad (5.24)$$

where Leonard \mathcal{L}_i , Cross \mathcal{C}_i and Reynolds \mathcal{R}_i terms are defined by the following equations:

$$\mathcal{L}_i = \overline{\bar{\alpha}_p \tilde{U}_{g,i}} - \bar{\alpha}_p \tilde{\tilde{U}}_{g,i} \quad (5.25)$$

$$\mathcal{C}_i = \overline{\bar{\alpha}_p U''_{g,i}} - \bar{\alpha}_p \tilde{U}''_{g,i} + \overline{\alpha'_p \tilde{U}_{g,i}} - \bar{\alpha}'_p \tilde{\tilde{U}}_{g,i} \quad (5.26)$$

$$\mathcal{R}_i = \overline{\alpha'_p U''_{g,i}} - \bar{\alpha}'_p \tilde{U}''_{g,i} \quad (5.27)$$

with the fluctuation of volume fraction $\alpha'_p = \alpha_p - \bar{\alpha}_p$ and the fluctuation of the gas velocity $U''_{g,i} = U_{g,i} - \tilde{U}_{g,i}$. The averages of decompositions along the mean flow direction are shown in Figure 56. Leonard stresses are good approximations for $\bar{\alpha}_p \tilde{V}_{d,z}$ up to the filter size equal to $5\Delta_{DNS}$. Between the filter sizes $5\Delta_{DNS}$ and $10\Delta_{DNS}$, $\bar{\alpha}_p \tilde{V}_{d,z}$ can be represented by the sum of Leonard and Cross terms and Reynolds stresses are negligible. However, Reynolds stresses become main contribution of $\bar{\alpha}_p \tilde{V}_{d,z}$ for intermediate and larger filters ($\Delta_f > 10 \Delta_{DNS}$). If the filter size is greater than $20\Delta_{DNS}$, $\langle \mathcal{L}_z + \mathcal{C}_z \rangle$ reaches constant values and $\langle \mathcal{R}_z \rangle$ increases linearly. Figure 57 shows Reynolds stresses along mean flow and radial directions. Reynolds stresses along mean flow direction are one order greater than those of radial directions. Parmentier (2010) performed a Taylor expansion of the sub-grid drift flux $\bar{\alpha}_p \tilde{V}_{d,i}$ given by following equation:

$$\bar{\alpha}_g \bar{\alpha}_p \tilde{V}_{d,i} = \frac{\bar{\Delta}^2}{12} \frac{\partial \alpha_p}{\partial x_j} \frac{\partial U_{g,i}}{\partial x_j} \quad (5.28)$$

1/12 is theoretical value and varies depending on filter type. The derivation in this study is carried out by expanding series with taking into account high order terms (for details, see A.1). The sub-grid drift flux $\bar{\alpha}_p \tilde{V}_{d,i}$ can be modelled by

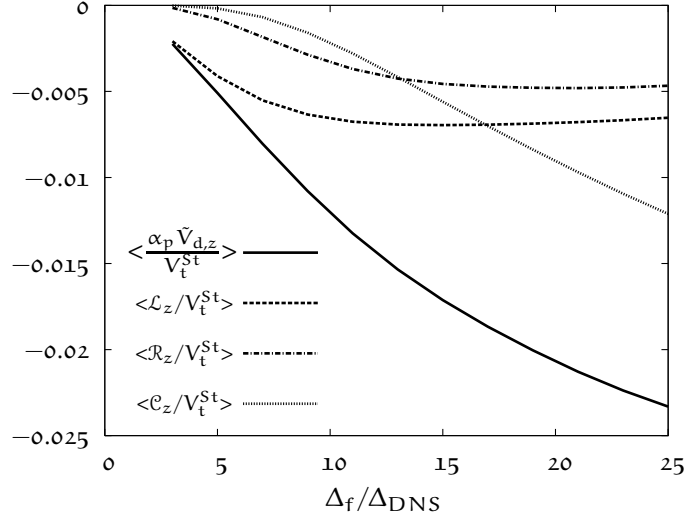


Figure 56: Averaged Germano's decomposition terms along the mean flow direction for different filter widths Δ_f .

$$\bar{\alpha}_p \tilde{V}_{d,i} = \frac{\bar{\Delta}^2}{12} \frac{\partial \alpha_p}{\partial x_j} \frac{\partial U_{g,i}}{\partial x_j} - \frac{\bar{\Delta}^4}{576} \frac{\partial^2 \alpha_p}{\partial x_j \partial x_k} \frac{\partial^2 U_{g,i}}{\partial x_j \partial x_k} + \mathcal{O}(\bar{\Delta}^6). \quad (5.29)$$

The combination of Leonard \mathcal{L}_i and cross-terms \mathcal{C}_i leads to the first term at the right-hand side:

$$\mathcal{L}_i + \mathcal{C}_i = \frac{\bar{\Delta}^2}{12} \frac{\partial \alpha_p}{\partial x_j} \frac{\partial U_{g,i}}{\partial x_j}. \quad (5.30)$$

Eq. (5.30) is referred to as the gradient model proposed by Clark et al. (1979). The sub-grid Reynolds term \mathcal{R}_i appears only as fourth-order term:

$$\mathcal{R}_i = \frac{\bar{\Delta}^4}{576} \frac{\partial^2 \alpha_p}{\partial x_j \partial x_k} \frac{\partial^2 U_{g,i}}{\partial x_j \partial x_k}. \quad (5.31)$$

5.3.2 Gradient Model (Tensor Diffusivity Model)

By neglecting the fourth-order term, the drift flux can be modelled by the following equation:

$$\bar{\alpha}_p \tilde{V}_{d,i} = A_{jk} \Delta^2 \frac{\partial \bar{\alpha}_p}{\partial x_j} \frac{\partial \tilde{U}_{g,i}}{\partial x_k}. \quad (5.32)$$

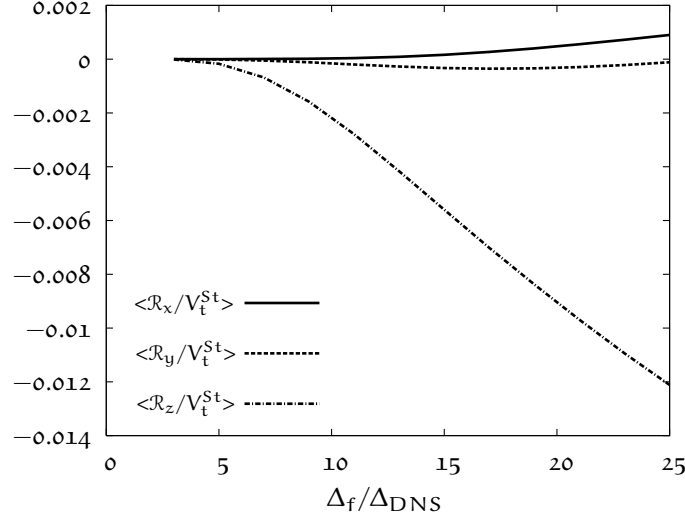


Figure 57: Averaged Reynolds terms along mean flow, transverse and longitudinal directions for different filter widths Δ_f .

A_{jk} is a second-order tensor based on filter type and the ratio between implicit filter and grid size $\bar{\Delta}/\Delta$. This model shows good performance in terms of correlation coefficient, because it represents the first term in the Taylor series expansion. It is assumed that A_{jk} is diagonal ($A_{jk} = 0$ if $j \neq k$) and $A_{xx} = A_{yy} = \lambda A_{zz}$ in the specific frame where the mean flow direction (z -) is aligned with the direction of gravity acceleration. We propose the Gradient model in general form as:

$$\bar{\alpha}_p \tilde{V}_{d,\beta} = A_{\beta\beta} \Delta^2 \frac{\partial \bar{\alpha}_p}{\partial x_j} \frac{\partial \tilde{U}_{g,\beta}}{\partial x_j}. \quad (5.33)$$

where $\beta = x, y, z$ and β is used to indicate that there is no implicit summation. The model coefficients were determined using a least-squares method from DNS database. The model coefficient A_{zz} for mean flow direction is close the theoretical value, $1/12$ (see Figure 58). In contrary, model coefficients for transverse and longitudinal directions linearly increase by filter width.

Vreman et al. (1996) investigated the Gradient model for the turbulent stress tensor in order to be applicable for compressible turbulent flows. It was yielded that the model rises instabilities for a weakly compressible turbulent temporal mixing layer and leads to a blowup in calculations. Vreman et al. (1996) performed a linear stability analysis of the Burger's equation supplemented by the Gradient model to clarify the nature of the instability and showed that the growth-rate of the instability is infinite. Eyink (2006) pointed out that the deconvolution operator to re-build unresolved scales by resolved field is unbounded in the natural function space for velocity and scalar fields. Vreman et al. (1996) added the eddy-viscosity part to stabilise the model. By following section, we present the extension of this model by resolving full tensor. Another reason to extended the model is the $\mathcal{O}(\Delta^4)$ term is not small. For rapidly fluctuating variables, such as the

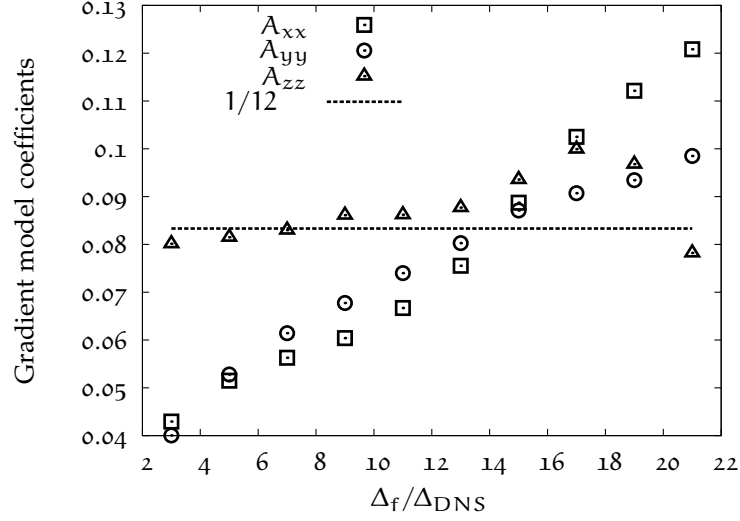


Figure 58: Gradient model coefficients $A_{\beta\beta}$ along mean, transverse and longitudinal directions for different filter widths Δ_f .

solid volume fraction, this term can not simply omitting. As shown in Figure 56, Reynolds stress of SGS solid volume fraction flux is dominant for large filter widths, so we have to taken into account this term. The challenging part of modelling is that we can not propose a dissipation part as done for turbulence energy cascade. For the numerical point of view, the rest-term is preferred to be $\mathcal{O}(\Delta^4)$ but in practice, the rest term is evaluated by $\mathcal{O}(\Delta^2)$ when the numerical scheme produces the same order errors, which is the case for second-order accurate schemes.

5.3.3 Full Tensor Model

Due to consequences of Germano decomposition (Fig. 56), it was pointed out that Reynolds terms are significant for large filter widths. The Gradient model does not take into account this term by assuming that resolution of Leonard and Cross terms is sufficient for modelling of sub-grid contribution to drag force. Following the analytical expansion, the drift flux can be modelled as

$$\bar{\alpha}_p \tilde{V}_{d,i} = B_{jk} \Delta^2 \frac{\partial \bar{\alpha}_p}{\partial x_j} \frac{\partial \tilde{u}_{g,i}}{\partial x_k} + C_{jklm} \Delta^4 \frac{\partial^2 \bar{\alpha}_p}{\partial x_j \partial x_k} \frac{\partial^2 \tilde{u}_{g,i}}{\partial x_l \partial x_m}. \quad (5.34)$$

B_{jk} is a second-order tensor and C_{jklm} is the fourth-order tensor and they are based on filter type and the ratio between implicit filter and grid size $\bar{\Delta}/\Delta$. We assume that B_{jk} and C_{jklm} are diagonal tensors and the full tensor model in general form can given by

$$\bar{\alpha}_p \tilde{V}_{d,\beta} = B_{\beta\beta} \Delta^2 \frac{\partial \bar{\alpha}_p}{\partial x_j} \frac{\partial \tilde{u}_{g,\beta}}{\partial x_j} + C_{\beta\beta} \Delta^4 \frac{\partial^2 \bar{\alpha}_p}{\partial x_j \partial x_k} \frac{\partial^2 \tilde{u}_{g,\beta}}{\partial x_j \partial x_k}. \quad (5.35)$$

where $\beta = x, y, z$ and β is used to indicate that there is no implicit summation.

The constants $B_{\beta\beta}$ and $C_{\beta\beta}$ can be determined by performing the multi-variate linear regression. Let \mathcal{E}_i be the error in Eq. (5.35)

$$\mathcal{E}_\beta = \sqrt{\bar{\alpha}_p \tilde{V}_{d,\beta} - (B_{\beta\beta} \Delta^2 \mathcal{M}_\beta + C_{\beta\beta} \Delta^4 \mathcal{N}_\beta)} \quad (5.36)$$

where $\mathcal{M}_\beta = \frac{\partial \bar{\alpha}_p}{\partial x_j} \frac{\partial \tilde{u}_{g,\beta}}{\partial x_j}$ and $\mathcal{N}_\beta = \frac{\partial^2 \bar{\alpha}_p}{\partial x_j \partial x_k} \frac{\partial^2 \tilde{u}_{g,\beta}}{\partial x_j \partial x_k}$. $B_{\beta\beta}$, $C_{\beta\beta}$ can be obtained by setting $\partial \mathcal{E}_\beta / \partial \mathcal{M}_\beta = 0$ and $\partial \mathcal{E}_\beta / \partial \mathcal{N}_\beta = 0$.

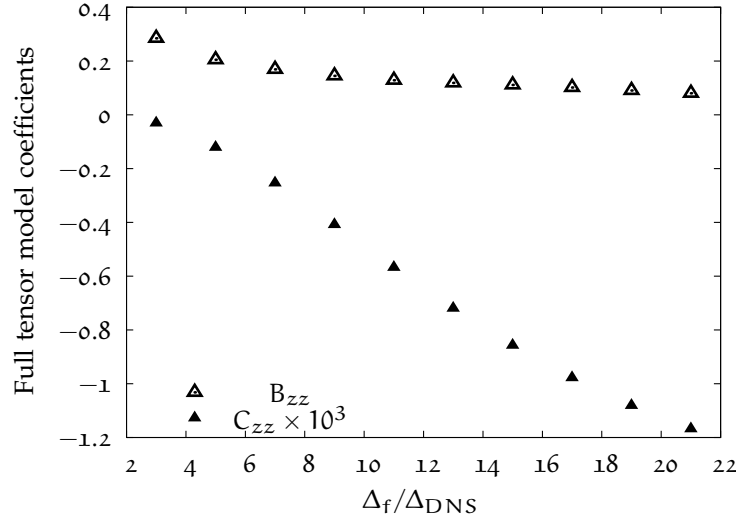


Figure 59: Full Tensor model coefficients B_{zz} and C_{zz} along the mean flow direction for different filter widths Δ_f .

The coefficients along mean flow direction B_{zz} and C_{zz} are shown in Figure 59. As expected, values of C_{zz} are very small compared with the B_{zz} , especially for small filter widths. The constant B_{zz} is independent for filter widths. C_{zz} is negative and increases dramatically by filter widths.

5.3.4 Mixed Model

In 5.2, we revealed that $\bar{\alpha}_p \tilde{V}_{d,i}$ can be predicted by $\bar{\alpha}_p (\tilde{u}_{g,i} - \tilde{u}_{p,i})$ for large filter widths. Afterwards, the structural gradient model was proposed and it was stated that the Gradient model predicts $\bar{\alpha}_p \tilde{V}_{d,i}$ in correct manner based on theoretical representations of Leonard and Cross terms for small filter widths. Herein, we present the Mixed model which can be constructed to take advantages of the both model. The residue of $\bar{\alpha}_p \tilde{V}_{d,i}$, which represents Reynolds terms, can be modelled by the functional model as

$$\bar{\alpha}_p \tilde{V}_{d,\beta} = D_{\beta\beta} \Delta^2 \frac{\partial \bar{\alpha}_p}{\partial x_j} \frac{\partial \tilde{u}_{g,\beta}}{\partial x_j} + E_{\beta\beta} h(\bar{\alpha}_p) \bar{\alpha}_p (\tilde{u}_{g,\beta} - \tilde{u}_{p,\beta}). \quad (5.37)$$

where $\beta = x, y, z$ and β is used to indicate that there is no implicit summation. D_{zz} and E_{zz} are shown in Figure 60. D_{zz} is independent of filter width and close to the theoretical value $1/12$. E_{zz} can be written by the function $f(\Delta_{sgs})$.

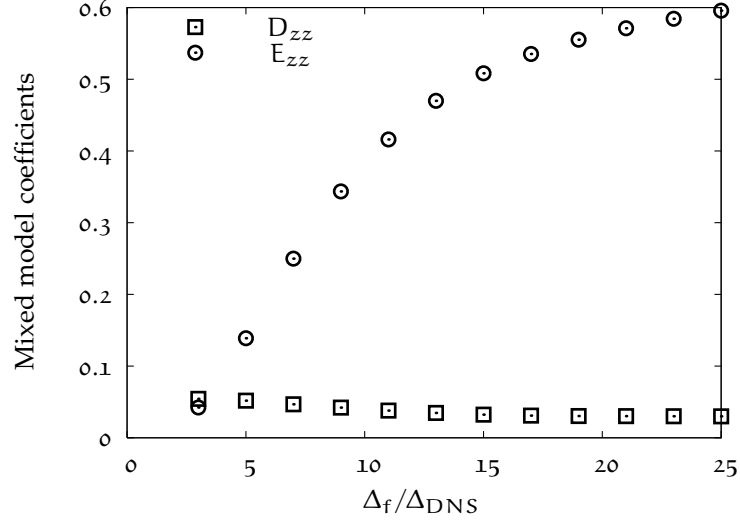


Figure 60: Mixed model coefficients D_{zz} and E_{zz} along the mean flow for different filter widths Δ_f .

We formulate the following relation in order to obtain the Dynamic Mixed model:

$$\bar{\alpha}_p \tilde{V}_{d,\beta} = \frac{\Delta^2}{12} \frac{\partial \bar{\alpha}_p}{\partial x_j} \frac{\partial \tilde{U}_{g,\beta}}{\partial x_j} + K_{\beta\beta} \frac{Fr_\Delta^{-1.6}}{0.3 + Fr_\Delta^{-1.6}} h(\bar{\alpha}_p) \bar{\alpha}_p (\tilde{U}_{g,\beta} - \tilde{U}_{p,\beta}). \quad (5.38)$$

The model constant of gradient part is assumed to be equal to the theoretical value $1/12$ along all directions. This assumption is a good approximation as shown in Figure 58. With this assumption, we do not need to perform second test filter to calculate the constant for the gradient part. In order to obtain an expression for $K_{\beta\beta}$, the similar procedure can be performed as given for the dynamic functional model. One can define the drift flux $\mathcal{T}_{\beta\beta}$ at test scale as:

$$\mathcal{T}_\beta = \frac{(\kappa \hat{\Delta})^2}{12} \frac{\partial \hat{\alpha}_p}{\partial x_j} \frac{\partial \hat{U}_{g,\beta}}{\partial x_j} + K_{\beta\beta} \frac{Fr_\Delta^{-1.6}}{0.3 + Fr_\Delta^{-1.6}} h(\hat{\alpha}_p) \hat{\alpha}_p (\hat{U}_{g,\beta} - \hat{U}_{p,\beta}). \quad (5.39)$$

The difference between the drift flux at the test scale and the filtered drift flux is

$$\begin{aligned} \mathcal{L}_\beta &= \mathcal{T}_\beta - \widehat{\bar{\alpha}_p \tilde{V}_{d,\beta}} \\ &= \bar{\alpha}_p (\widehat{\tilde{U}_{g,\beta} - \tilde{U}_{p,\beta}}) - \hat{\alpha}_p (\hat{U}_{g,\beta} - \hat{U}_{p,\beta}). \end{aligned} \quad (5.40)$$

$\widehat{\bar{\alpha}_p \tilde{V}_{d,\beta}}$ is calculated by

$$\overline{\alpha_p} \tilde{V}_{d,\beta} = \frac{\Delta^2}{12} \frac{\partial \widehat{\overline{\alpha_p}}}{\partial x_j} \frac{\partial \widehat{\tilde{U}}_{g,\beta}}{\partial x_j} + K_{\beta\beta} \frac{Fr_{\Delta}^{-1.6}}{0.3 + Fr_{\Delta}^{-1.6}} \widehat{h(\overline{\alpha_p}) \overline{\alpha_p}} (\tilde{U}_{g,\beta} - \tilde{U}_{p,\beta}). \quad (5.41)$$

Substitution of these expressions into Eq. (5.40) leads us to $\mathcal{L}_{\beta} \approx \mathcal{H}_{\beta} + K_{\beta\beta} \mathcal{M}_{\beta}$ where

$$\mathcal{M}_{\beta} = -\frac{Fr_{\Delta}^{-1.6}}{0.3 + Fr_{\Delta}^{-1.6}} h(\widehat{\overline{\alpha_p}}) \widehat{\overline{\alpha_p}} (\widehat{\tilde{U}}_{g,\beta} - \widehat{\tilde{U}}_{p,\beta}) + \frac{Fr_{\Delta}^{-1.6}}{0.3 + Fr_{\Delta}^{-1.6}} \widehat{h(\overline{\alpha_p}) \overline{\alpha_p}} (\tilde{U}_{g,\beta} - \tilde{U}_{p,\beta}) \quad (5.42)$$

and

$$\mathcal{H}_{\beta} = \frac{(\kappa\Delta)^2}{12} \frac{\partial \widehat{\overline{\alpha_p}}}{\partial x_j} \frac{\partial \widehat{\tilde{U}}_{g,\beta}}{\partial x_j} - \frac{\Delta^2}{12} \frac{\partial \widehat{\overline{\alpha_p}}}{\partial x_j} \frac{\partial \widehat{\tilde{U}}_{g,\beta}}{\partial x_j}. \quad (5.43)$$

We assume that the scale variance of $K_{\beta\beta}$ is negligible at two different scale level and κ is equal to $\sqrt{5}$ by following Lilly (1992). Then, **the domain averaged model coefficient** is calculated by

$$K_{\beta\beta} = \frac{\langle (\mathcal{L}_{\beta} - \mathcal{H}_{\beta}) \mathcal{M}_{\beta} \rangle}{\langle \mathcal{M}_{\beta} \mathcal{M}_{\beta} \rangle}. \quad (5.44)$$

The model coefficients along the longitudinal and transverse directions are given by Eq. (5.23).

5.3.5 Dynamic Structure Model

In this part, we attempt to propose a new class of sub-grid scale model for the drift flux. The proposed model uses the sub-grid scalar variance as a part of the scaling factor and an extrapolation of small-scale statistics is given to the knowledge of large-scale fields. The following model is proposed

$$\overline{\alpha_p} \tilde{V}_{d,i} = -C_{sgs} \frac{\overline{\alpha_p \alpha_p} - \overline{\alpha_p} \overline{\alpha_p}}{\overline{\alpha_p}^2} \overline{\alpha_p} (\tilde{U}_{g,i} - \tilde{U}_{p,i}) \quad (5.45)$$

where $\overline{\alpha_p \alpha_p} - \overline{\alpha_p} \overline{\alpha_p}$ is the sub-grid variance of α_p on the grid level. The sub-grid scalar variance also referred to as the scalar mixedness since it measures the degree of local non homogeneity of solid volume fraction within the characteristic length. First, we calculated the correlation coefficient between the drift flux and the dynamic structure model. Results will be shown in the next section. The model constant ranges from 1.5 to 0.8. The sub-grid scalar can not get from the resolved field and we need a closure term or an additional transport equation for the sub-grid variance.

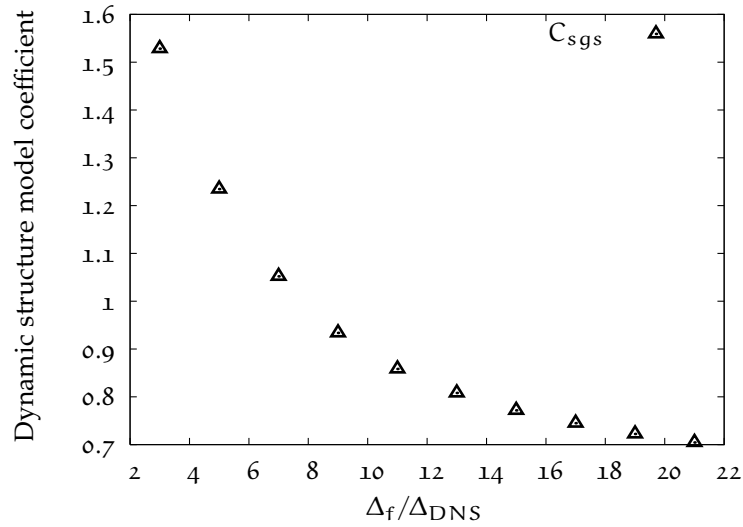


Figure 61: Dynamic Structure model coefficient C_{sgs} along the mean flow for different filter widths Δ_f .

5.4 A PRIORI ANALYSES OF EFFECTIVE DRAG MODELS' PREDICTABILITY

As a structural test of the models, r_i is computed as the correlation between the measured drift flux and the models predictions. Figure 62 shows correlation coefficients between the Smagorinsky-type, the Gradient, the Mixed, the Full Tensor, the Dynamic Structure models and the measured drift flux for different filter widths along the x -direction. The Full Tensor model shows the poorest performance with very low correlation coefficients ($-0.2 < r_x < 0.2$) while the Gradient model provides higher correlations (≈ 0.4). Correlation coefficients provided by the Smagorinsky-type, the Mixed and the Dynamic structure models are moderate (≈ 0.5) for small filter widths. For large filter widths, performances of these models are improved (≈ 0.6). Figure 63 shows correlation coefficients for the models for different filter widths along y -directions. Predictabilities of models are as similar as along the x -direction. Figure 64 shows correlation coefficients for the models for different filter widths along z -direction. The Gradient model shows moderate performance (≈ 0.5) for small filter widths. However, the correlations coefficients provided by the Gradient model is getting smaller by increasing of filter width. For large filter widths, correlation coefficients are around 0.3. It was expected that Reynolds stresses are dominant for large filter widths and the Gradient model cancels out these contributions. In order to improve the predictability of the Gradient model, Reynolds stresses modelled by high-order derivatives were introduced by the the Full Tensor model. We can not see any improvement in terms of correlation coefficients. The Dynamic Structure model provides higher correlations (≈ 0.8) independent of filter widths as the Smagorinsky-type and the Mixed models provide moderate correlation coefficients (≈ 0.6) for small filter sizes and high correlation coefficients (≈ 0.8) for intermediate and large filter widths.

Figure 65 shows pdfs of relative error of the drift flux, defined as in (5.3), for all the models along the mean flow direction with filter width $\Delta_f = 11\Delta_{DNS}$. The consistent

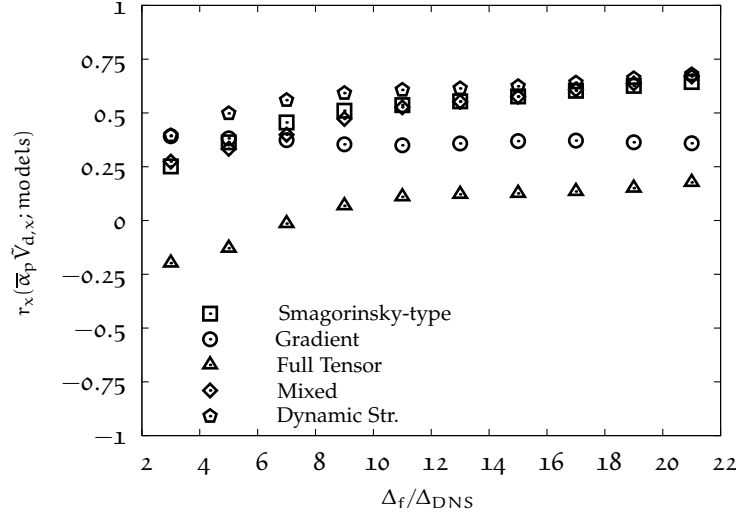


Figure 62: Correlation coefficients r_x between the x -component of measured and modelled $\bar{\alpha}_p \tilde{V}_{d,\beta}$ for different filter widths Δ_f . The test filter width is $\tilde{\Delta} = \sqrt{5}\Delta_f$.

shape of pdfs for the Smagorinsky-type, the Gradient, the Mixed and the Dynamic structure models were obtained. Statistically, these models predict comparable magnitudes of the drift flux. The pdf of relative error for the Smagorinsky-type model shows that there is a mismatch with the drift flux due the pick not settled at zero.

Figure 66 shows pdfs of relative error of effective drag correction g , defined as in Eq. (5.10), for all the models along the mean flow direction with the filter width $\Delta_f = 11\Delta_{DNS}$. The Smagorinsky-type and the Dynamic Structure models can predict the correction very well along the mean direction.

The mean squared errors E_i , calculated as in Eq. (5.4), are shown in Figures 67-69. The Full Tensor model was found to have the highest mean squared error for all filter widths and all directions while the Dynamic structure model had the lowest values for radial directions. The Smagorinsky-type model had the lowest mean squared error along the mean flow direction.

5.5 PARTICLE SGS STRESS TENSOR MODELS

The particle sub-grid stress tensor $\sigma_{p,ij}^{sgs}$ is defined in the filtered momentum equation of disperse phase as:

$$-\frac{\partial}{\partial x_j} \bar{\alpha}_p \rho_p \sigma_{p,ij}^{sgs} = -\frac{\partial}{\partial x_j} \bar{\alpha}_p \rho_p (\widetilde{u_{p,i} u_{p,j}} - \tilde{u}_{p,i} \tilde{u}_{p,j}) \quad (5.46)$$

A priori test on SGS stress tensor shows us that sub-grid correlated energy and dissipation have to be modelled. The particle sub-grid stress tensor $\sigma_{p,ij}^{sgs}$ can be divided into deviatoric and spherical parts. Smagorinsky (1963) model can be proposed for the

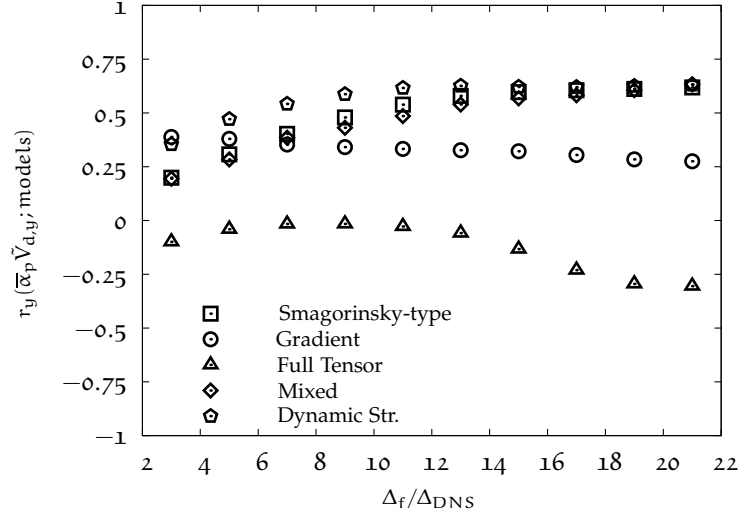


Figure 63: Correlation coefficients r_y between the y-component of measured and modelled $\bar{\alpha}_p \tilde{V}_{d,\beta}$ for different filter widths Δ_f . The test filter width is $\hat{\Delta} = \sqrt{5}\Delta_f$.

anisotropic parts of stresses and Yoshizawa (1986) model can be used for the trace of stress tensor as follows:

$$\bar{\alpha}_p \sigma_{p,ij}^{sgs} = \bar{\alpha}_p \sigma_{p,ij}^* + \bar{\alpha}_p \frac{1}{3} \sigma_{p,kk} \delta_{ij} \quad (5.47)$$

$$= -\bar{\alpha}_p C_s^2 \Delta^2 |\tilde{\mathcal{S}}_p^*| \tilde{\mathcal{S}}_{p,ij}^* + \bar{\alpha}_p \frac{2}{3} \sigma_{p,SGS} \delta_{ij} \quad (5.48)$$

with the trace of stress tensor $\sigma_{p,SGS}$ predicted by $\sigma_{p,SGS} = C_Y \Delta^2 |\tilde{\mathcal{S}}_p^*|^2$ and $\tilde{\mathcal{S}}_{p,ij}^*$ the trace free strain rate tensor of the filtered particle velocity and given by

$$\tilde{\mathcal{S}}_{p,ij}^* = \frac{\partial \tilde{U}_{p,i}}{\partial x_j} + \frac{\partial \tilde{U}_{p,j}}{\partial x_i} - \frac{2}{3} \frac{\partial \tilde{U}_{p,k}}{\partial x_k} \delta_{ij}. \quad (5.49)$$

$|\tilde{\mathcal{S}}_p^*|$ is the norm of $\tilde{\mathcal{S}}_{p,ij}^*$ and defined by $|\tilde{\mathcal{S}}_p^*|^2 = 1/2 \tilde{\mathcal{S}}_{p,ij}^* \tilde{\mathcal{S}}_{p,ij}^*$.

Assessment of Smagorinsky and Yoshizawa Models

The assessment of model is carried out on the tensor and the scalar level. At scalar level, sub-grid tensor is multiplied by the gradient of filtered particle velocities. Correlation coefficients between the deviatoric part of the filtered particle sub-grid stress tensor $\sigma_{p,zj}^*$ and Smagorinsky model are shown in Figure 70. The Smagorinsky model performs low performance in terms of correlation coefficients ($r \sim 0.2$) on the tensor level. It is well established the dissipation characteristics of Smagorinsky model, thereby correlation coefficients between the product of the deviatoric part of tensor by the gradients of filtered particles velocities and of the Smagorinsky model prediction are also presented (see Fig-

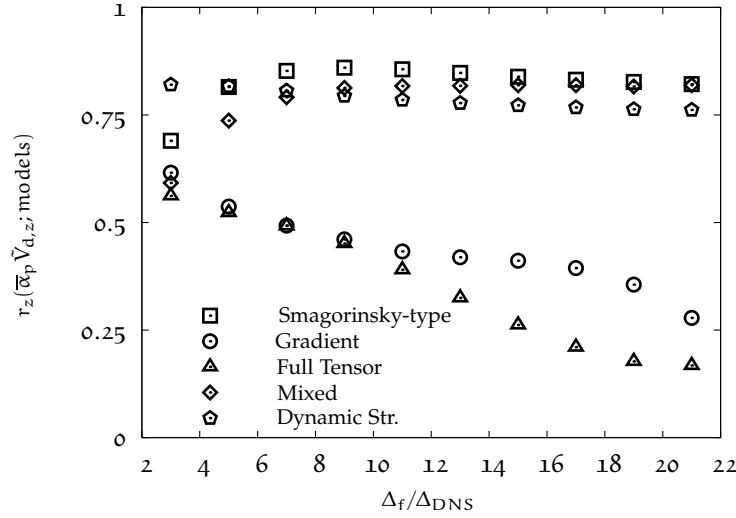


Figure 64: Correlation coefficients r_z between the z -component of measured and modelled $\overline{\alpha}_p \tilde{V}_{d,\beta}$ for different filter widths Δ_f . The test filter width is $\tilde{\Delta} = \sqrt{5}\Delta_f$.

ure 70). The model on the scalar level shows better performance than of the tensor level ($r \sim 0.4$).

In Figure 71, correlation coefficients between the particle sub-grid energy $\sigma_{p,SGS}$ and predictions by Yoshizawa model are shown. The Yoshizawa model predicts very well compression stress of particle phases and correlation coefficients are really high for tensor level. For scalar level, correlation coefficients are up to 0.95 even for larger filter sizes.

PDFs of the sub-grid energy and dissipation are compared with the predictions of viscosity models (Smagorinsky, Yoshizawa model) are shown in Figures 73 and 72. The Yoshizawa model overestimates the level of the sub-grid energy at its lows values, this poor prediction can be seen easily for filter size equal to 15Δ . The PDF of sub-grid dissipation $\sigma_{p,zj}^* \frac{\partial \tilde{u}_{p,zj}}{\partial x_j}$ has some negative values which represents the backscatter effect. However, the Smagorinsky model is not be able to resolve this backscatter as well known and underestimation of dissipation occurs for every filter sizes consistent with correlation coefficients as previously shown.

The viscosity model constants C_s (Smagorinsky part) and C_γ (Yoshizawa part) calculated from DNS results by least square method are shown in Figure 74. C_s was calculated by following the procedure for the dynamic Smagorinsky model Germano et al. (1991) for single phase turbulent flow along the homogeneous direction. C_s is smaller than of single phase flow model constants ($[0.1 : 0.2]$ for homogeneous isotropic turbulence, 0.079 channel flow). C_γ are independent for small and intermediate filter sizes can be evaluated to be 0.05 approximately. For large filter widths, C_γ linearly increases. Moreau et al. (2009) estimated 0.051 from DNS simulation of homogeneous isotropic turbulence in the frame of the mesoscopic Eulerian approach. However, it is quite higher than previous works as making comparison with single phase turbulent flow. Erlebacher et al. (1992) have performed direct simulations of compressible homogeneous turbulence at different Mach numbers ranging from 0.1 to 0.6 with Yoshizawa model and they evaluated C_γ equal to

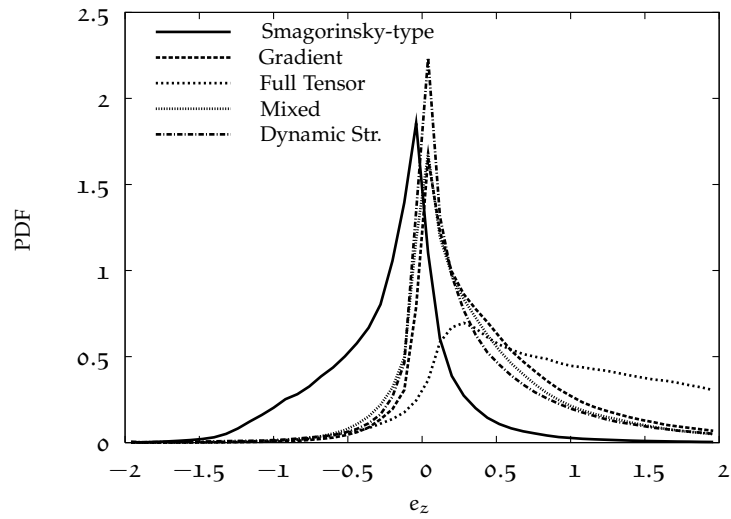


Figure 65: Pdfs of relative error e_z of $\bar{\alpha}_p \tilde{V}_{d,\beta}$, computed as in Eq. (5.3), for $\Delta_f = 11\Delta_{DNS}$ along the mean flow direction. The test filter width is $\hat{\Delta} = \sqrt{5}\Delta_f$.

0.0066. This value was determined with a linear least-squares regression method on the vector level. It was stated that it depends on the Mach number. Additionally, Zang et al. (1991) have studied the influence of this constant in LES of compressible homogeneous decaying turbulence at a turbulent Mach number of 0.1. C_γ was varied from its standard value (0.0066) to a value 50 times larger. Herein, we calculated 25 times larger than standard value for single phase flow and this can be result of high compressibility of disperse phase.

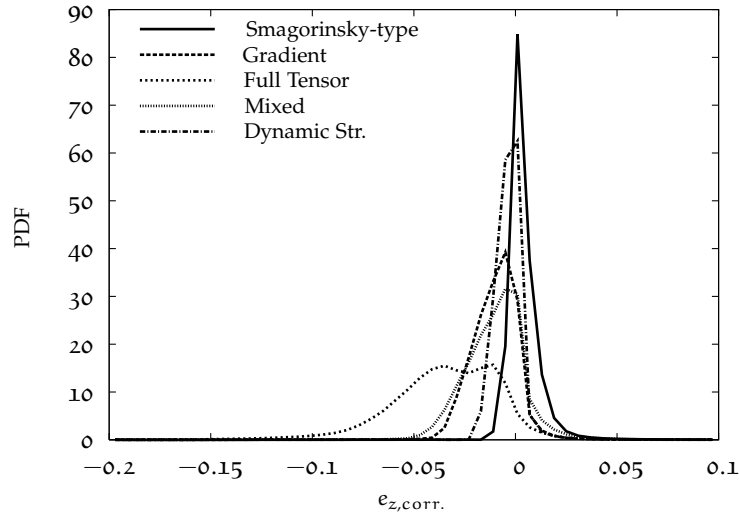


Figure 66: Pdfs of relative error e_z of the drag correction, computed as in Eq. (5.3), for $\Delta_f = 11\Delta_{DNS}$ along the mean flow direction. The test filter width is $\hat{\Delta} = \sqrt{5}\Delta_f$.

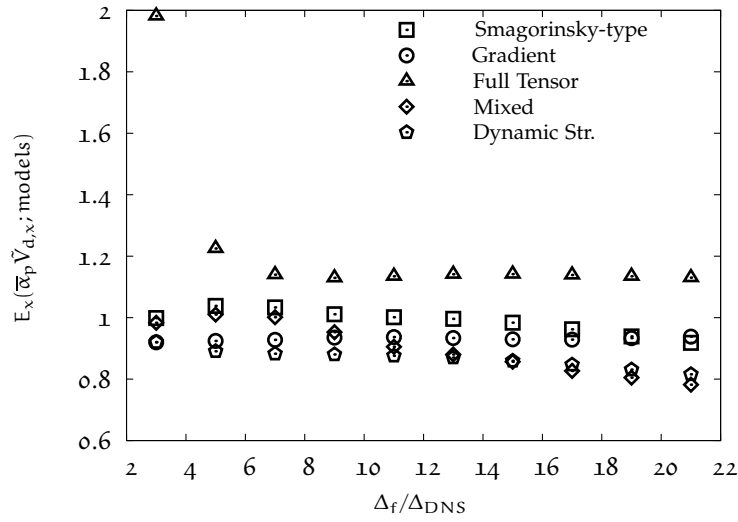


Figure 67: Mean squared error E_x , computed as in Eq. (5.4), for the x -component of measured and modelled $\bar{\alpha}_p \tilde{V}_{d,\beta}$ for different filter widths Δ_f . The test filter width is $\hat{\Delta} = \sqrt{5}\Delta_f$.

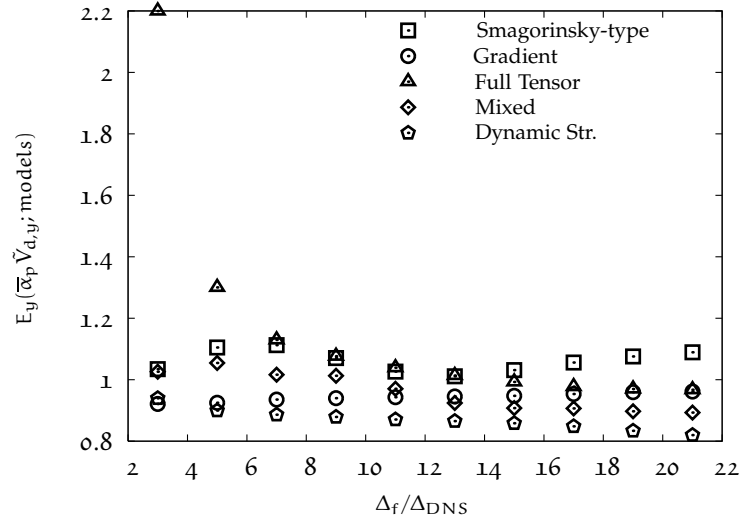


Figure 68: Mean squared error E_y , computed as in Eq. (5.4), for the y -component of measured and modelled $\bar{\alpha}_p \hat{V}_{d,\beta}$ for different filter widths Δ_f . The test filter width is $\hat{\Delta} = \sqrt{5}\Delta_f$.

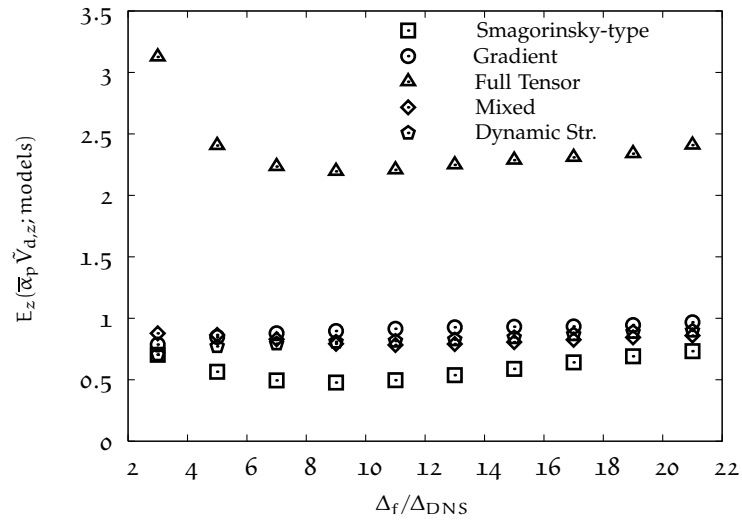


Figure 69: Mean squared error E_z , computed as in Eq. (5.4), for the z -component of measured and modelled $\bar{\alpha}_p \hat{V}_{d,\beta}$ for different filter widths Δ_f . The test filter width is $\hat{\Delta} = \sqrt{5}\Delta_f$.

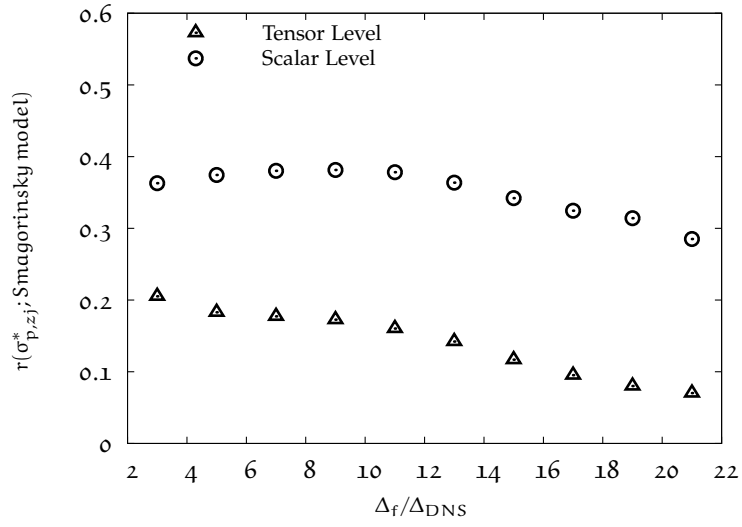


Figure 70: Correlation coefficients r between the deviatoric part of the filtered particle sub-grid stress tensor $\sigma_{p,zj}^*$ and Smagorinsky model for different filter widths Δ_f at the tensor and scalar level.

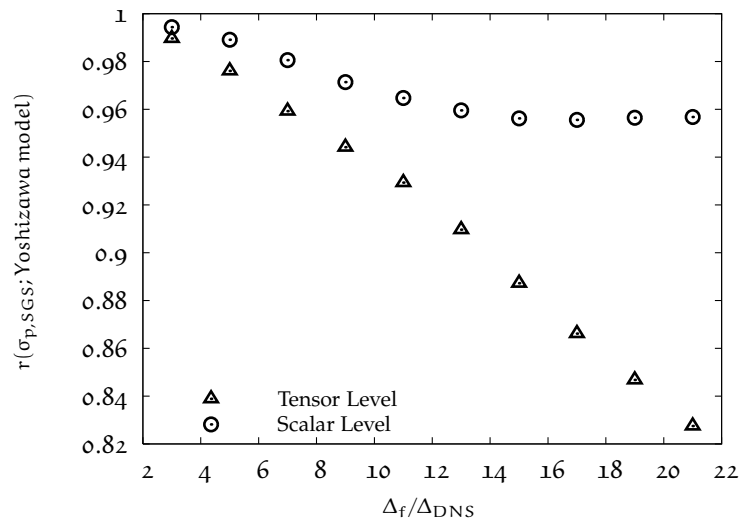


Figure 71: Correlation coefficients r between the filtered particle sub-grid energy $\sigma_{p,SGS}$ and Yoshizawa model for different filter widths Δ_f at the tensor and scalar level.

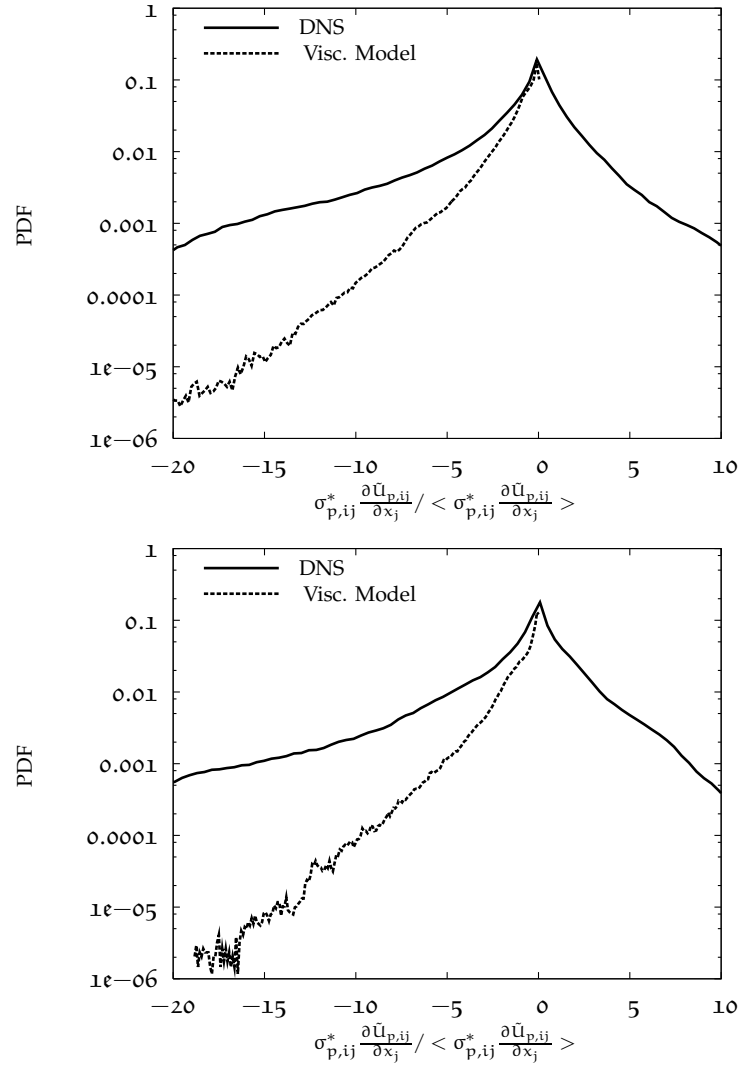


Figure 72: Pdfs of particle sub-grid dissipation from DNS data and by the Smagorinsky model for filter width ratios: $\Delta_f/\Delta_{DNS} = 7$ (top), 15 (bottom).

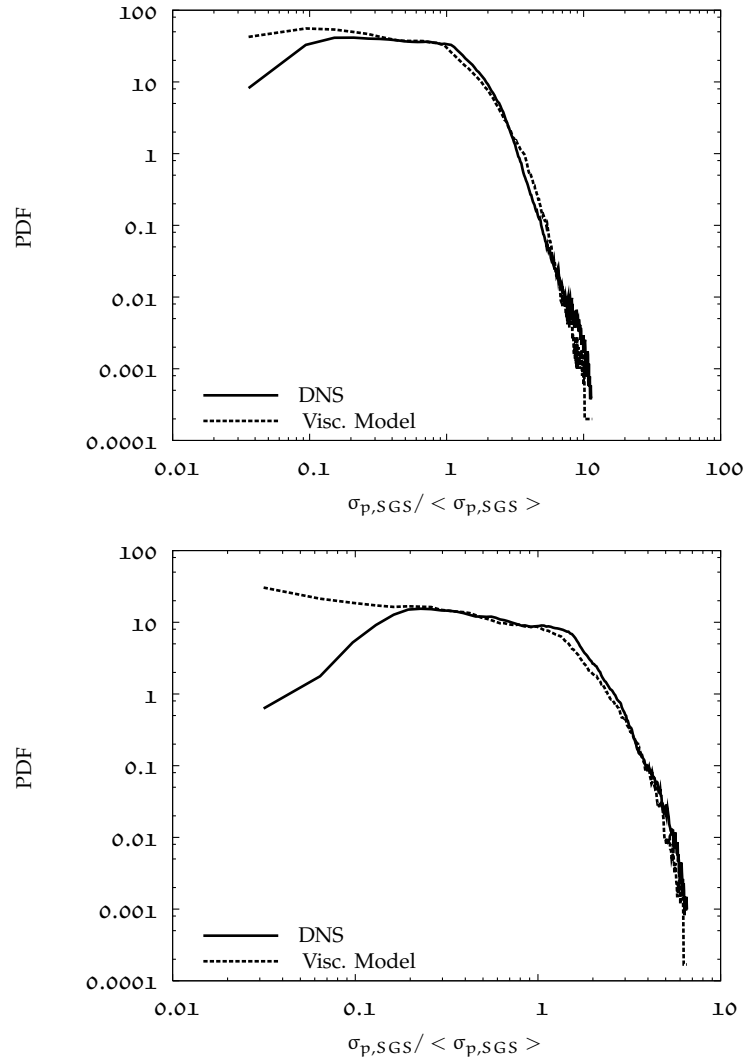


Figure 73: Pdfs of particle sub-grid energy $\sigma_{p,SGS}$ from DNS data and by the Yoshizawa model for filter width ratios: $\Delta_f / \Delta_{DNS} = 7$ (top), 15(bottom).

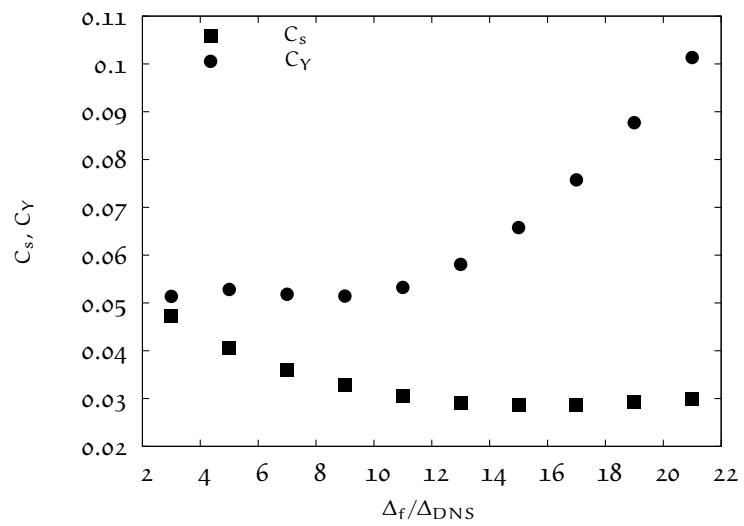


Figure 74: Yoshizawa and Smagorinsky model coefficients, C_Y and C_s , for different filter widths Δ_f .

6.1 A POSTERIORI STUDIES OF PERIODIC CIRCULATING FLUIDIZED BED

Mesh independent result of gas-solid flow in a 3-D PCFB was obtained in §4. This result was used to construct a systematic approach based on a priori methodology to investigate meso-scale structures effects on the bed hydrodynamics for coarse mesh simulations. The physical identification of over-prediction of drag force was determined and these results show that filtered momentum equation can be computed on coarse grid simulation but must take into account the particle to fluid drift velocity (sub-grid drift velocity) due to the sub-grid correlation between the local fluid velocity and the local particle volume fraction. The drift flux, which is equal to the multiplication of the sub-grid drift velocity by the solid volume fraction, were defined by an analogy with turbulent scalar flux. Some family of functional (Smagorinsky-type) and structural models (Gradient, full tensor, mixed and dynamic structure models) were proposed for this sub-grid contribution. Additionally, the particle sub-grid stresses were first divided into two parts; deviatoric and spherical. The spherical part, also called sub-grid correlated energy, is closed by the Yoshizawa model. The deviatoric part can be modelled by standard compressible Smagorinsky model as in the single phase flows. The objective of this part is to verify these models in a posteriori studies. For a posteriori studies, mesh independent result (simulation with mesh resolution $Fr_{\Delta}^{-1} = 0.032$) of PCFB was used to make comparisons.

Effective Drag Models

Smagorinsky-type (SGM) model and the mixed (MM) model were employed for a posteriori simulations. The **SGM model** is based on the interpretation of the drift flux by the resolved relative velocity between gas and particulate phases. It is given by

$$\bar{\alpha}_p \tilde{V}_{d,\beta} = K_{\beta\beta} f(\Delta_{sgs}) h(\bar{\alpha}_p) \bar{\alpha}_p (\tilde{U}_{g,\beta} - \tilde{U}_{p,\beta}) \quad (6.1)$$

where $\beta = x, y, z$ and β is used to indicate that there is no implicit summation. The length scale is given by

$$f(\Delta_{sgs}) = \frac{Fr_{\Delta}^{-1.6}}{\alpha + Fr_{\Delta}^{-1.6}} \quad (6.2)$$

where α is equal to 0.3. The non-dimensional mesh size Fr_{Δ}^{-1} is given by

$$Fr_{\Delta}^{-1} = \frac{(\Delta x \Delta y \Delta z)^{1/3}}{(\tau_p^{St})^2 |g|}. \quad (6.3)$$

with the **Stoke's relaxation time** τ_p^{St} given by $\frac{\rho_p d_p^2}{\rho_g 18\nu_g}$. The correction function is

$$h(\bar{\alpha}_p) = -\tanh\left(2\frac{\bar{\alpha}_p}{0.2}\right) \sqrt{\frac{\bar{\alpha}_p}{\alpha_{p,\max}}} \left(1 - \frac{\bar{\alpha}_p}{\alpha_{p,\max}}\right)^2 \quad (6.4)$$

$$\left(1 - C_{h,1} \frac{\bar{\alpha}_p}{\alpha_{p,\max}} + C_{h,2} \left(\frac{\bar{\alpha}_p}{\alpha_{p,\max}}\right)^2\right)$$

with $C_{h,1}$ equal to 1.88 and $C_{h,2}$ equal to 5.16. The maximum volume fraction of solid phase $\alpha_{p,\max}$ is set to 0.64.

The **MM model** is given by

$$\bar{\alpha}_p \tilde{V}_{d,\beta} = \frac{\Delta^2}{12} \frac{\partial \bar{\alpha}_p}{\partial x_j} \frac{\partial \tilde{u}_{g,i}}{\partial x_j} + K_{\beta\beta} f(\Delta_{sgs}) h(\bar{\alpha}_p) \bar{\alpha}_p (\tilde{u}_{g,i} - \tilde{u}_{p,i}). \quad (6.5)$$

The constant $K_{\beta\beta}$ is **dynamically calculated and averaged over the domain** to avoid numerical instabilities for the SGM and the MM models as detailed in §5.2.

SGS Particle Stress Models

The dynamic Smagorinsky model (DSM) can be proposed for the anisotropic parts of stresses and the dynamic Yoshizawa model (DYM) can be used for the trace of stress tensor as follows:

$$\bar{\alpha}_p \sigma_{p,ij}^{sgs} = \bar{\alpha}_p \sigma_{p,ij}^* + \bar{\alpha}_p \frac{1}{3} \sigma_{p,kk} \delta_{ij} = -\bar{\alpha}_p C_s^2 \Delta^2 |\tilde{S}_p^*| \tilde{S}_{p,ij}^* + \bar{\alpha}_p \frac{2}{3} \sigma_{p,SGS} \delta_{ij}$$

with the trace of stress tensor $\sigma_{p,SGS}$ predicted by

$$\sigma_{p,SGS} = C_Y \Delta^2 |\tilde{S}_p^*|^2 \quad (6.6)$$

where $\Delta = (\Delta x \Delta y \Delta z)^{1/3}$ and $S_{p,ij}^* = \frac{\partial \tilde{u}_{p,i}}{\partial x_j} + \frac{\partial \tilde{u}_{p,j}}{\partial x_i} - \frac{2}{3} \frac{\partial \tilde{u}_{p,m}}{\partial x_m} \delta_{ij}$.

The constants C_s and C_Y are dynamically calculated by performing domain averaging along the mean flow (Germano et al. 1991).

6.1.1 Instantaneous Volume Fraction Field

Instantaneous solid volume fraction in PCFB for kinetic theory simulations with different mesh resolutions; $Fr_{\Delta}^{-1} = 0.128$ and $Fr_{\Delta}^{-1} = 0.032$ are shown in Figure 75. Coarse mesh simulation with $Fr_{\Delta}^{-1} = 0.128$ can not predict segregation along the centre-line in the PCFB. In this figure, coarse mesh simulations with $Fr_{\Delta}^{-1} = 0.128$ by using the SGM and MM model for the effective drag force and SGS particle stress models (DSM and DYM) are also shown. Both simulation is capable to capture segregation of particles along the centre line.

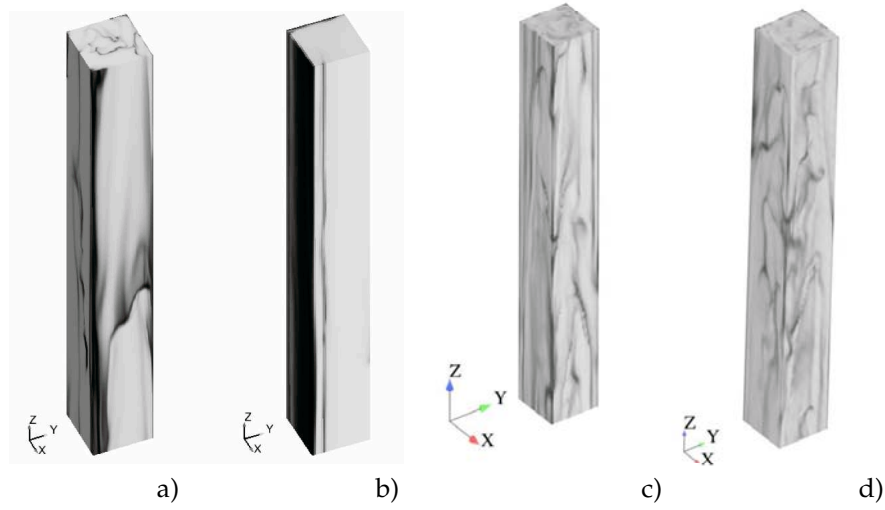


Figure 75: Instantaneous of solid volume fraction in the PCFB. White color corresponds to $\alpha_p = 0$. Black colour corresponds to $\alpha_{p,max} = 0.64$. a) Kinetic theory simulation with mesh resolution, $Fr_{\Delta}^{-1} = 0.032$ ($128 \times 128 \times 1024$), b) Kinetic theory simulation with mesh resolution, $Fr_{\Delta}^{-1} = 0.128$ ($32 \times 32 \times 256$), c) Simulation with SGM and SGS particle stress models with mesh resolution $Fr_{\Delta}^{-1} = 0.128$ ($32 \times 32 \times 256$), d) Simulation with MM and SGS particle stress models with mesh resolution $Fr_{\Delta}^{-1} = 0.128$ ($32 \times 32 \times 256$).

6.1.2 Global Quantities

The procedure, as given in §4, was followed to obtain domain statistics for coarse mesh simulations. For all simulations, Smagorinsky and Yoshizawa models were used while effective drag models were being tested. The weighted averaged relative velocity $\overline{\langle \alpha_p (\mathbf{U}_{p,z} - \mathbf{U}_{g,z}) \rangle^t}$ with effective drag models for three mesh resolutions: coarse ($24 \times 24 \times 192$, $Fr_{\Delta}^{-1} = 0.175$), moderate ($32 \times 32 \times 256$, $Fr_{\Delta}^{-1} = 0.128$), fine ($40 \times 40 \times 320$, $Fr_{\Delta}^{-1} = 0.104$) and mesh dependency study of $\overline{\langle \alpha_p (\mathbf{U}_{p,z} - \mathbf{U}_{g,z}) \rangle^t}$ performed by using kinetic theory relations are shown in Figure 76. Simulations with SGM overestimates the magnitude of $\overline{\langle \alpha_p (\mathbf{U}_{p,z} - \mathbf{U}_{g,z}) \rangle^t}$ for three mesh simulations. $\overline{\langle \alpha_p (\mathbf{U}_{p,z} - \mathbf{U}_{g,z}) \rangle^t}$ slightly changes by increasing mesh resolution and it was very well predicted with $Fr_{\Delta}^{-1} = 0.104$ as comparing with mesh independent result. Magnitudes of $\overline{\langle \alpha_p (\mathbf{U}_{p,z} - \mathbf{U}_{g,z}) \rangle^t}$ with MM are slightly bigger than of results with SGM for three mesh simulations. MM predictions are nearly independent of the mesh resolution.

The non-dimensional solid fluxes with the effective drag for three mesh resolutions : coarse ($24 \times 24 \times 192$, $Fr_{\Delta}^{-1} = 0.175$), moderate ($32 \times 32 \times 256$, $Fr_{\Delta}^{-1} = 0.128$), fine ($40 \times 40 \times 320$, $Fr_{\Delta}^{-1} = 0.104$) and mesh dependency study of non-dimensional fluxes by using kinetic theory relations are shown in Figure 77. Solid fluxes were predicted very well by simulations with both effective drag force models. Solid fluxes obtained by MM are slightly different from results obtained with SGM for three mesh simulations.

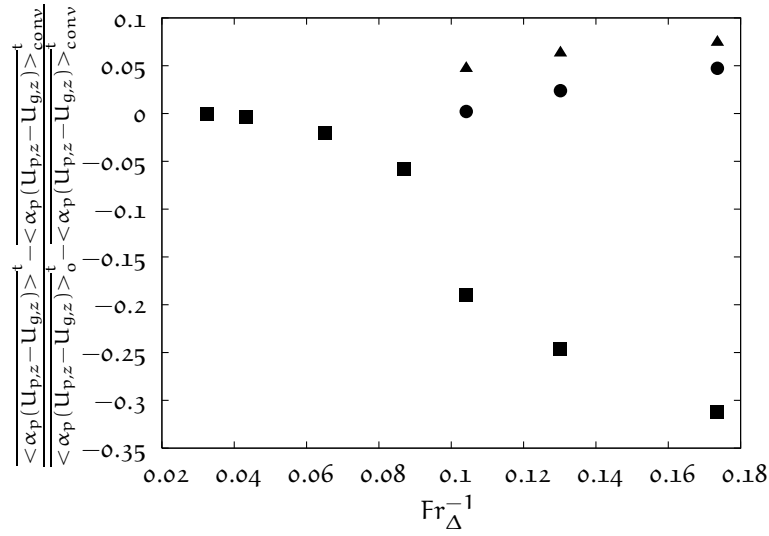


Figure 76: The influence of mesh size on the weighted relative velocity $\frac{\overline{\langle \alpha_p (U_{p,z} - U_{g,z}) \rangle^t}}{\overline{\langle \alpha_p (U_{p,z} - U_{g,z}) \rangle_0^t} - \overline{\langle \alpha_p (U_{p,z} - U_{g,z}) \rangle_{conv}^t}}$. Simulations with the effective drag and SGS particle stress models were performed for three mesh resolutions : coarse ($24 \times 24 \times 192$, $Fr_{\Delta}^{-1} = 0.175$), moderate ($32 \times 32 \times 256$, $Fr_{\Delta}^{-1} = 0.128$) and fine ($40 \times 40 \times 320$, $Fr_{\Delta}^{-1} = 0.104$). ●: SGM model for effective drag+SGS particle stress models, ▲: MM model for effective drag+SGS particle stress models, ■: Kinetic theory based simulations without models.

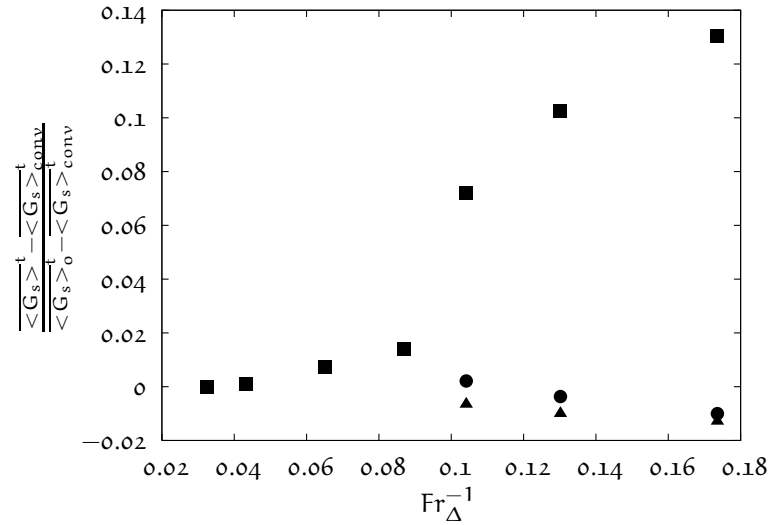


Figure 77: The influence of mesh size the non-dimensional total volumetric mass flux, $\frac{\overline{\langle G_s \rangle^t}}{\overline{\langle G_s \rangle_0^t} - \overline{\langle G_s \rangle_{conv}^t}}$ where $G_{s,0}$ corresponds to the homogeneous case and $G_{s,conv}$ corresponds to the converged case. Simulations with the effective drag and SGS particle stress models were performed for three mesh resolutions : coarse ($24 \times 24 \times 192$, $Fr_{\Delta}^{-1} = 0.175$), moderate ($32 \times 32 \times 256$, $Fr_{\Delta}^{-1} = 0.128$) and fine ($40 \times 40 \times 320$, $Fr_{\Delta}^{-1} = 0.104$). ●: SGM model for effective drag+SGS particle stress models, ▲: MM model for effective drag+SGS particle stress models, ■: Kinetic theory based simulations without models.

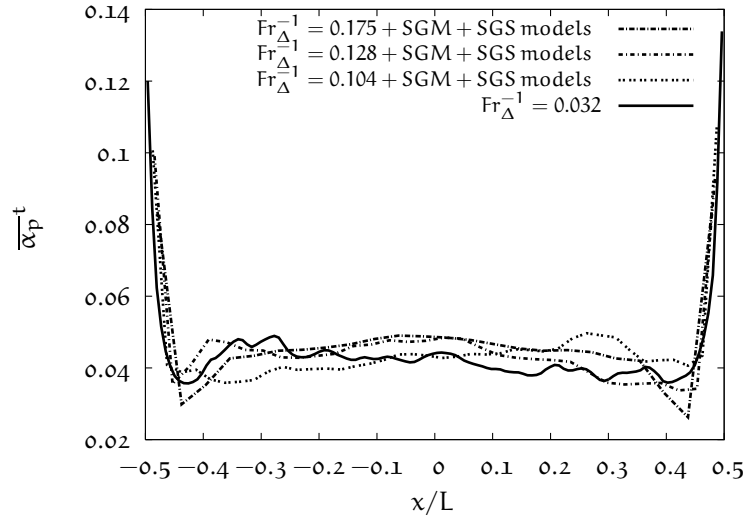


Figure 78: The time-averaged solid volume fraction along the radial direction with SGM model for effective drag and SGS particle stress models for three mesh resolutions : coarse ($24 \times 24 \times 192$, $Fr_{\Delta}^{-1} = 0.175$), moderate ($32 \times 32 \times 256$, $Fr_{\Delta}^{-1} = 0.128$), fine ($40 \times 40 \times 320$, $Fr_{\Delta}^{-1} = 0.104$) and the mesh independent result obtained by kinetic theory based simulation ($128 \times 128 \times 1024$, $Fr_{\Delta}^{-1} = 0.032$) ($z = 0.11\text{m}$, $y = 0$).

6.1.3 Radial Profiles of Time-averaged Variables by Smagorinsky-type Model (SGM)

The radial distribution of time-averaged variables are shown in Figures 78-81 for three mesh resolutions: coarse ($24 \times 24 \times 192$, $Fr_{\Delta}^{-1} = 0.175$), moderate ($32 \times 32 \times 256$, $Fr_{\Delta}^{-1} = 0.128$) and fine ($40 \times 40 \times 320$, $Fr_{\Delta}^{-1} = 0.104$). In Figure 78, the time-averaged of solid volume fraction is shown for different resolutions. Particles tend to accumulate close to the wall for all cases. Results are in good agreement with the mesh independent result. The time-averaged gas velocities normalised by the terminal settling velocity V_t^{St} are shown in Figure 79. For coarse mesh resolution, the gas velocity has positive values close to the wall. With mesh refinement, we obtained the negative gas velocity close to the wall and augmentation of the magnitude of mean flow through the correct value. We present negative, positive and total mass flux normalised by uniform distribution of solid falling down with terminal settling velocity in Figures 80 and 81. The core-annulus flow are obtained for all mesh resolutions. Solids are transported at the centreline and close to wall, but they descend only at the vicinity to wall. The negative and positive solid fluxes for all cases are almost identical but underestimation of positive solid fluxes with respect to the mesh independent result is observed close to the wall.

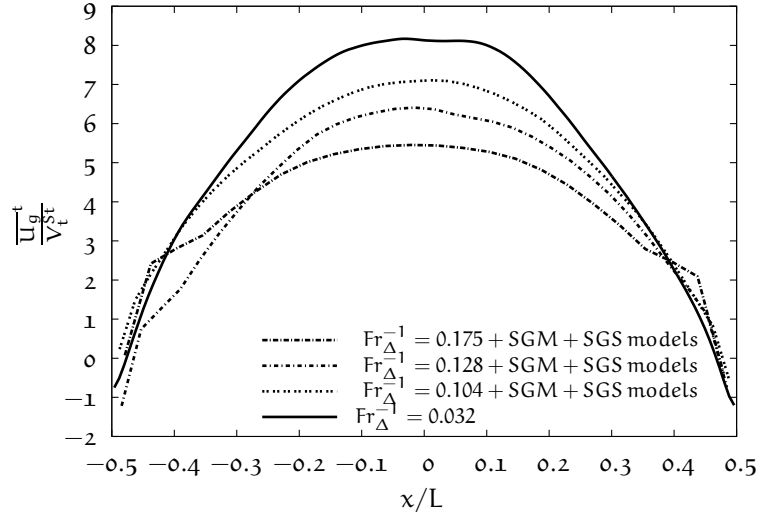


Figure 79: The time-averaged gas velocity along the radial direction with SGM model for effective drag and SGS particle stress models for three mesh resolutions: coarse ($24 \times 24 \times 192$, $Fr_{\Delta}^{-1} = 0.175$), moderate ($32 \times 32 \times 256$, $Fr_{\Delta}^{-1} = 0.128$), fine ($40 \times 40 \times 320$, $Fr_{\Delta}^{-1} = 0.104$) and the mesh independent result obtained by kinetic theory based simulation ($128 \times 128 \times 1024$, $Fr_{\Delta}^{-1} = 0.032$) ($z = 0.11\text{m}$, $y = 0$).

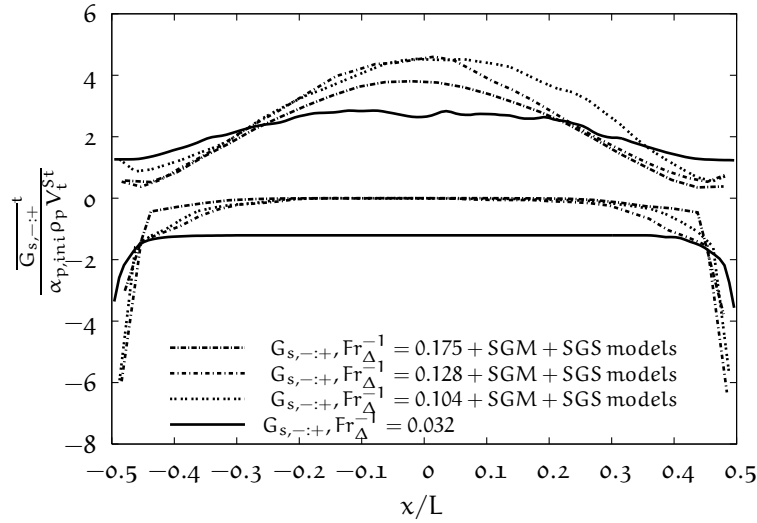


Figure 80: The time-averaged negative and positive solid mass flux along the radial direction with SGM model for effective drag and SGS particle stress models for three mesh resolutions: coarse ($24 \times 24 \times 192$, $Fr_{\Delta}^{-1} = 0.175$), moderate ($32 \times 32 \times 256$, $Fr_{\Delta}^{-1} = 0.128$), fine ($40 \times 40 \times 320$, $Fr_{\Delta}^{-1} = 0.104$) and the mesh independent result obtained by kinetic theory based simulation ($128 \times 128 \times 1024$, $Fr_{\Delta}^{-1} = 0.032$) ($z = 0.11\text{m}$, $y = 0$).

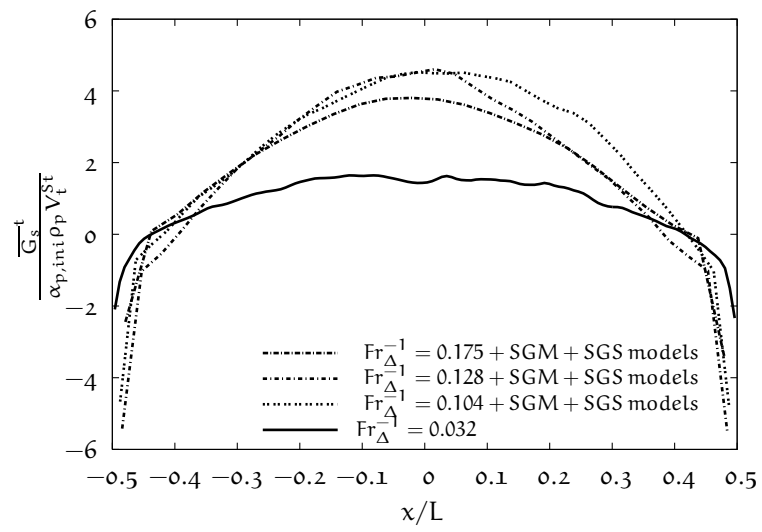


Figure 81: The time-averaged total solid mass flux along the radial direction with SGM model for effective drag and SGS particle stress models for three mesh resolutions: coarse ($24 \times 24 \times 192$, $Fr_{\Delta}^{-1} = 0.175$), moderate ($32 \times 32 \times 256$, $Fr_{\Delta}^{-1} = 0.128$), fine ($40 \times 40 \times 320$, $Fr_{\Delta}^{-1} = 0.104$) and the mesh independent result obtained by kinetic theory based simulation ($128 \times 128 \times 1024$, $Fr_{\Delta}^{-1} = 0.032$) ($z = 0.11\text{m}$, $y = 0$).

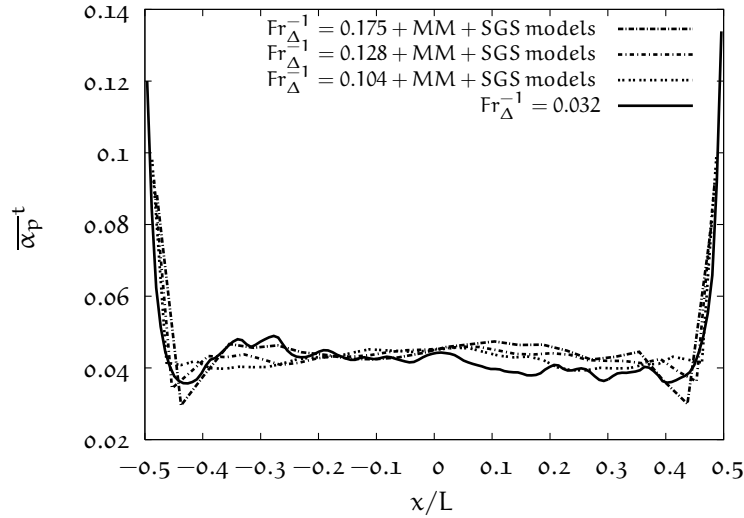


Figure 82: The time-averaged solid volume fraction along the radial direction with MM model for effective drag and SGS particle stress models for three mesh resolutions: coarse ($24 \times 24 \times 192$, $Fr_{\Delta}^{-1} = 0.175$), moderate ($32 \times 32 \times 256$, $Fr_{\Delta}^{-1} = 0.128$), fine ($40 \times 40 \times 320$, $Fr_{\Delta}^{-1} = 0.104$) and the mesh independent result obtained by kinetic theory based simulation ($128 \times 128 \times 1024$, $Fr_{\Delta}^{-1} = 0.032$) ($z = 0.11\text{m}$, $y = 0$).

6.1.4 Radial Profiles of Time-averaged Variables by Mixed Model (MM)

The radial distribution of time-averaged variables are shown in Figures 82-85 for three mesh resolutions: coarse ($24 \times 24 \times 192$, $Fr_{\Delta}^{-1} = 0.175$), moderate ($32 \times 32 \times 256$, $Fr_{\Delta}^{-1} = 0.128$) and fine ($40 \times 40 \times 320$, $Fr_{\Delta}^{-1} = 0.104$). In Figure 82, the time-averaged of solid volume fraction is shown for different resolutions. We obtained similar results as that of SGM model. Radial profiles of time-averaged solid volume fraction are in good agreement with the mesh independent result. The time-averaged gas velocities are shown in Figure 83. The difference between results with SGM model is that we obtained the negative gas velocity for coarse mesh simulation. The same trend for gas velocity augmentation is observed for this case. We present negative, positive and total mass flux in Figures 84 and 85. The core-annulus flow are obtained for all mesh resolutions.

6.2 A POSTERIORI STUDIES OF DENSE FLUIDIZED BED

6.2.1 Flow Configuration

Parmentier (2010) studied the unresolved structures effect on the resolved flow dynamics in dense bubbling fluidized beds. Gas-particle flow was simulated in a two-dimensional dense fluidized bed. FCC particles ($d_p = 75 \mu\text{m}$, $\rho_p = 1500 \text{ kg/m}^3$), which are interacting with the ambient gas ($\rho_g = 1.186 \text{ kg/m}^3$, $\mu_g = 1.8 \times 10^{-5}$), are used for simulations. The computational domain is shown in Figure 86. In this case, we performed simulations with SGM and MM models.

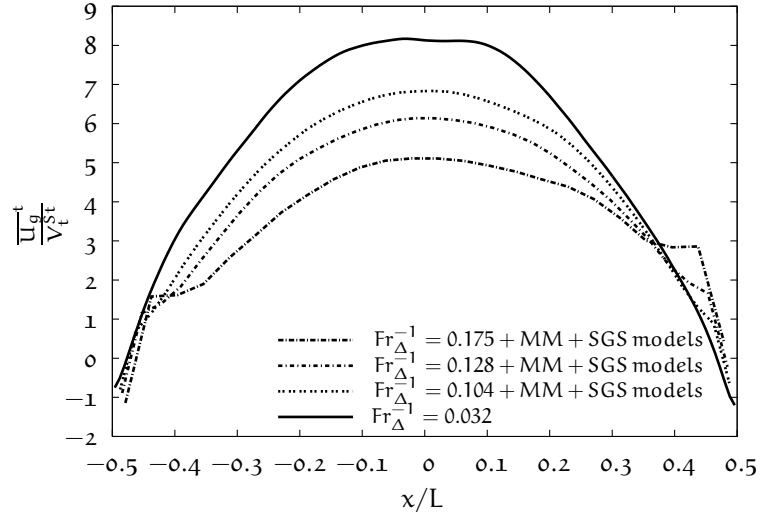


Figure 83: The time-averaged gas velocity along the radial direction with MM model for effective drag and SGS particle stress models for three mesh resolutions: coarse ($24 \times 24 \times 192$, $Fr_{\Delta}^{-1} = 0.175$), moderate ($32 \times 32 \times 256$, $Fr_{\Delta}^{-1} = 0.128$), fine ($40 \times 40 \times 320$, $Fr_{\Delta}^{-1} = 0.104$) and the mesh independent result obtained by kinetic theory based simulation ($128 \times 128 \times 1024$, $Fr_{\Delta}^{-1} = 0.032$) ($z = 0.11\text{m}$, $y = 0$).

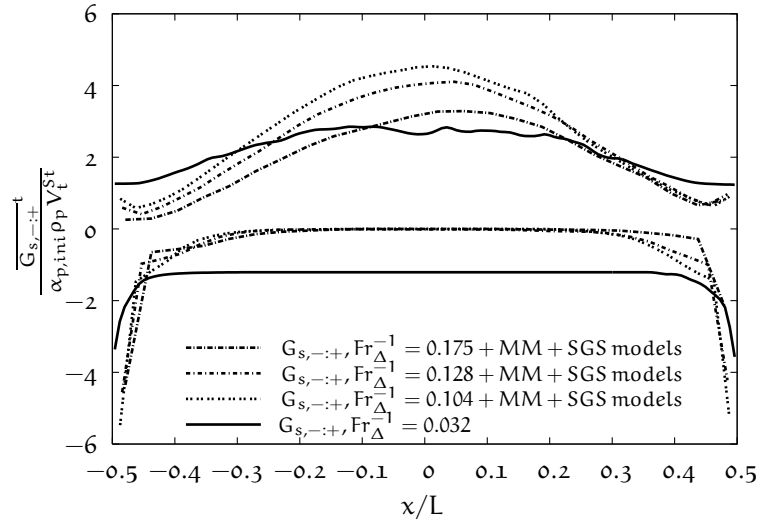


Figure 84: The time-averaged negative and positive solid mass flux along the radial direction with MM model for effective drag and SGS particle stress models for three mesh resolutions: coarse ($24 \times 24 \times 192$, $Fr_{\Delta}^{-1} = 0.175$), moderate ($32 \times 32 \times 256$, $Fr_{\Delta}^{-1} = 0.128$), fine ($40 \times 40 \times 320$, $Fr_{\Delta}^{-1} = 0.104$) and the mesh independent result obtained by kinetic theory based simulation ($128 \times 128 \times 1024$, $Fr_{\Delta}^{-1} = 0.032$) ($z = 0.11\text{m}$, $y = 0$).

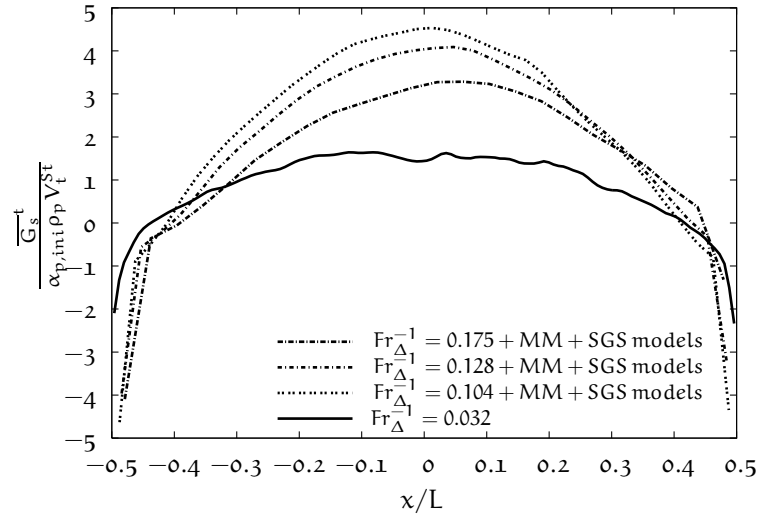


Figure 85: The time-averaged total solid mass flux along the radial direction with SGM model for effective drag and SGS particle stress models for three mesh resolutions: coarse ($24 \times 24 \times 192$, $Fr_{\Delta}^{-1} = 0.175$), moderate ($32 \times 32 \times 256$, $Fr_{\Delta}^{-1} = 0.128$), and fine ($40 \times 40 \times 320$, $Fr_{\Delta}^{-1} = 0.104$) and the mesh independent result obtained by kinetic theory based simulation ($128 \times 128 \times 1024$, $Fr_{\Delta}^{-1} = 0.032$) ($z = 0.11\text{m}$, $y = 0$).

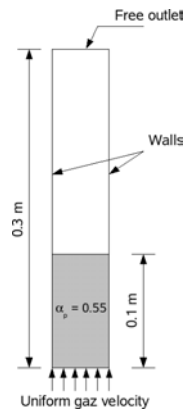


Figure 86: The 2-D bubbling fluidized bed (see Parmentier 2010).

The dense fluidized bed is initialised by the homogeneous distribution with the particle volume fraction equal to 0.55 and the fluidization velocity U_f is set to 0.2 m/s. No-slip condition was imposed for the gas phase and free slip boundary condition with zero kinetic energy flux was applied for the particulate phase at the walls. The computational domain was constructed by using uniform square cells. Three different mesh resolutions are used for simulations; the coarsest resolution, $\Delta_x = \Delta_y = 2$ mm, the intermediate resolution, $\Delta_x = \Delta_y = 1$ mm and the finest resolution, $\Delta_x = \Delta_y = 100$ μm . Parmentier (2010) pointed out that time-averaged quantities become mesh-independent for mesh size smaller than 500 μm . The reference case with the mesh size equal to $\Delta_x = \Delta_y = 100$ μm is used to make comparisons with coarse mesh simulations performed with developed effective drag models in terms of the bed height. For transient regime of flow, we performed simulation during 5 s physical time and then we calculated time-averaged values during additional 10 s physical time.

6.2.2 Simulation Results

Parmentier (2010) pointed out that the implicit length scale $\bar{\Delta}$ is unknown and it was assumed that the length scale is related the mesh size by

$$\bar{\Delta} = \sqrt{2}\Delta_x = \sqrt{2}\Delta_y. \quad (6.7)$$

The scale factor of $\sqrt{2}$ was empirically determined. Herein, we used this scale factor for mesh dependencies of models for coarse-grid simulations. Simulations with sub-grid models were performed on mesh sizes of $\Delta_{x,y} = 1$ mm and $\Delta_{x,y} = 2$ mm. Bed expansions by the Smagorinsky-type model (SGM) are independent of mesh size and good predicted with two mesh resolutions (see Figure 87). The Mixed model (MM) predicted same bed expansions for two mesh sizes. However, bed heights are slightly higher than of the Smagorinsky-type model (see Figure 88).

6.3 APPLICATION TO DILUTE GAS-PARTICLE FLOW IN FCC RISER

A full description of the FCC system and the measurements may be found in Gauthier (2002) and in §3. The computational domain was constructed by using uniform square cells. Two different mesh resolutions are used for simulations; the coarsest resolution, ($14 \times 14 \times 675, Fr_{\Delta}^{-1} = 18$), the intermediate resolution, ($28 \times 28 \times 1350, Fr_{\Delta}^{-1} = 9$). In this case, we performed simulations with SGM model and SGS particle stresses models.

Results

The simulation run for 25 s of physical time, then time-averaged quantities are calculated during 50 physical time for mesh resolution, $Fr_{\Delta}^{-1} = 18$. Due to computational cost, we run case with $Fr_{\Delta}^{-1} = 9$ for 15 s of physical time, then time-averaged quantities are calculated during 10 physical time. Time evolution of mass in the riser are shown in Figure 89a. Total mass in the riser shows oscillating behaviour and the mean value is 115 ± 5 kg for both cases. Predicted pressure drop are shown in Figure 89b. Axial pressure profile trend is well captured by simulations with the SGM and SGS particle stress models for

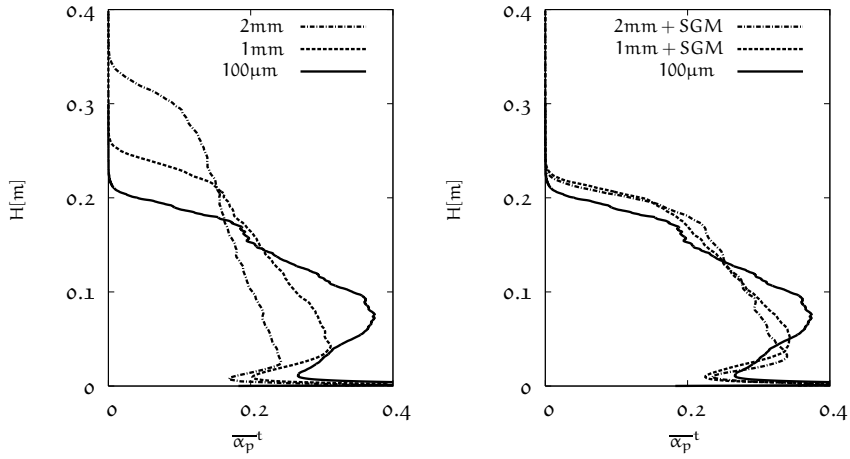


Figure 87: Vertical profiles of time-averaged solid volume fraction. Simulations results without and with the Smagorinsky-type model are the left and the right, respectively, for mesh resolution: $\Delta_{x,y} = 1 \text{ mm}$ and $\Delta_{x,y} = 2 \text{ mm}$. The reference case mesh size is equal to $\Delta_{x,y} = 100 \mu\text{m}$.

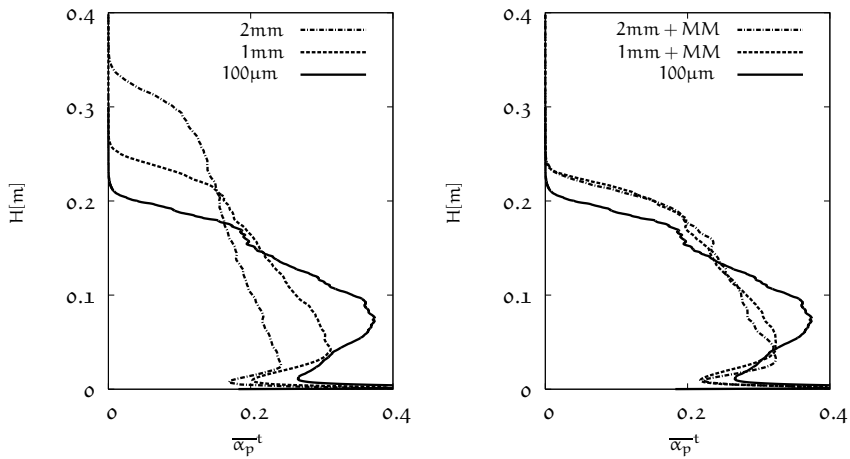
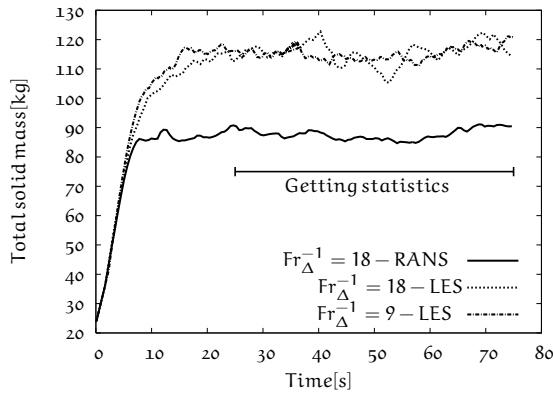


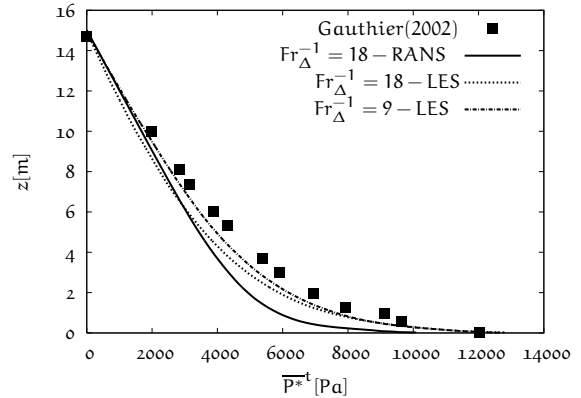
Figure 88: Vertical profiles of time-averaged solid volume fraction. Simulations results without and with the Mixed model are the left and the right, respectively, for mesh resolution: $\Delta_{x,y} = 1 \text{ mm}$ and $\Delta_{x,y} = 2 \text{ mm}$. The reference case mesh size is equal to $\Delta_{x,y} = 100 \mu\text{m}$.

both resolution, but mass inventory is underestimated. Predictions by proposed models are insensitive to mesh size and particle diameter.

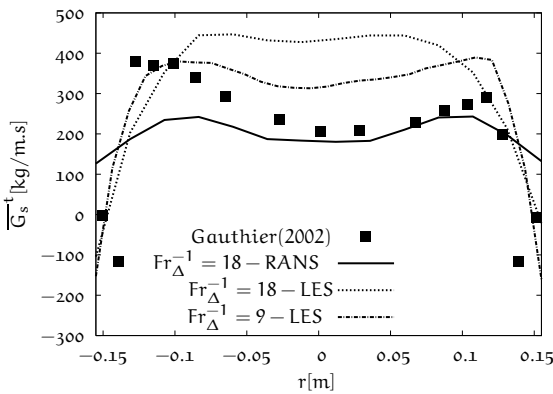
Negative, positive and total mass fluxes by simulations and measured total mass flux are shown at two different elevations, $z = 1.325$ m and $z = 7$ m (see Figures 89c-89f). At 1.325 m, the simulation can not capture the trend but negative fluxes can be very well predicted close to the wall. At 7 m, the flux shape is parabolic and smoother and it is away from effects of feeding of particles. Trend is very well captured with overestimation of solid fluxes at the centre of the pipe. Negative flux is also seen at this level, simulations with both mesh resolutions were able to reproduce this behaviour.



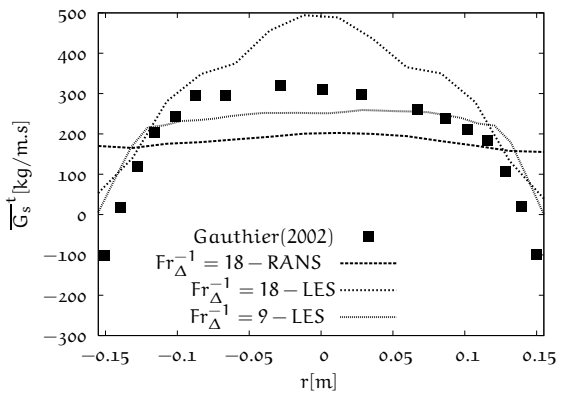
(a) The evolution of total solid mass in the riser.



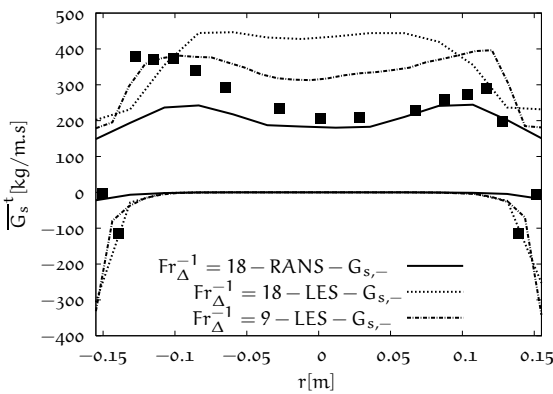
(b) Time-averaged gas pressure along the vertical direction.



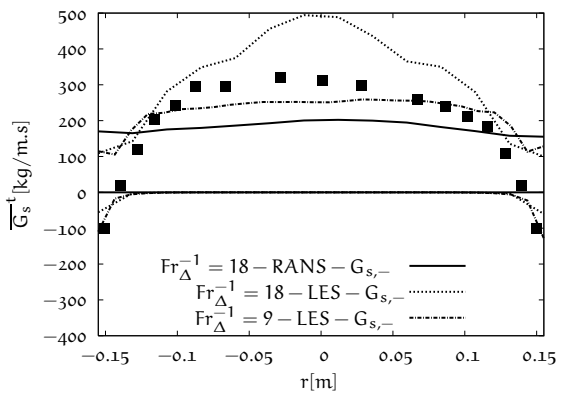
(c) Profiles of time-averaged vertical mass flow rate at $z = 1.325$ m along the radial direction.



(d) Profiles of time-averaged vertical mass flow rate at $z = 7$ m along the radial direction.



(e) Profiles of time-averaged vertical negative and positive mass flow rate at $z = 1.325$ m along the radial direction.



(f) Profiles of time-averaged vertical negative and positive mass flow rate at $z = 7$ m along the radial direction.

Figure 89: Predictions with different mesh resolutions (mesh: $14 \times 14 \times 675$ - $Fr_{\Delta}^{-1} = 18$, $28 \times 28 \times 1350$ - $Fr_{\Delta}^{-1} = 9$) versus experimental data of Gauthier (2002).

CONCLUSION

Meso-scale structures are continuously formed in the circulating fluidized bed and they can be resolved through Eulerian approach by supplementing the kinetic theory of granular flows on high resolution computational grid. However, simulations on coarse grid cancel out these structures and this causes poor predictions of bed hydrodynamic.

For investigation of effects of unresolved structures on resolved field for coarse grid simulations, we first obtained mesh independent result of gas-solid in the 3D periodic circulating fluidized bed. Then, we used this result to perform a systematic approach based on a priori methodology. We performed the filtering procedure on a given two-fluid model and obtained filtered momentum equation of particulate phase and particle agitation. Additional terms rising due to the filtering procedure in the filtered equations are investigated by budget analyses to determine their importance. It was yielded that meso-scale structures affect the flow characteristics profoundly. In particular, cancellation of these structures by coarse grid simulations overestimates the drag force between gas and particle phases. We showed that the sub-grid drift velocity, defined by the difference between the filtered gas velocity seen by particulate phase and the filtered gas velocity, has to be modelled to obtain the correct drag.

Some family of functional and structural models were proposed for sub-grid drift flux and models' predictions were tested in a priori manner with correlation coefficients, mean squared error and probability density functions of local relative error.

As the functional model, the Smagorinsky-type model was proposed as an continuation work of Parmentier (2010). The solid volume fraction dependency of model was given by the function "h". The shape of this function obtained from the high resolution simulation of 2D dense fluidized bed by Parmentier (2010) was tuned with the high resolution simulation 3D dilute gas-solid flow in the periodic circulating fluidized bed. The function "h" obtained from the high resolution simulation of the periodic circulating fluidized bed shows less drag correction for the case of the solid volume fraction smaller than 0.2. This result has an obvious physical meaning since gas passing through 3D structures is easier than of 2D structures. The mesh dependency of the Smagorinsky-type model was defined by the cell volume, the single particle Stoke's relaxation time and acceleration due to the gravity. It is noted that the sub-grid scale length is still an open question.

As structural models, we proposed the Gradient, the Full Tensor, the Mixed and the Dynamic Structure model. The Gradient model, which takes into account only Leonard and Cross terms of Germano's decomposition of sub-grid drift flux, shows good performance in terms of correlation coefficient for small filter widths. We introduced the high-order terms, which are fourth order of the filter width, to take into account Reynolds stresses. The Mixed model was proposed where high-order terms were modelled by the functional model (Smagorinsky-type model). We obtained high correlation coefficients for even for large filter widths. Sub-grid structure properties are transferred to resolved field by introducing the sub-grid scalar variance of the solid volume fraction in the Dynamic Structure model. It gives high correlation coefficients independent of filter widths.

By secondary effect, the meso-scale structures increase the effective viscosity and normal stresses of particulate phase. The Smagorinsky model, as used in single phase turbulent flow, were used to model the effective viscosity but it shows poor performance in terms of correlation coefficient. The model constant of the Smagorinsky model is smaller than of single phase turbulent flows. The Yoshizawa model were used to close the sub-grid correlated energy and its predictions were higher in terms of correlation coefficients. The model coefficient of the Yoshizawa model is the consistent with of applications of this model for gas-solid flows. We also performed the budget analysis of the filtered random kinetic energy equation and it was pointed out that coarse grid simulations underestimate the production of the particle random kinetic energy.

We tested these sub-grid scale models by a posteriori studies. We determined the flow dependent model coefficients in a transient manner and made comparisons between proposed models predictions with available ones. Smagorinsky and Yoshizawa models were used while effective drag models, the Smagorinsky-type and the Mixed model, were being tested for gas-solid flows in the 3D periodic circulating fluidized bed. The global quantities and the time-averaged profiles of variables obtained by the filtered two-fluid model with sub-grid scale models were compared with the mesh independent result obtained by the kinetic based simulations without models for three mesh resolutions: coarse ($Fr_{\Delta}^{-1} = 0.175$), moderate ($Fr_{\Delta}^{-1} = 0.128$) and fine ($Fr_{\Delta}^{-1} = 0.104$). Time-domain averaged solid fluxes were predicted very well by simulations with both effective drag force models and nearly independent of mesh resolution. Solid fluxes obtained by the Mixed model are slightly different from results obtained with the Smagorinsky-type model for three mesh simulations. Time-averaged radial profiles obtained by simulations with both effective drag force models show that predictions with the Smagorinsky-type and the Mixed model for the effective drag force and SGS particle stress models capture segregation of particles along the centre line while kinetic theory based simulations with coarse moderate and fine mesh resolutions can not predict segregation along the centreline. The second a posteriori test is a two-dimensional dense fluidized bed. Bed expansions by the Smagorinsky-type and Mixed model were compared with the high mesh resolution result. Bed expansions predicted by The Smagorinsky model are independent of mesh size for two mesh resolution. However, bed expansions are slightly over-predicted as comparing with high resolution simulation. The Mixed model also predicted same bed expansions for two mesh sizes, however, bed heights are slightly higher than of the Smagorinsky-type model. The last case is the circulating fluidized bed conducted with A-type particles. In this case, we compared results obtained by the Smagorinsky-type model for the effective drag force and SGS particle stress models with experimental data. Results in terms of pressure gradient and solid fluxes are in good agreement with experimental for two mesh resolutions.

Discussions & Perspectives

The mesh dependency of the Smagorinsky-type model is defined as a function of a single particle Stoke's relaxation time, acceleration due to the gravity and a given mesh size. Note that the mesh dependency has to verified with different scales of periodic circulating fluidized to quantify its asymptotic value. We showed that the exact shape of the volume fraction dependency of the model obtained from the high resolution simulation of the three-dimensional periodic circulating fluidized bed quantitatively differed

from the shape obtained by the high resolution simulation of two-dimensional dense fluidized bed. Improvement of the exact shape of the function can be performed by dense gas-solid flow in the periodic circulating fluidized. We perform domain averaged of the model constant $K_{\beta\beta}$ for flow in the periodic circulating bed, but the averaging procedure along the homogeneous direction may be invalid for the dense fluidized bed. The value of $K_{\beta\beta}$ was dynamically adjusted following a methodology adapted from single phase turbulent flows and the second filter width was chosen as same as in single phase turbulent flows. The second filter width can be verified by difference filter widths from the mesh independent results by a priori tests.

In this study, a priori tests were performed in flow regions away from solid boundaries. Corrections to take into account the effects of walls on the proposed models have to be investigated.

The filtered two-fluid was studied for uniformly size particles. The further study will be such filtered models for coarse-grid simulations of poly-disperse distribution of particles. We showed that cancelling of meso-scale structures causes underestimation of the particle agitation and this underestimation can be crucial for the correct prediction of bed hydrodynamic for poly-disperse system.

The present study can be extended to reacting gas-solid flows. Reacting gas-solid flows simulating by coarse grid also require filtered transport equation of species and energy balances with supplementing the filtered momentum equations of phases. The effects of meso-scale structures on the micro-scale mixing of species and chemical reaction rate will a challenging topic for further studies.

APPENDIX

A.1 APPENDIX SECTION

The gradient and full tensor model can be derived from the Taylor series expansion for a variable ϕ ,

$$\phi(\mathbf{x}) = \phi(\mathbf{x}_0) + \frac{\partial\phi}{\partial x_j}(\mathbf{x}_0)I_j + \frac{1}{2} \frac{\partial^2\phi}{\partial x_j\partial x_k}(\mathbf{x}_0)I_{jk} + \mathcal{O}(\bar{\Delta}^3) \quad (\text{A.1})$$

where $I_j = (x_j - x_{j_0})$ and $I_{jk} = (x_j - x_{j_0})(x_k - x_{k_0})$. Performing filtering on this expansion gives us

$$\bar{\phi}(\mathbf{x}) = \phi(\mathbf{x}_0) + \frac{\partial\phi}{\partial x_j}(\mathbf{x}_0)\bar{I}_j + \frac{1}{2} \frac{\partial^2\phi}{\partial x_j\partial x_k}(\mathbf{x}_0)\bar{I}_{jk} + \mathcal{O}(\bar{\Delta}^3). \quad (\text{A.2})$$

Multiplying the series expansions for the scalar ϕ and the vector λ_i then filtering yields

$$\begin{aligned} \overline{\phi\lambda_i}(\mathbf{x}) &= \phi(\mathbf{x}_0)\lambda_i(\mathbf{x}_0) + \left[\phi(\mathbf{x}_0)\frac{\partial\lambda_i(\mathbf{x}_0)}{\partial x_j} + \lambda_i(\mathbf{x}_0)\frac{\partial\phi(\mathbf{x}_0)}{\partial x_j} \right] \bar{I}_j \\ &\quad + \left\{ \frac{1}{2} \left[\phi(\mathbf{x}_0)\frac{\partial^2\lambda_i(\mathbf{x}_0)}{\partial x_j\partial x_k} + \lambda_i(\mathbf{x}_0)\frac{\partial^2\phi(\mathbf{x}_0)}{\partial x_j\partial x_k} \right] + \frac{\partial\phi}{\partial x_j}(\mathbf{x}_0)\frac{\partial\lambda_i}{\partial x_k}(\mathbf{x}_0) \right\} \bar{I}_{jk}. \end{aligned} \quad (\text{A.3})$$

Multiplying the series expansion for the scalar $\bar{\phi}$ and the vector $\bar{\lambda}_i$ leads us

$$\begin{aligned} \overline{\phi\lambda_i}(\mathbf{x}) &= \phi(\mathbf{x}_0)\lambda_i(\mathbf{x}_0) + \phi(\mathbf{x}_0)\frac{\partial\lambda_i(\mathbf{x}_0)}{\partial x_l}\bar{I}_l + \phi(\mathbf{x}_0)\frac{\partial^2\lambda_i(\mathbf{x}_0)}{\partial x_l\partial x_m}\bar{I}_l\bar{I}_m \\ &\quad + \frac{\partial\phi}{\partial x_j}(\mathbf{x}_0)\lambda_i(\mathbf{x}_0)\bar{I}_j + \frac{\partial\phi}{\partial x_j}(\mathbf{x}_0)\frac{\partial\lambda_i(\mathbf{x}_0)}{\partial x_l}\bar{I}_j\bar{I}_l + \frac{\partial\phi}{\partial x_j}(\mathbf{x}_0)\frac{\partial^2\lambda_i(\mathbf{x}_0)}{\partial x_l\partial x_m}\bar{I}_j\bar{I}_l\bar{I}_m \\ &\quad + \frac{\partial^2\phi(\mathbf{x}_0)}{\partial x_j\partial x_k}\lambda_i(\mathbf{x}_0)\bar{I}_j\bar{I}_k + \frac{\partial^2\phi(\mathbf{x}_0)}{\partial x_j\partial x_k}\frac{\partial\lambda_i(\mathbf{x}_0)}{\partial x_l}\bar{I}_j\bar{I}_k\bar{I}_l \\ &\quad + \frac{\partial^2\phi(\mathbf{x}_0)}{\partial x_j\partial x_k}\frac{\partial^2\lambda_i(\mathbf{x}_0)}{\partial x_l\partial x_m}\bar{I}_j\bar{I}_k\bar{I}_l\bar{I}_m \end{aligned} \quad (\text{A.4})$$

The series expansion of the particle volume fraction α_p is

$$\bar{\alpha}_p(\mathbf{x}) = \alpha_p(\mathbf{x}_0) + \frac{\partial\alpha_p}{\partial x_j}(\mathbf{x}_0)\bar{I}_j + \frac{1}{2} \frac{\partial^2\alpha_p}{\partial x_j\partial x_k}(\mathbf{x}_0)\bar{I}_{jk} \quad (\text{A.5})$$

The series expansion of the filtered gas velocity $\tilde{U}_{g,i}$ by replacing the unweighted filtering with Favre-filtering is given as:

$$\tilde{U}_{g,i}(\mathbf{x}) = \tilde{U}_{g,i}(\mathbf{x}_0) + \frac{\partial \tilde{U}_{g,i}}{\partial x_l}(\mathbf{x}_0) \tilde{I}_l + \frac{1}{2} \frac{\partial^2 \tilde{U}_{g,i}}{\partial x_l \partial x_m}(\mathbf{x}_0) \tilde{I}_{lm}. \quad (\text{A.6})$$

The filtering of the multiplication of the particle volume fraction and gas velocity is

$$\begin{aligned} \overline{\alpha_p U_{g,i}}(\mathbf{x}) &= \alpha_p(\mathbf{x}_0) U_{g,i}(\mathbf{x}_0) + \left[\alpha_p(\mathbf{x}_0) \frac{\partial U_{g,i}(\mathbf{x}_0)}{\partial x_j} + U_{g,i}(\mathbf{x}_0) \frac{\partial \alpha_p(\mathbf{x}_0)}{\partial x_j} \right] \bar{I}_j \\ &\quad + \frac{1}{2} \left[\alpha_p(\mathbf{x}_0) \frac{\partial^2 U_{g,i}(\mathbf{x}_0)}{\partial x_j \partial x_k} + U_{g,i}(\mathbf{x}_0) \frac{\partial^2 \alpha_p(\mathbf{x}_0)}{\partial x_j \partial x_k} \right] \bar{I}_{jk} \\ &\quad + \frac{\partial \alpha_p}{\partial x_j}(\mathbf{x}_0) \frac{\partial U_{g,i}}{\partial x_j}(\mathbf{x}_0) \bar{I}_{jk}. \end{aligned} \quad (\text{A.7})$$

The general model for the sub-grid drift flux, $\bar{\alpha}_p \tilde{V}_{d,i} = \overline{\alpha_p U_{g,i}} - \bar{\alpha}_p \tilde{U}_{g,i}$, can be obtained by the subtraction of the multiplication of Eq. (A.5) and Eq. (A.6) from Eq. (A.7) as

$$\begin{aligned} \bar{\alpha}_p \tilde{V}_{d,i} &= \frac{1}{2} \alpha_p \frac{\partial^2 U_{g,i}}{\partial x_j \partial x_k} \bar{I}_{jk} - \frac{1}{2} \alpha_p \frac{\partial^2 U_{g,i}}{\partial x_l \partial x_m} \tilde{I}_{lm} + \frac{\partial \alpha_p}{\partial x_j} \frac{\partial U_{g,i}}{\partial x_k} \bar{I}_{jk} \\ &\quad - \frac{1}{4} \frac{\partial^2 \alpha_p}{\partial x_j \partial x_k} \frac{\partial^2 U_{g,i}}{\partial x_l \partial x_m} \bar{I}_{kl} \tilde{I}_{lm}. \end{aligned} \quad (\text{A.8})$$

with $\bar{I}_k = 0$ if \mathbf{x}_0 is the centroid of the filtering volume. By following Okong'o and Bellan (2004), we assume $\bar{I}_j \simeq \tilde{I}_j$ and $\bar{I}_{jk} \simeq \tilde{I}_{jk}$. For a cubic top-hat filter, \bar{I}_{jk} is equal to $\bar{\Delta}^2 \delta_{jk}/12$ leading to

$$\bar{\alpha}_p \tilde{V}_{d,i} = \frac{\bar{\Delta}^2}{12} \frac{\partial \alpha_p}{\partial x_j} \frac{\partial U_{g,i}}{\partial x_j} - \frac{\bar{\Delta}^4}{576} \frac{\partial^2 \alpha_p}{\partial x_j \partial x_k} \frac{\partial^2 U_{g,i}}{\partial x_j \partial x_k}. \quad (\text{A.9})$$

BIBLIOGRAPHY

- Agrawal, K., Loezos, P., Syamlal, M. and Sundaresan, S. (2001), 'The role of meso-scale structures in rapid gas–solid flows', *Journal of Fluid Mechanics* **445**, 151–185.
- Andreux, R. (2001), Etude expérimentale et numérique d'un séparateur gaz-solide en sortie du riser d'un pilote froid de FCC, PhD thesis.
- Andreux, R., Petit, G., Hemati, M. and Simonin, O. (2008), 'Hydrodynamic and solid residence time distribution in a circulating fluidized bed: Experimental and 3D computational study', *Chemical Engineering and Processing: Process Intensification* **47**(3), 463–473.
- Andrews, A. I., Loezos, P. N. and Sundaresan, S. (2005), 'Coarse-grid simulation of gas-particle flows in vertical risers', *Industrial Engineering Chemistry Research* **44**(16), 6022–6037.
- Arastoopour, H. (2001), 'Numerical simulation and experimental analysis of gas/solid flow systems: 1999 Fluor-Daniel plenary lecture', *Powder Technology* **119**(2-3), 59–67.
- Balzer, G., Böelle, A. and Simonin, O. (1995), Eulerian gas-solid flow modelling of dense fluidized bed, in 'FLUIDIZATION VIII, Proc. International Symposium of the Engineering Foundation', pp. 409–418.
- Bardina, J., Ferziger, J. H. and Reynolds, W. C. (1983), Improved turbulence models based on large eddy simulation of homogeneous, incompressible turbulent flows, Technical report, Rep. TF-19, Dept. of Mech. Engng, Stanford University, Stanford, CA.
- Batrak, O. (2005), Etudes numérique et expérimentale de l'hydrodynamique des lits fluidisés circulants gaz-particules avec prise en compte de la polydispersion granulométrique, PhD thesis.
- Benyahia, S., Arastoopour, H., Knowlton, T. M. and Massah, H. (2000), 'Simulation of particles and gas flow behavior in the riser section of a circulating fluidized bed using the kinetic theory approach for the particulate phase', *Powder Technology* **112**(1-2), 24–33.
- Cao, J. and Ahmadi, G. (1995), 'Gas-particle two-phase turbulent flow in a vertical duct', *International Journal of Multiphase Flow* **21**(6), 1203–1228.
- Chapman, S. and Cowling, T. G. (1991), 'The mathematical theory of non-uniform gases'.
- Clark, R. A., Ferziger, J. H. and Reynolds, W. C. (1979), 'Evaluation of subgrid-scale models using an accurately simulated turbulent flow', *Technical Report, Stanford University TF-19 5/83* **91**(01), 1–16.
- Dasgupta, S., Jackson, R. and Sundaresan, S. (1994), 'Turbulent gas-particle flow in vertical risers', *AIChE Journal* **40**(2), 215–228.
- De Wilde, J. (2005), 'Reformulating and quantifying the generalized added mass in filtered gas-solid flow models', *Physics of Fluids* **17**(11), 113304.

- Gidaspow, D. (1994), *Multiphase Flow and Fluidization*, Academic.
- Gidaspow, D., Jung, J. and Singh, R. K. (2004), 'Hydrodynamics of fluidization using kinetic theory: an emerging paradigm: 2002 Flour-Daniel lecture', *Powder Technology* **148**(2-3), 123–141.
- Gobin, A., Neau, H., Simonin, O., Llinas, J.-R., Reiling, V. and Selo, J.-L. (2003), 'Fluid dynamic numerical simulation of a gas phase polymerization reactor', *International Journal for Numerical Methods in Fluids* **43**(10-11), 1199–1220.
- Grad, H. (1949), 'On the kinetic theory of rarefied gases', *Communications on Pure and Applied Mathematics* **2**(4), 331–407.
- Hansen, K. G. (2005), A Three-Dimensional Numerical Study of Gas-Particle Flow and Chemical Reactions in Circulating Fluidized Bed Reactors, PhD thesis, Aalborg University.
- He, J. and Simonin, O. (1993), Non-equilibrium prediction of the particle phase stress tensor in vertical pneumatic conveying, in 'ASME FED Gas Solid Flows', Vol. 166.
- Heynderickx, G. J., Das, A. K., Wilde, J. D. and Marin, G. B. (2004), 'Effect of clustering on gas-solid drag in dilute flows', *Industrial Engineering Chemistry Research* **43**(16), 4635–4646.
- Hosseini, S. H., Zivdar, M., Rahimi, R. and A, S. (2009), 'CFD simulation of solid hold-up in gas-solid fluidized bed at high gas velocities', *Chemical Product and Process Modeling* **4**(1).
- Hrenya, C. M. and Sinclair, J. L. (1997), 'Effects of particle-phase turbulence in gas-solid flows', *AIChE Journal* **43**(4), 853–869.
- Igci, Y., Andrews, A. T., Sundaresan, S., Pannala, S. and O'Brien, T. (2008), 'Filtered two-fluid models for fluidized gas-particle suspensions', *AIChE Journal* **54**(6), 1431–1448.
- Igci, Y. and Sundaresan, S. (10.1021/ie200190q), 'Constitutive models for filtered Two-Fluid models of fluidized Gas-Particle flows', *Industrial & Engineering Chemistry Research* **0**(0).
- Jenkins, J. and Richman, M. (1985), 'Grad's 13-moment system for a dense gas of inelastic spheres', *Archive for Rational Mechanics and Analysis* **87**(4).
- Jones, D. S. J. and Pujadó, P. R. (2006), *Handbook of petroleum processing*, Springer.
- Kuipers, J., van Swaaij, W. and Wei, J. (1998), Computational fluid dynamics applied to chemical reaction engineering, Vol. Volume 24, Academic Press, pp. 227–328.
- Kunii, D. and Levenspiel, O. (1991), *Fluidization engineering*, Butterworth-Heinemann.
- Li, J. and Kwauk, M. (1994), *Particle-Fluid Two-Phase Flow Energy-Minimization Multi-scale Method*, Metallurgical Industry Press: Beijing.
- Lilly, D. K. (1992), 'A proposed modification of the germano subgrid-scale closure method', *Physics of Fluids A: Fluid Dynamics* **4**(3), 633.

- Liu, S., Meneveau, C. and Katz, J. (1994), 'On the properties of similarity subgrid-scale models as deduced from measurements in a turbulent jet', *Journal of Fluid Mechanics* **275**, 83–119.
- Lun, C. K. K. and Savage, S. B. (1986), 'The effects of an impact velocity dependent coefficient of restitution on stresses developed by sheared granular materials', *Acta Mechanica* **63**(1-4), 15–44.
- Lun, C. K. K., Savage, S. B., Jeffrey, D. J. and Chepuruiy, N. (1984), 'Kinetic theories for granular flow: Inelastic particles in couette flow and slightly inelastic particles in a general flowfield', *Journal of Fluid Mechanics* **140**, 223–256.
- Ma, D. and Ahmadi, G. (1986), 'An equation of state for dense rigid sphere gases', *The Journal of Chemical Physics* **84**(6), 3449.
- Maxey, M. R. (1983), 'Equation of motion for a small rigid sphere in a nonuniform flow', *Physics of Fluids* **26**(4), 883.
- McKeen, T. and Pugsley, T. (2003), 'Simulation and experimental validation of a freely bubbling bed of FCC catalyst', *Powder Technology* **129**(1-3), 139–152.
- Moreau, M., Simonin, O. and Bédard, B. (2009), 'Development of gas-particle Euler-Euler LES approach: a priori analysis of particle sub-grid models in homogeneous isotropic turbulence', *Flow, Turbulence and Combustion* **84**(2), 295–324.
- Neri, A. and Gidaspow, D. (2000), 'Riser hydrodynamics: Simulation using kinetic theory', *AIChE Journal* **46**(1), 52–67.
- Nieuwland, J. J., van Sint Annaland, M., Kuipers, J. A. M. and van Swaaij, W. P. M. (1996), 'Hydrodynamic modeling of gas/particle flows in riser reactors', *AIChE Journal* **42**(6), 1569–1582.
- O'Brien, T. J. and Syamlal, M. (1993), Particle cluster effects in the numerical simulation of a circulating fluidized bed, in A. A., ed., 'Circulating Fluidized Bed Technology. IV. Proceedings of the Fourth International Conference on Circulating Fluidized Beds'.
- Ogawa, S., Umemura, A. and Oshima, N. (1980), 'On the equations of fully fluidized granular materials', *Zeitschrift für angewandte Mathematik und Physik ZAMP* **31**(4), 483–493.
- Okong'o, N. A. and Bellan, J. (2004), 'Consistent Large-Eddy simulation of a temporal mixing layer laden with evaporating drops. part 1. direct numerical simulation, formulation and a priori analysis', *Journal of Fluid Mechanics* **499**, 1–47.
- Özel, A., Parmentier, J. F., Simonin, O. and Fedde, P. (2010), A priori test of effective drag modeling for filtered two-fluid model simulation of circulating and dense gas-solid fluidized beds, in '7th International Conference on Multiphase Flow - ICMF 2010 Proceedings', International Conference on Multiphase Flow (ICMF).
- Parmentier, J.-F. (2010), Extension of the Euler-Euler formalism for numerical simulations of fluidized beds of Geldart A particles, PhD thesis.

- Parmentier, J., Simonin, O. and Delsart, O. (2012), 'A functional subgrid drift velocity model for filtered drag prediction in dense fluidized bed', *AIChE Journal* **58**(4), 1084–1098.
- Petit, G. (2005), Contribution A L'étude Experimentale Et Numerique du Comportement Des Phases Gaz Et Solide Dans Un Lit Fluidise Circulant: Application Au Procédé FCC, PhD thesis.
- Reeks, M. W. (1991), 'On a kinetic equation for the transport of particles in turbulent flows', *Physics of Fluids* **3**(3), 446–456.
- Sadeghbeigi, R. (2000), *Fluid catalytic cracking handbook: design, operation, and troubleshooting of FCC facilities*, Gulf Professional Publishing.
- Sagaut, P. (2004), *Large Eddy Simulation for Incompressible Flows*, 2nd edn, Springer.
- Samuelsberg, A. and Hjertager, B. H. (1996), 'An experimental and numerical study of flow patterns in a circulating fluidized bed reactor', *International Journal of Multiphase Flow* **22**(3), 575–591.
- Schiller, L. and Naumann, Z. (1935), 'A drag coefficient correlation', *Z. Ver. Deutsch. Ing.* **77**, 318.
- Simonin, O. (1990), Eulerian formulation for particle dispersion in turbulent two-phase flows, in '5th Workshop on Two-Phase Flow Predictions, Erlangen, FRG', pp. 156–166.
- Simonin, O. (1991b), Prediction of the dispersed phase turbulence in particle-laden jets, in 'Proc. 4th Int. Symp. on Gas-Solid Flows, ASME FED', Vol. 121, pp. 197–206.
- Simonin, O. (1996), *Continuum modeling of dispersed two-phase flows*, In: Combustion and Turbulence in Two-Phase Flows, Lecture Series 1996-02, von Karman Institute for Fluid Dynamics, Brussels, Belgium.
- Simonin, O., Deutsch, E. and Minier, J. P. (1993), 'Eulerian prediction of the fluid/particle correlated motion in turbulent two-phase flows', *Applied Scientific Research* **51**(1-2), 275–283.
- Simonin, O. and Viollet, P. L. (1990), Modelling of turbulent two-phase jets loaded with discrete particles, in G. F. Hewitt, F. Mayinger and J. R. Riznic, eds, 'Phase-Interphase Phenomena in Multiphase Flow', Hemisphere Publishing Corp., pp. 259–269.
- Smagorinsky, J. (1963), 'General circulation experiments with the primitive equations', *Monthly Weather Review* **91**(3), 99–164.
- Sundaresan, S. (2000), 'Modeling the hydrodynamics of multiphase flow reactors: Current status and challenges', *AIChE Journal* **46**(6), 1102–1105.
- van der Hoef, M., van Sint Annaland, M., Deen, N. and Kuipers, J. (2008), 'Numerical simulation of dense gas-solid fluidized beds: a multiscale modeling strategy', *Annual Review of Fluid Mechanics* **40**(1), 47–70.

- van der Meer, E. H., Thorpe, R. B. and Davidson, J. F. (2000), 'Flow patterns in the square cross-section riser of a circulating fluidised bed and the effect of riser exit design', *Chemical Engineering Science* **55**(19), 4079–4099.
- Vermorel, O., Bedat, B., Simonin, O. and Poinso, T. (2003), 'Numerical study and modelling of turbulence modulation in a particle laden slab flow', *Journal of Turbulence* **4**.
- Viollet, P. L. and Simonin, O. (1994), 'Modelling dispersed Two-Phase flows: Closure, validation and software development', *Applied Mechanics Reviews* **47**(6S), S80–S84.
- Vreman, B., Geurts, B. and Kuerten, H. (1996), 'Large-eddy simulation of the temporal mixing layer using the clark model', *Theoretical and Computational Fluid Dynamics* **8**(4), 309–324.
- Wang, J. (2009), 'A review of eulerian simulation of geldart A particles in gas-fluidized beds', *Industrial Engineering Chemistry Research* **48**(12), 5567–5577.
- Wang, J., Ge, W. and Li, J. (2008), 'Eulerian simulation of heterogeneous gas-solid flows in CFB risers: EMMS-based sub-grid scale model with a revised cluster description', *Chemical Engineering Science* **63**(6), 1553–1571.
- Wang, W. and Li, J. (2007), 'Simulation of gas-solid two-phase flow by a multi-scale CFD approach—of the EMMS model to the sub-grid level', *Chemical Engineering Science* **62**(1–2), 208–231.
- Weinstein, H., N. S. and Wasserzug, L. (1984), 'Radial solid density in vertical gas-solid contact systems', *AIChE Symp. Ser* **80**, 117.
- Wen, C. Y. and Yu, Y. H. (1966), 'Mechanics of fluidization', *Chem. Engng Prog. Symp. Ser* **62**, 100–111.
- Yang, N., Wang, W., Ge, W. and Li, J. (2003), 'CFD simulation of concurrent-up gas-solid flow in circulating fluidized beds with structure-dependent drag coefficient', *Chemical Engineering Journal* **96**(1–3), 71–80.
- Yang, W. (2003), *Handbook of Fluidization and Fluid-Particle Systems*, CRC Press.
- Yoshizawa, A. (1986), 'Statistical theory for compressible turbulent shear flows, with the application to subgrid modeling', *Physics of Fluids* **29**(7), 2152.
- Zang, T. A., Dahlburg, R. B. and Dahlburg, J. P. (1991), Direct and large-eddy simulations of three-dimensional compressible Navier-Stokes turbulence, Technical report, Interim Rept., Naval Research Lab. , Washington DC.
- Zhang, D. Z. and VanderHeyden, W. B. (2002), 'The effects of mesoscale structures on the macroscopic momentum equations for two-phase flows', *International Journal of Multiphase Flow* **28**(5), 805–822.
- Zimmermann, S. and Taghipour, F. (2005), 'CFD modeling of the hydrodynamics and reaction kinetics of FCC fluidized-bed reactors', *Industrial Engineering Chemistry Research* **44**(26), 9818–9827.

PUBLICATIONS

A. Ozel, P. Fede, O. Simonin. *3D Numerical Prediction of gas-solid flow behaviour in CFB risers for Geldart A and B particles*, Proceedings of the 20th International Conference on Fluidized Bed Combustion: Yue, G.; Zhang, H.; Zhao, C.; Luo, Z. (Eds.), Springer, 2009.

A. Ozel, D. Wunsch, M. Maglio, Z. Zeren, B. Bedat, P. Fede, D. Legendre, O. Simonin. *Modelling of Multiphase Flows: From micro to macro-scale approaches*, ERFOCTAC/Combustion Institute Workshop on Measurement and Computation of Turbulent Spray Combustion, Corsica, France, 2009.

A. Ozel, P. Fede, O. Simonin. *The Effective Drag Closure for Gas-Solid Flows in Vertical Risers*, AIChE Annual Meeting, Nashville, USA, November 8-13, 2009.

A. Ozel, J.F. Parmentier, O. Simonin, P. Fede. *A Priori Test of Effective Drag Modeling for Filtered Two-Fluid Model Simulation of Circulating and Dense Gas-Solid Fluidized Beds*, International Conference on Multiphase Flow 2010, Tampa, May 30 -June 4, 2010, USA.

he is like a man using candle to look for the sun

Rumi

philosophy, art, and science are not the mental objects of an objectified brain but the
three aspects under which the brain becomes subject

Gilles Deleuze

Kid A, petit a

Radiohead, Jacques Lacan